Quantifying supraglacial debris thickness at local to regional scales

Michael James McCarthy

Scott Polar Research Institute

University of Cambridge

&

British Antarctic Survey

This dissertation is submitted for the degree of

Doctor of Philosophy

Jesus College

December 2018

Declaration

This dissertation is the result of my own work and includes nothing which is the outcome of work done in collaboration except as declared in the preface and specified in the text. It is not substantially the same as any that I have submitted, or, is being concurrently submitted for a degree or diploma or other qualification at the University of Cambridge or any other university or similar institution except as declared in the preface and specified in the text. I further state that no substantial part of my dissertation has already been submitted, or, is being concurrently submitted for any such degree, diploma or other qualification at the University of Cambridge or any other university or similar institution except as declared in the preface and specified in the text. It does not exceed the prescribed page limit of 225 pages.

Michael James McCarthy

December 2018

Abstract

Quantifying supraglacial debris thickness at local to regional scales

Michael James McCarthy

Supraglacial debris thickness is a key control on the surface energy balance of debris-covered glaciers, which are common in temperate mountain ranges around the world. As such, it is an important input variable to the sorts of models that are used to understand and predict glacier change, which are essential for determining future water supply in glacierised regions and glacier contributions to sea-level rise. However, to quantify supraglacial debris thickness is difficult: making direct measurements is laborious and existing remote sensing approaches have not been thoroughly validated, so there is a general paucity of supraglacial debris thickness data. This thesis investigates methods of quantifying supraglacial debris thickness at local to regional scales. First, it makes *in-situ* field measurements of debris thickness at the local scale on glaciers in the Himalaya and the European Alps by manual excavation and by ground-penetrating radar (GPR). Second, it uses some of these field measurements to test and develop thermal remote sensing approaches to quantifying supraglacial debris thickness at the glacier scale. Third, it uses a dynamic energy-balance model in an inverse approach to quantify debris thickness on the glaciers of three watersheds in High Mountain Asia from thermal satellite imagery and high-resolution meteorological reanalysis data.

At the local scale, GPR is found to be useful for measuring supraglacial debris thickness accurately and precisely, at least in the range 0.16-4.9 m. Debris thickness is highly variable over horizontal distances of < 10 m on individual glaciers due to gravitational reworking, which necessarily implies higher sub-debris ice melt rates than if debris thickness was spatially invariable. At the glacier scale, thermal remote sensing approaches can reproduce field measurements, and remote sensing estimates of supraglacial debris thickness can be used successfully to model sub-debris melting. If well-distributed field measurements are available, supraglacial debris thickness should be extrapolated using remote sensing-derived pseudo daily mean surface temperatures. Otherwise, it should be determined iteratively by minimising the mismatch between remotely sensed surface temperatures, preferably from night-time thermal images, and surface temperatures determined using a dynamic

energy-balance model. At the regional scale, thermal satellite imagery and high-resolution meteorological reanalysis data can be used to provide reasonable estimates of supraglacial debris thickness. However, modelled uncertainties are not always able to explain ground-truth measurements, and there is a tendency towards underestimation due to problems associated with supraglacial ponds and ice cliffs and the spatial resolution of input data.

The findings of this thesis will lead to improvements in the quantification of supraglacial debris thickness at a range of scales and, therefore, in the understanding and prediction of glacier change in temperate mountain ranges.

Acknowledgements

This thesis has been made possible by a large number of people and organisations, to whom I am incredibly grateful. Therefore, **thank you…**

To my PhD supervisors, Hamish Pritchard and Ian Willis, for guiding and inspiring me, for helping me plan and carry out fieldwork, and for sharing their glaciological expertise.

To all those who provided me with data, advice, model code, funding, or helped with fieldwork. Huge thanks are due to Lindsey Nicholson, whose support has been invaluable, for sharing ideas, enthusiasm, debris thickness and meteorological data, thermistor-string code, and for making possible many of my numerous field trips. To Dave Rounce, for sharing energy-balance modelling expertise and debris thickness data. To Christoph Mayer, for providing the GPR system that was used on Ngozumpa Glacier, and for sharing debris thickness data. To Tim Reid, for providing the code for the DEB model, which was modified and used to perform parts of the modelling and remote sensing work of chapters 4 and 5. To the Ngozumpa Glacier field team, who helped collect GPR data: Anna Wirbel, Costanza del Gobbo, Mohan Chand, Anna Sinisalo, Ursula Blumthaler. To Tek and his team of porters, for facilitating fieldwork on Lirung Glacier. To Ed King, for sharing his expertise in radioglaciology, and to Rob Arthern, for providing advice on uncertainties and Monte Carlo simulations. To Neil Arnold, for providing code with which to account for topographic shading, and to Gareth Rees, for providing First Year Report advice. To Adam Copeland and Steve Boreham, for helping to procure field equipment. To the reviewers of the papers that parts of this thesis were published in, for their insightful comments: Adam Booth, Peter Moore, and two who remained anonymous. To Lorenzo Rieg for sharing the Ngozumpa Glacier elevation model. To John Reynolds for sharing his expertise in geophysics, and to Reynolds International Ltd for generously providing CASE sponsorship. To the UK Natural Environment Research Council, NERC, for providing funding under DTP grant number NE/L002507/1. To the NERC Geophysical Equipment Facility, for the loan of the GPR system that was used on Lirung Glacier, under grant number 1014. To the Ev-K2-CNR Association for making available Pyramid Station meteorological data, some of which was used in Chapter 3. To the Autonomous Province of Bozen Weather Service team, who provided some of the

meteorological data used in Chapter 4. To those who helped make the Suldenferner Glacier debris thickness measurements used in Chapter 3. To Philip Kraaijenbrink for making publicly available the glacier surface classification code that was used in Chapter 5. To Maussion et al. (2014), for making publicly available the High Asia Refined analysis dataset, which was used in Chapter 5. To NASA, JAXA and Google Earth for making publicly available the satellite images and data products that were used throughout this thesis. To the authors of functions that were used from the MATLAB File Exchange.

To my friends and family. Particularly to Mum, Dad and Meg for constant support and encouragement.

Contents

List of figures

List of tables

Acronyms and abbreviations

a.s.l	Above sea level
ALOS	Advanced Land Observation Satellite
AST05	ASTER L2 Surface Emissivity V003 product
AST08	ASTER L2 Surface Temperature V003 product
AST14DMO	ASTER L3 Orthorectified Radiance at the Sensor V003 product
ASTER	Advanced Spaceborne Thermal Emission and Reflection Radiometer
AW3D30	ALOS Global Digital Surface Model v.2.1
AWS	Automatic weather station
B	Spectral band of satellite image
BQA	Quality assessment band of satellite image
CGIAR-CSI	Consortium for Spatial Information
CMP	Common midpoint
CO_2	Carbon dioxide
DC	Direct current
DEB	Dynamic energy-balance approach used for debris thickness quantification
DEM	Digital elevation model
DGPS	Differential Global Positioning System
ESA	European Space Agency
Exp't	Experiment
EXT	Extrapolation approach used for debris thickness quantification
GDEM	ASTER Global Digital Elevation Map
GED	Global Emissivity Dataset
GLOF	Glacial lake outburst flood
GPR	Ground-penetrating radar
GPS	Global Positioning System
HAR	High Asia Refined analysis dataset
HEG	Hdf-Eos to GIS (conversion tool)

HMA	High Mountain Asia
IDW	Inverse distance weighted
IPCC	Intergovernmental Panel on Climate Change
IQ	Interquartile
JAXA	Japan Aerospace Exploration Agency
MAD	Median absolute deviation
MAE	Median absolute error
ME	Median error
NASA	National Aeronautics and Space Administration
NCAR	National Center for Atmospheric Research
NCEP	National Centers for Environmental Prediction
NDBI	Normalised Difference Blue Index
NDSI	Normalised Difference Snow Index
NDVI	Normalised Difference Vegetation Index
NR	Not reported
NSE	Nash-Sutcliffe model efficiency coefficient
PALSAR	Phased Array type L-band Synthetic Aperture Radar
r	Correlation coefficient
r^2	Coefficient of determination
RGI	Randolph Glacier Inventory
RMSE	Root-mean-square error
ROC	Receiver operating characteristic
SAR	Synthetic-aperture radar
SCA	Scaling approach used for debris thickness quantification
SD	Standard deviation
SEB	Static energy-balance approach used for debris thickness quantification
SRTM	Shuttle Radar Topography Mission
TES	ASTER temperature/emissivity separation algorithm
TPR	True positive rate
TWTT	Two-way travel time
UAV	Unmanned aerial vehicle
UTC	Coordinated Universal Time
UTM	Universal Transverse Mercator coordinate system
w.e	Water equivalent
IACS	International Association of Cryospheric Sciences

WRF	Weather Research and Forecasting model

Mathematical notation

A	Amplitude, solar azimuth
a	Antenna separation
A'	Surface aspect
A_{deb}	Debris-covered area including missed ponds and ice cliffs
$A_{deb_{corr}}$	Debris-covered area excluding missed ponds and ice cliffs
A_l	Landsat 8 B10 radiance additive scaling factor
A_{miss}	Area of missed ponds and ice cliffs
b_γ	Constant used to calculate surface temperature from thermal satellite imagery
c_1, c_2 …	Free parameters
c_{1_n}, c_{2_n}	Earth-sun distance coefficients
c_a	Specific heat capacity of air
C_d	Debris volumetric heat capacity
c_d	Debris specific heat capacity, concentration of debris in ice
c_p	Specific heat capacity of air at constant pressure
c_r	Specific heat capacity of rock
c_w	Specific heat capacity of water
D	Digitisation interval
d	Earth-sun distance
E	Solar elevation
e_a	Partial pressure of water vapour at the measurement height
e_{a_s}	Saturation vapour pressure at the measurement height
e_s	Partial pressure of water vapour at the surface
e_x	Partial pressure of water vapour at the surface or at the measurement height
F	Factor of safety
f	GPR operating frequency
f_{deb}	Debris pixel fraction

f_{diff}	Diffuse radiation fraction
f_{ip}	Pixel fraction comprising ponds and ice cliffs
FN	False negative (ROC terminology)
FP	False positive (ROC terminology)
f_{pix}	Whole pixel fraction
G	Conductive heat flux
g	Acceleration due to gravity
G_i	Conductive heat flux at the ice surface
h	Debris thickness
H	Sensible heat flux
HC_n	Index-number of chosen half cycle
h_{lower}	Debris thickness lower limit
h_{max}	Maximum debris thickness value
h_{min}	Minimum debris thickness value
h_{new}	New debris thickness value
h_{upper}	Debris thickness upper limit
I	Clear-sky direct shortwave radiation
I_0	Solar constant
I_{AWS}	Clear-sky direct shortwave radiation at AWS
I_{HAR}	HAR clear-sky direct shortwave radiation
K_d	Debris saturated hydraulic conductivity
k_d	Debris thermal conductivity
k_{vk}	Von Karman constant
L	Longwave radiative heat flux
$L\uparrow$	Outgoing longwave radiation
$L\downarrow$	Incoming longwave radiation
LE	Latent heat flux
L_f	Latent heat of fusion of water
L_{sen}	Top-of-atmosphere spectral radiance
L_v	Latent heat of vaporisation of water
M	Melt rate
M_a	Molar mass of dry air
M_l	Landsat 8 B10 multiplicative scaling factor
mod	Modelled value

n_c	Cloud-cover fraction
n_{ip}	Number of ponds and ice cliffs
obs	Observed value
p_0	Standard pressure at sea level
p_a	Atmospheric pressure
P_r	Reflection power
q_a	Specific humidity at the measurement height
Q_{cal}	Digital numbers representing scaled radiance values
q_s	Specific humidity at the debris surface
q_x	Specific humidity at the surface or at the measurement height
R	Standard atmospheric universal gas constant
r	Precipitation rate
RH	Relative humidity
Ri_b	Bulk Richardson number
S	Shortwave radiative heat flux
$S\uparrow$	Outgoing shortwave radiation
$S\downarrow$	Incoming shortwave radiation
$S\downarrow_{AWS}$	Incoming shortwave radiation at AWS
$S\downarrow_{HAR}$	HAR incoming shortwave radiation
S_{ip}	Size of ponds and ice cliffs
S_{pix}	Pixel size
s_w	Fraction of debris saturated with water
T	Period of time
t	Time, TWTT
T_0	Standard temperature at sea level
t_0	Zero-offset TWTT
$T_{0.1}$	Temperature at 0.1 m depth within the debris
T_a	Air temperature
t_a	TWTT at some antenna separation
$T_{a_{AWS}}$	Air temperature at the AWS
$T_{a_{HAR}}$	HAR air temperature
T_d	Debris temperature
T_i	Temperature of melting ice
T_m	Mean air temperature between debris surface and measurement height

TN	True negative (ROC terminology)
TP	True positive (ROC terminology)
T_r	Precipitation temperature
T_s	Surface temperature
$T_{s_{deb}}$	Unmixed pixel debris surface temperature
$T_{s_{deb_{corr}}}$	Corrected unmixed pixel debris surface temperature
T_{sen}	Top-of-atmosphere brightness temperature
$T_{s_{ip}}$	Surface temperature of ponds and ice cliffs
$T_{s_{max}}$	Maximum surface temperature
$T_{s_{min}}$	Minimum surface temperature
$T_{s_{miss}}$	Temperature of missed ponds and ice cliffs
$T_{s_{P95}}$	95th percentile surface temperature
$T_{s_{pix}}$	Mixed pixel surface temperature
U	Upstream catchment area
u	Wind speed, glacier surface velocity
v	Wave speed
V_p	Debris volume
v_s	Stacking wave speed
w_p	Precipitable water
x	Distance downglacier
Z	Solar zenith angle
z	Elevation, depth in debris
Z'	Surface slope
z_0	Surface roughness length
z_{0_h}	Roughness length of temperature
z_{0_m}	Roughness length of momentum
z_{0_v}	Roughness length of water vapour
z_a	Height of air temperature measurements
z_{AWS}	Elevation of AWS
z_{HAR}	HAR elevation
z_u	Height of wind speed measurements
α	Debris angle of repose
α_d	Debris albedo

Γ	Environmental lapse rate
γ	Parameter for calculating surface temperature from thermal satellite imagery
δ	Parameter for calculating surface temperature from thermal satellite imagery
ΔD	Heat flux due to change in heat storage
Δt	Model time step
ε_{as}	All-sky emissivity
ε_{as}	Clear-sky emissivity
ε_d	Debris surface emissivity
ε_s	Surface emissivity
θ	Incidence angle of solar beam and glacier surface
θ_d	Time of year
κ_d	Debris thermal diffusivity
λ	Wavelength
μ	Debris-ice interface friction coefficient
ξ	First temperature minimum at depth within debris
ρ_a	Density of air
ρ_d	Density of debris
ρ_{d_w}	Density of wet debris
ρ_i	Density of ice
ρ_r	Density of rock
ρ_w	Density of water
σ	Stefan-Boltzmann constant
σ_h	Debris thickness uncertainty
σ_t	TWTT uncertainty
σ_v	Wave speed uncertainty
$\tau_1, \tau_2 \ldots$	Atmospheric functions
φ	Debris porosity
ϕ_h	Non-dimensional stability function for temperature
ϕ_m	Non-dimensional stability function for momentum
ϕ_v	Non-dimensional stability function for water vapour
ψ	Atmospheric transmissivity
ω	Angular frequency of temperature oscillations at the debris surface

1 Introduction

1.1 Background and motivation

Mountain glaciers play a central role in the Hydrological Cycle by storing water during cold, wet periods and releasing it during warm, dry periods (e.g. Kaser et al., 2010). As such, they are an important water resource, an indicator of climatic change, and an existential threat to low-lying island nations via sea-level rise. In the major river basins of South Asia, it is estimated that 800 million people rely on water from glaciers and snowmelt for both domestic and commercial purposes (Bolch et al., 2012; Immerzeel et al., 2010), while glacier length change records describe a trend towards global warming since the mid-1800s and a 0.5°C warming in the course of the 1900s (Oerlemans, 2005; Leclercq and Oerlemans, 2012). Glaciers and ice caps contain ice volumes equivalent of 0.43 +/- 0.06 m of sea-level rise (Huss and Farinotti, 2012), and are contributing 29 +/- 13% to sea-level rise in the present day (Gardner et al., 2013). Mountain glaciers sustain biodiversity and are often sites of cultural and historical significance (Jacobsen et al., 2012; Quincey et al., 2017). They can be sites of potential geomorphological hazards, such as Glacial Lake Outburst Floods (GLOFs) and, at the same time, they can provide ecosystem services such as flood prevention and provision of water for agriculture and hydropower (Dahlke et al., 2012; Milner et al., 2017). They are sites of recreation and tourism, sometimes significantly boosting local economies (Purdie, 2013), and they often straddle international boundaries, which means they are potential objects of political instability and interstate conflict, given that water scarcity is considered to be the largest global risk in terms of potential impact over the coming decade (World Economic Forum, 2015).

Considering the above, and that the global climate is changing rapidly, with global warming likely to reach 1.5°C above pre-industrial levels between 2030 and 2052 (IPCC, 2018), it is important that we are able to predict glacier change as accurately as possible into the future and, in order to do this, that we are able to understand past and present glacier change, and the processes and variables that drive it.

Understanding[1] and predicting glacier change is achieved using numerical models that are forced with either local, regional or global-scale climate data, depending on the scale at which they are being operated. When such models are being used to forecast change, they are often highly simplified, requiring only a few input variables such as air temperature, precipitation, glacier area and ice thickness (e.g. Marzeion et al., 2012; Radić et al., 2014; Huss and Hock, 2015). When they are being used to hindcast glacier change, more complex, fully-distributed energy balance approaches are more common (e.g. Oerlemans, 1992; Arnold et al., 1996; Mölg et al., 2014). Whatever the objective, it is important that models are able to realistically represent the key processes by which glacier change occurs. Such processes could include ice dynamics, frontal ablation or snow redistribution due to wind and avalanching. Omitting or overabstracting important processes will inevitably lead to increased uncertainty and model results that are inconsistent with observations. For example, if a glacier model does not include some representation of ice dynamics, it will not account for mass balance-dynamic feedbacks and may therefore under or overestimate mass balance during periods of advance and retreat, respectively (e.g. Oerlemans, 2001). If a model does not account for variations in incoming shortwave radiation due to shading, there will be too much energy available for melting and the model may overestimate summer mass loss and cause the spatial distribution of melt to be poorly represented (e.g. Arnold et al., 1996; Hock, 1999).

A process that has received lots of attention in recent years, and one that is increasingly included in the sorts of glacier models described above, is modulation of the surface mass balance by supraglacial debris cover. This is because debris-covered glaciers, which are those whose surfaces are covered in a layer of supraglacial rock debris, are common in mountain ranges around the world, and because the effect of supraglacial debris on surface mass balance can be strong. In particular, the melt rate of ice below a layer of supraglacial debris may be either significantly reduced or significantly enhanced from the melt rate of debris-free ice in the same geographic location (e.g. Oestrem, 1959; Mattson et al., 1993). As a result, the presence of supraglacial debris can affect ice dynamics, glacier hydrology and mountain meteorology. For example, in terms of dynamics, debris-covered glaciers have been found to respond quite differently from debris-free glaciers to the same climatic forcing: their fronts are typically stable while nearby debris-free glaciers advance and retreat (Scherler et al., 2011). In terms of hydrology, debris cover promotes the formation of extensive englacial drainage systems and supra and proglacial lakes and ponds, which in turn promote the formation of ice cliffs (e.g. Sakai et al., 2000; Benn et al., 2012; Benn et al., 2017; Miles et al., 2017). In terms of meteorology, debris cover affects glacier-atmosphere interactions and has been found to cause daytime along-glacier winds to be

[1] Often via hindcasting

anabatic rather than katabatic and to strongly alter environmental lapse rates and the conditions of the atmospheric surface layer (Collier et al., 2015; Steiner and Pellicciotti, 2016; Potter et al., 2018).

There are a number of physical properties of a supraglacial debris layer that affect the extent to which it modulates surface mass balance, some or all of which may be included in a glacier model. Primarily, these include its albedo, surface roughness, thermal conductivity, emissivity, density and heat capacity. The albedo of a debris layer, for example affects how much incoming shortwave radiation is absorbed versus how much is reflected back into the atmosphere (e.g. Brock and Arnold, 2000). A debris layer's surface roughness modulates the turbulent exchanges of sensible and latent heat (e.g. Reid and Brock, 2010; Miles et al., 2017; Quincey et al., 2017). However, one of the key physical properties of a debris layer, and the property that is included most in glacier models that include debris cover, is its thickness (e.g. Mihalcea et al., 2006; Juen et al., 2014; Carenzo et al., 2016). Supraglacial debris thickness is a strong control on the conductive heat flux to the ice below the debris, in accordance with Fourier's law, where the conductive heat flux becomes increasingly negligible with increasing debris thickness, and increasingly important with decreasing debris thickness (Evatt et al., 2015). Unfortunately, there are very few glaciers on which supraglacial debris thickness has been measured *in situ* because methods of measuring debris thickness in the field are physically difficult and time consuming. Various remote sensing methods have been proposed for mapping debris thickness over large areas but there are difficulties and uncertainties around these due to a lack of data for calibration and validation (Mihalcea et al., 2008; Foster et al., 2012; Rounce and McKinney, 2014). Ultimately, there is a paucity of debris thickness data at all scales: from the local scale to the glacier scale to the regional and global scales.

An important research question, then, in modern glaciology, is how can we quantify supraglacial debris thickness? Our current inability to quantify supraglacial debris thickness is a limiting factor in our ability to understand and predict glacier change.

This question is particularly pertinent for glaciers in High Mountain Asia, where supraglacial debris cover is unusually prevalent, and where large downstream communities are socially and economically dependent on glacier-fed runoff and vulnerable to drought because of water stress (Pritchard, 2017).

1.2 Aims and approach

Section 1.1 outlines some of the effects of supraglacial debris cover on glacier surface mass balance and the importance of being able to quantify supraglacial debris thickness at a range of scales.

Specifically, it highlights the fact that there is a lack of *in-situ* measurements of debris thickness, and that there is considerable uncertainty associated with methods of quantifying debris thickness by remote sensing. The second of these two points follows naturally from the first because *in-situ* measurements are required to validate remote sensing methods. Therefore, this thesis begins by making *in-situ* field measurements of debris thickness at the local scale, then moves on to test and validate remote sensing methods of quantifying debris thickness over progressively larger areas.

The broad aims of this thesis are:

First, to make local-scale *in-situ* field measurements of debris thickness on a number of glaciers and, in doing this, to test the use of ground-penetrating radar as a method of measuring debris thickness.

Second, to test and develop different thermal remote sensing approaches to quantifying debris thickness at glacier scale using some of the *in-situ* field measurements, and to develop an understanding of the limitations and sensitivities of these approaches.

Third, to test the most appropriate thermal remote sensing approach identified above over some large areas of High Mountain Asia, again using the *in-situ* field measurements, in order to identify its wider transferability.

1.3 This thesis

In accordance with the three aims that are described above, three data chapters (Chapter 3, Chapter 4 and Chapter 5) make up the bulk of this thesis. Before the data chapters, previous work is identified and reviewed (Chapter 2), while after the data chapters, the outcomes of the research are synthesised, conclusions are drawn and suggestions are outlined for future research (Chapter 6). The data and methods that were used are described in sections within the data chapters for ease of reading because different data and methods were used in each part of the research. The study sites that were chosen are also described in sections within the data chapters, although there is some crossover between the study sites of chapters 3 and 4, and chapters 3 and 5.

Most numerical data are reported to two significant figures for readability, unless reporting to more significant figures was necessary for reproducibility. However, calculations were carried out to full precision. Temperatures are presented in degrees Celsius in the text, in figures and in tables because this is conceptually easier. However, the equations require temperature variables to be in kelvin.

2 Previous work

2.1 Glaciology of High Mountain Asia

High Mountain Asia, which encompasses, amongst others, the Himalaya, Karakoram, Hindu Kush, Pamir, Kunlun Shan and Tien Shan mountain ranges, comprises 96000 glaciers and has a total glacierised area of 98000 km^2 (RGI v.5; Pfeffer et al., 2014). This makes it the largest glacierised area outside the Polar Regions. Stored within the glaciers of High Mountain Asia is an estimated ice mass of 4800 Gt (Kraaijenbrink et al., 2017). Via major rivers such as the Indus, the Ganges and the Brahmaputra, these glaciers provide water to an estimated 800 million people, which makes them an important water resource (Immerzeel et al., 2010; Bolch et al., 2012).

Similar to glaciers in other parts of the world, most glaciers in High Mountain Asia are shrinking and losing mass (Bolch et al., 2012; Gardelle et al., 2013; Kääb et al., 2012) and since the 1960s, both mass loss and shrinkage rate have been increasing (Bolch et al., 2012). Brun et al. (2017) found that from 2000 to 2016, glaciers in High Mountain Asia underwent a net mass loss of 0.18 +/- 0.04 m w.e., or 16.3 +/- 3.5 Gt yr^{--1}, but that while most regions are losing mass, some regions are gaining mass (Figure 2.1). Specifically, they found that mass loss is highest in southeast Tibet, while mass gain is highest in the Kunlun Shan. Consistent with the idea of a Karakoram or Pamir-Karakoram anomaly (e.g. Hewitt, 2011; Gardelle et al., 2013), they found that mass balance is near zero in the Pamirs and in the Karakoram. On the other hand, mass balance is moderately negative across the Himalaya and in the Tien Shan. Unsurprisingly, while there are clear trends in regional net mass balance, the net mass balance of individual glaciers in High Mountain Asia ranges widely, from -2 to 0.5 m w.e. yr^{-1} (Brun et al., 2017), with highest mass losses often occurring at lake-terminating glaciers (King et al., 2017; King et al., 2018).

The different regions of High Mountain Asia exhibit different mass balance signals due to differences in their climates, which affect their sensitivity to changes in precipitation and temperature. For example, in the Pamir-Karakoram, the westerlies cause glaciers to be mostly winter-accumulation type

(e.g. Mayer et al., 2006), while in the Himalaya, precipitation is dominated by the Indian and Southeast Asian monsoons, meaning glaciers are mostly summer-accumulation type (Wagnon et al., 2007). Increasing air temperature has more of an effect on summer-accumulation type glaciers because, in addition to increasing ice-melt rates, it causes precipitation to fall as rain rather than snow at lower elevations, reducing accumulation (Fujita, 2008).

Figure showing HMA mass balances removed for copyright reasons. Copyright holder is Springer Nature, 2017.

Figure 2.1 – High Mountain Asia mass balances from 2000 to 2016, taken from Brun et al (2017) and labelled with major mountain ranges.

The dynamics of glaciers in High Mountain Asia are also changing: the surface and therefore the horizontal velocities of most glaciers are decreasing (Scherler et al., 2008; Quincey et al., 2009; Dehecq et al., 2016; Azam et al., 2018). It is likely that this is due to the above-described mass loss trend and an associated reduction in ice flux; as ice thicknesses, and sometimes surface slopes, decrease due to mass loss, ice fluxes and horizontal velocities must also decrease due to decreased driving stress (e.g. Hooke, 2005). However, in regions such as the Karakoram or Kunlun Shan, where mass balance is near zero or slightly positive, surface velocity is mostly stable or increasing. It has been suggested that this might be an artifact of the surging that is common in these regions (Heid and Kääb, 2012; Quincey et al., 2011; Chudley and Willis, 2018). On individual glaciers, surface velocities

range from 0 m yr^{-1} at ice divides and on stagnant, often debris-covered, glacier tongues, to 200 m yr^{-1} at ice falls and areas of glacier with steep surface slope (Dehecq et al., 2015). As glacier dynamics have changed, there has also been a growth and proliferation of glacial lakes (Zhang et al., 2015; Azam et al., 2018), which can become potential hazards (Richardson and Reynolds, 2000).

As mentioned above, one of the main features of glaciers in High Mountain Asia is their debris cover. As with mass balance and dynamics, debris-covered area varies significantly between regions of High Mountain Asia, ranging from around 30% in the Hindu Kush and 25 to 36% in the Everest region, to almost no debris cover in Inner Tibet and the Qilian Shan (Nuimura et al., 2012; Shea, Immerzeel, et al., 2015; Thakuri et al., 2014; Kraaijenbrink et al., 2017). However, the average debris-covered area of glaciers in High Mountain Asia is estimated to be 11% of total glacier area (i.e. 11000 km^2; Kraaijenbrink et al., 2017). Considering that most of this debris cover occurs in ablation zones where ice thickness tends to be great, 18% of ice mass is stored under debris (i.e. 860 Gt). Further, as ice mass is lost, debris-covered area is increasing due to the melting out of englacial debris (Thakuri et al., 2014; Bolch et al., 2008), and there are strong links between the existence of supraglacial debris cover and the occurrence of supraglacial ponds and ice cliffs.

Current forecasts of glacier change indicate that 36% of the ice mass of High Mountain Asia's glaciers (i.e. 1700 Gt) will be lost by 2100 if global warming is limited to 1.5°C in line with the aims of the Paris Agreement of 2015.

2.2 Debris-covered glaciers

2.2.1 Occurrence and characteristics

Debris-covered glaciers are those whose surfaces are partly covered with a continuous layer of rock debris (Figure 2.2). They are common in temperate mountain ranges around the world, such as the Himalaya, the Caucasus, the European Alps, the Andes and the Alaska Range (Nakawo et al., 2000) and tend to form where debris supply rate is high and where accumulation rate is low (Benn et al., 2003). They are often characterised by highly heterogeneous surface topography, which develops due to differential melting, and surface features such as lakes or ponds, ice cliffs and avalanche deposits. They are often slow-flowing with shallow surface slopes near their terminuses, and the insulating effect of a continuous debris covers can cause their ablation zones to become unusually large (Benn et al., 2003). When debris-covered glaciers retreat, they often leave moraine-dammed proglacial lakes,

which means they are more associated with the risk due to Glacial Lake Outburst Floods (GLOFs) than debris-free glaciers (e.g. Quincey et al., 2005). The relationship between debris cover, surface mass balance and glacier evolution is complex and one of the leading uncertainties in predicting the future of high-mountain glaciers (Bolch et al., 2012).

Figure 2.2 – Photograph of Ngozumpa Glacier, Nepal, taken by Hamish Pritchard.

2.2.2 Debris sources, sinks and transport

Glacial debris is derived from a variety of sources. It is transported on, within or under a glacier by several distinct processes and deposited in a sink at the glacier's margin or bed. The nature of a glacier's debris sources and sinks, and of the mechanisms by which its debris is transported, determine whether or not it develops a layer of supraglacial debris, how that debris is distributed across the glacier's surface, and how thick it becomes.

Sources of glacial debris can be either supraglacial or subglacial (Bennett and Glasser, 2011). Primary supraglacial sources to the majority of temperate glaciers are their headwalls, valley sides and nunataks (Hambrey et al., 2008). Debris forms at these locations by erosion (mostly 'frost-shattering', where there is a large temperature range around freezing; Scherler et al., 2011) and is imported to the glacier by rock fall or within avalanches. Where lateral or medial moraines exist, debris can also be sourced from these, and import occurs by moraine failure or by debris flows. From elsewhere,

necessarily fine-grained debris, such as volcanic ash, dust and black carbon, is imported by the wind. In the Himalaya, black carbon is a particularly important form of wind-blown debris because it tends to enhance melting (Xu et al., 2009). The only subglacial debris source is the bed, from which debris is formed by erosion. Rocks and sediments at the bed are crushed, plucked, fractured and abraded by the overlying ice (Hambrey et al., 2008), then entrained either by pressure melting and regelation (refreezing) or by ice deformation processes such as thrusting and folding. However, neither pressure melting and regelation nor thrusting and folding are common in temperate glaciers, which do not typically freeze to the bed. Such processes are more often observed in cold-based glaciers, or those with a mixed thermal regime.

Once imported, debris is distributed around a glacier englacially, supraglacially or subglacially. From a supraglacial position, debris is transported by advection or by the movement of meltwater. In terms of meltwater transport, high-discharge supraglacial streams should be expected to transport more debris than low-discharge supraglacial streams, so more debris should be transported during high-melt periods. On some glaciers, sub-aqueous transport in supraglacial lakes is a consideration (Mertes et al., 2016), and slope processes may laterally redistribute debris if there are steep slopes and strong topographic variability. Debris buried in the accumulation zone by snowfall will be subsumed into the glacier and transported englacially downglacier by advection. The debris that falls into the accumulation zone becomes concentrated, initially, in layers parallel with the accumulation zone's surface (Bennett and Glasser, 2011), although these layers will later deform according to patterns of ice flow and deformation (Wirbel et al., 2018). Debris that is transported englacially by meltwater is often deposited in englacial cavities, from which it later melts out at the surface in distinctive 'dirt cones' (Goodsell et al., 2005). From a subglacial position, debris is transported by advection in regelation layers up to a few metres thick (Bennett and Glasser, 2011).

A glacier exports debris to its moraines, its bed and to the proglacial environment. The primary mechanisms of export are melting out and transport in meltwater, though it is also possible that some fine-grained glacial debris is removed by the wind. Debris is exported from the glacier to the proglacial environment primarily by the glacifluvial system; i.e. by water discharge from the glacier terminus (Benn et al., 2003). Efficient glacifluvial transport, usually in the form of powerful outwash rivers, delivers large volumes of debris to the proglacial environment and results in minimal moraine formation. If a glacier has an inefficient glacifluvial system, on the other hand, and there is not enough water to remove the debris that reaches its margins to the proglacial environment, its margins become 'choked', large lateral and terminal moraines will form, and it may become debris covered. Debris can

also be exported to medial moraines, which occur where flow units meet, or to the bed, by basal melting or downward ice flow in areas of extension (Bennett and Glasser, 2011).

The timescales of debris transport are poorly known. However, it is crucial that if import exceeds export, supraglacial debris will thicken with time and debris-covered area will increase (Gibson et al., 2017; Bolch et al., 2008). Conversely, if export exceeds import, debris will thin with time and debris-covered area will decrease.

2.2.3 Debris cover distribution

The spatial distribution of debris cover varies significantly between glaciers because of the location of debris sources in relation to the glacier surface. In the Himalaya, for example, debris cover is more common on south-facing glaciers because south-facing debris-supply slopes have high debris-production rates (Nagai et al., 2013). South-facing glaciers tend to have continuous debris layers on their ablation zones, while north-facing glaciers tend to develop medial moraines instead. However, a debris distribution characteristic that is ubiquitous is the greater prevalence of debris in ablation zones than in accumulation zones (e.g. Frey et al., 2012). This is because the debris that falls onto an accumulation zone is quickly buried by snow, and because there is a higher sediment flux to the ablation zone via melting. As such, debris cover hypsometry is skewed towards lower elevations, while debris-free hypsometry is skewed towards higher elevations.

Debris thickness varies spatially over the surface of a glacier depending on several factors: (1) on whether the debris layer is being extended or compressed by ice flow, (2) on how much debris is being transported to a particular location from upglacier, (3) on the extent of debris melt out from within the glacier, and (4) on rock fall and debris flows from valley sides and moraines. Key controls on debris thickness can include, therefore, englacial debris content, ice flow, glacier geometry, surface mass balance and the magnitude and frequency of rock fall, debris flow and avalanche events. Because of the way in which these controls interact, debris thickness distribution can be complex. However, existing data show that debris thickness usually increases downglacier, away from the equilibrium line and towards the margins (Nakawo et al., 1986; Kellerer-Pirklbauer, 2008; Figure 2.3). This is because ice flow tends to decrease in these directions and, in the case of increasing debris thickness downglacier, because melt rate and upward vertical (emergence) velocities tend to increase with decreasing elevation. Additionally, debris thickness tends to increase downglacier because glacier width decreases downglacier, and as glacier width decreases, the debris is compressed horizontally.

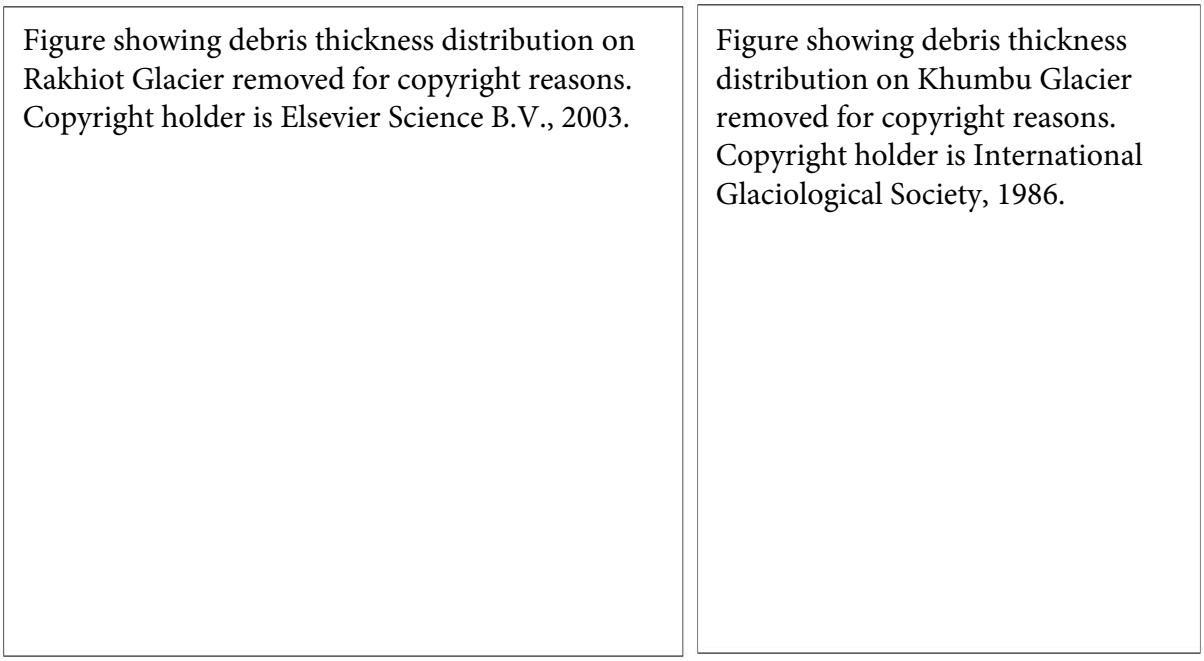

Figure 2.3 – Spatial distributions of supraglacial debris thickness from previous work. (a) Debris thickness on Rakhiot Glacier, Pakistan, Himalaya (taken from Owen et al. 2003). (b) Debris thickness on Khumbu Glacier, Nepal, Himalaya (taken from Nakawo et al. 1986).

Three of the processes that cause spatial variations in debris thickness are described by Equation (2.1), which is the conservation of mass equation of a debris layer in one dimension, where the glacier has a uniform width and debris thickness is in steady state (i.e. debris thickness is not changing with time, e.g. Nakawo et al., 1986; Anderson and Anderson, 2016; also see Benn and Evans, 2014):

$$M\frac{c_d}{\rho_d} = h\frac{du}{dx} + u\frac{dh}{dx} \tag{2.1}$$

Here, u is surface velocity, h is debris thickness, x is distance downglacier, c_d is concentration of debris in ice, ρ_d is the density of the debris and M is the surface melt rate. The first term on the right-hand side is debris thickness change as a result of downglacier variations in horizontal surface velocity. If the velocity gradient du/dx is negative (surface velocity is decreasing), debris thickness increases due to compression, while if the velocity gradient is positive (velocity is increasing), debris thickness decreases due to extension. The second term is debris thickness change due to the advection of debris from upglacier along the glacier surface. Here, if the debris thickness gradient dh/dx is positive, thick debris is being replaced by thin debris and the debris thins due to advection, while if the debris thickness gradient is negative, thin debris is replaced by thick debris and the debris thickens due

to advection. The term on the left-hand side is the addition of debris to the glacier surface by the melting out of englacial debris, which also depends on debris thickness, as discussed below. Effectively, high surface velocities and low debris supply rates (either by melting out or by advection) result in thin debris, while low surface velocities and high debris supply rates result in thick debris. A debris layer is not in steady state when the left-hand side does not balance the right-hand side, in which case debris thickness will vary both spatially and temporally (e.g. Gibson et al., 2017).

In both ablation and accumulation zones, locally thick debris can exist due to rock fall or moraine failure, and debris thickness might change by small amounts due to the deposition of windblown sediments, debris advection in surface water, or debris input to the surface via thrusting and folding.

2.2.4 Mass balance and dynamics

The mass balance and dynamics of debris-covered glaciers are complex and somewhat different from those of debris-free glaciers. This is primarily because the surface mass balance of debris-covered glaciers is modified in a complex way by debris cover and by some of the features with which debris-covered glaciers are often associated. This then has knock-on effects for the dynamics.

In terms of mass balance, while the mass balance distribution of debris-free glaciers is controlled largely by the effects of elevation on air temperature, precipitation patterns and topographic variability, the mass balance distribution of debris-covered glaciers is controlled additionally by the spatial distribution of debris cover and debris thickness, of ice cliffs and ponds, and of avalanche occurrence. An extensive cover of thick debris, for example, can cause debris-covered glaciers to have mass balance gradients that are inverted in the lower ablation zone (Figure 2.4; Benn and Lehmkuhl, 2000; Benn et al., 2012), while ponds and ice cliffs are typically sites of locally enhanced melting and can cause the mass balance distribution of debris-covered glaciers to be highly heterogeneous (Thompson et al., 2016; Nuimura et al., 2012; Pellicciotti et al., 2015; Miles et al., 2018). Avalanching, which is common on debris-covered glaciers because they tend to have shallow surface slopes in their ablation zones due to differential melting caused by debris thickness variability, means that debris-covered glaciers sometimes have mass balance gradients that are highly non-linear in the accumulation zone (Benn and Lehmkuhl, 2000), and the tendency of debris-covered glaciers to develop proglacial lakes means that frontal ablation can be a more important mechanism of mass loss for debris-covered glaciers than it might be for debris-free glaciers in similar locations (e.g. King et al. 2018).

Interestingly, there is some debate over the effects of debris cover on glacier mass balance at larger scales. In some regions, debris-covered glaciers have a more negative mass balance than nearby debris-free glaciers (Vincent et al., 2016; Ragettli et al., 2015; Gardelle et al., 2013), as should be expected if the debris is predominantly thick enough to insulate the ice below it and reduce surface melt rates. However, in other regions, they exhibit similar or even more positive mass balances than nearby debris-free glaciers (Gardelle et al., 2013; Kääb et al., 2012), possibly due to the melt-enhancing effects of ponds and ice cliffs (e.g. Buri et al., 2015; Miles et al., 2018), the presence of large areas of thin debris, or the fact that debris-covered glaciers are often out of equilibrium with their local climate (Banerjee et al., 2017).

In terms of dynamics, debris-covered glaciers do not advance and retreat as much as debris-free glaciers, which is likely because their typically large moraines act as a physical barrier to advance, and because insulation due to thick debris at their margins prevents retreat (Scherler et al., 2011; Benn et al., 2003; Figure 2.4). Instead, they tend to thicken and thin in response to changes in mass balance and often have relatively stable termini. The horizontal velocities and velocity gradients of the of the lower ablation zones of debris-covered glaciers can be significantly reduced compared with those of debris-free glaciers due to reduced driving stress at the bed caused by shallow surface slopes, and many debris-covered glacier tongues are stagnant (Quincey et al., 2009; Benn et al., 2012). Additionally, because of the insulating effect of the debris, debris-covered glaciers, when compared to debris-free glaciers often extend to lower elevations and tend to have bottom-heavy hypsometries, which means they tend to have lower accumulation-area ratios (Benn and Lehmkuhl, 2000).

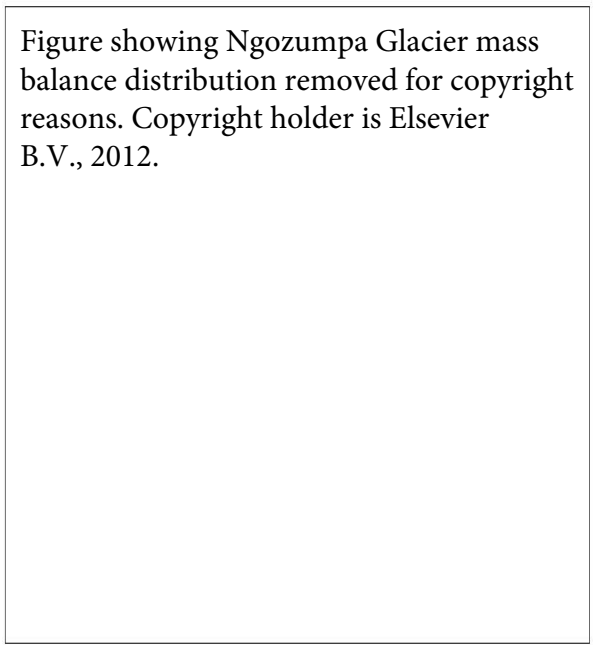

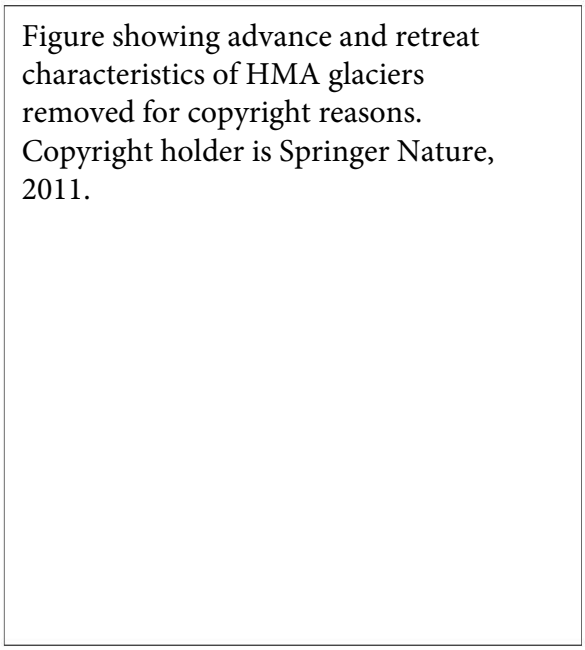

Figure 2.4 – (a) Modelled mass balance distribution of Ngozumpa Glacier, Nepal, taken from Benn et al (2012). (b) Advance and retreat characteristics of variably debris-covered glaciers in the Himalaya, taken from Scherler et al (2011).

2.3 Effects of debris thickness on ice melt

Many studies have explored the relationship between debris thickness and sub-debris ice-melt rate (e.g. Mattson et al., 1993; Kayastha et al., 2000). The first of these studies was carried out by Østrem (1959), so the graph that plots melt rate against debris thickness is often called the Østrem curve (Figure 2.5).

Figure showing Østrem curve removed for copyright reasons. Copyright holder is Springer Science+Business Media B.V., 2001.

Figure 2.5 – Showing the effects of supraglacial debris thickness on sub-debris melt rate, taken from Mattson et al (1993).

The Østrem curve shows that increasing debris thickness from a debris-free ice surface causes sub-debris melt rate to increase, initially, to a maximum value. Then, when a threshold thickness is reached, usually around one or two centimetres, it begins to decrease. At the 'critical thickness', typically around two or three centimetres, the sub-debris melt rate is the same as the debris-free melt rate. Then, from the critical thickness to around half a metre, melt rate initially drops rapidly before levelling out. Increasing debris thickness above half a metre has little effect on melt rate (Nicholson and Benn, 2006). Thus, sub-debris melt rate is high compared to debris-free melt rate if the debris is thinner than the critical thickness, and low if the debris is thicker than the critical thickness. Indeed, Figure 2.5 shows that sub-debris melt rate can vary by an order of magnitude depending on debris thickness. The dominant trend of the Østrem curve – that of decreasing melt rate with increasing debris thickness – occurs because thicker debris better insulates the ice from the radiative and turbulent heat fluxes at the debris surface. However, two mechanisms have been proposed to explain the curve's peak or 'turning point'. First, Mattson et al. (1993) suggested that the peak occurs because when the debris is thin it often only partially covers the ice below it. As the area of ice covered by debris increases, the albedo of that area decreases and the net shortwave radiation flux increases. Second, Evatt et al. (2015) suggested that the peak occurs because evaporation is suppressed as debris

thickness increases, leaving more energy for melting, because the wind is more able to blow through pore spaces in the debris at its surface than it is at depth.

2.4 Glacier models that include debris cover

Supraglacial debris affects mass balance and dynamics primarily by modulating the melt rate of the ice it overlies. For this reason, mass balance models are typically modified for debris only in the way they calculate melt. Accumulation is dealt with as it is for debris-free glaciers (e.g. Fujita and Sakai, 2014; Shea et al., 2015; Kraaijenbrink et al., 2017), i.e. precipitation is assumed to be solid or liquid using a temperature threshold and may or may not be assumed to vary with elevation (e.g. Benn et al., 2012; Marzeion et al., 2012; Maussion et al., 2018). Dynamics are also dealt with as they are for debris-free glaciers, i.e. some sort of ice-flow model is used, usually with a parameterisation for basal sliding (e.g. Huss et al., 2007). A large number of models exist to calculate melt below debris and, as with melt models for debris-free glaciers, these vary in complexity, from simple temperature-index models, or degree-day models, to more sophisticated energy-balance models, depending on the scope of their intended use and on the completeness and quality of the meteorological data with which they are forced. All of the below-mentioned sub-debris melt models, except for the model of Shea et al. (2015), require debris thickness as an input variable in some form or other. Because of the strong effect of debris thickness on melt rate, debris thickness input data should to be as accurate as possible, otherwise melt will be over or underestimated.

2.4.1 Temperature-index and enhanced temperature-index models

Despite their simplicity, temperature-index and enhanced temperature-index models are often used for large-scale, long-duration and future-predictive studies of glacier mass balance, where there is limited or no on-glacier meteorological data available for forcing. They tend to be computationally inexpensive.

For debris-free glaciers, temperature-index models calculate melt on the assumption that melt rate varies linearly with air temperature as long as air temperature is greater than some threshold near 0°C (Braithwaite and Olesen, 1989; Hock, 2003). Air temperature is usually assumed to vary linearly with elevation according to a given lapse rate. As such, temperature-index models require hypsometry, and time-series air temperature and precipitation data as input variables, along with a degree-day factor for ice, and sometimes for snow. They are not usually spatially distributed, but altitudinally distributed.

Degree-day factors vary significantly between sites due to differences in the relative importance of different energy sources for melt, and with albedo and elevation (Hock, 2003). They also vary seasonally due to, e.g. changes in solar radiation and albedo, and are often calibrated or tuned by minimising the differences between model results and historic data.

When applied to debris-covered glaciers, temperature-index models usually require, as additional input variables, altitudinally-distributed debris thickness data and degree-day melt factors for the debris thickness range that exists within the study area (e.g. Kayastha et al., 2000; Kraaijenbrink et al., 2017). They are then used in much the same way as for debris-free glaciers. Studies that have used temperature-index models to calculate melt under debris include those of Juen et al. (2014), Lambrecht et al. (2011), Douglas et al. (2016), Shea et al. (2015), and Kraaijenbrink et al. (2017).

Temperature-index models often reproduce melt quite successfully at large spatial scales and over time periods of longer than a day. However, incoming shortwave radiation can vary considerably both spatially and temporally on glacier surfaces due to topographic effects such as slope, aspect and shading, and is an important source of energy to be used in melting. For this reason, enhanced temperature-index models, which calculate melt from incoming shortwave radiation as well as air temperature, were developed (Hock, 1999; Pellicciotti et al., 2005). In these models, which are often used in a distributed manner, melt is calculated taking topographic effects, as well as elevation, and sometimes albedo into account (e.g. Pellicciotti et al., 2005). Here, in addition to the input data required for temperature index models, radiation factors for snow and ice, an elevation model for topographic effects, and incoming shortwave radiation (either measured or potential) data are often required.

Enhanced temperature-index modelling is more complex for debris-covered glaciers than it is for debris-free glaciers because heat conduction through the debris needs to be accounted for. However, Carenzo et al. (2016) developed an enhanced temperature-index model for sub-debris melting, which includes lag parameters to deal with this problem. In addition to the required input data for debris-free enhanced temperature-index models, the Carenzo et al. (2016) model requires both temperature factors and solar-radiation factors for the debris thickness range that exists within the study area, a lag factor, and distributed debris thickness data.

2.4.2 Energy-balance models

Energy-balance models are typically used to calculate melt accurately at the scale of individual glaciers where there is high quality on-glacier meteorological data (e.g. Arnold et al., 1996), often for

hindcasting, process understanding and sensitivity analyses. They are not usually used for studies of future mass balance, or for mass balance studies at larger scales, because bias correction and downscaling to individual glaciers is difficult for GCM and reanalysis outputs other than temperature and precipitation (Radić and Hock, 2006; Rye et al., 2010).

For debris-free glaciers, energy-balance models usually calculate the radiative and turbulent heat fluxes at the glacier surface using meteorological data, finding the energy available for melting as a residual assuming conservation of energy. Sometimes heat conduction into the ice is considered as well (e.g. Pellicciotti et al., 2009). Melt rates are calculated by dividing the energy available for melting by the product of the density of water and the latent heat of fusion of water. Energy-balance models typically require a relatively full meteorological dataset as input, including incoming shortwave radiation, incoming longwave radiation, air temperature, wind speed and humidity. They also require knowledge of glacier surface properties including surface albedo, roughness length and emissivity, plus an elevation model for topographic effects.

For debris-covered glaciers, energy-balance models usually calculate heat fluxes at the debris surface instead of at the ice surface (e.g. Nicholson and Benn, 2006; Reid and Brock, 2010). As such, they consider there to be a conductive heat flux through the debris as well as radiative and turbulent heat fluxes, and the heat fluxes are calculated by iteratively solving for debris surface temperature such that energy is conserved, assuming that the ice surface below the debris is melting at 0°C. Using daily time steps or longer, heat conduction through the debris is often assumed to be steady state and the temperature gradient through the debris is assumed to be linear. Using sub-daily time steps, heat conduction is assumed to be transient and the debris layer is split into layers so the temperature gradient can be nonlinear. In the first case, the conductive heat flux is assumed equal to the energy available for melting, which is then used to calculate melt rate. In the second case, the conductive heat flux of the debris layer adjacent to the ice surface is the energy available for melting. Studies that have used energy-balance models to calculate melt under debris include those of Han et al. (2006), Mihalcea et al. (2008), Nicholson and Benn (2006), Reid and Brock (2010), Rounce et al. (2015), Lejeune et al. (2013), Evatt et al. (2015), Collier et al. (2014), Collier et al. (2015), Fyffe et al. (2014), Shaw et al. (2016).

2.5 Methods of quantifying debris thickness

Various methods of quantifying supraglacial debris thickness have been used or developed over recent years. Some of these methods are field-based and can only realistically be applied at the scale of individual glaciers, or parts of individual glaciers. Others use remote sensing techniques and have been designed for implementation at the scale of individual or multiple glaciers. Between field- and remote sensing-based methods, there is a trade-off of accuracy and practicability. An assessment is made of the advantages and disadvantages of the various methods in Chapter 6. Since work on this thesis was begun, there has been significant progress in the development of methods of quantifying supraglacial debris thickness.

2.5.1 Manual excavation

Where debris is thin, its thickness can often most easily be measured manually by digging pits from the debris surface to the ice surface. Once a pit has been dug, an ice axe or some other item of field equipment is usually placed across its opening to mark the debris surface and a tape measure is used to measure straight down from the debris surface to the ice surface. Because pits provide only point measurements, they are usually dug at intervals along transects of the debris surface in order to achieve good spatial coverage.

2.5.2 Surveying exposures above ice cliffs

Debris thickness can also be measured in the field by surveying debris exposures above ice cliffs. This can be done using a tape measure from the top of an ice cliff, using a theodolite, or by photogrammetry. Using a theodolite, the distance and angle from the theodolite to a point on the debris surface above an ice cliff are measured. This is repeated for a point on the ice surface below the first point, and the vertical distance between the two points is calculated trigonometrically (Nicholson and Benn, 2012). Using photogrammetry, a DEM of the glacier surface is created and vertical distances between points on the debris surface and points on the ice surface below it are calculated (Nicholson and Mertes, 2017).

2.5.3 Ground-penetrating radar

Ground-penetrating radar (GPR) is a geophysical method of imaging the subsurface using radio waves. Pulses of radio waves are transmitted into the ground and the power and timing of their return from subsurface reflectors is recorded. If the speed of the radio waves is known, the depth to subsurface reflectors can be determined. GPR has been used to image ice below debris in the proglacial environment (Moorman and Michel, 2000) and in terminal moraines (Hambrey et al., 2008), and to estimate the thickness of thick debris on the tongue of a debris-covered glacier (Wu and Liu, 2012). GPR profiles are usually collected in transects, and wave speed is typically determined by carrying out common mid-point surveys.

2.5.4 Thermal remote sensing

The surface temperature of a debris layer is controlled, at least in part, by debris thickness, on the basis that debris thickness modifies the debris surface energy balance. Therefore, several studies have used thermal-band satellite images to quantify debris thickness. Mihalcea et al. (2008), Mihalcea et al. (2008) and Gibson et al. (2017) used *in-situ* field measurements of debris thickness with satellite image-derived surface temperatures to develop an empirical relationship between the two. They then extrapolated debris thickness to the rest of the glacier using the satellite image surface temperatures. Foster et al. (2012) and Rounce and McKinney (2014) used satellite image surface temperatures with distributed local meteorological data to solve static debris-surface energy balances for debris thickness. They took broadly similar approaches, except in the way they approximated the conductive heat flux at the debris surface. Schauwecker et al. (2015) used satellite image surface temperatures with a combination of local and NCEP/NCAR reanalysis meteorological data to quantify debris thickness by the static energy-balance approach, developing further the Foster et al. (2012) method of approximating the conductive heat flux. Finally, Kraaijenbrink et al. (2017) developed an ‘exponential scaling’ approach, whereby debris thickness is calculated as a function only of surface temperature. Thermal remote sensing approaches are described in more detail in Section 4.4.1.

Variations of the thermal remote sensing approaches outlined above have been used to estimate debris thermal resistance (Rana et al., 1998; Nakawo and Rana, 1999; Suzuki et al., 2007; Zhang et al., 2011), which has sometimes been used in place of debris thickness in surface mass balance models.

2.5.5 Elevation change remote sensing

It is also possible to estimate debris thickness using digital elevation models (DEMs) and a sub-debris melt model (Rounce et al., 2018). Here, surface mass balance 'observations' are made from surface lowering and ice flux divergence fields, which are generated from a pair of elevation models, and remotely sensed surface velocities and modelled ice thicknesses, respectively. A sub-debris melt model is then used, forced with local meteorological data, to model surface mass balance for each pixel of the 'observed' surface mass balance field under a range of debris thickness values. The debris thickness value that minimises the mismatch between modelled and 'observed' surface mass balance for each pixel of the surface mass balance field is taken as the 'correct' debris thickness. Ragettli et al. (2015) used a similar but slightly less sophisticated approach, having developed an empirical relationship between sub-debris melt rate and debris thickness.

2.5.6 Synthetic-aperture radar remote sensing

Synthetic-aperture radar (SAR) is a remote sensing technology that uses a (typically satellite-mounted) radar system to transmit pulses of radio waves towards target scenes of Earth's surface. A variety of information is recorded about the radio waves that are reflected from these target scenes in order to make images. SAR polarimetry is concerned with the polarisation of the returned radio waves, and polarimetric synthetic-aperture radar images have been used to estimate debris thickness remotely via a decomposition process (Huang et al., 2017; Huang et al., 2018). This is done on the principle that the return power for each pixel of a SAR image is determined by the amount of surface scattering, double bounce and volume scattering that takes place in its target scene, and that the radar power returned by volume scattering depends, amongst other things, on debris thickness. Images are decomposed to derive volume scattering power, then debris thickness is calculated using knowledge of the debris' dielectric properties, the wavelength of the radio wave pulses, the radio wave's angle of incidence with the debris surface, and the shape of the debris' grains. Huang et al. (2017) used L-band Phased Array type L-band Synthetic Aperture Radar (PALSAR) images, the penetration depth of which, in debris, is limited to around 0.5 m.

2.6 Existing debris thickness data

Despite the prevalence of debris-covered glaciers in temperate mountain ranges around the world, globally there is a paucity of *in-situ*-collected debris thickness data. This is because glaciers are often

difficult to access and debris thickness data are physically difficult to collect. The data that do exist are concentrated in the European Alps, the Himalaya and the Tien Shan, were mostly collected by digging pits, and are likely biased towards thinner debris, which is easier than thicker debris to excavate manually. They often cover only a small portion of the total debris-covered area of each glacier. Table 2.1 provides details of studies that have collected debris thickness data worldwide. The debris thickness range column shows that debris thickness can be highly variable on an individual glacier.

Table 2.1 – A summary of *in-situ* debris thickness measurements in previous work. NR is not reported.

Study	Glacier, country	No. of measurements	Thickness range (m)	Glacier coverage, method, sampling strategy
Nakawo et al. (1986)	Khumbu, Nepal	> 100	0 - 2	Complete, NR, NR
Nicholson and Benn (2012)	Ngozumpa, Nepal	218	< 0.5 - > 4	Partial, ice cliff survey, NR
Mihalcea et al. (2006)	Baltoro, Pakistan	56	0 - 0.4	Complete, NR, transects
Wu and Liu (2012)	Koxkar, China	NR	1 - 3.4	Partial, GPR, transects
Zhang et al. (2011)	Haluogou, China	300	0 - 1	Complete, pits, transects
Hagg et al. (2008)	Inylchek, Kyrgyzstan	22	0 - 0.35	Partial, pits, transects
Wang et al. (2011)	72, China	> 100	0 - 0.7	Complete, NR, transects
Wang et al. (2011)	74, China	> 100	0 - 1	Complete, NR, transects
Wang et al. (2011)	Tuomer, China	> 100	NR	Partial, NR, transects
Wei et al. (2010)	24K, Tibet	14	0.1 - 0.7	Complete, pits, transects
Nakawo (1979)	G2, Nepal	50	0 - > 2	Complete, ice cliff survey, NR
Pratap et al. (2015)	Dokriani, India	30	0.01 - 0.4	Complete, pits, NR
Mihalcea et al. (2008)	Miage, Italy	40	0 - 0.55	Complete, pits, transects
Lambrecht et al. (2011)	Djankuat, Russia	11	0 - 0.61	Complete, pits, NR
Lambrecht et al. (2011)	Zopkhito, Russia	13	0 - 0.17	Partial, pits, NR
Kellerer-Pirklbauer (2008)	Pasterze, Austria	317	0.075 – 0.47	Complete, pits, transects
Reid et al. (2012)	Haut d'Arolla, Switzerland	1058	0 - > 0.5	Complete, pits, NR
Richardson and Brook (2010)	Mt Ruapehu, New Zealand	12	0 - 4	Partial, pits, NR
Diolaiuti et al. (2003)	Belvedere, Italy	260	0.04 - 0.8	Complete, pits, NR
Owen et al. (2003)	Rakhiot, Pakistan	210	< 0.01 - > 1	Complete, pits, NR
Shroder et al. (2000)	Shaigiri, Pakistan	15	0.38 - 1.5	Partial, pits and ice cliff survey, Transect

3 Local-scale *in-situ* field measurements

3.1 Context

There is a paucity of *in-situ* field measurements of supraglacial debris thickness on glaciers worldwide (see Section 2.6), which is largely due to difficulties of data collection. Making field measurements of debris thickness can be both physically difficult and time consuming, partly because glaciers tend to exist in remote geographic locations. This is problematic for three main reasons.

First, in lieu of reliable remote sensing-derived debris thickness estimates, field measurements of debris thickness are necessary to accurately model the surface mass balance of debris-covered glaciers (e.g. Reid et al., 2012). In addition, they are necessary to test and develop distributed surface mass balance models for debris-covered glaciers (e.g. Fyffe et al., 2014; Rounce et al. 2015; Reid et al., 2012). Second, field measurements of debris thickness are necessary to validate remote sensing methods of quantifying debris thickness and, more fundamentally, to identify which remote sensing quantities debris thickness may best be quantified from. Without robust remote sensing methods of quantifying debris thickness, it is impossible to accurately model the surface mass balance of debris-covered glaciers at scales larger than a few glaciers. Third, field measurements of debris thickness are necessary to understand processes, such as those that distribute debris over the surfaces of debris-covered glaciers, and their effect on surface mass balance (Kirkbride and Deline, 2013; Kellerer-Pirklbauer, 2008; Nakawo et al., 1986; Moore, 2018).

Therefore, it is important to make field measurements of debris thickness on as many glaciers as possible, and to develop new methods of measuring supraglacial debris thickness in the field that are less difficult than those that exist currently.

3.1.1 Aims and objectives

This chapter makes *in-situ* field measurements of debris thickness on Suldenferner Glacier, Italy, and Lirung and Ngozumpa glaciers, Nepal, then uses them to address some of the problems outlined above. Some of its contents are included in recently published papers (McCarthy et al. 2017; Nicholson et al. 2018). The aims of this chapter are:

- To make ground-truth measurements of debris thickness against which to test remote sensing methods of quantifying debris thickness in chapters 4 and 5, and, in the process, to investigate how debris thickness varies between glaciers and on individual glaciers.
- To test the use of ground-penetrating radar (GPR) for measuring debris thickness by investigating the strength and continuity of the ice surface reflection through a debris layer in radargrams collected on debris-covered glaciers, by investigating the different radar facies of debris and ice, and by comparing GPR measurements of debris thickness to pit measurements of debris thickness.
- To investigate the relationships of debris thickness with surface velocity, elevation, elevation change rate and surface temperature (i.e. physical properties that can be measured remotely).
- To examine how debris thickness relates to local surface topography, and to investigate the processes of gravitational reworking of supraglacial debris.

3.2 Study sites

3.2.1 Suldenferner Glacier, Italy

Suldenferner Glacier is a valley glacier in the Central Eastern Alps, South Tyrol, on the Italian side of the Italy-Austria border. It is around 3 km long and its tongue, which is debris-covered, is around 0.7 km wide (Figure 3.1c, g). It has a total area of 2.6 km^2 and a debris-covered area of around 1.1 km^2. It is fed by Payerferner icefall from between Monte Zebrù and Königspitze in the south, and by avalanching from snowfields on Ortler and Monte Zebrù to the west. The debris-covered tongue has a gentle slope of around 10° and is slow-flowing. There are scattered ponds and ice cliffs and the glacier surface is irregular and crevassed in places. While length change records show that glaciers in the region underwent a period of advance in the decades prior to 1920, in which Suldenferner may have surged, the mid-1900s were characterised by retreat (Kuhn et al., 1997). Glacier inventory and airborne laser-scanner data show that Suldenferner and other valley glaciers in South Tyrol have undergone a major decrease in area and volume in recent decades (Knoll and Kerschner, 2009).

Suldenferner is now much smaller than it was during early surveys and paintings (Finsterwalder et al., 1887). The dominant rock types are dolomite, limestone and metapelite (Finsterwalder et al., 1887; Figure 3.2f).

3.2.2 Lirung Glacier, Nepal

Lirung Glacier is a mostly avalanche-fed valley glacier in the Nepal Himalaya near the border between Nepal and Tibet (Figure 3.1a, e). It has a total area of 6.3 km^2 and a debris-covered area of 1.7 km^2. The debris-covered part of the glacier spans 4000-5300 m elevation and is dominated by a detached, debris-covered tongue, which has a low surface gradient of < 10° (Pellicciotti et al., 2015). The tongue is largely stagnant (Kraaijenbrink et al., 2016) and has a highly heterogeneous, locally complex topography with numerous supraglacial ponds and ice cliffs (Sakai et al., 2000; Steiner et al., 2015; Miles et al., 2016). Satellite images and elevation change data indicate that in the last quarter of the 1900s, Lirung Glacier retreated, decreased in area and lost mass (Pellicciotti et al., 2015). Gades et al. (2000) reported a debris thickness range of ~0.5 m on the upper ablation zone to ~3 m near the terminus. The debris cover is predominantly granitic (Reddy et al., 1993) and has a grain size range of < 0.001- > 5 m (Figure 3.2e).

3.2.3 Ngozumpa Glacier, Nepal

Ngozumpa Glacier is a valley glacier in the Everest region of the Nepal Himalaya. It originates on the southeast face of Cho Oyu and the southwest face of Gyachung Kang (Figure 3.1b, f). It has a total area of 61 km^2 and a debris-covered area of 21 km^2. It is 18 km long and its lower 15 km are almost entirely debris-covered. Its lower 6.5 km are largely stagnant (Quincey et al., 2009), and there is a large moraine-dammed lake at its terminus (Thompson et al., 2012). Similar to the debris-covered part of Lirung Glacier, the debris-covered part of Ngozumpa Glacier has a highly variable, 'hummocky' surface topography with lots of ponds and ice cliffs. In recent decades, Ngozumpa Glacier has both lost mass, particularly at high-altitude where the ice is debris-free, and decreased in surface area (Thakuri et al., 2014; King et al., 2017). Nicholson and Benn (2012) made observations of debris thickness that suggest an increase down-glacier, from a modal thickness of < 0.5 m at 7 km from the terminus to a modal thickness of 1-1.5 m at 1 km from the terminus. The dominant rock types are schist and leucogranite (Nicholson and Benn, 2012), and grain size ranges from < 0.001 to > 5 m (Figure 3.2c, d).

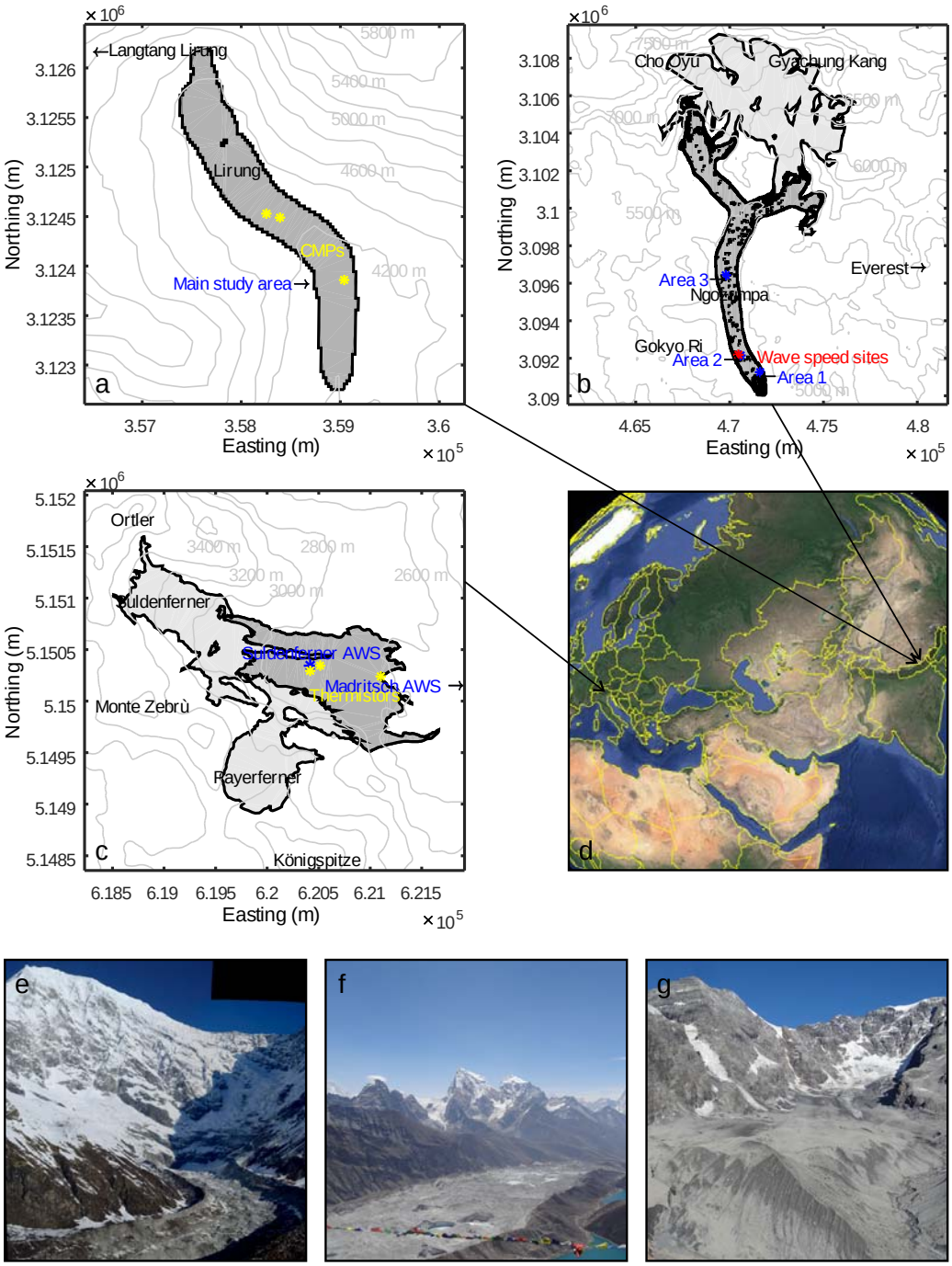

Figure 3.1 – Study sites at which *in-situ* field measurements of debris thickness were made. (a) Lirung Glacier, (b) Ngozumpa Glacier, (c) Suldenferner Glacier. Debris-covered ice is shown in dark grey. Debris-free ice is shown in light grey. Lirung and Ngozumpa outlines are from the Randolph Glacier Inventory v.6 (RGI Consortium, 2017). Elevation data are from the SRTM (Jarvis et al., 2008). Coordinate systems are WGS84 UTM. UTM zones are 45N, 45N and 32N for Lirung, Ngozumpa and Suldenferner, respectively. (d) Study site locations on a Google Earth image. (e), (f), (g) Photos of Lirung, Ngozumpa and Suldenferner, respectively, taken during fieldwork.

3.3 Data

In addition to the debris thickness measurements that were made in the field (sections 3.4.1 and 3.4.2), a number of existing datasets were used to carry out the analyses of this chapter.[2] For Suldenferner Glacier, two elevation models were used, one surface temperature satellite image and a glacier outline shapefile, which was delineated manually. The elevation models – one from summer 2013 and the other from summer 2016 – were both generated from airborne-laser scanner data at 1-m spatial resolution. The surface temperature satellite image was an ASTER image from 26-Aug-2016 10:22:29 UTC (see Section 4.3.2). For Ngozumpa Glacier, some meteorological data were used along with an elevation model (and associated orthophoto), some additional debris thickness data, and some sub-debris melt rate data. The meteorological data were from the nearby Pyramid Station, which is maintained by the Ev-K2-CNR Association.[3] The elevation model was generated from Pleiades optical tri-stereo imagery from April 2016, at 5-m spatial resolution. The additional debris thickness data were from Nicholson and Benn (2012) and were made from debris exposures above ice cliffs using a theodolite. The sub-debris melt rate data were generated following Evatt et al. (2015), using the Pyramid Station meteorological data.

3.4 Methods

3.4.1 Measuring debris thickness by manual excavation

3.4.1.1 Data collection

134 measurements of debris thickness were made on Suldenferner Glacier in August 2015 and August 2017, by manual excavation.[4] To make each measurement, an ice axe was used to dig a pit from the debris surface to the ice surface, and a tape measure was used to measure the vertical distance between the two. To mark the location of the debris surface, the ice axe was placed across the top of each pit

[2] The elevation models for both Suldenferner and Ngzoumpa glaciers, the Ngozumpa orthophoto, the additional debris thickness data, the sub-debris melt rate data and the Suldenferner Glacier outline shapefile were provided by Lindsey Nicholson. The Suldenferner elevation models were generated as part of the Multitemporal Airborne Laserscanning Südtirol project (PI Rudolf Sailer). The Ngozumpa elevation model and orthophoto were generated by Christoph Klug.
[3] http://www.evk2cnr.org/cms/en/home.html
[4] I made 21 of these measurements. The rest were provided by Lindsey Nicholson.

before its depth was measured (Figure 3.2b). Measurements were made on a 100-m grid over the whole debris-covered area of the glacier.

Figure 3.2 – (a) Making a pit measurement of debris thickness on Lirung Glacier. (b) Collecting GPR data on Ngozumpa Glacier (photograph taken and provided by Mohan Chand). (c), (d), (e), (f) Examples of different types of debris cover on Ngozumpa, Ngozumpa, Lirung and Suldenferner glaciers.

3.4.2 Measuring debris thickness using GPR

In-situ field measurements of debris thickness are typically made by digging pits to the ice surface, or by surveying exposures above ice cliffs. However, digging pits can be time consuming, physically difficult, biased towards smaller thicknesses, and yields only spatially discrete, single point measurements. Debris thickness measurements made at exposures above ice cliffs are likely to be biased because ice cliffs occur in atypical glacier surface settings. Achieving adequate sampling is difficult by both methods, and inaccuracies result from interpolating between sparse measurement points.

Radar is commonly used in glaciology to determine the ice thickness, internal structure and basal conditions of glaciers (Plewes and Hubbard, 2001; Nobes et al., 1994; Gades et al., 2000). Commercially available GPR systems have been used to measure snow depth and permafrost active layer thickness at shallow depths, and have been used to investigate at wide variety of frozen materials

and glacial sediments, including those of rock glaciers, ice-cored moraines and talus deposits (Sinisalo et al., 2003; Booth et al., 2013; Moorman et al., 2003; Bradford et al., 2005; Gusmeroli et al., 2015; Neal, 2004; Woodward and Burke, 2007; Degenhardt et al., 2003; Lønne and Lauritsen, 1996; Hambrey et al., 2008; Sass and Wollny, 2001; Sass, 2006; Dallimore and Davis, 1992; Brandt et al., 2007). Wu and Liu (2012) used GPR to estimate the thickness of thick debris on Koxkar Glacier, China.

3.4.2.1 Data collection

On Lirung Glacier, fieldwork was carried out in March and April 2015. GPR data were collected using a Sensors and Software pulseEKKO 1000 with 225, 450, 900 and 1200 MHz antennas. 29 radargrams were collected along 15 transects near the glacier terminus. Nine common midpoint (CMP) surveys were carried out following Jol and Bristow (2003), to measure the radar wave speed of the debris . The lengths and locations of both the transects and the CMP surveys were limited by the existence of patches of wet snow on the glacier surface. On the basis that attenuation and range resolution typically decrease with decreasing operating frequency (Davis and Annan, 1989), operating frequency was varied by switching antennas until the ice surface had been successfully imaged. The 15 transects crossed each other in 11 places, giving 11 tie points. To ensure good ground coupling and to allow GPR measurements at individual traces to be compared with pit measurements, both radargrams and CMPs were collected in 'step-mode'. The step sizes that were used were those recommended by the manufacturer (Sensors and Software, 1999), traces were stacked 64 times, and the digitisation interval (sample rate; 0.1-0.4 ns) and time window (up to 100 ns) were varied depending on operating frequency and expected debris thickness. The GPR transects were geolocated at 0.25 m intervals by differential global positioning system (DGPS), achieving 0.2 m vertical accuracy and 0.1 m horizontal accuracy. To validate the GPR measurements of debris thickness, 34 pits were dug through the debris to the ice surface (as described in Section 2.5.1), ranging from 0.16-0.58 m deep, along seven of the 15 transects. A total of 6200 radar measurements were made.

On Ngozumpa Glacier, fieldwork was carried out in March and April 2016. GPR data were collected using a dual-frequency IDS RIS One with 200 and 600 MHz antennas (Figure 3.2b). 72 radargrams were collected along 36 transects – one 200 MHz radargram and one 600 MHz radargram per transect,

again near the glacier terminus (Figure 3.1).[5] Radargrams were collected in 'continuous-mode', with a time window of 100 ns and a digitisation interval of 0.024 ns. The transects were geolocated every second using both a low-precision GPS, achieving ~3 m accuracy, and a high-precision DGPS, achieving < 0.05 m after post-processing.[6] Where both GPS and DGPS locations were collected, DGPS locations were used. In instances where DGPS locations were not able to be collected, GPS locations were used. In order to determine debris wave speed, a steel bar was dug into the debris, over which additional radargrams were collected, in two different locations. These transects crossed each other in 40 places, giving 40 tie points. A total of 140000 measurements were made.

3.4.2.2 Data quality

On both glaciers, data quality was found to be largely dependent on the acquisition parameters, particularly operating frequency, used during data collection (see Section 3.5.2.1). Poor quality radargrams collected using inappropriate acquisition parameters were discarded. All the radargrams were checked for artefacts and noise and slight trace-to-trace variations in direct wave arrival were identified prior to processing. These were probably due to variable ground coupling. First breaks were found to represent the arrival of the air wave by fitting straight lines of gradient 0.3 m ns^{-1} to direct waves in the Lirung Glacier CMP plots.

3.4.2.3 Processing

The radargrams were processed using the software REFLEXW (Sandmeier Software) according to the following steps (after Cassidy, 2009): trace editing, plateau declipping, DC shift, align first breaks at $t = 0$ (where t is two-way travel time, TWTT), dewow, align first breaks at $t = a/v_l$ (timezero correction, where a is antenna separation and v_l is speed of light 0.3 m ns^{-1}), background removal, bandpass filter, gain correction. Dewow was applied after aligning first breaks at $t = 0$ because it causes a zero-phase filter precursor if applied before (Sensors and Software, 1999) and the dewow time window was set to the same length as the period of the signal of each operating frequency: 4.44, 2.22, 1.11 and 0.83 ns, for 225, 450, 900 and 1200 MHz antennas, respectively. For the bandpass filter, lower cut-off, lower plateau, higher plateau and higher cut-off were set to 0.25, 0.5, 1.5 and 3 times peak returned frequency, respectively, in order that the width of the plateau pass was similar to

[5] The field team that helped collect the GPR data was Ursula Blumthaler, Mohan Chand, Costanza del Gobbo, Anna Sinisalo, Hamish Pritchard, Lorenzo Rieg, Anna Wirbel and Lindsey Nicholson. Some of the radargrams were collected before I arrived in the field.
[6] Ngozumpa Glacier DGPS data were post-processed by Lindsey Nicholson and Christoph Mayer.

the bandwidth (Davis and Annan, 1989) and the taper slope was gentle (Bristow and Jol, 2003). Topographic correction was not applied as part of the processing flow because the amplitude of topographic change on both glaciers is typically much greater than the amplitude of debris thickness change, and this was found to make interpretation of the ice surface more difficult. In the case of the Lirung data, the top of each radargram was desaturated by applying a linear negative vertical gain from first breaks (−20 dB) to 1.5 times the pulse width from first breaks (0 dB). Horizontal gain was applied in some cases to counter variable penetration depth. In the case of the Ngozumpa data, a divergence compensation gain function was applied, with a scaling factor of $0.1t$.

CMP data were processed similarly to the radargrams but timezero was found by fitting a straight line (0.3 m ns^{-1}) to the air wave onset, and no background removal or gain correction was applied.

Processing significantly aided interpretation of the ice surface in both the radargrams and the CMPs. In particular, background removal helped to counteract 'transmitter blanking' at the top of the radargrams due to the high-energy direct wave, and bandpass filtering effectively removed high-frequency noise. However, the choice of dewow time window was possibly not optimal because the period of the received signal is often different from that of the transmitted signal. Using a longer time window may have yielded better results.

All GPR data are presented visually as 'trace normalised', to account for differences in ground coupling. Ngozumpa Glacier GPR radargrams were topographically corrected for visual presentation (using a wave speed of 0.16 m ns^{-1}, as calculated for the debris in Section 3.4.2.5) in order that the relationships between debris thickness and surface topography could be seen.

3.4.2.4 Picking reflectors

First break picks were made using the REFLEXW function autopick, with an amplitude threshold of 0.2, and autocorrected back in time to zero amplitude. They were made after applying the DC shift filter in order that they were not affected by DC bias. The ice surface was picked manually at the onset of the first continuous high-amplitude reflection at depth, i.e. the first reflection below the direct wave reflection, in each radargram (Figure 3.3). Picking was carried out blind, i.e. without reference to pit measurements, to avoid interpreter bias. Ice surface picks were corrected to zero amplitude using the REFLEXW function autocorrect, and their positions were extracted as TWTTs. In each radargram, the debris layer manifests as a high-scatter radar facies and the ice below manifests as a low-scatter radar facies (see Section 3.5.2.1). This contrast was used as a quality check on picks of the ice surface. The

ice surface was only picked where it was clearly identifiable and was not picked where it was indistinct.

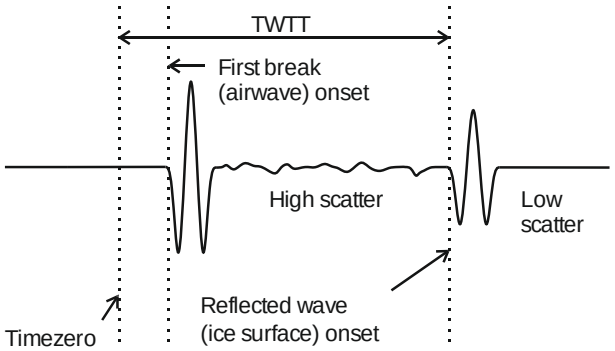

Figure 3.3 – An idealised trace through a debris layer showing first break and ice surface onset picks in relation to timezero. Debris is to the left of the ice surface onset and ice is to the right, i.e. downwards is to the right.

3.4.2.5 Wave speed analysis

On Lirung Glacier, debris wave speed was calculated from CMPs by way of coherence analysis and backshifting (Booth et al., 2010). Coherence analysis, which is similar to semblance analysis but uses a time window of the same length as the digitisation interval, facilitates assessment of the coherence of reflected waveforms across each CMP and therefore allowed the waveform associated with the ice surface to be picked confidently. Backshifting was necessary because GPR-derived depth measurements require root-mean-square wave speed rather than stacking wave speed, which is what is given by coherence analyses, especially for short-spread conditions, where antenna separation exceeds the depth of the reflector (Booth et al., 2010). First, ice surface waveform half-cycles were picked from coherence plots (produced in REFLEXW) using corresponding radargrams as a guide (Figure 3.4). These picks provided zero-offset TWTT t_0 and stacking wave speed v_s. Second, t_0 and v_s were substituted, with values of antenna separation a, into the normal moveout (NMO) equation (Yilmaz, 2001), to define ice surface waveform half cycle hyperbolas:

$$t_a = \sqrt{t_0^2 + a^2/v_s^2} \tag{3.1}$$

where t_a is the TWTT at some antenna separation or 'offset'. Third, a chosen hyperbola of each CMP was backshifted, according to the method outlined by Booth et al. (2010), by

$$\Delta t = \frac{T}{4} + \frac{(HC_n - 1)T}{2} \tag{3.2}$$

where T is the period of the waveform and HC_n is the index number of a chosen half-cycle. Lastly, debris wave speed v was calculated from backshifted hyperbolas by rearranging the NMO equation and substituting in new values of t_0 and t_a (Yilmaz, 2001):

$$v = \sqrt{a^2/(t_a^2 - t_0^2)} \tag{3.3}$$

Analysis of three CMPs gave debris wave speeds of 0.11, 0.12 and 0.13 m ns^{-1} (Figure 3.4). The mean these three wave speeds is 0.12 m ns^{-1}, which is similar to wave speeds found for other glacial sediments (e.g. 0.12 m ns^{-1}; Degenhardt et al., 2003). The remaining six CMPs were not used in wave speed analysis either because a coherent ice surface waveform was not observed or because another CMP taken in the same place with a different operating frequency produced a more coherent reflection.

On Ngozumpa Glacier, debris wave speed was calculated by rearranging Equation (3.4) for wave speed v, where t and h are the TWTT to and known depth of the steel bar buried within the debris, respectively. In one of the locations, the debris was fine grained and wave speed was calculated to be 0.15 m ns^{-1}. In the other of the locations, the debris was coarse grained and wave speed was calculated to be 0.16 m ns^{-1}. The mean of these two wave speeds was calculated to be 0.16 m ns^{-1}.

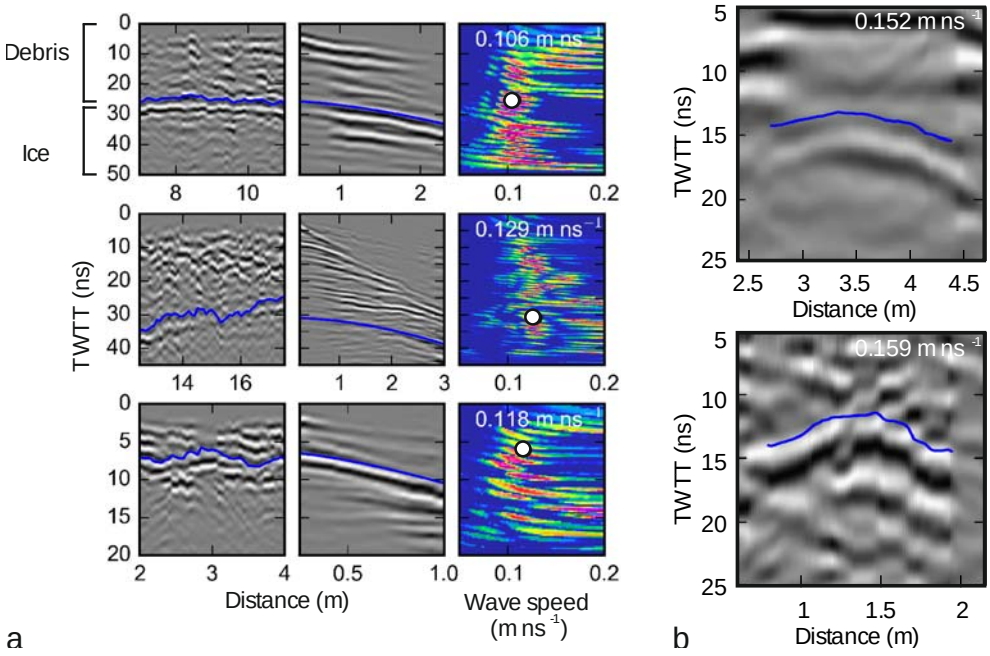

Figure 3.4 – Debris wave speed measurements. (a) Made by CMP survey on Lirung Glacier. (b) Made by digging a steel bar into the debris cover on Ngozumpa Glacier.

3.4.2.6 Calculating debris thickness

Debris thickness h was calculated from ice surface TWTT t, debris wave speed v and antenna separation a, thus taking system geometry into account, as such:

$$h = \frac{1}{2}\sqrt{t^2v^2 - a^2} \tag{3.4}$$

For Lirung and Ngozumpa glaciers, debris thickness calculations were made using wave speeds of 0.12 m ns^{-1} and 0.16 m ns^{-1}, respectively, i.e. the means of the measured wave speed values. It was found that correcting for system geometry is important in order to derive realistic debris thickness measurements.

In order to produce consistent debris thickness datasets from the GPR data, where multiple debris thickness measurements were made at a single location, e.g. because radargrams had been collected using multiple operating frequencies, the measurement made using the highest operating frequency, or with the strongest ice surface reflection, was retained, while other measurements were discarded.

3.4.2.7 Estimating uncertainty

Uncertainty was assigned to the GPR measurements of debris thickness by propagating uncertainties assigned to Equation (3.4) variables, assuming negligible uncertainty associated with a, because the antenna separations of both GPR systems are fixed and therefore subject only to manufacturing tolerances, as follows:

$$\sigma_h \approx \frac{vt\sqrt{v^2\sigma_t + t^2\sigma_v}}{2\sqrt{t^2v^2 - a^2}} \tag{3.5}$$

where σ_h is debris thickness uncertainty, σ_t is TWTT uncertainty and σ_v is wave speed uncertainty.

σ_t was attributed to two main sources: (1) misinterpretation of the ice surface due to poor data quality (we assumed the air wave was interpreted well), and (2) the uncertainty introduced by the digitisation interval on picking first break and ice surface onsets. It was assumed that the ice surface was not misinterpreted by more than one period either way (equivalent of $\lambda/2$ in terms of thickness or range resolution; cf. Lapazaran et al., 2016) and that ice surface and first break onsets were each picked within 1 times the digitisation interval. Because these two sources of uncertainty could occur in the same instance and in the same direction, σ_t was calculated as:

$$\sigma_t = T + 2D \tag{3.6}$$

where D is the digitisation interval.

σ_v was attributed to the inhomogeneity, i.e. the variable electromagnetic composition, of the debris, which is largely controlled by rock type, porosity and pore space filler (water/air/ice). Debris wave speed must vary with time and space across the glacier due to variable water content and debris composition. Debris wave speed was assumed to vary by 10% (after Booth et al., 2010), which captures the range of wave speeds determined by the three CMPs. This value would have to be much bigger if wave speed tests had not been carried out because the theoretical wave speed range is great. In the case of Lirung Glacier, it was assumed there was no covariance between TWTT and wave speed because TWTTs were found using radargrams and wave speeds were found by CMP, i.e. by independent means (Pellikka and Rees, 2009). In the case of Ngozumpa Glacier, the same assumption was made by way of simplification.

3.4.2.8 Calculating reflection power

In order to assess the different electromagnetic responses of ice and debris in the Lirung Glacier GPR data, reflection power was calculated for sections of some of the radargrams following Wilson et al. (2014):

$$P_r \propto \frac{1}{t_1 - t_0 + 1} \sum_{i=t_1}^{t_2} A_i^2 \tag{3.7}$$

where P_r is reflection power, t_2 and t_1 are the sample numbers that define the time window being analysed, and A is trace-normalised sample amplitude. Because A was calculated using trace-normalised amplitudes, P_r has no units and can range from 0-1.

3.4.2.9 Validation of GPR measurements

The Lirung GPR measurements of debris thickness were validated by comparing them to the pit measurements and by comparing them to each other at tie points. Ngozumpa GPR measurements were validated by comparing them to each other at tie points and by comparing them to each other where two measurements had been made at the same location using the two different operating frequencies. The correlation coefficient, r, and root-mean-square error, RMSE, were used as statistical measures of performance.

3.4.3 Estimating debris thickness variability

As a measure of debris thickness variability on the three glaciers, the horizontal distance and the debris thickness difference between every conceivable pair of debris thickness measurements on each glacier was determined. The maximum debris thickness difference to occur over horizontal distances of 10-100 m was then recorded.

3.4.4 Comparison to remote sensing quantities

In order to assess the relationship between debris thickness and physical quantities that can be remotely sensed, pit measurements of debris thickness collected on Suldenferner Glacier were compared to remotely sensed surface temperature, surface velocity, elevation change rate and elevation data. For each pit measurement, the four remote sensing quantities were interpolated by the

nearest neighbour method at the native resolution of the remote sensing data. Pearson correlation coefficients were determined using the MATLAB function corr. For elevation, the 2016 Suldenferner elevation model was used directly. For surface temperature, the 26-Aug-2016 AST08 image was used directly. However, surface velocity and elevation change rate had to be calculated.

Surface velocity was calculated using the two Suldenferner elevation models (see Section 3.3). Hillshade images were created from the elevation models using the ArcMap Hillshade tool, then topographic features occurring in both of the hillshade images were picked out manually. The distance per year by which each recurring feature had moved was determined from its start and end location, then the MATLAB function IDW (Fatichi, 2009) was used to extrapolate surface velocity from recurring feature midpoint locations to the rest of the glacier by the inverse distance weighting method. Inverse distance weighting was performed using the three nearest neighbour midpoint locations and a power setting of one. In total, 129 features were picked, both on and off glacier. Surface elevation change rate was calculated simply by subtracting the second from the first elevation model and dividing by the time interval that separated their collection.

3.4.5 Comparison to topographic parameters

In order to investigate the relationship between debris thickness and topography, Ngozumpa Glacier radargrams were visually inspected and measurements of debris thickness were compared to key topographic parameters. The topographic parameters that were investigated were slope, aspect and curvature. These were derived from the Ngozumpa elevation model using ArcGIS. If there were multiple debris thickness measurements within an individual pixel of the elevation model, the mean of those debris thickness measurements was taken. Measurements were excluded from the analysis if they were located within 5 m of ice cliffs or if DGPS locations were not available. Because debris thickness was found to be slope and aspect-dependent (see Section 3.5.4), the slope- and aspect-dependency of incoming shortwave radiation was also calculated, for comparison, using the Pyramid Station meteorological data. Incoming shortwave radiation was calculated according to the method outlined in Section 4.4.3.

3.4.6 Slope stability modelling

To examine the extent to which debris cover can undergo gravitational reworking, some slope stability modelling was carried out using the Ngozumpa Glacier GPR measurements of debris thickness, additional debris thickness data, elevation model, and melt rate data. This slope stability modelling

was carried out following Moore (2018), for three discrete areas of the debris surface in which the debris thickness measurements were concentrated: Area 1, Area 2 and Area 3 (Figure 3.1).

The debris was classified as being either stable or unstable, and then was further classified as being unstable due to oversteepening, saturation excess or meltwater weakening (after Moore, 2018). Oversteepening occurs where surface slope is great enough to cause the debris to slide regardless of its water content. Saturation excess occurs where the water table height of the debris is greater than the thickness of the debris. Meltwater weakening occurs where the water table height of the debris is lesser than the thickness of the debris but water in the debris causes debris pore pressures to be high, which causes instability. Following Moore (2018):

Debris was considered unstable due to meltwater weakening if:

$$F = \left(1 - \frac{MU\rho_w}{hK_d \sin Z' \rho_{d_w}}\right) \frac{\mu}{\tan Z'} \leq 1 \tag{3.8}$$

where F is the factor of safety, M is the melt rate, U is the upstream catchment area, ρ_w is the density of water, h is debris thickness, K_d is debris hydraulic conductivity, Z' is surface slope, ρ_{d_w} is the density of wet debris, and μ is the debris-ice interface friction coefficient.

Debris was considered unstable due to saturation excess if:

$$d = \frac{MU}{K_d \sin Z'} > h \tag{3.9}$$

where d is the height of the water table of the debris.

Debris was considered unstable due to oversteepening if:

$$\tan Z' \geq \mu \tag{3.10}$$

The debris thickness values that were used were the means of the debris thickness measurements in the three study areas, and are provided with the melt rate data in Figure 3.14. A value of 0.5 was used for the debris-ice interface friction coefficient (Barrette and Timco, 2008). Values of 1000 and 2190 kg m^{-3} were used for the densities of water and wet debris, respectively, where wet debris was assumed to have a porosity of 0.3 (Conway and Rasmussen, 2000), and the density of rock was assumed to be 2700 kg m^{-3} (Nicholson and Benn, 2006).

The saturated hydraulic conductivity of the debris, which is the variable around which there is most uncertainty, was determined using the GPR data. On the basis of its morphology, the debris cover in the radargrams and its corresponding elevation model pixels were defined, by visual inspection, as being either stable or unstable. Thin debris on steep slopes was considered to be unstable, while thick debris on shallow slopes was considered to be stable. Debris stability was then modelled using a wide range of saturated hydraulic conductivity values, and the conductivity value that best identified stable and unstable elevation model pixels, compared to those identified as stable and unstable in the radargrams, was considered to be optimal. This calibration procedure was carried out using ROC (receiver operating characteristic) analysis performance statistics, as described in Section 5.4.9. An optimal hydraulic conductivity of 40 m d^{-1} was determined, which is well within the expected range of 10^{-7}-10^{3} m d^{-1} (Fetter, 2018), and which is consistent with the debris being well-drained (Figure 3.5).

Slope was calculated as in Section 3.4.5, and upstream catchment area was determined from the elevation model using the ArcGIS Flow Direction and Flow Accumulation tools. Sinks in the elevation model were filled if they were less than 3 m deep (Miles et al., 2017), using the ArcGIS Sink and Fill tools. To see how slope stability might be related to glacier surface hydrology, surface-water flow paths were determined using the Stream to Feature tool.

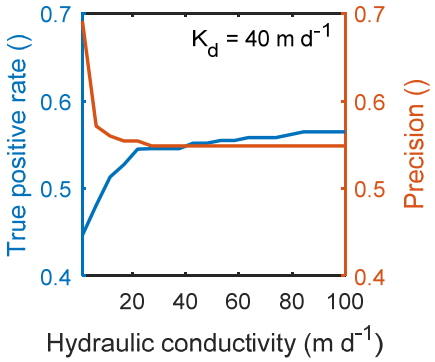

Figure 3.5 – Hydraulic conductivity of debris cover on Ngozumpa Glacier, as calibrated by ROC analysis from GPR data.

Areal-percentage debris instability was calculated for each of the three study areas, both including and excluding ice cliffs and ponds, which were digitised manually from an orthophoto associated with the elevation model.

3.5 Results

3.5.1 *In-situ* measurements of debris thickness

On Suldenferner Glacier, pits were dug to depths of 0.01-1.5 m. However, the maximum depth to which the ice surface was reached within the glacier outline was 1 m, therefore the measured debris thickness range is 0.01-1 m (Figure 3.6). GPR measurements of debris thickness made on Lirung Glacier range from 0.11 +/- 0.23 to 2.3 +/- 0.39 m (Figure 3.6), and GPR measurements of debris thickness made on Ngozumpa Glacier range from 0.18 +/- 0.14 to 7.3 +/- 0.83 m (Figure 3.6). There are clear spatial patterns of debris thickness on all three glaciers (Figure 3.6). For example, on Suldenferner Glacier, the debris cover is particularly thick near the margins (particularly the northern margin), near the terminus and around the confluence between the Payerferner icefall and Suldenferner Glacier proper. The debris is particularly thin upglacier and towards the centreline. On Lirung Glacier, the debris cover further upglacier is considerably thinner than the debris cover downglacier, and on Ngozumpa Glacier, the debris is particularly thick in Area 1, near the eastern margin, and notably thin on steeply sloping surfaces in Area 2.

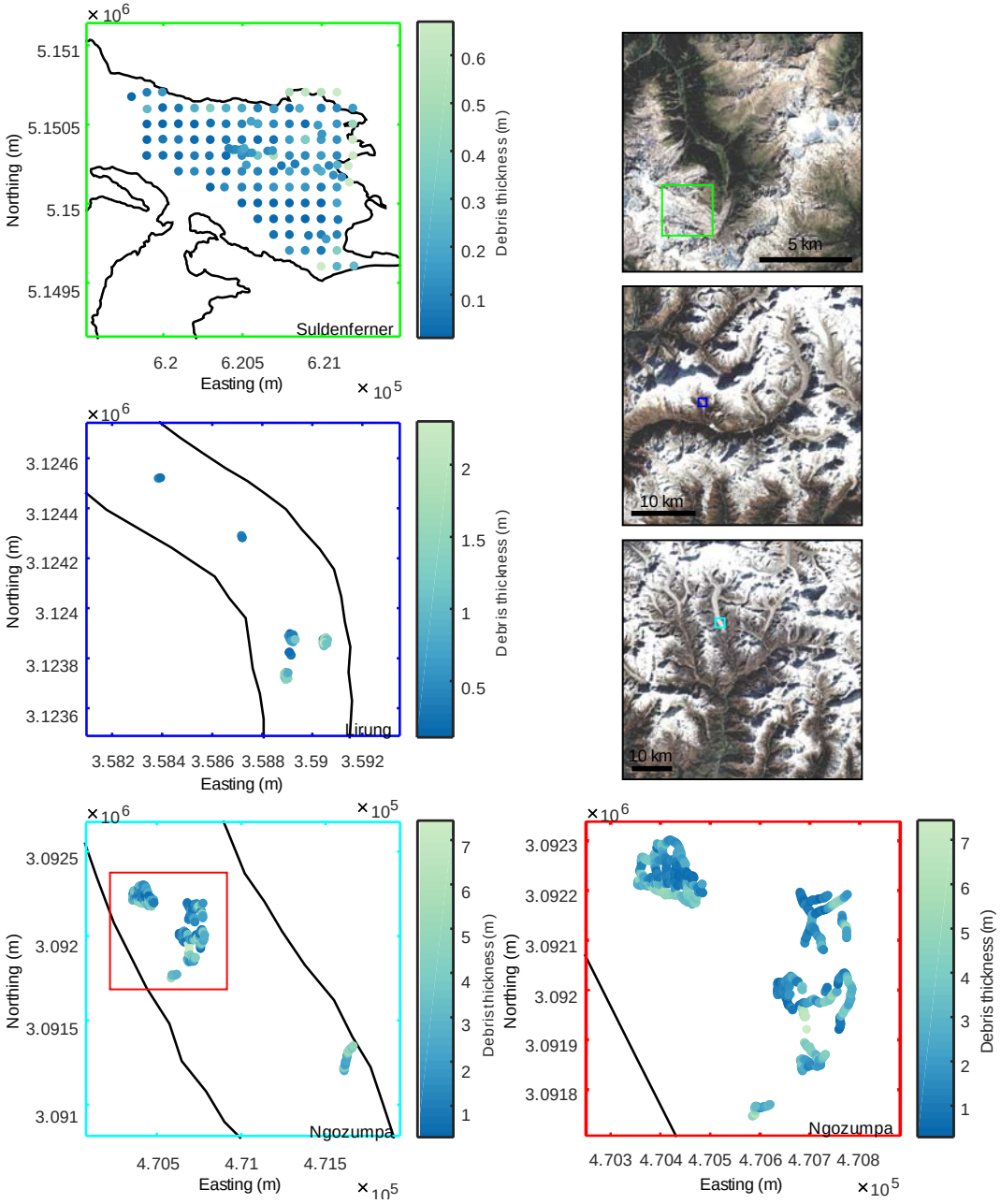

Figure 3.6 – Debris thickness measurements made on Lirung, Suldenferner and Ngozumpa glaciers, shown with glacier outlines. The Lirung and Ngozumpa measurements were made using GPR, while the Suldenferner measurements were made by digging pits. Bottom right is zoomed in from bottom left, and the coloured boxes on the satellite images show the study sites in the context of their broader catchments. Coordinate systems are WGS84 UTM. UTM zones are 45N, 45N and 32N for Lirung, Ngozumpa and Suldenferner, respectively.

In terms of debris thickness variability, Figure 3.7 shows that debris thickness can vary by several metres over short spatial scales of < 10 m, and that debris thickness is particularly variable on Lirung and Ngozumpa glaciers.

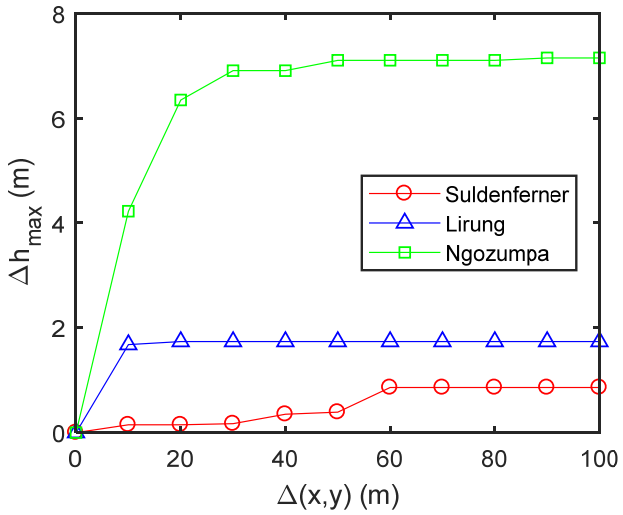

Figure 3.7 – Maximum measured debris thickness range against horizontal distance for the three glaciers.

3.5.2 Using GPR to measure debris thickness

3.5.2.1 Ice surface reflection

A strong, continuous reflection occurs below the direct wave in 16 of the 29 radargrams that were collected on Lirung Glacier. Above this reflection, there is typically a high-scatter radar facies, and below it there is typically a low-scatter radar facies. Strong, continuous reflections were interpreted as the ice surface (see Section 3.4.2.4), while high- and low-scatter radar facies were interpreted as debris and ice, respectively (Figure 3.8). Four radargrams, each showing a strong continuous reflection at the ice surface, and each collected using a different operating frequency, are presented in Figure 3.8. Ice surface reflection power varies with distance along each of these radargrams. For example, the reflection power is 0.03 at the 'weak reflection' label and 0.39 at the 'strong reflection' label in Figure 3.8a. Reflection power within the debris is typically high, while reflection power within the ice is typically low. For example, reflection power is 0.24 in Box (i) and 0.04 in Box (ii) in Figure 3.8d. The polarity of the ice surface reflection is predominantly – + –, although it is sometimes reversed to + − +. Before processing, the direct wave was seen in all radargrams as a continuous, high amplitude, − + − reflection.

In the other 13 of the 29 radargrams, a strong, continuous reflection is not always evident. Strong reflections occur in parts of these radargrams but show little continuity (e.g. Figure 3.8e, f). In places

there are strong reflections at multiple depths, and some radargrams, such as the radargram shown in Figure 3.8e, which was collected using an operating frequency of 1200 MHz, are dominated by noise.

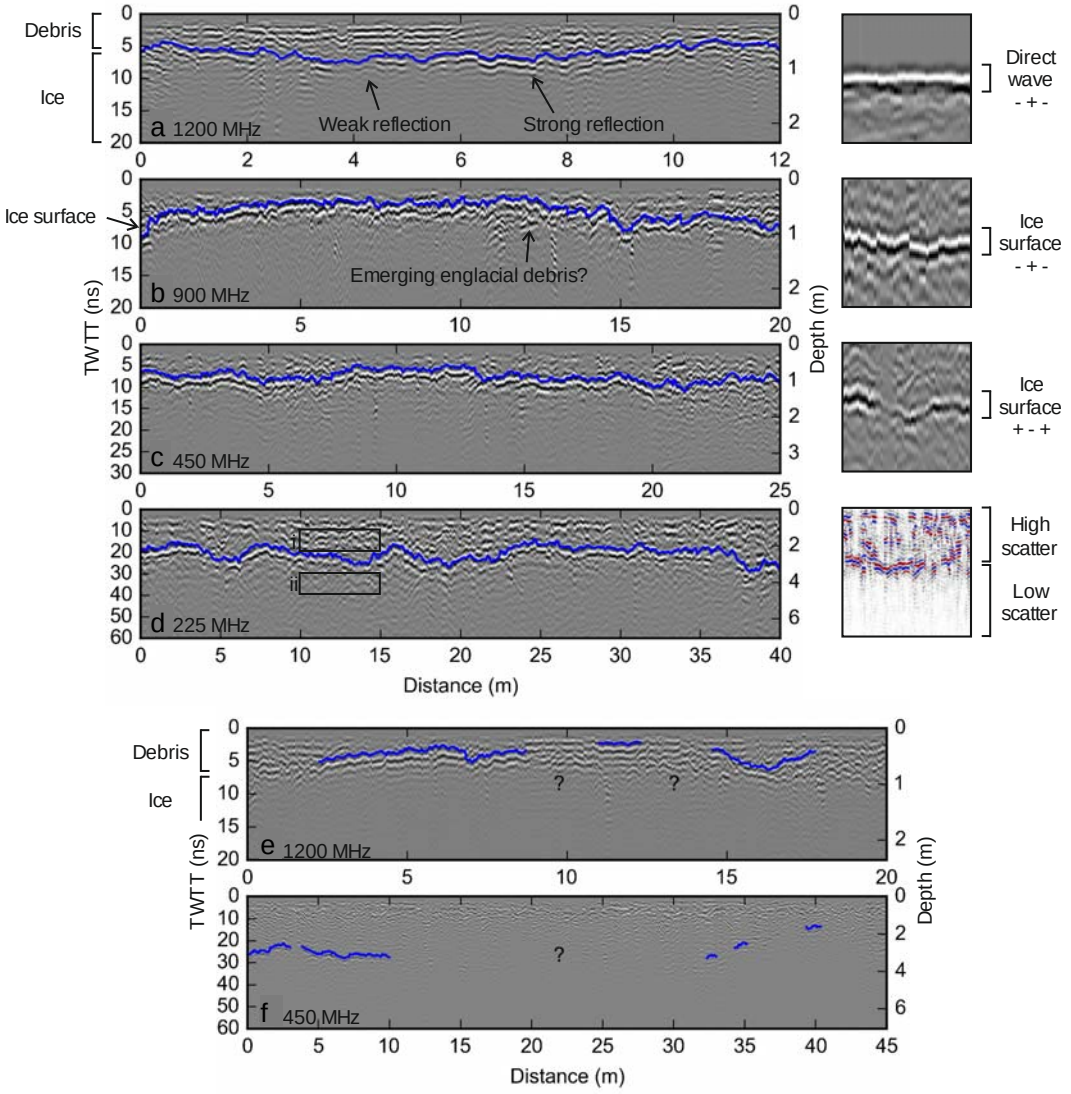

Figure 3.8 – Lirung Glacier radargrams with ice surface reflection picks (blue). In (a) to (d), the ice surface was clearly identifiable, while in (e) to (f) it was not. Boxes on the right show direct wave and ice surface wavelets and the different radar facies of debris and ice.

As in the Lirung Glacier radargrams, in most of the Ngozumpa Glacier radargrams, there is a strong continuous reflection below a high-scatter radar facies (Figure 3.9), which was interpreted as the ice surface. In some sections of some of the radargrams, usually where the debris was very thick, the ice surface is indistinct. This can be seen in the thicker debris towards the glacier margin and in the

section labelled ‘meltwater incision’, in the radargram shown in Figure 3.9f. Greater depth penetration was achieved using the 200 MHz antennas than using the 600 MHz antennas.

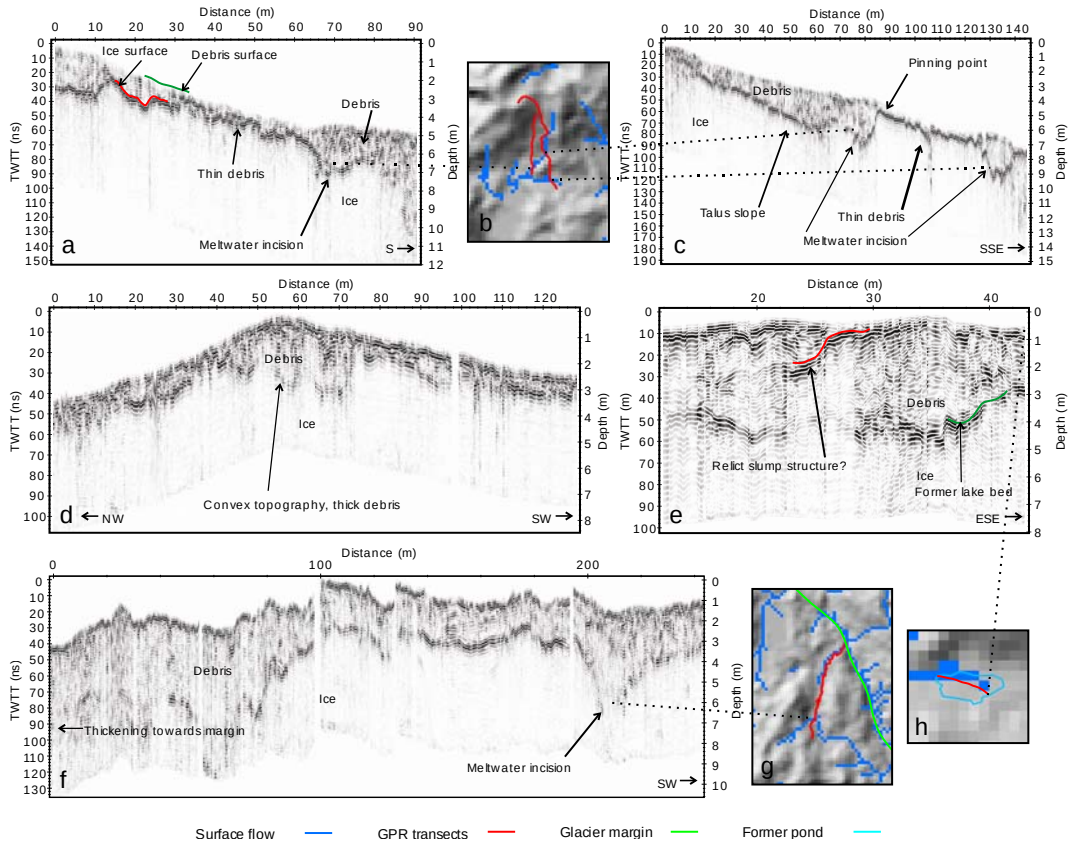

Figure 3.9 – Ngozumpa Glacier radargrams (200 MHz) in the context of their topography as given by the Ngozumpa Glacier elevation model.

Figure 3.10 shows the minimum, maximum and mean uncertainty of all the Lirung Glacier debris thickness measurements that were made using each operating frequency, and, as such, describes the measurable debris thickness range of each operating frequency. Using all four operating frequencies (225-1200 MHz), debris thickness measurements could be made through 0.08 ± 0.29 to 2.30 ± 0.39 m of debris cover. However, in general, a strong ice surface reflection can only be observed through thick debris if a low operating frequency was used and through thin debris if a high operating frequency was used. Therefore, penetration depth, measurable debris thickness range and uncertainty (ranging from 0.07 to 0.39 m) are each large for low operating frequencies and small for high operating frequencies.

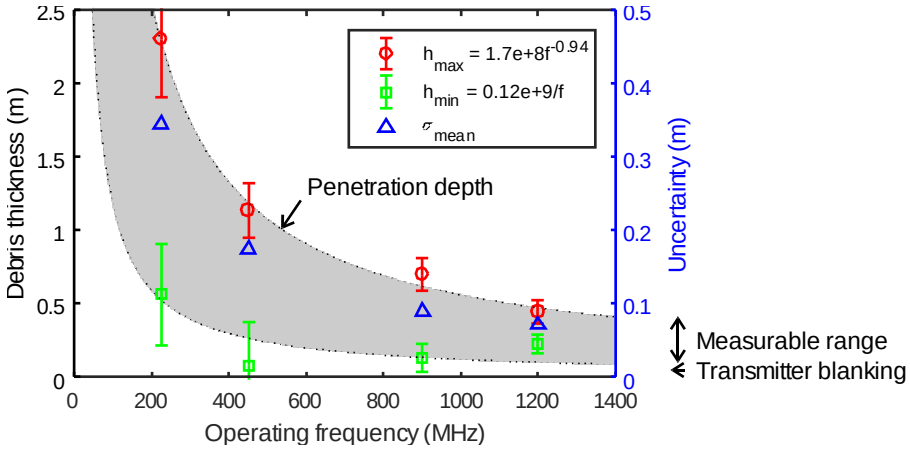

Figure 3.10 – Penetration depth, measurable debris thickness range and mean uncertainty against operating frequency for the Lirung Glacier GPR measurements. The shaded region is measurable debris thickness range.

3.5.2.2 Validation of GPR measurements

On Lirung Glacier, debris thickness measurements made by GPR agree well with those made by digging pits to the ice surface (RMSE = 0.042 m and correlation coefficient r = 0.91; Figure 3.11a). There is also good agreement between GPR measurements of debris thickness at tie points, which are the locations where the transects crossed each other (r = 0.97; Figure 3.11b). On Ngozumpa Glacier, GPR measurements of debris thickness made using the 200 MHz antennas agree closely with those made using the 600 MHz antennas (r = 0.99; Figure 3.11c) and, again, there is good agreement between GPR measurements of debris thickness at tie points (r = 0.96; Figure 3.11d). In all four plots of Figure 3.11, data points are both close to and centred around the line of equality, and the estimated uncertainties are able to explain the majority of the errors.

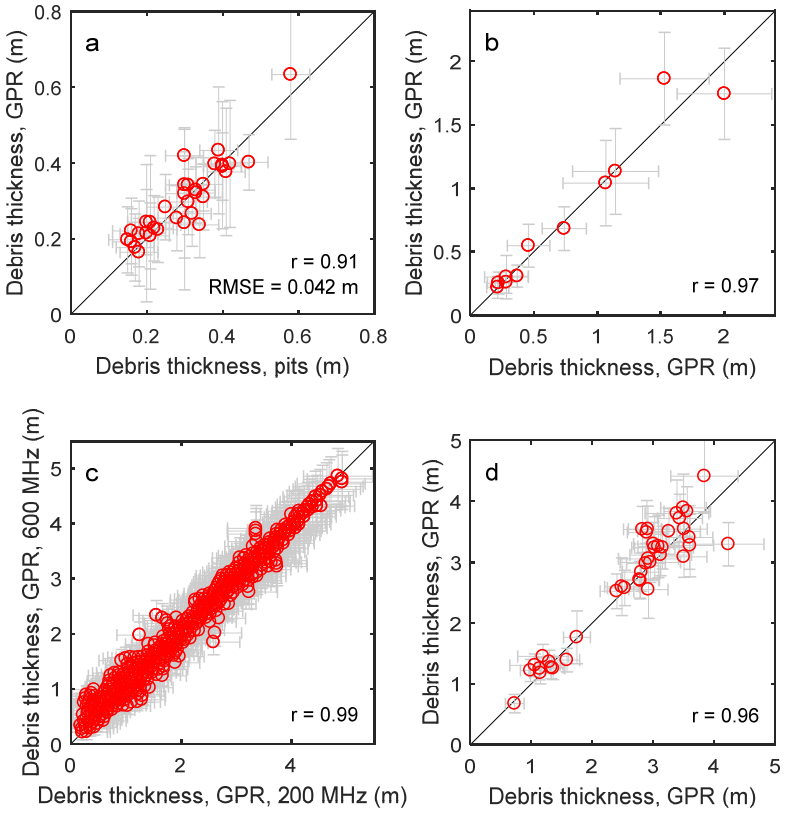

Figure 3.11 – GPR validation plots. (a) and (b) show measurements made on Lirung Glacier. (c) and (d) show measurements made on Ngozumpa Glacier. GPR-derived debris thicknesses in (a), (b) and (c) were calculated from data collected using antennas of several different operating frequencies.

3.5.3 Comparison to remote sensing quantities

Suldenferner Glacier debris thickness was found to vary nonlinearly with surface temperature, surface velocity, elevation change rate and elevation (Figure 3.12). Thin debris has a relatively low surface temperature while thick debris tends to have a relatively high surface temperature, and the surface temperature-debris thickness relationship has a steep positive gradient at low values of debris thickness and a shallow positive gradient at high values of debris thickness. Conversely, thin debris maps to high surface velocity and thick debris maps to low surface velocity, while the surface velocity-debris thickness relationship has a steep negative gradient at smaller debris thicknesses and a shallow negative gradient at larger debris thicknesses. Elevation change rate shows a more complex relationship with debris thickness, whereby thick debris maps to moderately negative elevation change rates and thin debris maps to both negative and moderate positive elevation change rates. Elevation

has a relationship with debris thickness similar to that of surface velocity, whereby thin debris maps to high elevations, thick debris maps to low elevations, and the gradient of the elevation-debris thickness relationship is steeply negative at low values of debris thickness and shallowly negative at high values of debris thickness. Pearson correlation coefficients indicate the strongest linear relationship exists between debris thickness and surface temperature ($r = 0.43$), followed by surface velocity ($r = -0.4$), elevation ($r = 0.1$) and elevation change rate ($r = -0.3$).

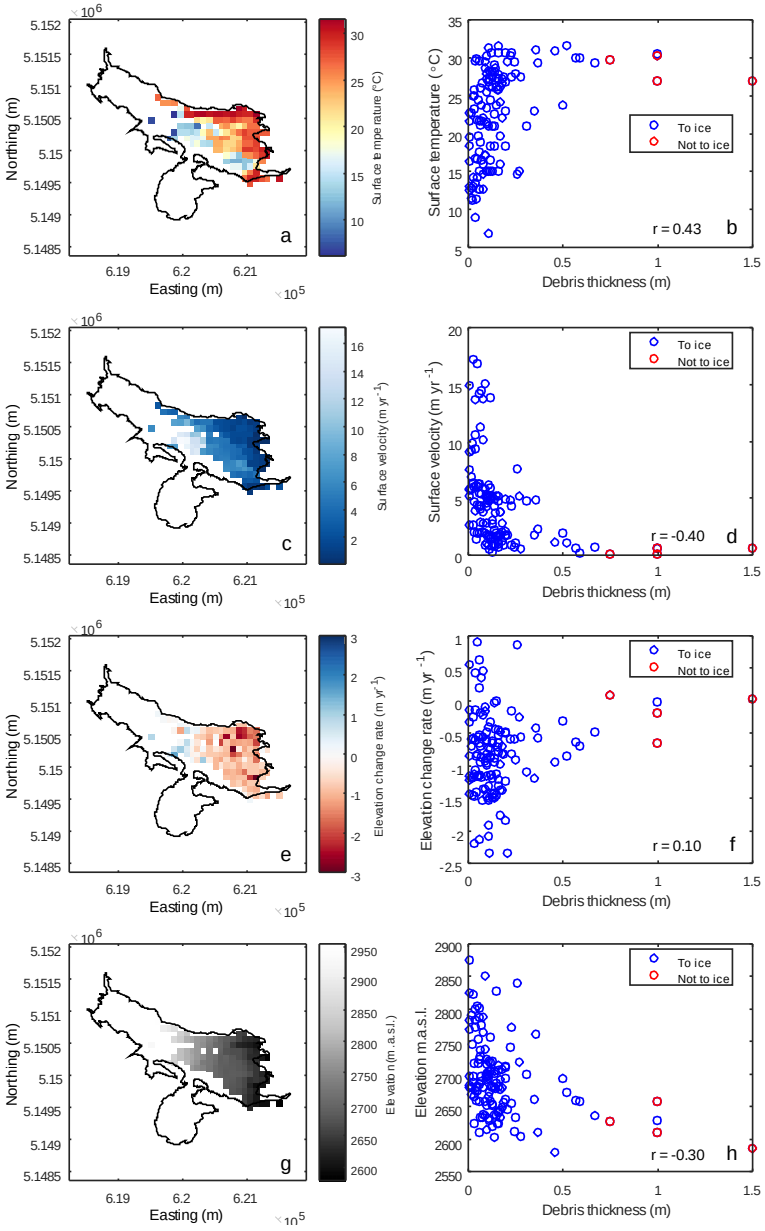

Figure 3.12 – Comparison of Suldenferner Glacier pit measurements of debris thickness to remote sensing quantities. (a), (c), (e) and (g) are the surface temperature, surface velocity, elevation change rate and elevation of the debris-covered part of the glacier. (b), (d), (f) and (h) are the same variables against debris thickness. Coordinate system is WGS84 UTM. UTM zone is 32N.

3.5.4 Topography and gravitational reworking

The radargrams collected on Ngozumpa Glacier reveal diverse debris thicknesses on different topographic features. In particular, thin debris occurs on steep slopes (e.g. Figure 3.9a, b) and thick

debris occurs at the base of steep slopes. Thick debris occurs where there are depressions in the ice surface (e.g. Figure 3.9a, c, f) and where debris surface topography is convex (e.g. Figure 3.9a, d). The debris surface tends to be almost parallel to the ice surface on steep slopes (Figure 3.9a, c, d), while on slightly shallower slopes, talus deposits develop behind pinning points of the underlying ice (Figure 3.9c). It is particularly noticeable that the ice surface is highly variable compared to the debris surface above it.

Thick debris in ice surface depressions tends to coincide with the occurrence of modelled surface-water flow paths (e.g. Figure 3.9a, b, c, f, g). In Figure 3.9a and c, there appears, further, to be a correlation between the occurrence of thin debris on steep slopes and the occurrence of modelled surface flow paths, whereby thin debris occurs on steep slopes above modelled surface flow paths. Additionally, the debris cover is thick in the location of a former supraglacial pond (Figure 3.9e, h) and towards the glacier margin (Figure 3.9f).

Comparing individual GPR measurements of debris thickness with their surface slope, aspect and curvature values indicates that there are no clear relationships (Figure 3.13a, b, c). However, if the data are binned it becomes apparent that debris is thinner on slopes steeper than around 20-23°, and on aspects of around 50-150°. Plotting debris thickness against slope and aspect simultaneously indicates that debris cover is particularly thin on steep slopes of, moving clockwise, northeast- to southwest-facing aspect (Figure 3.13e), and particularly thick on shallow, northwest facing slopes. However, this relationship is poorly resolved and would benefit from a larger sample of observations across all slopes and aspects. In particular, the existence of thick debris on northwest-facing slopes is indicated largely by only two data points. Further, there appears to be some correspondence between the pattern of debris thickness variability with slope and aspect and the pattern of incoming shortwave radiation variability with slope and aspect (Figure 3.13f).

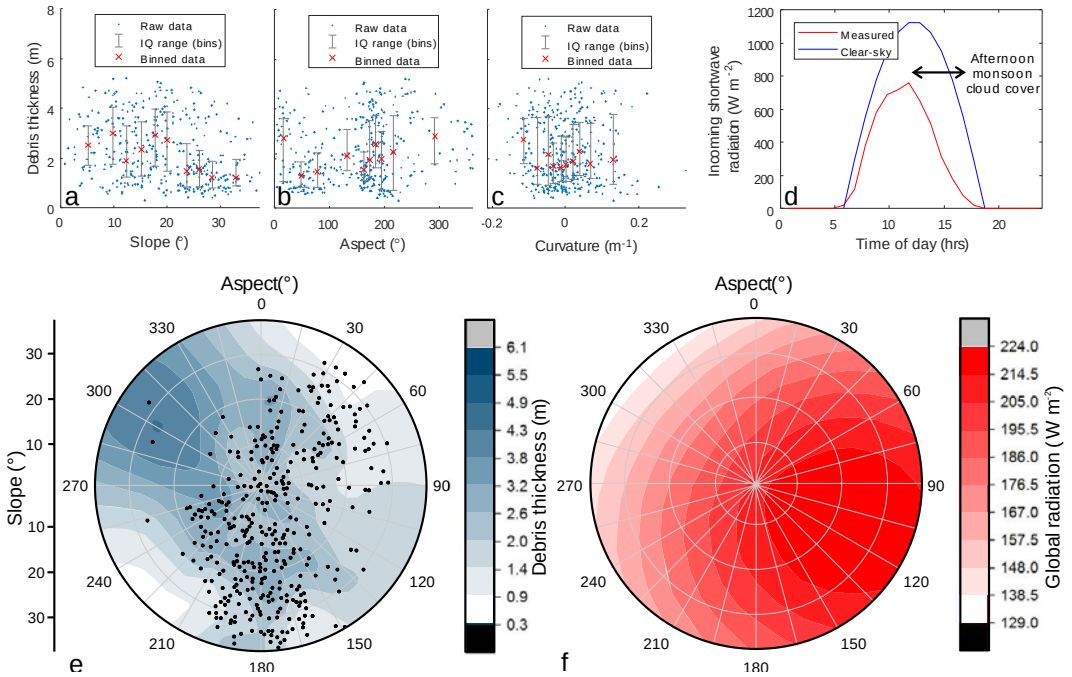

Figure 3.13 – Comparison of debris thickness to topographic parameters (a) slope, (b) aspect, (c) curvature on Ngozumpa Glacier. (d) Incoming shortwave radiation as given by Pyramid Station meteorological data. (e) Debris thickness against slope and aspect. (f) Incoming shortwave radiation on different slopes and aspects.

The slope stability modelling that was carried out indicates that potentially unstable debris cover exists on relatively large areas of the surface of Ngozumpa Glacier (Figure 3.14). If ponds and ice cliffs within the study areas are considered to be debris covered, 13, 29 and 34% of the debris cover within areas 1, 2 and 3, respectively, is estimated to be potentially unstable (under the prescribed conditions). If ponds and ice cliffs are not considered to be debris-covered, 13, 26 and 32% of the debris cover within areas 1, 2 and 3, respectively, is estimated to be potentially unstable. The areal percentage of debris cover that is potentially unstable increases upglacier as debris thickness decreases and melt rate increases. In all three areas, oversteepening is the dominant cause of potential instability, followed by saturation excess, and then meltwater weakening. Oversteepening occurs where surface slope is greater than the inverse tangent of the debris-ice interface friction coefficient, which, given a debris-ice interface friction coefficient of 0.5, is 27°. It is notable that there is good overlap between where oversteepening is predicted and where ice cliffs have been delineated, and that there is also overlap between where saturation excess is predicted and where surface ponds have been delineated.

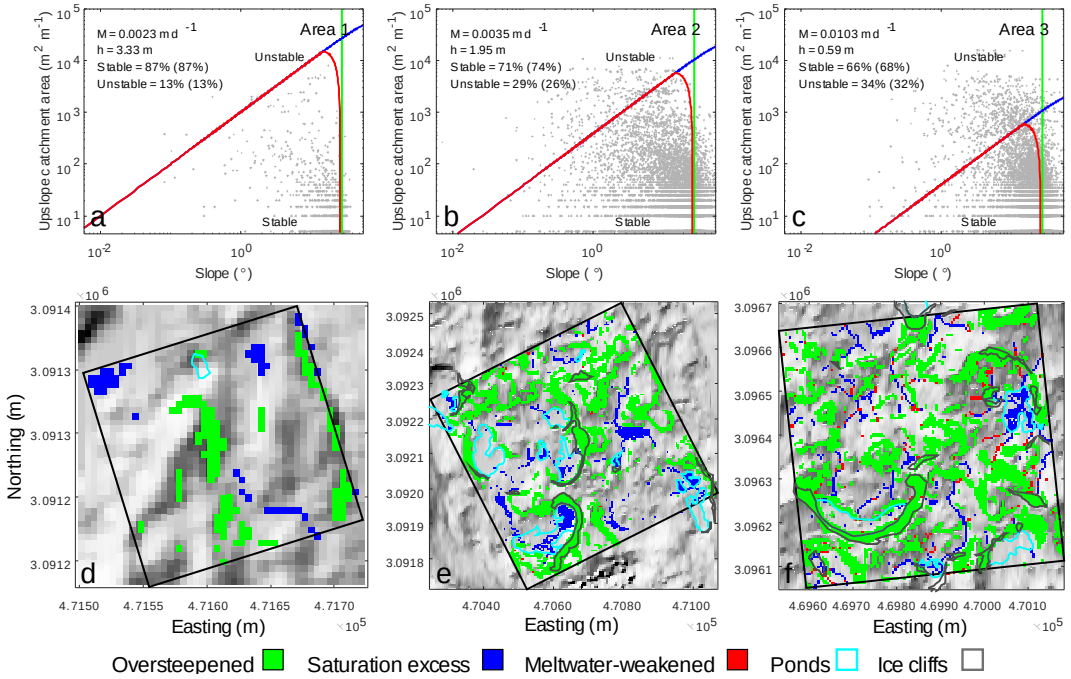

Figure 3.14 – Slope stability modelling outputs for areas 1, 2 and 3 on Ngozumpa Glacier. (a) corresponds to (d), (b) to (e) and (c) to (f). h is debris thickness and M is melt rate. Percentage stabilities are given including ponds and ice cliffs without brackets and excluding ponds and ice cliffs with brackets. Coordinate system is WGS84 UTM. UTM zone is 45N.

3.6 Discussion

3.6.1 *In-situ* measurements of debris thickness

Data presented in Section 3.5.1 show that debris thickness can be highly variable between glaciers in different geographic locations. This confirms what is shown in Table 2.1, and highlights the need for robust remote sensing methods of quantifying supraglacial debris thickness. It is particularly noticeable that the debris thickness measurements made on Suldenferner Glacier are thinner than those made on the Nepalese glaciers. This is probably a reflection of the different climatic and topographic settings of the different glaciers and of where the measurements were made on each glacier. As low-latitude glaciers (both 28° N), Lirung and Ngozumpa might be subject to high debris supply rates due to high rates of mechanical weathering, which is correlated to mean annual temperature (Hales and Roering, 2007). Further, these glaciers have steep catchments that encompass large vertical expanses of exposed rock, and debris thickness measurements were made where ice flow is slow or nearly stagnant (Quincey et al., 2009; Kraaijenbrink et al., 2016). Slow ice flow combined with high debris

supply will result in a thicker debris layer (see Section 2.2.3). The catchment of Suldenferner Glacier has less extreme relief and is located at a higher latitude (46° N), where debris supply rates are likely to be lower. Additionally, many of the Suldenferner debris thickness measurements were made where ice flow is relatively fast (see Figure 3.12). Fast ice flow combined with low debris supply rates will result in a thinner debris layer.

Data presented in Section 3.5.1 also show that debris thickness can be highly variable over short spatial scales of < 10 m on individual glaciers. This is particularly notable for Lirung and Ngozumpa glaciers but also for Suldenferner Glacier. The implications of this are that debris thickness should be treated as being non-uniform over glacier surfaces when modelling surface mass balance, and that debris thickness should be input to surface mass balance models as a probability density function or frequency distribution (e.g. Reid et al., 2012; Nicholson and Benn, 2012). Because there is considerable debris thickness variability within narrow elevation ranges, surface mass balance models for debris-covered glaciers that are altitudinally distributed (e.g. Kraaijenbrink et al., 2017) may not perform as well as those that are spatially distributed (Reid et al., 2012; Fyffe et al., 2014).

The measurements that were made on Lirung and Ngozumpa glaciers are too sparsely distributed to infer the potential response of these glaciers to future climatic forcing. However, it is notable that thin debris, below which melt rates will be relatively high, exists to low elevations. The existence of thin debris at low elevations may partly explain observations of highly variable surface lowering on Lirung and Ngozumpa glaciers (Immerzeel et al., 2014; Pellicciotti et al., 2015; Thompson et al., 2016). In the case of Suldenferner Glacier, there is a clear increase in debris thickness downglacier and with decreasing elevation, which will result in differential melting, and which will ultimately cause surface slope shallowing and stagnation due to reduced driving stress (Benn et al., 2012).

3.6.2 Using GPR to measure debris thickness

The results presented in Section 3.5.2 confirm that GPR is a useful tool with which to measure supraglacial debris thickness at local scales.

3.6.2.1 Ice surface reflection

For each of the GPR transects completed on Lirung Glacier, at least one operating frequency produced a radargram showing a strong, continuous ice surface reflection. This shows that GPR can be used to image the ice surface through a debris layer, even at shallow depths (cf. Lønne and Lauritsen, 1996;

Moorman and Michel, 2000; Wu and Liu, 2012). It was also possible to make debris thickness measurements from the majority of the radargrams collected on Ngozumpa Glacier. However, measurable debris thickness ranges shown in Figure 3.10 indicate that choice of operating frequency is crucial. For example, if the operating frequency is too high, attenuation prevents detection of the ice surface, e.g. Figure 3.8f (cf. Annan, 2009), while if the operating frequency that is used is too low, the ice surface reflection is ambiguous because it coincides with the high-energy direct wave, which is usually wider (longer lasting) at lower operating frequencies. The second of these phenomena has been referred to as 'transmitter blanking' (Annan, 2009). Plotting maximum debris thickness against operating frequency (Figure 3.10) suggests penetration depth is approximately proportional to $f^{-0.9}$, where f is operating frequency, as described by Cook (1975). Plotting minimum debris thickness against operating frequency indicates minimum debris thickness $h = v/f$, where v is debris wave speed 0.12 m ns^{-1}, suggesting transmitter blanking is limited to one wavelength below the debris surface. Measurable debris thickness range is wide for low operating frequencies and narrow for high operating frequencies, and uncertainty increases (largely because range resolution decreases) with decreasing operating frequency. Therefore, a three-way trade-off exists between penetration depth, measurable debris thickness range and uncertainty (cf. Davis and Annan, 1989). An additional complication could be that if the wavelength of the GPR signal is similar to debris grain size, scattering is likely to inhibit interpretation of the ice surface, as is shown in Figure 3.8e.

Reflection strength is a function of the difference in relative permittivity (and therefore wave speed) of the materials either side of a reflector, where a large difference in relative permittivity results in a strong reflection (Reynolds, 2011). Reflection strength is also controlled by the attenuation of a signal as it travels to and from a reflector. As such, the variable strength of the ice surface reflection observed in the radargrams, both on Lirung and Ngozumpa glaciers, could represent lateral changes in: (1) debris composition, which would cause changes in both the relative permittivity contrast at the ice surface (e.g. due to a change from wet to dry debris or vice versa) and the rate of attenuation in the debris (e.g. due to variable clay content or large point-scatterers), or (2) ice surface properties (e.g. melt water, emerging englacial debris, or frozen debris on the ice surface, as opposed to a sharp debris-ice interface), which would also cause changes in the relative permittivity contrast at the ice surface. In particular, a high debris clay or water content should result in a weaker ice surface reflection due to increased attenuation, while a layer of meltwater at the ice surface should give a stronger reflection due to an increased relative permittivity contrast. The ice surface reflection can often be interpreted confidently due to its continuity, despite its variable strength in some radargrams. The continuity of the reflection from any non-horizontal subsurface reflector is largely determined by

step size between traces, with small steps giving a more continuous reflection than large steps (Jol and Bristow, 2003). Lirung Glacier GPR data were collected in 'step-mode' in order that individual traces could be matched to pit measurements of debris thickness. The step size that was used was generally small enough to result in a continuous ice surface reflection. However, the Ngozumpa Glacier GPR data were collected at higher spatial resolution, in 'continuous-mode', and the continuity of the ice surface reflection is better in the Ngozumpa GPR data.

Penetration depth was limited on both glaciers, but much more so on Lirung Glacier than Ngozumpa Glacier. Given the geology of the debris on both glaciers and that there was considerable snow cover on Lirung Glacier during data collection, it is likely that this was because the debris cover on Lirung Glacier had higher water and clay contents than the debris cover on Ngozumpa Glacier. On Lirung Glacier, the thickest debris that was encountered was 2.30 ± 0.39 m. The ice surface here produced a strong reflection at 225 MHz frequency. On Ngozumpa Glacier, the thickest debris that was encountered was 7.3 +/- 0.83 m, beyond which the ice surface could not be easily identified.

Debris and ice are apparent in all radargrams as distinctly different radar facies, where debris is seen as a high-scatter radar facies and ice is seen as a low-scatter radar facies. This is likely due to the different electromagnetic properties of the different materials and was helpful with regard to interpreting the ice surface. Specifically, debris is comprised largely of heterogeneous point-scatterers, while ice is relatively homogenous.

3.6.2.2 Validation of GPR measurements

The pit measurements of debris thickness show a good fit to GPR measurements in Figure 3.11a, indicating that the ice surface can be reliably interpreted as distinct from processing artefacts or multiples of the debris surface and that GPR can be used to measure debris thickness accurately, at least in the range 0.16-0.58 m. Here, the spread of data around the equality line likely represents a combination of picking imprecision and spatiotemporal wave speed variability, and outliers are assumed to be mispicks of the ice surface, where the reflections picked are artefacts of processing or the physical expressions of other, possibly off-nadir, subsurface features. The calculated correlation coefficient r = 0.91 is similar to that of other GPR method validation studies in similar environments (e.g. Machguth et al., 2006; r = 0.92), and the good fit of the data suggests that both CMP-derived debris wave speeds and uncertainty estimates are realistic. In Figure 3.11b, c and d, the close fits of tie points to the equality line indicate consistent interpretation of the ice surface and an absence of

processing artefacts or multiples of the debris surface. They suggest that GPR can be used to measure debris thickness with a useful degree of precision, at least in the range 0.18-4.9 m.

Together, the four validation plots of Figure 3.11 suggest that GPR is a useful tool for measuring debris thickness at least in the range 0.16-4.9 m (the combined range of all validation measurements). In all these plots, errors on individual measurements of debris thickness are largely accounted for by calculated uncertainties, suggesting the uncertainties assigned to the GPR measurements of debris thickness are appropriate.

3.6.2.3 Technical issues and recommendations

The highly variable topography and rough surfaces of debris-covered glaciers can make carrying out GPR surveys physically difficult and time consuming. However, GPR offers certain benefits over alternative methods of measuring debris thickness. For example, GPR is quicker than digging pits if the debris is relatively thick, less biased than measuring debris thickness at ice cliffs and allows a wide debris thickness range to be measured at high spatial resolution. Jol and Bristow (2003) make general recommendations for a successful GPR survey, many of which were found to be very useful in carrying out the work in this chapter. With respect to measuring debris thickness, it is recommended that:

- Surveys should be carried out in snow-free conditions to permit a strong ice surface reflection. Long transects should be set up where possible, in order to make the ice surface easier to interpret.
- An appropriate multi-frequency GPR can be used to cover most debris thickness eventualities, significantly reducing survey time. The dual-frequency 200-600 MHz GPR used on Ngozumpa Glacier was very effective, and Figure 3.10 can be used as a guide to choosing acquisition parameters. Collecting GPR data in ‘continuous-mode’ results in a clearer reflection at the ice surface than collecting GPR data in step-mode.
- GPR should be used in conjunction with pits or CMPs in order to determine debris wave speed to make realistic debris thickness calculations. Topographic correction using DGPS measurements does not significantly improve ice surface interpretability.
- Transmitter blanking limits the use of GPR for measuring the thickness of thin debris (< 0.1 m), in which case digging pits is more appropriate.

3.6.3 Comparison to remote sensing quantities

The results of the comparison of debris thickness to remote sensing quantities show that there are clear relationships between debris thickness and surface temperature, debris thickness and elevation, debris thickness and elevation change rate, and debris thickness and surface velocity. In the case of debris thickness and surface temperature, surface temperature asymptotes towards a maximum value as debris thickness increases because the conductive heat flux at the debris surface becomes negligible as debris thickness increases (Evatt et al., 2015). Here, debris thickness variability is a cause of the observed surface temperature variability. In the case of debris thickness and elevation change rate, the observed relationship is more complex. This is because elevation change rate is controlled both by surface mass balance and by ice flow, and because debris thickness exerts a direct control on surface mass balance but not on ice flow. The sign of the elevation change rate at a given location on the glacier then depends on whether surface mass balance, as a function of debris thickness, or flux divergence is dominating at that location (e.g. Hooke, 2005). In the case of debris thickness and surface velocity, the debris cover is thick where surface velocity is slow due to compression and advection effects associated with ice flow (see Section 2.2.3). Here, ice flow is a cause of variations in debris thickness. Finally, in the case of debris thickness and elevation, there is no direct, causal relationship. The debris cover is thicker at lower elevations because of the effects of ice flow.

Efforts have been made to estimate debris thickness from both remotely sensed surface temperature and elevation change rate (see Section 2.5), and surface velocity could be used to this end as well. However, the relationships between surface velocity and debris thickness and elevation change rate and debris thickness are considerably more complex than the relationship between surface temperature and debris thickness, as is evidenced by calculated Pearson correlation coefficients, so surface temperature is possibly the most appealing remote sensing quantity from which to quantify debris thickness.

3.6.4 Topography and gravitational reworking

Radargrams showing thin debris on steep slopes above thick debris at the base of steep slopes provide visual evidence of gravitational reworking of supraglacial debris by slope processes such as those described by Moore (2018). Because debris sliding was often experienced while collecting the Ngozumpa Glacier GPR data, and because the ice surface is parallel to the debris surface where the debris on steep slopes is thin, indicating debris transport by failure-plane parallel motion (Varnes, 1978), it is assumed that these slope processes occur, at least sometimes, in the form of shallow sliding

events (Lawson, 1979; Heimsath et al., 2012). Other slope processes that have been observed on debris-covered glaciers include topples, flows, slumps and falls (e.g. Lawson, 1979).

That debris thickness varies with surface slope and aspect indicates that topography is a control on debris thickness, presumably via such slope processes as those evidenced by the radargrams. Where slope processes are initiated, the debris become will become thin, while where they are terminated, the debris will become thick. Slope processes are initiated, causing debris to be thin, on steep slopes because increasing slope angle increases the shear stress on a potential failure plane. There is a possible connection with southeast-facing slopes because these slopes receive the most incoming shortwave radiation in the Himalaya due to monsoonal afternoon cloud-cover (e.g. Figure 3.13d; cf. Buri and Pellicciotti, 2018), which should cause high melt rates, and which should, in turn, cause the ice surface to be more slippery and debris pore pressures to be increased.

The occurrence of modelled surface flow paths and the former pond in relation to the morphology of the debris in the radargrams indicates that surface hydrological processes are also a control on local debris thickness. For example, it is likely that the debris in the location of the former pond is thick because debris is transported to and deposited in ponds by meltwater movement, and that the debris cover around sites of modelled surface flow paths is thick because meltwater incision creates hollows in which debris can accumulate. Further, the fact that modelled surface flow paths occur below areas of thin debris on steep slopes suggests that surface-water flow may act to trigger certain slope processes by increasing slope angles and by undercutting slopes on which there is the potential for failure.

The results of the slope stability modelling imply that large areas of the surfaces of debris-covered glaciers like Ngozumpa can experience enhanced sub-debris melt rates due to slope processes, even if their debris cover is mostly thick. This is because sub-debris melt rate has a highly non-linear relationship with debris thickness, whereby melt rates under thin debris are much higher than those under thick debris (Section 2.3), and because slope processes act to increase debris thickness variability, which increases the amount of thin debris. Figure 3.15 shows a conceptual model of the process of shallow sliding as it might occur on a debris-covered glacier, and how sub-debris melt rates might be affected. Via differential melting, with locally high melt rates where the debris is thin, the effects of slope processes on debris thickness may have a considerable effect on the evolution of debris-covered glacier surfaces, enhancing topographic variability, and, in turn, encouraging the occurrence of slope processes in a positive feedback (Sharp, 1949; Nicholson and Benn, 2012; Reid et al., 2012).

Finally, it seems likely that the thick debris on convex topography observed in the radargrams is the result of topographic inversion by differential melting, and that thick debris near the margin of Ngozumpa Glacier is likely the result of slow ice flow at the margin and debris falling or flowing from the moraines on to the glacier surface as the glacier thins. The fact that modelled surface flow paths occur in the same locations as ice surface depressions observed in the radargrams indicates that meltwater is probably transported in sub-debris supraglacial streams, the existence of which is described by Miles et al. (2017).

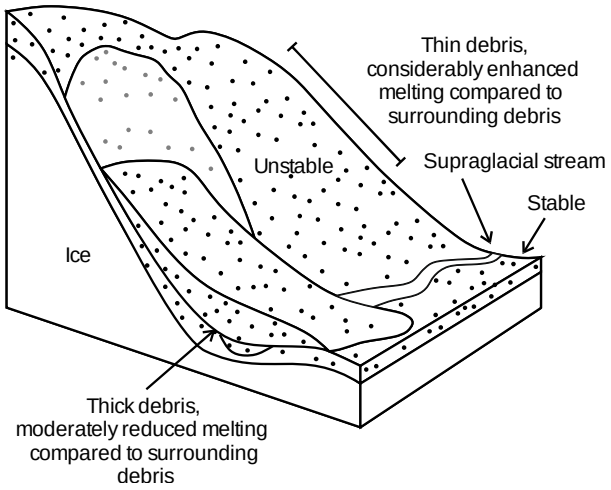

Figure 3.15 – Schematic of gravitational reworking of supraglacial debris by shallow sliding.

3.7 Summary

In-situ field measurements of debris thickness were made on three glaciers: Suldenferner Glacier, Italy, and Lirung and Ngozumpa glaciers, Nepal. The Suldenferner Glacier measurements were made by digging pits through the debris to the ice, while the Lirung and Ngozumpa glacier measurements were made using GPR (supplemented by pit measurements for validation and wave speed tests). The measurements were used with an elevation model to investigate the relationship between debris thickness and topographic parameters, with a slope stability model to investigate the processes of gravitational reworking of supraglacial debris, and with various satellite products to explore the relationships between debris thickness and a number of remote sensing quantities. In making the GPR measurements, GPR was tested or validated as a method of measuring supraglacial debris thickness. The key findings are as follows:

- Supraglacial debris thickness is highly variable between glaciers and over short spatial scales on individual glaciers. The total debris thickness range on all three glaciers was found to be 0.01-7.3 m, and debris thickness can be expected to vary by several metres within 10 m horizontal distance. High inter-glacier debris thickness variability highlights the need for suitable remote sensing methods of quantifying supraglacial debris thickness, and high intra-glacier debris thickness variability has implications both for how sub-debris melting is modelled and for how debris thickness is remotely sensed.
- Debris thickness patterns are broadly as expected at the glacier scale (cf. Nakawo et al., 1986). However, GPR data from Ngozumpa Glacier show that topography is an important additional control on debris thickness at local scales through the action of slope and hydrological processes. Specifically, radargrams provide evidence that slope processes and gravitational reworking can take the form of shallow sliding events, and that there is a correlation between debris thickness, slope and aspect, whereby thinner debris is likely to occur on steep, southeast-facing slopes and thicker debris is likely to occur on shallow, northwest-facing slopes.
- Slope stability modelling indicates that the debris cover on large areas of the surface of Ngozumpa Glacier is potentially unstable. Because slope processes act to increase debris thickness variability, and because of the highly nonlinear relationship between debris thickness and sub-debris melt rate, debris instability must cause surface mass balance to be more negative. Therefore, gravitational reworking provides a mechanism by which large areas of debris-covered glaciers are subject to relatively high melt rates. Effectively, thin patches of debris due to gravitational reworking will increase melt rates on debris-covered glaciers in a similar way to ponds and ice cliffs (e.g. Thompson et al., 2016).
- Relationships between debris thickness and remote sensing quantities indicate that surface temperature and elevation change rate are both potentially useful quantities with which to quantify debris thickness by remote sensing, but that the relationship between debris thickness and elevation change is more complex.
- GPR can be used successfully to measure debris thickness at least in the range 0.16-4.9 m (the range covered by the validation plots) and could be a valuable tool with which to make extensive *in-situ* debris thickness measurements. As such, the use of GPR in this capacity could lead to improved surface mass balance modelling of debris-covered glaciers at local scales. Radargrams often show a strong, continuous reflection at the ice surface, and debris is easily distinguishable from ice because it presents as a high-scatter radar facies while ice presents as a low-scatter radar facies. GPR measurements of debris thickness correlate well with pit measurements and show

good agreement at tie-points and when made using different operating frequencies. Uncertainties can be estimated successfully using Equation (3.5).

- In order to derive accurate debris thickness measurements by GPR, measuring debris wave speed is important, as is taking account of system geometry, particularly if the debris is thin and the antenna separation is large. Additionally, there exists a three-way trade-off exists between penetration depth, measurable debris thickness range and uncertainty. It is recommended that GPR should be used to measure debris thickness if the debris is relatively thick (more than 10-20 centimetres), but that pits should be dug if the debris is relatively thin.

The debris thickness measurements that were reported here are used as ground-truth against which thermal remote sensing methods of quantifying debris thickness are tested in the following chapters, 4 and 5.

4 Glacier-scale thermal remote sensing

4.1 Context

It can be exceedingly challenging to make *in-situ* field measurements of supraglacial debris thickness that are representative of debris thickness at the glacier scale. Individual glaciers can be large and methods of measuring debris thickness in the field can be physically demanding and time consuming. For example, to make pit measurements of debris thickness on Ngozumpa Glacier, Nepal, on a 100-m grid would require 2100 individual pits to be dug. At a rate of 20 measurements per day, this would take 105 days. Using GPR would be faster, but the challenge would still be substantial. However, being able to quantify supraglacial debris thickness at such a scale is a prerequisite for forecasting surface mass balance and therefore runoff volumes from debris-covered glaciers, and for understanding the processes that occur at their surfaces. For these reasons, remote sensing methods of quantifying debris thickness should be explored.

Unfortunately, there are no remote sensing methods capable of measuring supraglacial debris thickness directly, and debris thickness cannot be determined accurately by forward modelling because the processes that distribute debris on a glacier are varied and occur over long time periods (Rowan et al., 2015; Konrad and Humphrey, 2000; Anderson and Anderson, 2016, Section 2.2.3). As a result, quantifying debris thickness at the glacier scale by remote sensing must be treated as an inverse problem, whereby remote sensing observations are made of a physical quantity that can be measured remotely and whose magnitudinal variations are, at least in part, caused by debris thickness. Examples of such physical quantities include surface temperature, SAR backscatter and surface elevation change (Section 2.5). Section 3.5.3 shows that there is a strong relationship between debris thickness and surface temperature and between debris thickness and surface elevation change, and Huang et al. (2017) show that the same is true for debris thickness and SAR backscatter. Given an understanding of the physical processes by which debris thickness causes variations in these physical quantities, it follows that it should be possible to determine debris thickness from them. Effectively,

the cause (i.e. debris thickness) can be determined from the results (e.g. surface temperature). Unfortunately, variations in the three physical quantities listed above have additional causes other than debris thickness, which complicates matters. Surface temperature varies as a result of air temperature, wind speed and humidity, for example; SAR backscatter varies due to surface roughness, the incidence angle of the radar signal and debris moisture content; and surface elevation varies as a result of ice flow.

Of the possible remote sensing approaches to quantifying supraglacial debris thickness, thermal remote sensing approaches, i.e. those that use surface temperature as the physical quantity from which to determine debris thickness, have received the most attention in the literature (see Section 2.5.4). This is probably because thermal satellite imagery is readily available at relatively high spatial resolution and no cost; two of the reasons they are the focus of this chapter. For similar reasons, there is a long history of using thermal remote sensing to quantify, for example, soil moisture and evapotranspiration in vegetation and agricultural studies (Carlson et al., 1995; Bastiaanssen et al., 1998; Bastiaanssen et al., 1998; Courault et al., 2005; Petropoulos et al., 2009).

The principle behind thermal remote sensing approaches to quantifying debris thickness is that if the ice below the debris is melting, increasing debris thickness reduces the conductive heat flux at the debris surface in accordance with Fourier's law, causing surface temperature also to increase. Effectively, thick debris is a better insulator than thin debris. Previous work suggests that this principle is valid, and that thermal remote sensing shows promise towards the goal of quantifying debris thickness (Mihalcea et al., 2008; Foster et al., 2012; Rounce and McKinney, 2014; Schauwecker et al., 2015). However, while various studies have developed approaches to quantifying debris thickness by thermal remote sensing, none have been rigorously validated. This is understandable because, as is discussed above, making *in-situ* measurements of debris thickness is difficult. However, it means we can have little confidence in their results. Additionally, existing approaches have not been compared with each other, so it is difficult to know which approach should be used or is most appropriate.

4.1.1 Aims and objectives

This chapter develops and tests nine thermal remote sensing approaches to quantifying supraglacial debris thickness against each other and against pit measurements of debris thickness made on Suldenferner Glacier, Italy. The aims of this chapter are to answer the following questions:

- Can thermal remote sensing methods of quantifying debris thickness reproduce debris thickness values measured in the field at the glacier scale?

- If so, what is the best way of doing this, i.e. what are the best approaches and what are their limitations? Can night-time thermal imagery be used to quantify debris thickness?
- How sensitive are the different approaches to changes in their input data and, therefore, how transferable are they?
- Can remote sensing estimates of debris thickness, as opposed to field measurements, be used to model sub-debris melting on debris-covered glaciers?

4.2 Study site

The study site for this chapter is Suldenferner Glacier, Italy (see Section 3.2.1). While Suldenferner Glacier is not in High Mountain Asia, the primary geographical focus of this thesis, it was deemed to be a good choice of study site for this work for a number of reasons. First, it is small, meaning debris thickness could be measured over the entire debris-covered part of the glacier. Second, it is easily accessible, making fieldwork straightforward. Third, there are few supraglacial ponds and ice cliffs, which are problematic because they cause a skew towards lower surface temperatures. Finally, a good meteorological record was available for forcing the debris thickness quantification approaches.

4.3 Data

4.3.1 Ground-truth debris thickness data

In order to test and validate the different remote sensing approaches, ground-truth debris thickness data were collected by manual excavation, as described in section 2.5.1 and 3.4.1.1. A total of 134 debris thickness measurements were made in a 100-m grid, covering the majority of the debris surface. Measurements were made in summer 2015 and summer 2017, and debris thickness was found to range from 0.01 to > 1.5 m.

4.3.2 Satellite imagery and elevation models

Glacier surface temperature and emissivity, which were used as input to the debris thickness models tested in this study, were derived from ASTER higher-level data products. For surface temperature, the L2 Surface Temperature V003 (AST08) product was used. For emissivity, the L2 Surface Emissivity V003 (AST05) product was used. These products are generated on request by NASA LP

DAAC, using the ASTER temperature/emissivity separation (TES) algorithm, which uses all five of ASTER's thermal bands in an inverse approach centred on Planck's and Kirchoff's laws (Gillespie et al., 1998). Atmospheric and ozone correction options were set to 'climatology'[7], while the moisture, temperature and pressure correction option was set to 'NOAA/NCEP GDAS model'[8]. The accuracy of the surface temperature product is typically within 1.5°C, while precision is typically within 0.4°C. For the emissivity product, accuracy and precision are typically within 0.015 and 0.006, respectively (Gillespie et al., 1998). The spatial resolution of the ASTER thermal bands (B10 to B14) is 90 m, and the spectral range is 8.125 to 11.650 μm. While both products are georectified, neither is orthorectified.[9] The ASTER instrument is deployed on the Terra satellite platform, which has a near-polar, sun-synchronous orbit. Daytime imagery is collected during the Terra satellite's descending orbits (crossing the equator at around 10:30:00 UTC), while night time imagery is collected during ascending orbits (crossing the equator at around 22:30:00 UTC). The satellite's repeat time is every 16 days. Contemporaneous surface temperature and emissivity and products are created for each pass where image quality is sufficient. Associated metadata files were used to get the time and date of each satellite pass.

After filtering, five surface temperature-emissivity image sets were ordered from NASA's Earthdata Search website[10] in hdf format. Four of these image sets consisted of daytime images and one set consisted of night time images. Because clouds obscure the land surface, and because the debris thickness quantification approaches tested here require the ice to be melting, image sets were filtered using a cloud cover of < 10% and an acquisition date of June 01 to September 30, which was deemed to represent the melt season. Image sets were also filtered by year, from 2013 to 2017, around the time the ground-truth debris thickness measurements were made. The hdf files were converted to geotiff files using NASA's Hdf-EoS to GIS conversion tool (HEG). During conversion, the tool performs a nearest neighbour resampling because ASTER images are not north-oriented. However, 90-m spatial resolution is maintained. To ensure the quality of the input data, the image sets were visually inspected for snow cover, clouds and accurate georeferencing. Two daytime image sets were deemed unsuitable for further analysis and were discarded, leaving two daytime image sets and one night-time image set. Visual inspection was carried out using contemporaneous optical L3 Orthorectified Radiance at the Sensor V003 images (AST14DMO), B1, B2 and B3N.

[7] Aerosol and ozone climatology are monthly average products produced by the Naval Research Laboratory
[8] The NOAA/NCEP GDAS model provides a 4 times daily assimilation of meteorological observations.
[9] Orthorectifying the images may have moderately improved the results. However, the debris-covered part of Suldenferner is relatively flat, so orthorectification was not considered to be a major concern.
[10] https://search.earthdata.nasa.gov/

For surface elevation, the ALOS Global Digital Surface Model v.2.1 was used (AW3D30). This product is supplied by JAXA and was generated from satellite-collected optical stereo pairs collected between 2006 and 2011. Its spatial resolution is 30 m, although it was resampled to 90 m to match the resolution of the thermal images. The height accuracy of the AW3D30 product has been found to be better than 6 m RMSE (Santillan and Makinano-Santillan, 2016). Initially, the AST14DMO elevation product was used for elevation but the quality of the georectification of this product was found to be poor.

Details of all the satellite data products that were used are given in Table 4.1.

Table 4.1 – Overview of the satellite data products that were used in this study.

Product(s)	Time and date (UTC)
ASTER AST08 surface temperature, ASTER AST05 surface emissivity, ASTER AST14DMO optical	02-Aug-2013 10:22:02 (day) 26-Aug-2016 10:22:29 (day) 02-Jul-2015 21:13:02 (night)
ALOS AW3D30 elevation	2006-2011

ASTER rather than Landsat products were used for surface temperature for a number of reasons. First, ASTER has a longer record than either Landsat 7 or Landsat 8, and is still in operation unlike Landsat 5. Second, ASTER thermal bands have no known problems, while Landsat 7 has a fault in its scan-line corrector, causing its images to be incomplete and Landsat 8 has a far out-of-field stray light problem in its second thermal band (Band 11), causing large brightness temperature offsets. Third, the ASTER surface temperature product is provided at native resolution, while the Landsat thermal bands (5, 7 and 8) are all resampled to 30 m, which is problematic for comparison with pit measurements.

Examples of the satellite data products that were used in this study are shown in Figure 4.1.

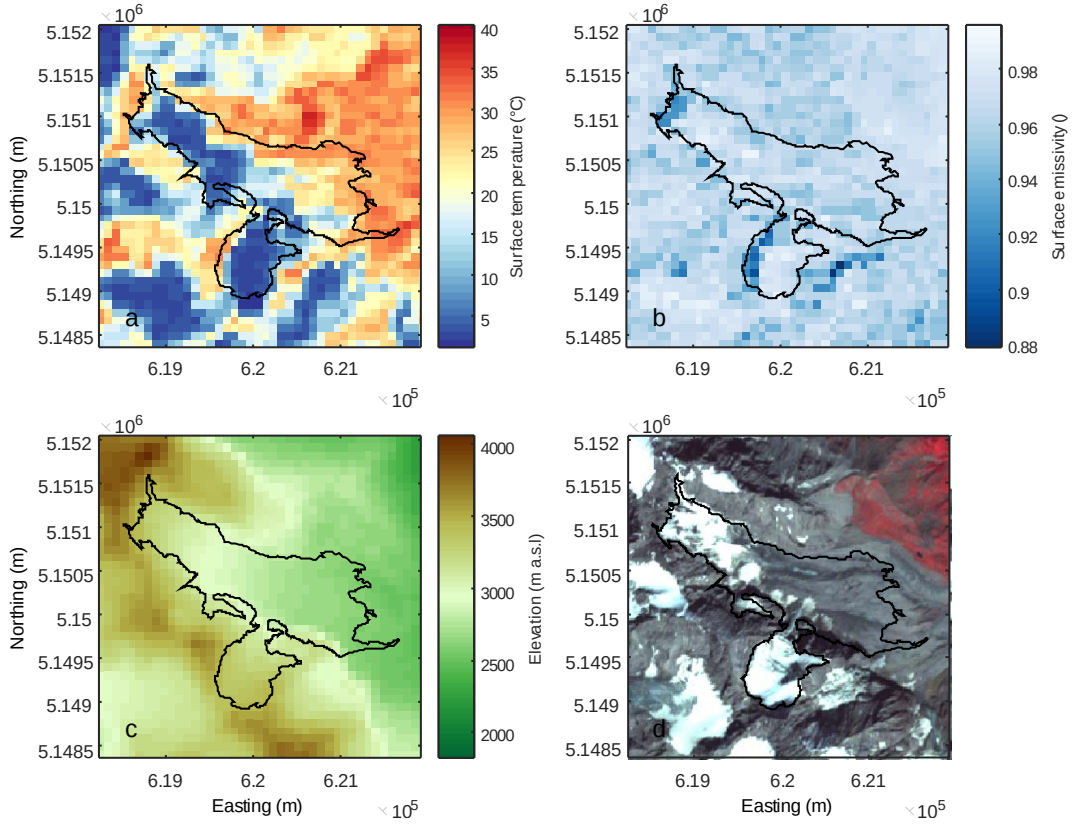

Figure 4.1 – Examples of the satellite data products used in this chapter. (a) AST08 surface temperature. (b) AST05 surface emissivity. (c) ALOS AW3D30 elevation, resampled to 90-m resolution. (d) ASTDMO14 optical composite. Coordinate system is WGS84 UTM. UTM zone is 32N.

4.3.3 Meteorological data

Five of the debris thickness quantification approaches tested require meteorological data as input. Meteorological data were provided from two automatic weather stations (AWSs): one on-glacier AWS and one off-glacier AWS (referred to from here as the Suldenferner AWS and the Madritsch AWS, respectively). The Suldenferner AWS is operated and maintained by Lindsey Nicholson, while the Madritsch AWS is operated and maintained by the Autonomous Province of Bozen Weather Service team.[11]

The Suldenferner AWS is located on debris cover near the upper limit of the glacier's debris cover. It has been in operation since July 2014. The Madritsch AWS is located on the other side of the valley,

[11] Suldenferner AWS data were provided by Lindsey Nicholson and Madritsch AWS data were provided by the Autonomous Province of Bozen Weather Service team.

around 2.7 km from the terminus of Suldenferner Glacier, and has been in operation since January 1999. AWS metadata (measurement height, altitude and location) are provided in Table 4.2.

Table 4.2 – AWS metadata. Superscripts describe: (1) the height of the AWS measurements at time of 2016 images, (2) the height of the AWS measurements at time of 2015 images, (3) the height of the AWS measurements during surface roughness length calibration period.

	Suldenferner AWS	**Madritsch AWS**
Location (WGS84 32 N)	620417 5150345	623889 5150181
Altitude (m a.s.l)	2725	2825
Measurement height (m)	4.13^{1}, 2.42^{2}, 2.83^{3}	2
Slope (°)	0	0
Aspect (°)	0	0
Debris thickness (m)	0.09	NA
Time step (s)	1800	1800

Both weather stations collect shortwave radiation, air temperature, wind speed and relative humidity data. The Suldenferner AWS also collects longwave radiation data but does not collect snow depth or precipitation data. The Madritsch AWS does collect snow depth and precipitation data but does not collect longwave radiation data. To complete the Suldenferner AWS dataset, snow depth and precipitation data were added from the Madritsch AWS dataset. To complete the Madritsch dataset, incoming longwave radiation was parameterised, as discussed in Section 4.4.5. The Madritsch AWS collects data in Central European Time, using a 10-minute time step, while the Suldenferner AWS collects data in UTC using a 30-minute time step. For consistency, Madritsch data were converted to UTC and downsampled to a 30-minute time step.

As a result of instrument failure, or due to insufficient power, particularly in winter, when solar panels are often obscured by snow cover, both datasets contain gaps. However, the longest gap in the data that were used to force the models tested in this study was a few hours. Therefore, all gaps were filled by linear interpolation. To ensure their quality, meteorological data were quality checked using the World Meteorological Organization Guidelines[12] as a guide.

The 26-Aug-2016 daytime and 02-Jul-2015 night-time image sets were contemporaneous with meteorological data from both the Suldenferner and the Madritsch AWSs. The 02-Aug-2013 image set was contemporaneous only with the Madritsch AWS data.

[12] https://www.wmo.int/pages/prog/www/OSY/Meetings/ET-AWS3/Doc4(1).pdf

An example of some meteorological data collected at the Suldenferner AWS is shown in Figure 4.2.

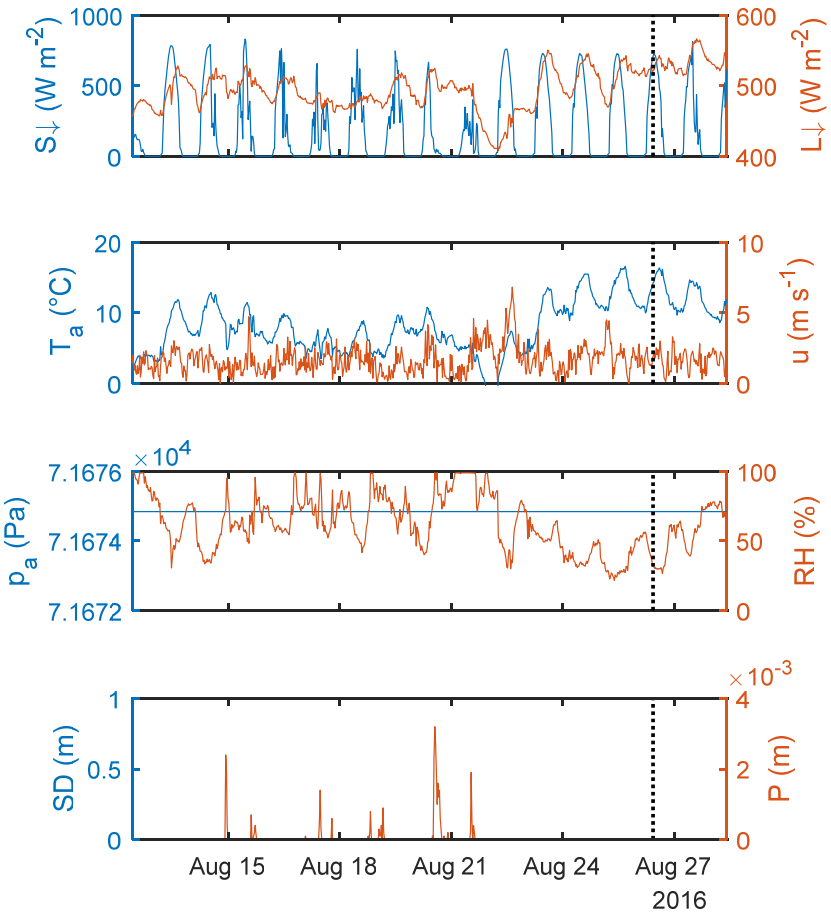

Figure 4.2 – Meteorological data collected at the Suldenferner AWS for the two weeks in advance of the 26-Aug-2016 satellite pass. The time of the satellite pass is shown by the dotted, black vertical line.

4.3.4 Geospatial data

The glacier outline was provided by Lindsey Nicholson. It was manually digitised using elevation differences determined from successive high-resolution elevation models; areas in which there was no elevation change were deemed not to be glacier. Debris-covered parts of the glacier surface were delineated manually in ArcGIS using high-resolution WorldView satellite imagery.

4.4 Methods

In order to meet the aims set out in Section 4.1.1, and to use all the available data, the bulk of this chapter is centred around 29 model runs, which were carried out as part of five 'experiments'. Each model run consisted of using one of the nine debris thickness quantification approaches (see Section 4.4.1) with one of the three image sets and meteorological data from one of the two weather stations. Each experiment tested some or all of the approaches using a specific combination of images and meteorological data. The five experiments are detailed in Table 4.3. The dynamic energy-balance approach (DEB1) was the only approach that could produce realistic debris thickness estimates using the night-time satellite images and is therefore the only model included in experiments 4 and 5. A further 169 model runs were carried out to test the sensitivities of the different approaches.

Table 4.3 – Experimental setup, detailing the model runs, satellite images, approaches AWS data associated with each of the five experiments.

Exp't	Model runs	Temperature-emissivity images	Approach(es)	Corresponding AWS
1	1-9	26-Aug-2016 10:22:29 (day)	All	Suldenferner (on-glacier)
2	10-18	26-Aug-2016 10:22:29 (day)	All	Madritsch (off-glacier)
3	19-27	02-Aug-2013 10:22:02 (day)	All	Madritsch (off-glacier)
4	28	02-Jul-2015 21:13:02 (night)	DEB1	Suldenferner (on-glacier)
5	29	02-Jul-2015 21:13:02 (night)	DEB1	Madritsch (off-glacier)

4.4.1 Quantifying debris thickness

There are six published approaches to quantifying debris thickness by thermal remote sensing. Three further approaches or variations are presented in this thesis. The approaches fall into four categories: (1) scaling approaches, which calculate debris thickness in terms of surface temperature and a number of parameters, (2) static energy-balance approaches, which solve the debris surface energy balance at the time of a thermal satellite image by making an assumption about the temperature gradient in the debris at that time, (3) dynamic energy-balance approaches, which model debris surface temperature over a spin-up period in advance of a thermal satellite image under different values of debris thickness until modelled surface temperature at the time of the satellite image matches satellite image surface temperature, and (4) extrapolation approaches, which use observations of debris thickness to define the parameters of a function that relates debris thickness to surface temperature. The different approaches tend to have different input data requirements, depending on their complexity.

Table 4.4 – Values of constants and variables used. The debris emissivity value of 0.94 was only used when calculating the heat storage factor for the SEB2 approach and when optimising surface roughness length, otherwise satellite-image emissivity was used. The density of air value was only used when calculating debris volumetric heat capacity, otherwise it was calculated.

Constant or variable	Value	Reference (if applicable)
Albedo of debris ()	0.16	-
Atmospheric clear-sky transmissivity ()	0.82	-
Debris porosity ()	0.33	Nicholson and Benn (2012)
Density of air (kg m^{-3})	1.2	-
Density of debris (kg m^{-3})	1.8423×10^{3}	-
Density of ice (kg m^{-3})	915	Reid and Brock (2010)
Density of rock (kg m^{-3})	2700	Nicholson and Benn (2012)
Density of water (kg m^{-3})	999.7	Reid and Brock (2010)
Diffuse radiation factor ()	0.15	Konzelmann and Ohmura (1995)
Duration of a Julian year (s)	31557600	-
Emissivity of debris ()	0.94	Brock et al. (2010)
Environmental air temperature lapse rate (K m^{-3})	0.0065	-
Gas constant (J mol^{-1} K^{-1})	8.31447	-
Grain size of debris (m)	0.006624	-
Gravitational acceleration (m s^{-2})	9.81	-
Latent heat of fusion of water (J kg^{-1})	334000	Reid and Brock (2010)
Latent heat of vaporisation of water (J kg^{-1})	2476000	Reid and Brock (2010)
Melting point of ice (K)	273.15	-
Molar mass of dry air (kg mol^{-1})	0.0289644	-
Solar constant (W m^{-2})	1368	-
Specific heat capacity of air (J kg^{-1} K^{-1})	1005	Brock et al. (2010)
Specific heat capacity of debris (J kg^{-1} K^{-1})	811.49	-
Specific heat capacity of rock (J kg^{-1} K^{-1})	750	Nicholson and Benn (2012)
Specific heat capacity of water (J kg^{-1} K^{-1})	4181.3	Reid and Brock (2010)
Standard sea level pressure (Pa)	101325	-
Standard sea-level temperature (K)	288.15	-
Stefan-Boltzmann constant (W m^{-2} K^{-4})	5.67×10^{-8}	-
Surface roughness length of debris (m)	0.003560	-
Temperature of melting ice (K)	273.15	-
Thermal conductivity of debris (W m^{-1} K^{-1})	0.6949	-
Thermal diffusivity of debris (m^2 s^{-1})	4.65×10^{-7}	-
Volumetric heat capacity of debris (J m^{-3} K^{-1})	1.495×10^{6}	-
Von Karman's constant ()	0.41	-
Water content of debris pore spaces ()	0.1	Nicholson and Benn (2012)

For all the approaches to quantifying debris thickness, modelled debris thicknesses greater than the maximum pixel-mean pit depth, which was 0.67 m, were fixed at that value. This was done on the basis that surface temperature sensitivity to debris thickness is very low for thick debris because surface temperature approaches an asymptotic limit with increasing debris thickness as the conductive heat flux becomes negligible. In this chapter, values of 0.67 m should therefore be seen as a lower limit. In terms of the melt modelling that is carried out, this is not a major concern because melt rate is

insensitive to debris thickness for thick debris. However, there are also implications of fixing maximum debris thickness for the performance statistics that were used to assess the various approaches. These implications are discussed in Section 4.4.6. Additionally, modelled debris thicknesses less than the grain size, i.e. 0.0066 m (see Section 4.4.4.3), were fixed at the grain size. This was done on the assumption that the minimum debris thickness on the glacier is the grain size of the debris.

It should be noted that while a number of the approaches tested here are based on approaches published in the literature, they are not necessarily exactly the same as those approaches. In these cases, differences are highlighted in the text.

All modelling and calculations were carried out using MATLAB. The values of the constants and variables that were used are provided in Table 4.4.

4.4.1.1 A scaling approach

This approach assumes that debris thickness is the dominant control on debris surface temperature and therefore that debris thickness can be described as a function of surface temperature. It requires no meteorological data, so spatial variations in air temperature and wind speed, for example, are assumed to be relatively unimportant. It effectively assumes that a full debris thickness range (i.e. from thin to thick debris) exists on the glacier surface and that this must be reflected in the surface temperature range. This is perhaps not unreasonable, as debris tends to be thin upglacier where ice-flow is fast, and thick downglacier, near the terminus, where it piles up due to advection and where ice-flow is slow (see Section 2.2.3). The main appeal of this approach is that, because it requires little in the way of input data, it can be applied relatively easily and over large areas (Kraaijenbrink et al., 2017).

4.4.1.1.1 SCA1

Debris thickness was calculated broadly following the empirical 'exponential scaling' approach of (Kraaijenbrink et al., 2017), which assumes that the minimum surface temperature of the debris-covered part of the glacier corresponds to a minimum debris thickness value, that the 95th percentile surface temperature corresponds to a maximum debris thickness value, and that debris thickness increases exponentially with surface temperature between the two:

$$h = h_{min} e^{\left[\frac{T_s - T_{s_{min}}}{T_{s_{P95}} - T_{s_{min}}} \ln\left(\frac{h_{max}}{h_{min}}\right)\right]} \quad (4.1)$$

where h_{min} and h_{max} are minimum and maximum debris thickness, and $T_{s_{min}}$ and $T_{s_{P95}}$ are minimum and 95th percentile surface temperatures. The equation was modified here to include h_{min} explicitly, in order that sensitivity to h_{min} could be tested, and so the units of h_{min} and h_{max} can be metres rather than centimetres. Minimum and 95th percentile surface temperatures were found by generating a debris cover mask and using the MATLAB min and prctile functions. Following Kraaijenbrink et al. (2017), a value of 0.5 m was used for h_{max}. However, whereas Kraaijenbrink et al. (2017) used a value of 0.01 m for h_{min}, here the grain size of the debris was used. Additionally, Kraaijenbrink et al. (2017) used a 'brightest pixel' method to produce a cloud-free surface temperature composite (i.e. from all available satellite images) from which to calculate debris thickness. Here, on the other hand, individual surface temperature images were used in order to make the different approaches more comparable and because cloudy images had already been excluded. Kraaijenbrink et al (2017) developed their approach from the approach of Mihalcea et al. (2008). Calculated values of $T_{s_{min}}$ and $T_{s_{P95}}$ are presented in Table 4.6.

4.4.1.2 Static energy-balance approaches

These approaches use satellite image-derived surface temperature combined with meteorological data and varying amounts of *in-situ* data, such as *in-situ* surface temperature or thermistor string data, to solve a debris surface energy balance for debris thickness. They are 'static' because they solve the energy balance only at the time of the satellite image, when there is glacier-wide surface temperature information available. The appeal of these approaches is that computing time is minimal on a desktop computer, e.g. using a GIS, and that they are simple. The downside is that, in being static, they have to make an approximation of the conductive heat flux at the debris surface. This is because the temperature gradient at the debris surface is unknown (the debris is usually heating up at the time of a satellite pass, so debris temperature profiles are typically non-linear e.g. Figure 4.5)[13], and the temperature gradient is needed to calculate the conductive heat flux. The temperature gradient at the debris surface is controlled by past as well as present meteorology and by debris properties, including debris thickness. However, these approaches assume no spatiotemporal meteorological variability[14] and either no variation in the nonlinearity of the debris temperature profile with debris thickness (Foster et al., 2012; Rounce and McKinney, 2014) or a variation in the nonlinearity of the debris temperature profile with debris thickness that is defined empirically (Schauwecker et al., 2015). They

[13] The thicker the debris, the more non-linear the temperature profile and the less likely the debris is in thermal equilibrium/steady state. Very thin debris may be effectively in steady state.
[14] Although they do assume meteorological spatial variability.

also typically assume that debris properties other than debris thickness (e.g. albedo and surface roughness length) are spatially invariable.

The four approaches of this type are similar in the way they solve the energy balance. However, they account for the nonlinearity of the temperature profile within the debris in different ways. Heat fluxes were calculated as in Section 4.4.2. All of the approaches were prevented from outputting negative debris thicknesses and very large debris thicknesses by applying a minimum net heat flux rule, after Rounce and McKinney (2014), where if the net heat flux ($S + L + LE + H$) towards the debris surface was less than or equal to 0 W m^{-2}, debris thickness was set to the maximum debris thickness that was recorded on the glacier. Meteorological data were determined by linear interpolation at the time of each set of satellite images.

Figure 4.3 is a schematic of the debris surface energy balance as discussed in this thesis. Energy is conserved at the debris surface in accordance with the First Law of Thermodynamics.[15]

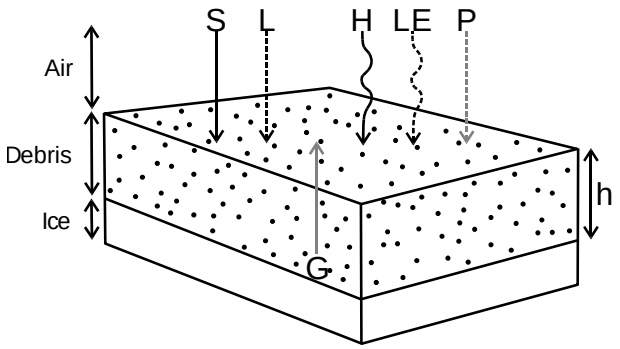

Figure 4.3 – Schematic of debris surface energy balance, modified from Oke (2002), where S and L are the shortwave and longwave radiative heat fluxes, H and LE are the sensible and latent heat fluxes, G is the conductive heat flux, and P is the heat flux due to precipitation.

4.4.1.2.1 SEB1

Debris thickness was calculated by solving the debris surface energy balance assuming that the debris was in thermal equilibrium, or steady state, at the time of each satellite image, where the energy balance was defined as:

[15] Which states that the energy added to a system must be equal to the change in internal energy of the system plus or minus the work extracted from the system.

$$S + L + H + LE + G = 0 \quad (4.2)$$

Here, S is the shortwave radiative heat flux, L is the longwave radiative heat flux, H is the (turbulent) sensible heat flux, LE is the (turbulent) latent heat flux, and G is the conductive heat flux through the debris (e.g. Nakawo and Young, 1982). There was assumed to be no heat flux due to precipitation because the satellite images that were used have < 10% cloud cover. Given the assumption of steady-state heat conduction, the conductive heat flux was calculated assuming a linear temperature gradient within the debris (a special case of Fourier's law):

$$G = -k_d \frac{T_s - T_i}{h} \quad (4.3)$$

where T_s is the surface temperature at the time of the satellite image and h is debris thickness, T_i is the temperature of melting ice and k_d is debris thermal conductivity. Substituting Equation (4.3) into Equation (4.2) means debris thickness can be found according to:

$$h = k_d \frac{T_s - T_i}{S + L + H + LE} \quad (4.4)$$

Rounce and McKinney (2014) used a similar approach to this in the development of their nonlinear static energy-balance approach to quantifying debris thickness.

4.4.1.2.2 SEB2

Debris thickness was calculated broadly following Foster et al. (2012). The debris surface energy balance was defined as follows:

$$S + L + H + LE + G + \Delta D = 0 \quad (4.5)$$

where the heat fluxes are the same as for the SEB1 approach except for an additional heat flux ΔD. Foster et al. (2012) described this additional heat flux as a flux due to change in heat storage, and defined it as being proportional to the conductive heat flux:[16]

[16] Brutsaert (1982) suggests the conductive heat flux into soil can be approximated by assuming it is proportional to, e.g. sensible or radiative heat fluxes.

$$\Delta D = c_1 G \tag{4.6}$$

Where c_1 is a free parameter, described as a heat storage factor. Using Equation (4.3) for the conductive heat flux, the debris surface energy balance was solved for debris thickness as such:

$$h = (1 + c_1) k_d \frac{T_s - T_i}{S + L + H + LE} \tag{4.7}$$

where c_1 was found by calculating mean daily cycles of ΔD and G for melt-season months June to September and interpolating for the time of day of each satellite image, following Foster et al. (2012), using Suldenferner AWS data. ΔD was calculated following Brock et al. (2010):

$$\Delta D = -C_d \frac{\partial T_d}{\partial t} h \tag{4.8}$$

where h is debris thickness at the weather station, C_d is the volumetric heat capacity of the debris, and T_d is mean debris temperature at the weather station: $T_d = (T_s - T_i)/2$. T_s at the Suldenferner weather station was calculated by rearranging the Stefan-Boltzmann law:

$$T_s = \left(\frac{L \uparrow}{\sigma \varepsilon_d} \right)^{\frac{1}{4}} \tag{4.9}$$

where $L \uparrow$ is outgoing longwave radiation, ε_d is debris surface emissivity (a value of 0.94 was used for the weather station, after Brock et al., 2010) and σ is the Stefan-Boltzmann constant. Mean daily cycles of the conductive heat flux at the weather station were calculated as in Equation (4.3), again using T_s calculated from outgoing longwave radiation. Here, the value of c_1 was consistently calculated to be around 0.1 (Table 4.6). Foster et al. (2012) calculated c_1 to be 0.64 for Miage Glacier, Italy. Mean daily cycles of the conductive and 'change in heat storage' fluxes are shown in Figure 4.4, along with a calculated value of the heat storage factor c_1.

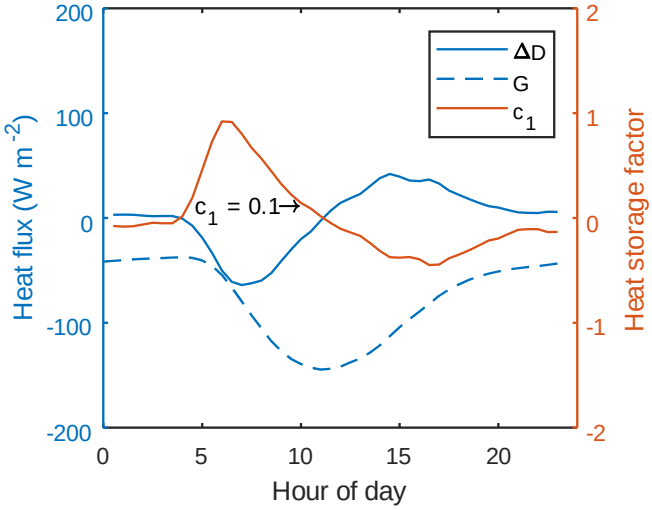

Figure 4.4 – Mean daily cycles of the heat storage factor, according to the SEB2 approach. The heat storage factor is labelled c_1 at the time of the 26-Aug-2016 satellite pass.

4.4.1.2.3 SEB3

Debris thickness was calculated following Rounce and McKinney (2014), with the debris surface energy balance defined as in Equation (4.2). Rounce and McKinney (2014) accounted for the fact that heat conduction through the debris is not steady state by attaching a coefficient (c_1, described as G-ratio) to the conductive heat flux like so:

$$G = -c_1 k_d \frac{T_s - T_i}{h} \tag{4.10}$$

Equation (4.2) was combined with Equation (4.10) and debris thickness was calculated as such:

$$h = c_1 k_d \frac{(T_s - T_i)}{S + L + H + LE} \tag{4.11}$$

c_1 was calculated, following Rounce and McKinney (2014), using thermistor strings deployed in the debris (see Section 4.4.4.1), as the ratio of the temperature gradient in the top 0.1 m of the debris to the temperature gradient in the whole debris layer, as such:

$$c_1 = h \frac{(T_s - T_{0.1})}{0.1(T_s - T_i)} \tag{4.12}$$

Because three thermistor strings were installed on the glacier, the mean of the three values of the coefficient c_1 was used. Here, h is debris thickness at the location of the thermistor string, and $T_{0.1}$ is the debris temperature at a depth of 0.1 m. Similar to Rounce and McKinney (2014), the thermistor strings were only installed for a short period of time, during which no satellite passes occurred. Therefore, c_1 was calculated for the time of day, not the exact time and date, of each surface temperature image. Figure 4.5 shows debris temperature profiles at the time of the August 2016 images, along with calculated values of c_1. Here, the value of c_1 was consistently calculated to be around 1.3 (Table 4.6). Rounce and McKinney (2014) calculated a value of c_1 of 2.7 for Imja-Lhotse Shar Glacier, Nepal. It is notable that Equation (4.11) is very similar to Equation (4.7) and, therefore, that the SEB2 and SEB3 approaches are similar except in the way they calculate the values of their coefficients. It is also notable that Rounce and McKinney (2014) calculated the sensible and latent heat fluxes in a different way from how they were calculated here.

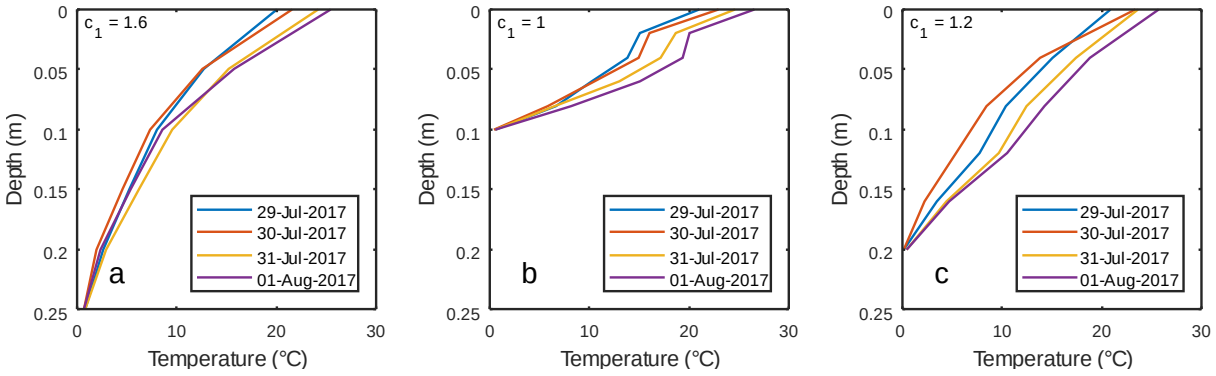

Figure 4.5 – Temperature profiles within the debris, as measured at the three thermistor strings at the same time of day as the 26-Aug-2016 satellite pass. c_1 values were calculated according to the SEB3 approach.

4.4.1.2.4 SEB4

Debris thickness was calculated following Schauwecker et al. (2015), who extended the Foster et al. (2012) approach (SEB2) by redefining its 'heat storage factor', such that its value increases linearly with debris thickness, and multiplying the net heat flux by 0.5 to give the following two equations:

$$h = (1 + c_1)k_d \frac{T_s - T_i}{0.5(S + L + H + LE)} \tag{4.13}$$

$$c_1 = 6.71h + 1 \tag{4.14}$$

Schauwecker et al. (2015) solve these equations numerically by iteration. However, here they were solved analytically by substituting one into the other and rearranging as such:

$$h = 2\left[\frac{S + L + H + LE}{0.5k_d(T_s - T_i)} - 6.17\right]^{-1} \quad (4.15)$$

This approach recognises that the nonlinearity of the debris temperature profile must vary with debris thickness. However, there seems to be no physical justification for multiplying the net heat flux by 0.5, other than to increase modelled debris thickness.

4.4.1.3 A dynamic energy-balance approach

Similar to the static energy-balance approaches, this approach uses satellite-image derived surface temperature, meteorological data, and knowledge of debris properties, to solve the debris surface energy balance for debris thickness. However, unlike the static approaches, it solves the energy balance through time for a period in advance of each satellite image, i.e. it is dynamic. The advantage of this approach is that it is physically realistic in the way it solves heat conduction through the debris. The temperature gradient at the debris surface, and the temperature history of the debris, which are required to solve the debris surface energy balance, are known; the conductive heat flux does not need to be approximated, it can be calculated. The disadvantages are that it more complex than the other approaches presented, and that it is more computationally expensive.

4.4.1.3.1 DEB1

Debris thickness was calculated by modelling debris surface temperature at the time of each satellite image using a dynamic debris surface energy-balance model, then minimising the mismatch between that modelled surface temperature and the measured surface temperature of the satellite image, by iteratively varying debris thickness. Effectively, when modelled surface temperature matches measured surface temperature, an appropriate debris thickness value is deemed to have been determined. This was done on a pixel-by-pixel basis over the debris-covered area of the glacier. Egli et al. (2016) presented a similar approach, though this is as yet unpublished. The dynamic energy-balance model that was used was a modified version of the DEB model, which was written by Reid and Brock (2010).[17]

[17] Unmodified DEB model code was provided by Tim Reid.

The DEB model solves heat conduction through the debris using the one-dimensional heat equation:[18]

$$\rho_d c_d \frac{\partial T_d}{\partial t} = \frac{\partial}{\partial z}\left(k_d \frac{\partial T_d}{\partial z}\right) \tag{4.16}$$

where T_d is the temperature of the debris, z is depth in the debris, t is time, c_d is debris specific heat capacity and ρ_d is debris density. The boundary condition at the debris surface is the debris surface energy balance, given as:

$$S + L + H + LE + P + G = 0 \tag{4.17}$$

where P is the heat flux due to precipitation. The boundary condition at the ice surface is the temperature of melting ice T_i (0°C). The debris is split into layers: one layer per 0.01 m of debris or 10 layers if debris thickness is less than 0.1 m, and the conductive heat flux is calculated according to:

$$G = -k_d \frac{\partial T_d}{\partial z} \tag{4.18}$$

where the temperature gradient is linear in each debris layer. Because surface temperature is required by multiple heat fluxes, the DEB model solves the debris surface energy balance for surface temperature using the Newton-Raphson method. In order to do this, it calculates debris internal temperatures, because these are used to calculate the conductive heat flux. Debris internal temperatures are calculated using the Crank-Nicolson method. The model effectively makes sure that the change in internal energy of the debris with time (i.e. the change over a time step) is equal to the change in internal energy of the debris with depth, i.e. energy is conserved at the surface of each debris layer. The initial temperature profile was set to be linear between satellite image T_s and T_i (i.e. this is how the model was kick-started).

The mismatch between modelled and measured surface temperature was minimised by bisection. As a root-finding method, bisection is slow to converge, but was chosen because it is simple and robust. Upper and lower debris thickness limits were defined (0.67 and 0.0066 m, respectively), then a first estimate of debris thickness was taken as the midpoint of those two limits:

[18] This says that the change in temperature of the debris with time must be equal to the change in temperature with depth (heat is conserved). The problem is transient. There are two boundary conditions, both of which are of the first-type (i.e. Dirichlet): the temperature of the boundary conditions, rather than e.g. the heat flux, is prescribed. The ice surface boundary condition is a temperature of 0°C, while the debris surface boundary condition is the temperature that the energy balance and the one dimensional heat conduction equations are solved for.

$$h_{new} = \frac{h_{lower} + h_{upper}}{2} \tag{4.19}$$

and the modified DEB model was run using this value. Here, h_{new} is the new estimate of debris thickness and h_{lower} and h_{upper} are the lower and upper limits respectively. If the modelled surface temperature that was calculated for the time of the satellite image using this new debris thickness value was less than the measured surface temperature, the lower debris thickness limit was set to the midpoint debris thickness and a new midpoint debris thickness was calculated. If the modelled surface temperature was greater than the measured surface temperature, the upper debris thickness limit was set to the midpoint debris thickness and a new midpoint was calculated. The DEB model was then run again and the process was repeated iteratively until successive iterations caused debris thickness to vary by less than a given tolerance (0.001 m). At this stage, an appropriate debris thickness value was deemed to have been determined. This process is described by Figure 4.6. For each iteration, modelled surface temperature was interpolated linearly at the time of the satellite image using the time step before and the time step after the satellite image.

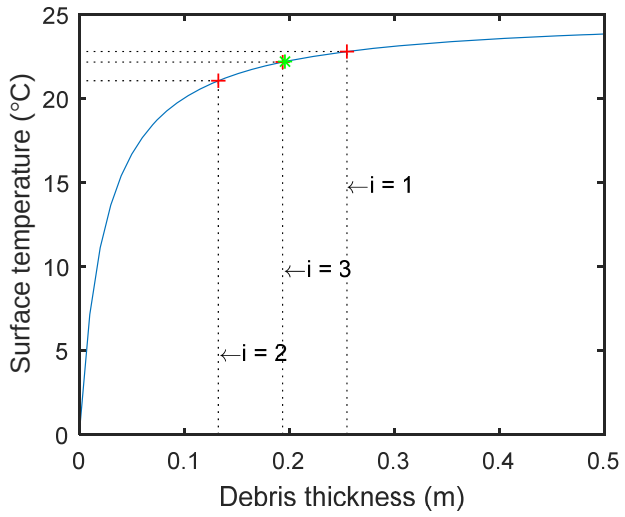

Figure 4.6 – Schematic illustrating bisection, the root-finding method used to determine debris thickness from surface temperature according to the DEB1 approach. Red crosses are modelled surface temperature solutions for successive iterations (i) using different values of debris thickness. The green star is observed surface temperature vs. 'true' debris thickness. The blue line is the relationship between surface temperature and debris thickness for the given pixel and meteorological conditions.

In order to get a realistic value for modelled surface temperature, and in order to be sure the initial condition was not influencing the results, the DEB1 approach was run using a spin-up time of 14 days before each satellite image. Plotting debris thickness against spin-up time (Figure 4.7) shows that debris thickness does not change with increasing spin-up time after around 9 days, indicating that this is the time required for the model to reach statistical equilibrium under the applied meteorological forcing. It is notable here that a longer spin-up time is required for thicker debris. If there was snow on the debris during the spin-up period, surface temperature was set to the temperature of melting snow (0°C), and the debris temperature profile was updated accordingly. Heat fluxes were calculated as in 4.4.2, with topographic shading determined through time and meteorological data distributed for each time step of the model.

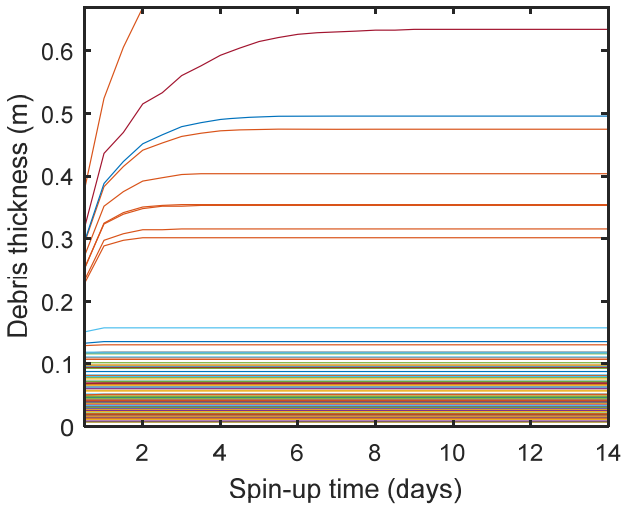

Figure 4.7 – Debris thickness versus spin-up time for the DEB1 approach using Experiment 1 data. Each line represents the evolution of modelled debris thickness with spin-up time for a single pixel of the debris field. The debris thickness of every pixel is fixed after 9 days of spin-up time.

4.4.1.4 Extrapolation approaches

These approaches are based on that of Mihalcea et al. (2008), who used pit measurements of debris thickness to define an empirical relationship between debris thickness and satellite image-derived surface temperature on Baltoro Glacier, Pakistan, then extrapolated this relationship to the rest of the debris-covered area of the glacier. They require only a sample of debris thickness measurements and surface temperature images as inputs. However, the debris thickness measurements ideally need to be representative of the debris thickness of the pixel of the satellite image they fall within and cover a

range of debris thicknesses across the glacier surface. Similar to the scaling approach, these approaches assume that debris thickness is the dominant control on surface temperature, and do not consider e.g. meteorological variability. The advantages of these approaches are that they are very simple to implement, and that previous work suggests they are robust (Gibson et al., 2017). The main disadvantage is that debris thickness measurements are required, which, as discussed above, can be difficult to make in the field, especially in remote places.

4.4.1.4.1 EXT1

Debris thickness was calculated following Mihalcea et al. (2008), and Gibson et al. (2017) by fitting, to each surface temperature image and a random sample of 20 of the ground-truth pit measurements of debris thickness, a curve of the form:

$$h = e^{c_1 T_s - c_2} \tag{4.20}$$

where c_1 and c_2 are free parameters. Fitting was carried out using the MATLAB function fit. Random sampling was carried out using the MATLAB function randsample. Debris thickness was then extrapolated, using the fitted curve, to the rest of the debris-covered area of the glacier. Mihalcea et al. (2008) got an optimal fit for Baltoro Glacier using $c_1 = 0.019$ and $c_2 = 58$. In this study, values of c_1 were 0.44 and 0.28, and values of c_2 were 130 and 86 (Table 4.6).

4.4.1.4.2 EXT2

Averaged over daily timescales, debris temperature profiles are approximately linear, so heat conduction through the debris can be assumed to be steady state (Nicholson and Benn, 2006; Nicholson and Benn, 2012). On this basis, by collecting the surface temperature terms of the debris surface energy balance (i.e. assuming steady-state heat conduction), debris thickness can be parameterised as:

$$h = k_d \frac{T_s - T_i}{c_1 + c_2(T_s - T_i)} \tag{4.21}$$

where c_1 and c_2 are free parameters, T_s is mean daily surface temperature and k_d is thermal conductivity.

In the EXT2 approach, debris thickness was extrapolated from ground-truth pit measurements to the rest of the glacier using quasi-daily mean surface temperature images, which were generated by taking the mean of each daytime surface temperature image and the night-time surface temperature image. A curve of the form described by Equation (4.21) was fitted to the quasi-daily mean surface temperature and debris thickness values of a random sample of 20 of the ground-truth pit measurements. Fitting and sample generation were carried out as for the EXT1 approach. The seed of the random number generator was fixed, so the same pit measurement samples were used. In order for this approach to be comparable to the other extrapolation approaches and not require thermal conductivity as an input, thermal conductivity was also found by fitting. To ensure a reasonable value of thermal conductivity, it was fitted using upper and lower bounds of 0.5 and 1.5 W m^{-1} K^{-1} (Conway and Rasmussen, 2000). Values of c_1 were found to be 210 and 240, while values of c_2 were found to be -9.3 and -11 (Table 4.6). Fitted values of thermal conductivity, 0.74 and 0.78 W m^{-1} K^{-1} (also Table 4.6), are surprisingly similar to those determined using thermistor strings (0.69 W m^{-1} K^{-1}; Section 4.4.4.1).

4.4.1.4.3 EXT3

Debris thickness was extrapolated from the same 20 pit measurements using only the daytime surface temperature images, according to the following equation, which is similar to Equation (4.21):

$$h = \frac{T_s - T_i}{c_1 + c_2(T_s - T_i)} \tag{4.22}$$

where T_s is surface temperature at the time of the satellite image and c_1 and c_2 are, again, free parameters. Because this approach uses only daytime surface temperatures, the functional form of Equation (4.22) is not predicted by theory, so there is no need in it for thermal conductivity, as there is in Equation (4.21). Values of c_1 were found to be 790 and 630, while values of c_2 were found to be -25 and -18 (Table 4.6).

4.4.1.4.4 Other

For completeness, two further extrapolation approaches were tested: one where debris thickness was expressed as a power law function of surface temperature, as such:

$$h = c_1(T_s - T_i)^{c_2} \tag{4.23}$$

The other where debris thickness was expressed as an exponential function of surface temperature, as such:

$$h = c_1^{(T_s - T_i)c_2} \tag{4.24}$$

Neither resulted in realistic debris thickness values so no further analysis was carried out.

There are many conceivable choices of relationship between debris thickness and surface temperature, and this thesis tests only those that were thought to be most likely. In fact, the static and dynamic energy-balance approaches could also be in an extrapolation-type approach, whereby *in-situ* debris thickness measurements would be used to constrain some of the more difficult to determine input variables. Effectively, the energy-balance approaches could be calibrated using debris thickness measurements.

4.4.2 Calculating heat fluxes

The static and dynamic energy-balance approaches require heat fluxes to be calculated at the debris surface. The heat fluxes considered were the shortwave and longwave radiative heat fluxes, the turbulent sensible and latent heat fluxes, the conductive heat flux and the precipitative heat flux.

The shortwave radiative heat flux, which is the heat flux that arises as a result of solar radiation, was calculated as follows:

$$S = S\downarrow (1 - \alpha_d) \tag{4.25}$$

where $S\downarrow$ is incoming shortwave radiation (both direct and diffuse), and α_d is the albedo of the debris. The greater the albedo, the more incoming shortwave radiation is reflected and vice versa.

The longwave radiative heat flux, which is the heat flux that arises due to radiation emitted by the atmosphere (mainly water vapour, clouds, CO_2 and ozone), was calculated as:

$$L = L\downarrow - \varepsilon_d \sigma {T_s}^4 \tag{4.26}$$

where ε_d is the emissivity of the debris surface and $L\downarrow$ is incoming longwave radiation. Here, the surface temperature term represents outgoing longwave radiation, where outgoing longwave radiation is proportional to the fourth power of the surface temperature, according to the Stefan-Boltzmann law.

The longwave radiative heat flux is often negative towards the debris surface during the day, if debris surface temperature is high.

The turbulent sensible and latent heat fluxes, which are those that are associated with turbulent mixing in the atmosphere above the debris surface due to wind, were calculated using the bulk aerodynamic approach (Equations (4.27) and (4.28)), following e.g. Oke (2002), Brutsaert (2013), Mölg and Hardy (2004) and Reid and Brock (2010). The sensible heat flux accounts for heat transfer between the debris surface and the atmosphere by convection, where if the surface temperature of the debris is greater than the air temperature, the debris transfers heat to the atmosphere and vice versa. The latent heat flux, on the other hand, accounts for heat transfer between the debris surface and the atmosphere by evaporation and condensation,[19] where if specific humidity at the debris surface is greater than the specific humidity of the atmosphere directly above the debris, evaporation occurs and heat is transferred away from the debris surface. On the other hand, if the specific humidity of the atmosphere is greater than at the surface, condensation occurs and heat is transferred towards the debris surface. The magnitude of both sensible and latent heat fluxes is controlled largely by wind speed, where high wind speed leads to heat fluxes of a greater magnitude (whether positive or negative).

$$H = \rho_a \frac{c_p k_{vk}^2 u (T_a - T_s)}{\left(\ln \frac{z_a}{z_{0_m}}\right)\left(\ln \frac{z_u}{z_{0_h}}\right)} (\phi_m \phi_h)^{-1} \tag{4.27}$$

$$LE = \rho_a \frac{L_v k_{vk}^2 u (q_a - q_s)}{\left(\ln \frac{z_a}{z_{0_m}}\right)\left(\ln \frac{z_u}{z_{0_v}}\right)} (\phi_m \phi_v)^{-1} \tag{4.28}$$

Here, H is the sensible heat flux and LE is the latent heat flux. ρ_a is the density of air, c_p is the specific heat capacity of air at constant pressure, k_{vk} is the Von Karman constant, u is wind speed, T_a is air temperature, q_a is the specific humidity at the measurement height, q_s is the specific humidity at the debris surface, z_a is the height of the air temperature measurements, z_u is the height of wind speed measurements, L_v is the latent heat of vaporisation of water, and ϕ_m, ϕ_h, and ϕ_v are the non-dimensional stability functions for momentum, heat and water vapour, respectively. z_{0_m}, z_{0_h} and z_{0_v} are the roughness lengths of momentum, temperature and water vapour, respectively, or the heights above the debris surface at which wind speed equals zero, and air temperature and vapour pressure

[19] While there is heat transfer involved in the latent heat flux, there is no associated change in temperature.

equal the temperature and vapour pressure at the surface. z_{0_m}, z_{0_h} and z_{0_v} were all assumed to be equal, as is common practice, and are referred to from here as the surface roughness length z_0.

The specific heat capacity of air was calculated as $c_p = c_a(1 + 0.84q_a)$ after Reid and Brock (2010), and where c_a is the specific heat capacity of dry air.

The stability of the atmospheric surface layer, which is the lowermost part of the troposphere, was accounted for by calculating bulk Richardson numbers and the non-dimensional stability functions for momentum, temperature and vapour pressure. The non-dimensional stability functions were calculated as:

$$(\phi_m\phi_h)^{-1} = (\phi_m\phi_v)^{-1} = (1 - 5Ri_b)^2 \tag{4.29}$$

for bulk Richardson numbers, Ri_b, more than or equal to zero, and

$$(\phi_m\phi_h)^{-1} = (\phi_m\phi_v)^{-1} = (1 - 16Ri_b)^2 \tag{4.30}$$

for bulk Richardson numbers of less than zero following Oke (2002). Bulk Richardson numbers were calculated as:

$$Ri_b = \frac{g(T_a - T_s)(z_a - z_0)}{T_m u^2} \tag{4.31}$$

where T_m is mean air temperature between the surface and the measurement height ($T_m = T_a - T_s/2$), after Reid and Brock (2010) and g is acceleration due to gravity. Positive bulk Richardson numbers typically occur at night, when air temperature is higher than surface temperature, and indicate a stable atmospheric surface layer in which convection is minimal and turbulent heat fluxes are small. Here, the stability functions act to dampen the turbulent heat flux. Negative bulk Richardson numbers typically occur during the day, when air at the debris surface is warmed by the debris, which causes it to rise, and indicate an unstable atmospheric surface layer in which convection is considerable and turbulent heat fluxes are large. Here, the stability functions act to intensify the turbulent heat fluxes.

The specific humidity at the debris surface and of the atmosphere above the debris surface was calculated following e.g. Peixoto and Oort (1996):

$$q_x = \frac{0.622e_x}{p_a + (1 - 0.622)e_x} \tag{4.32}$$

where e_x is the partial pressure of water vapour at the debris surface or at the measurement height in the atmospheric surface layer and p_a is atmospheric pressure. 0.622 is the ratio of the gas constant of dry air to the gas constant of water vapour. 0.378 is 1 – 0.622. The partial pressure of water vapour in air at the measurement height (i.e. the pressure exerted by the amount of water in the air) was calculated according to:

$$e_a = \frac{RH}{100} e_{a_s} \tag{4.33}$$

where RH is relative humidity and e_{a_s} is the saturation vapour pressure.

Saturation vapour pressure, which is the pressure exerted by the maximum amount of water that can be in the air at a given temperature (commonly known simply as the vapour pressure), was calculated at the measurement height using the Tetens equation (Murray, 1967):

$$e_{a_s} = 610.78 e^{\frac{17.27(T_a - 273.15)}{T_a - 35.86}} \tag{4.34}$$

Because relative humidity was not measured at the debris surface, the partial pressure of water vapour in air at the debris surface was calculated following Collier et al. (2014):

$$e_s = e_a \frac{T_s}{T_a} \tag{4.35}$$

assuming that the water vapour in the atmospheric surface layer is well mixed, i.e. the pressure being exerted by water vapour in the air, per degree of temperature, is the same at the measurement height and the debris surface. If debris surface temperature is greater than air temperature, this results in a latent heat flux that is negative towards the debris surface. If air temperature is greater than debris surface temperature, there will be a latent heat flux that is positive towards the debris surface. This is generally consistent with evaporation occurring during the day and condensation at night.

In the static energy-balance approaches, the conductive heat flux, which is the heat transferred through the debris by conduction, was calculated as in Section 4.4.1.2. In the dynamic energy-balance approaches, it was calculated as in Section 4.4.1.3.

The heat flux due to precipitation, though it is often very small, was also taken into account in the dynamic energy-balance approach, as such (Hay and Fitzharris, 1988):

$$P = \rho_w c_w r(T_r - T_s) \tag{4.36}$$

where ρ_w is the densitiy of water, c_w is the specific heat capacity of water and r is the precipitation rate. Precipitation temperature T_r, was assumed to be equal to air temperature, following Reid and Brock (2010). If the air temperature is greater than the surface temperature, the precipitation heats up the debris, whereas if the surface temperature is greater than the precipitation temperature, the debris heats up the precipitation. The precipitative heat flux was not considered to be important in the static energy-balance approaches on the basis that there is very little cloud in the surface temperature satellite images, meaning there should be no precipitation.

4.4.3 Distributing meteorological data

In order to calculate distributed debris thickness using the energy-balance approaches, meteorological data were distributed around the glacier. Specifically, atmospheric pressure, air temperature, incoming shortwave radiation and air density were distributed around the glacier surface in order to account for variable altitude, slope, aspect and shading. Figure 4.8 shows the calculated spatial distributions of key meteorological variables at the time of one of the satellite images.

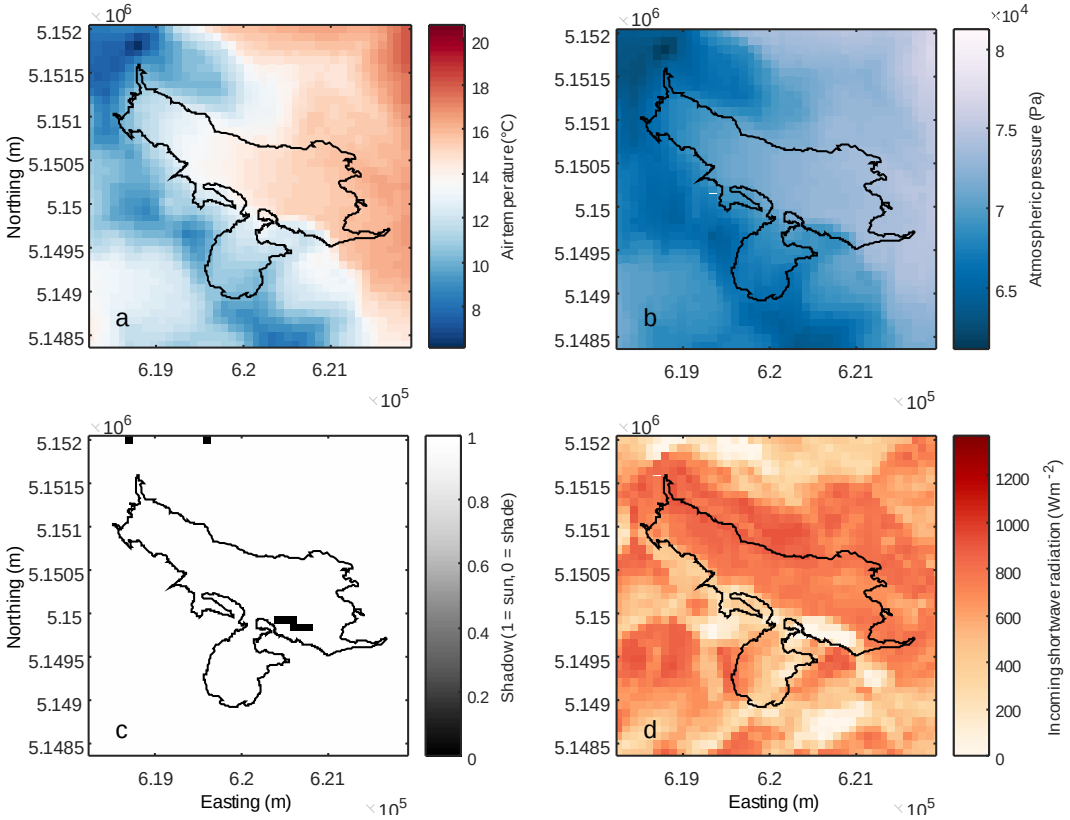

Figure 4.8 – Distributed meteorological data at the time of the 26-Aug-2016 satellite pass. (a) Air temperature. (b) Atmospheric pressure. (c) Shading. (d) Incoming shortwave radiation. Coordinate system is WGS84 UTM. UTM zone is 32N.

Atmospheric pressure, which decreases with altitude due to the decreasing weight of the overlying atmosphere, was calculated at the appropriate AWS and for each pixel of the elevation model using altitude and an environmental air temperature lapse rate, according to the barometric formula:

$$p_a = p_0 \left[1 - \frac{\Gamma z}{T_0}\right]^{\frac{gM_a}{R\Gamma}} \tag{4.37}$$

where p_0 is standard pressure at sea level, T_0 is standard temperature at sea level, Γ is environmental air temperature lapse rate, M_a is the molar mass of dry air and R is the standard atmospheric universal gas constant.

Air temperature, which decreases with altitude due to decreasing atmospheric pressure[20], was calculated and distributed around the glacier from the AWS using an environmental lapse rate of 0.0065 K m^{-1} and the difference in altitude between each elevation model pixel and the AWS:

$$T_a = T_{a_{AWS}} - \Gamma(z - z_{AWS}) \tag{4.38}$$

where the subscript AWS designates a variable as being associated with the AWS.

Following Foster et al. (2012), a second method of distributing air temperature was also tested in conjunction with the static energy-balance approaches, whereby a relationship was defined between air temperature and surface temperature on the basis that the debris heats the atmospheric surface layer in a type of glacier-atmosphere feedback process:

$$T_a = c_1 T_s + c_2 \tag{4.39}$$

The parameters of this empirical relationship, c_1 and c_2, were determined using surface temperature (calculated from outgoing longwave radiation using the Stefan-Boltzmann law, Equation (4.9)) and air temperature values from the Suldenferner AWS over the melt season (June to September) between the hours of 08.00 and 14.00 UTC. After Foster et al. (2012), AWS time steps for which there was snow on the ground, as determined using data from the nearby Madritsch weather station, were excluded, as were time steps for which the sky was not clear. Clear-sky time steps were defined as having a cloud cover (Equation (4.52)) of less than 0.3. While a strong relationship was found between air temperature and surface temperature (Figure 4.9), this method provided unrealistically low air temperatures for some pixels of the surface temperature images and was therefore deemed unsuitable for use in further analyses. Incidentally, the air temperature-surface temperature relationship determined by Foster et al. (2012) is very different from the one determined here, which is probably because the AWS used by Foster et al. (2012) was located at low altitude on thick debris (~0.5 m), while the AWS of this study was located at high altitude on thin debris (0.09 m). It seems unlikely that altitude can be neglected when distributing air temperature over debris-covered glaciers and that glacier-atmosphere feedbacks can be accurately represented in this way.

[20] Gay-Lussac's law states that pressure and absolute temperature are proportional for a gas of fixed mass and volume.

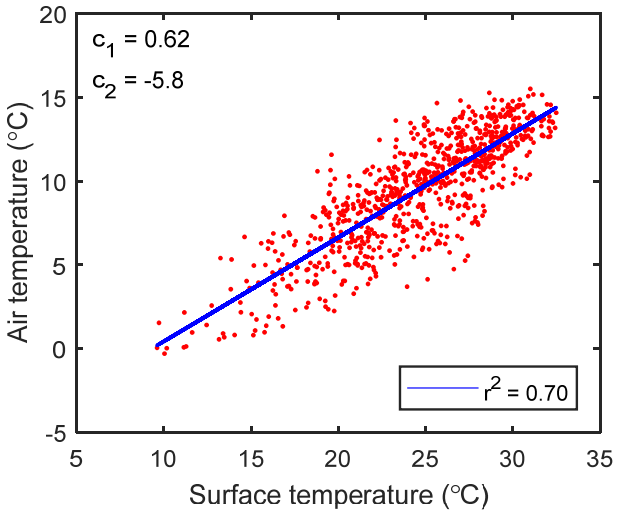

Figure 4.9 – Air temperature-surface temperature relationship for Suldenferner AWS in the months June to September.

Incoming shortwave radiation, which is greatest on surfaces normal to the solar beam when the sky is clear, was extrapolated to each pixel of the glacier surface following Hock and Noetzli (1997), using incoming shortwave radiation measured at the AWS and calculated clear-sky direct radiation. For each pixel of the elevation model and for the weather station, clear-sky direct radiation was calculated after Hock (1999) as:

$$I = I_0 \left(\frac{\bar{d}}{d}\right)^2 \psi^{\frac{p_a/p_0}{\cos Z}} \cos\theta \tag{4.40}$$

where I_0 is the solar constant, $\left(\bar{d}/d\right)^2$ is a correction factor for the eccentricity of Earth's orbit (the squared ratio of the mean earth-sun distance to the earth-sun distance), ψ is atmospheric transmissivity, and Z is the solar zenith angle. θ is the incidence angle of the solar beam and the glacier surface, calculated following Oke (2002):

$$\theta = \arccos[\cos Z' \cos Z + \sin Z' \sin Z \cos(A - A')] \tag{4.41}$$

where Z' is surface slope, A' is surface aspect and A is solar azimuth. Solar elevation E and solar azimuth angle were determined using the MATLAB function SolarAzEl (Koblick, 2013), while solar zenith angle Z was calculated in degrees as $90 - E$. Atmospheric transmissivity was calculated following Oerlemans (2001):

$$\psi = (0.79 + 2.5 \cdot 10^{-5} z)\left(1 - 0.08\frac{Z}{90}\right) \tag{4.42}$$

where z is the mean altitude of the debris-covered area (2704 m.a.s.l), using a neutral Z value of 45°. The squared ratio of the mean earth-sun distance to the earth-sun distance was calculated for each day of the year following Spencer (1971), according to the Fourier series formula:

$$\left(\frac{\bar{d}}{d}\right)^2 = \sum_{n=0}^{3} c_{1_n}\cos(n\theta_d) + c_{2_n}\sin(n\theta_d) \tag{4.43}$$

where the coefficients c_{1_n} and c_{2_n} are defined as in Table 4.5, and where θ_d is the time of year in radians: $\theta_d = 2\pi d_n/365.25$. Day number, d_n, is 0 on January 01 and 364 on December 31 (Hartmann, 2013).

Table 4.5 – Earth-sun distance coefficients, according to Spencer (1971).

n	c_{1_n}	c_{2_n}
0	1.000110	0
1	0.034221	0.001280
2	0.000719	0.000077

Measured incoming shortwave radiation and calculated clear-sky direct radiation at the Suldenferner AWS are both plotted against time for an example time period of two weeks in Figure 4.10. Here, it can be seen that clear-sky direct radiation is always greater than measured incoming shortwave radiation, and that sometimes, due to the presence of clouds, the difference between the two can be large.

For each pixel of the elevation model and for the weather station, shading was determined using the MATLAB functions f_shade and f_whether_shaded (Arnold et al., 1996)[21]. These functions test whether any other pixels of the elevation model intersect the path of the solar beam from the sun to the pixel in question, given azimuth and solar zenith angle. If the weather station was in the sun, elevation model pixels in the sun (condition 1) were assigned incoming shortwave radiation calculated from the incoming shortwave radiation received at the weather station: $S\downarrow = I(S\downarrow_{AWS}/I_{AWS})$, while elevation model pixels in the shade (condition 2) were assigned diffuse radiation as such: $S\downarrow = f_{diff} I_{AWS}$, after

[21] The MATLAB code for these functions was provided by Neil Arnold.

Konzelmann and Ohmura (1995)[22], where f_{diff} is 0.15 (a minimum value). If the weather station was in the shade, elevation model pixels in the sun (condition 3)[23] were assigned clear-sky direct radiation: $S\downarrow = I$, while elevation model pixels in the shade (condition 4) were assigned the incoming shortwave radiation received at the weather station: $S\downarrow = S\downarrow_{AWS}$.

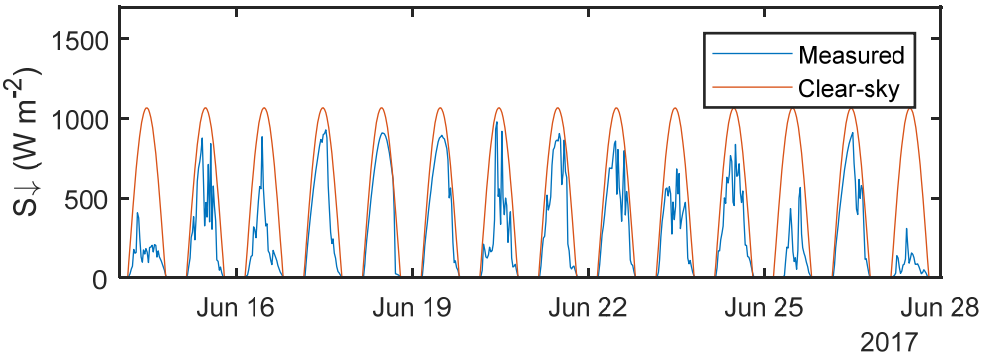

Figure 4.10 – Incoming shortwave radiation as measured at the Suldenferner AWS with clear-sky direct radiation as calculated for the location of the Suldenferner AWS.

Weather stations record both direct and diffuse shortwave radiation, so clouds are accounted for by conditions 1 and 4, assuming that cloud cover does not vary over the study area, which seems reasonable considering the glacier is small. However, clouds are not considered by conditions 2 or 3, with the result that condition 2 will underestimate incoming shortwave radiation (because an f_{diff} value of 0.15 assumes no clouds and clouds emit lots of diffuse radiation), and that condition 3 will overestimate incoming shortwave radiation (because clear-sky radiation assumes no clouds and clouds cause direct incoming shortwave radiation to be reduced). Fortunately, these conditions only occur on small portions of the glacier and over short periods of time, because both weather stations are located such that they represent most of the pixels of the glacier DEM most of the time, so the effect is likely to be minimal. Slope and aspect are considered when pixels are in the sun. However, when pixels are in the shade and incoming shortwave radiation is diffuse, slope and aspect are not considered. Effectively, therefore, diffuse radiation is considered to be isotropic at the point of incidence, which it

[22] Condition 2 is a slight deviation from the approach of Hock and Noetzli (1997), who used the clear-sky direct radiation of the pixel in question rather than of the weather station. However, Konzelmann and Ohmura (1995) calculated diffuse radiation fractions using clear-sky direct radiation data collected at weather stations (where slope would have been zero). Therefore, the approach taken here is more appropriate (and more consistent, on the basis that condition 4 equates incoming shortwave radiation for the pixel to incoming shortwave radiation at the weather station, where slope was zero).

[23] Condition 3 is also a slight deviation from Hock and Noetzli (1997), who used data for the last time step where the weather station wasn't shaded. However, this approach could not be used for the static energy balance methods where there is only one time step.

is not. In reality, diffuse radiation is isotropic at the point of emission and has directionality at the point of incidence. This is, therefore, a simplification.

Finally, air density, which reflects variability in air temperature and pressure, was calculated using the molar form of the ideal gas law:

$$\rho_a = \frac{p_a M_a}{R T_a} \tag{4.44}$$

4.4.4 Quantifying debris properties

4.4.4.1 Thermal conductivity

In order to measure the thermal conductivity of the debris, i.e. the ability of the debris to conduct heat, three thermistor strings were deployed for a week in August 2017, in debris layers of different thickness (their locations are shown in Figure 3.1). In each thermistor string there were six thermistors, each of which was buried at a different depth within the debris. The first three days' worth of thermistor string data were discarded in order to allow the debris around the thermistor strings to thermally equilibrate after being dug in, meaning there were four days' worth of thermistor string data from which thermal conductivity could be determined.

Debris thermal conductivity, k_d, was calculated to be 0.69 W m^{-1} K^{-1} following Conway and Rasmussen (2000) and Nicholson and Benn (2012):

$$k_d = \kappa_d C_d \tag{4.45}$$

where the apparent thermal diffusivity of the debris, κ_d, was calculated using MATLAB functions calc_ATD and calc_ETC[24] (Nicholson and Benn, 2012), which rearrange the one-dimensional heat equation, Equation (4.16), as such:

$$\frac{\partial T_d}{\partial t} = \kappa_d \frac{\partial^2 T_d}{\partial z^2} \tag{4.46}$$

Thermal diffusivity was calculated for each thermistor within the debris, then for each thermistor string by taking the mean of the values for the individual thermistors (see Figure 4.11), then for the

[24] The MATLAB code for these functions was provided by Lindsey Nicholson.

debris as a whole by taking the mean of the values for the individual thermistor strings. Thermal diffusivity for the debris as a whole was estimated to be 4.7×10^{-7} m^2 s^{-1}. The volumetric heat capacity of the debris was calculated to be 1.5×10^{6} J m^{-3} K^{-1}, following Oke (2002):

$$C_d = c_r\rho_r(1-\varphi) + c_a\rho_a\varphi(1-s_w) + c_w\rho_w\varphi s_w \quad (4.47)$$

where c_r, c_a and c_w are the specific heat capacities of rock, air and water, ρ_r, ρ_a and ρ_w are their densities, φ is a fraction representing the porosity of the debris, and s_w is the fraction of the debris that is saturated with water. The values of these properties were taken from the literature, as given in Table 4.4.

The thermal conductivity value reported here is 'effective' because the debris is considered as a single material, when in reality it is comprised of rock, air and water, which each have their own thermal conductivities.

Figure 4.11 shows that debris temperature is increasingly damped with depth, and that temperature changes at depth lag behind temperature changes at the surface. Further, it shows that the bottom-most thermistor of each thermistor string consistently reported a temperature of around 0°C, which indicates that the ice below the debris was melting while the thermistor strings were deployed. It is notable from the thermistor string data that there is an apparent increase in debris thermal diffusivity with increasing debris thickness. Considering the low thermal diffusivity of water, this may be because debris water content decreases with increasing debris thickness as meltwater production is reduced.[25]

[25] Thin debris has more water, which has a low thermal diffusivity, therefore thinner debris has a lower thermal diffusivity.

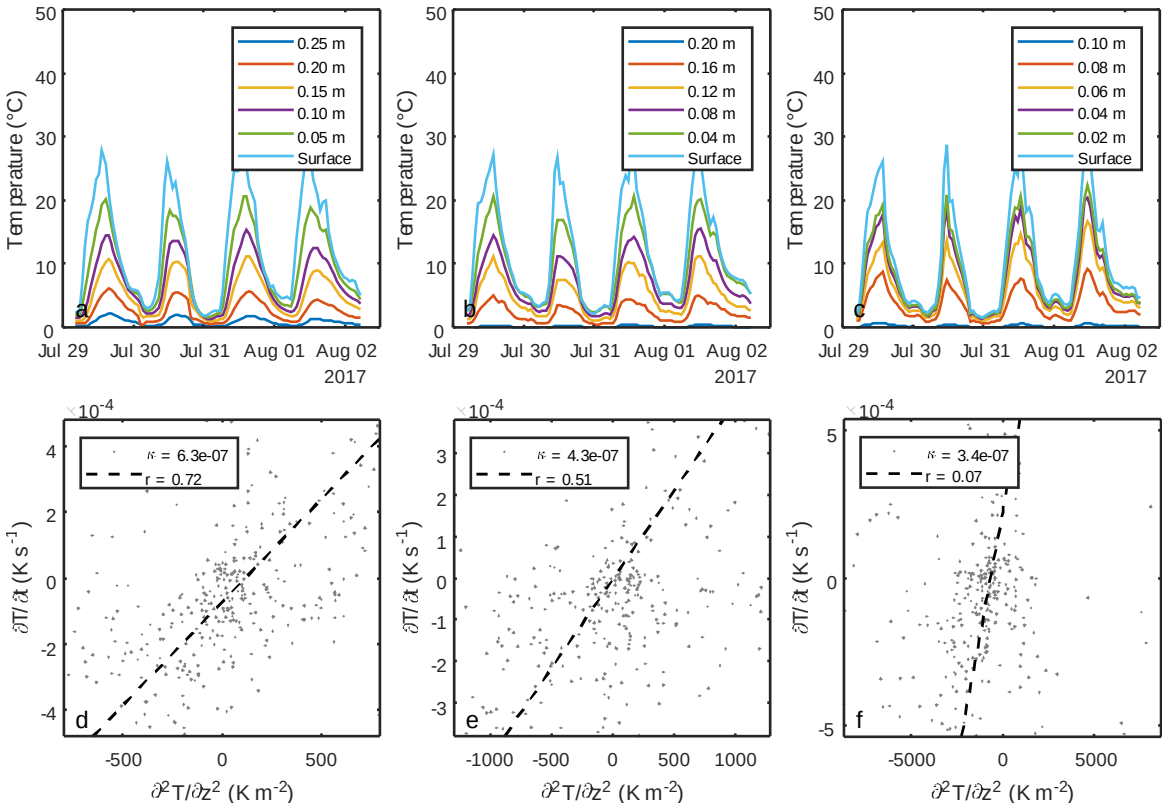

Figure 4.11 – Thermistor string data. (a), (b), (c) Debris temperatures at different depths for a four day period in August 2017 at the three thermistor strings. (d), (e), (f) Thermal diffusivity values as calculated by total least squares regression, using the thermistor string data.

4.4.4.2 Albedo

Mean debris albedo was calculated to be 0.16 (SD 0.01) using incoming and outgoing shortwave radiation data from the Suldenferner AWS, which was situated on debris cover, such that $\alpha_d = S\uparrow/S\downarrow$ (Figure 4.12). Albedo was calculated only for melt season months (June 01 to September 30) and for times between 11.00 and 13.00 UTC, when there was no snow on the ground. The albedo measurements have a normal distribution.

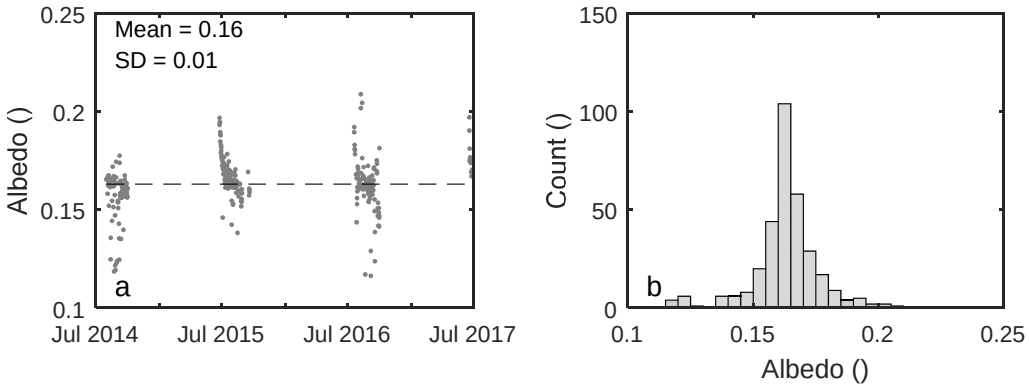

Figure 4.12 – Debris albedo as determined from Suldenferner AWS data. (a) Changes in debris albedo with time. (b) Frequency distribution of debris albedo.

4.4.4.3 Grain size

Median debris grain size was estimated to be 0.0066 (MAD 0.0023) m from a photograph taken near the equilibrium line (Figure 4.13). The grain size of each grain of the debris in the photograph was estimated using the MATLAB function gsd (Rabbani and Ayatollahi, 2015). The photograph was scaled using the known length of the handheld GPS that is also in the photograph. Grains of debris smaller than the pixel size will have been missed by this approach. However, there are no large grains in the photograph either, so the estimated value is thought to be representative. The grain size distribution is close to lognormal.

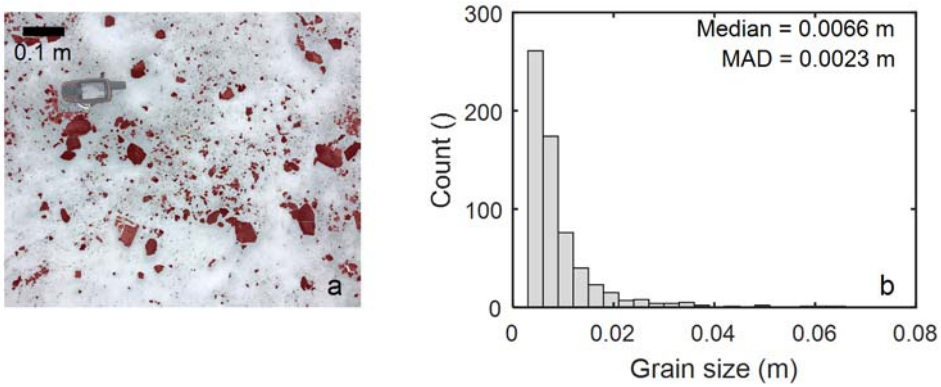

Figure 4.13 – Debris grain size. (a) Photograph of debris near equilibrium line. (b) Grain size frequency distribution.

4.4.4.4 Surface roughness length

Surface roughness length is a key control on the turbulent heat fluxes but was unknown for Suldenferner Glacier, so was determined from the Suldenferner AWS data by calibration. 'Measured' surface temperature at the AWS was calculated from measured outgoing longwave radiation, as in Equation (4.9), then, using the known debris thickness at the AWS, the forward model of the DEB1 approach was used to model surface temperature, for the same time period as the measured surface temperature, while iteratively varying surface roughness length. Optimal surface roughness length, which was found to be 0.0036 m (Figure 4.14), was the value that maximised the Nash-Sutcliffe Efficiency coefficient (NSE) of modelled versus measured surface temperature at the weather station. This calibration procedure was carried out using the MATLAB function fmincon, with which constraints of 0.001 and 0.5 m were imposed on the surface roughness length (cf. Miles et al., 2017). An initial value of 0.016 m was used after Brock et al. (2010). The time period of the meteorological data that were used was June 13 2015 to August 28 2015, inclusive of a seven-day spin-up period. This was the longest continuous snow-free period of time in the Suldenferner AWS record. The debris is relatively thin at the AWS (0.09 m), so a spin-up time of seven days was considered to be more than sufficient. The value that was used for surface roughness length was found to be important in terms of modelling debris thickness. Indeed, optimising surface roughness length was found to significantly improve results over using a value from the literature. The NSE of modelled versus measured surface temperature using the optimised surface roughness length was 0.76. NSE was calculated as such:

$$\mathrm{NSE} = 1 - \frac{\sum(mod - obs)^2}{\sum(obs - \overline{obs})^2} \tag{4.48}$$

where mod are the modelled values, obs are the observed values and $\overline{obs}$ is the mean of the observed values.

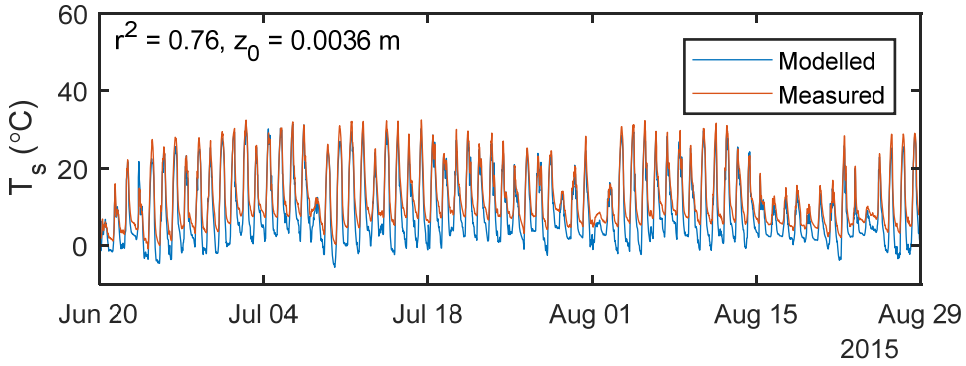

Figure 4.14 – Surface temperature as measured at the Suldenferner AWS and as modelled using an optimal surface roughness length of 0.0036 m.

4.4.5 Parameterising incoming longwave radiation

There were no incoming longwave radiation data available for the Madritsch AWS. Therefore incoming longwave radiation was calculated using an all-sky parameterisation, i.e. a parameterisation that takes cloud cover into account. Juszak and Pellicciotti (2013) carried out a comparison of incoming longwave radiation parameterisations over glaciers and found the following pairing of clear-sky and all-sky emissivity parameterisations to give the best results.

Incoming longwave radiation was calculated according to the Stefan-Boltzmann equation:

$$L\downarrow = \varepsilon_{as}\sigma T_a^4 \tag{4.49}$$

where all-sky emissivity, ε_{as}, was calculated following Unsworth and Monteith (1975):

$$\varepsilon_{as} = \varepsilon_{cs}(1 + c_1 n_c) + c_2 n_c \tag{4.50}$$

Here, n_c is cloud cover, given as a fraction, and c_1 and c_2 are free parameters. Clear-sky emissivity, ε_{cs}, was calculated according to Dilley and O'Brien (1998):

$$\varepsilon_{cs} = \frac{c_3 + c_4(T_a/273.15)^6 + c_5\sqrt{w_p/25}}{\sigma {T_a}^4} \tag{4.51}$$

where w_p is precipitable water and where c_3, c_4 and c_5 are free parameters. Daytime cloud cover was calculated following Crawford and Duchon (1999):

$$n_c = 1 - \frac{S\downarrow}{I} \tag{4.52}$$

As such, there is extensive cloud cover when incoming shortwave radiation is only a small fraction of clear-sky direct radiation, and minimal cloud cover when incoming shortwave radiation is a large fraction of clear-sky direct radiation. Night-time cloud cover was estimated using a moving median filter. It was assumed to be night-time when clear-sky direct radiation was less than 200 W m^{-2}. Clear-sky direct radiation was calculated as given by Equation (4.40).

Precipitable water, which is the depth of rainwater that would be precipitated from a column of the atmosphere at the measurement location, was calculated following Prata (1996):

$$w_p = 4.65\frac{e_a}{T_a} \tag{4.53}$$

where the partial pressure of water vapour e_a was calculated as in Equation (4.33).

The values of the free parameters in Equations (4.50) and (4.51) were determined by multi-parameter optimisation using Suldenferner and Madritsch AWS data for which there was a temporal overlap. This was done using the MATLAB function fminsearch, where the objective of the optimisation was the NSE of the parameterised Madritsch incoming longwave radiation versus the measured Suldenferner AWS radiation. Effectively, different parameter combinations were tried iteratively with the aim of maximising the NSE. Optimal values of c_1, c_2, c_3, c_4 and c_5 were found to be 0.59, -0.36, 130 m^2 W^{-1}, 30 m^2 W^{-1} K^{-6} and 170 m^3 $kg^{-0.5}$ W^{-1}, respectively. Initial parameter values used for the optimisation were those given in the original literature (Unsworth and Monteith, 1975; Dilley and O'Brien, 1998). The parameterised longwave radiation had an NSE of 0.70 and an RMSE of 25 W m^{-2}, which is the same as the lowest RMSE derived by Juszak and Pellicciotti (2013), indicating the parameterisation was successful.

Figure 4.15 shows incoming longwave radiation as parameterised at the Madritsch AWS and as measured at the Suldenferner AWS plotted against time for a two-week period. The two datasets are well matched on daily timescales. However, on sub-daily timescales, the parameterisation does not always capture the full range of incoming longwave radiation values that is captured by the measurements. This may be due, in part, to the difference in location of the two weather stations.

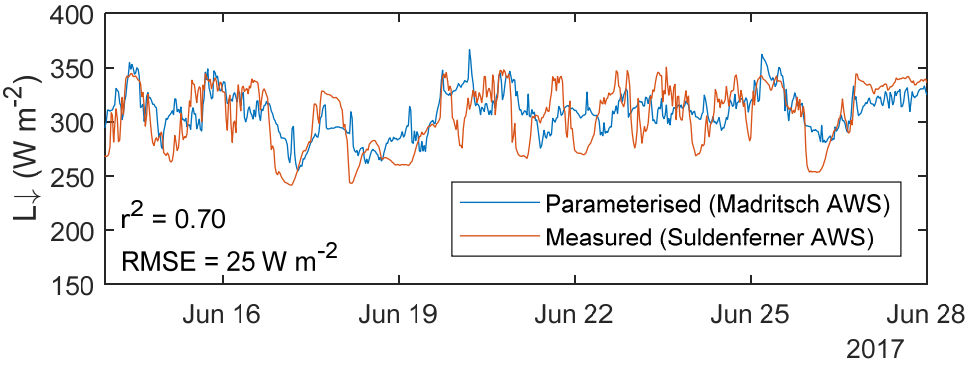

Figure 4.15 - Incoming longwave radiation as measured at the Suldenferner AWS and as parameterised at the Madritsch AWS.

4.4.6 Comparison to ground-truth data

In order to compare the remote sensing estimates of debris thickness (modelled debris thickness) with the ground-truth pit measurements of debris thickness (measured debris thickness), the remote sensing estimates were interpolated at the location of each pit measurement by the nearest neighbour method. Performance statistics were then calculated using the deviations of modelled from measured debris thickness. The performance statistics that were used were the median error (ME) and the median absolute error (MAE). These statistics were chosen specifically because they are robust and therefore insensitive to the maximum debris thickness value that was used (i.e. 0.67 m). Statistics such as the mean error and the RMSE were avoided because they were found to favour approaches that predicted thinner debris. This is because the surface temperature versus debris thickness curve is very nonlinear: small errors in surface temperature or other input variables have a much greater effect on the debris thickness estimates derived from higher surface temperature values than from lower surface temperature values. ME is an indicator of overall accuracy, while MAE is an indicator of overall precision. ME was calculated as:

$$\mathrm{ME} = \mathrm{median}(h_{mod} - h_{meas}) \tag{4.54}$$

where h_{mod} is modelled debris thickness and h_{meas} is measured debris thicknesss. MAE was calculated as:

$$\mathrm{MAE} = \mathrm{median}(|h_{mod} - h_{meas}|) \tag{4.55}$$

If several pit measurements were within the same pixel of the modelled or remote sensing-derived debris thickness output, the mean of those pit measurements was taken. Pit measurements of debris thickness were excluded from the analysis if the ice surface was not reached during excavation, if the glacier surface at the location of the measurement was debris-free, or if the location of the measurement was outside the designated glacier margin.

4.4.7 Comparing different approaches

The different remote sensing approaches to quantifying debris thickness were compared with each other by ranking them in terms of the statistical measures of performance (ME and MAE) described above. The approaches were ranked in terms of each of the performance statistics, using the MATLAB function tiedrank, and then in terms of mean of the two ranks. This was done for each experiment and for each model run. An overall ranking was determined for each approach by ranking the approaches in terms of the mean of their model run rankings.

4.4.8 Sensitivity testing

The sensitivities of the different approaches were tested by perturbing their input variables, one-by-one, towards smaller and larger values, and observing the change in modelled glacier-wide median debris thickness. Meteorological variables were perturbed using approximations of instrument accuracy. Debris properties and atmospheric variables were perturbed using approximations of on-glacier variability if the variable had been measured, or data from the literature, if the variable had not been measured. All perturbations were symmetric for each variable, i.e. the perturbation towards the larger value was the same as the perturbation towards the smaller value. However, meteorological variables of which it is impossible to have a negative value were forced to be positive. Perturbation values are shown in Figure 4.21.

4.4.9 Data preparation

Satellite image time and date were extracted from the metadata of the AST08 image of each image set. The elevation model and emissivity images were resampled to the same resolution as the surface temperature images using a nearest neighbour approach. Slope and aspect were calculated from the resampled elevation model using the MATLAB functions gradient, atand and atan2d. Decimal degrees were converted to UTM and vice versa (this was necessary for doing the solar calculations) using the

MATLAB functions utm2ll and ll2utm (Beauducel, 2015). Debris and glacier masking were carried out using the MATLAB function inpolygons (Kearney, 2016).

4.4.10 Melt modelling

A forward model of sub-debris melting was used to investigate the effect of using remote sensing estimates instead of field measurements of debris thickness to model sub-debris melting. Melt modelling was carried out using both the field measured thicknesses and the highest ranked remotely sensed thicknesses as the debris thickness input. The forward model that was used was the modified DEB model (Reid and Brock, 2010) that was inverted for use in the DEB1 approach, as described above. Meteorological data were distributed as described in Section 4.4.3, and the model was run pixel-by-pixel over the whole debris-covered area. Melt modelling was carried out over the 2017 melt season, from June 01 to September 30, exclusive of a 14-day spin-up period, using meteorological data from the Madritsch AWS. The debris properties and physical constants that were used are as given in Table 4.4. Inverse distance weighting, using the three nearest neighbours and a distance weighting of one, was used to get the field measurements of debris thickness into a grid of the same size and shape as the elevation model. This was done with the MATLAB function IDW (Fatichi, 2009). For each 90-m pixel of the debris-covered area, melt rate was calculated in terms of metres water equivalent per time step, using:

$$M = \frac{G_i \Delta t}{\rho_w L_f} \tag{4.56}$$

where M is melt rate, G_i is the conductive heat flux at the debris surface, Δt is the AWS time step, ρ_w is the density of water and L_f is the latent heat of fusion (Arnold et al., 1996; Reid and Brock, 2010).

4.5 Results

4.5.1 Comparison to ground-truth data

The results of the five experiments and 29 model runs are provided in Table 4.6. The different model runs estimate median debris thickness on Suldenferner Glacier to be between 0.035 and 0.17 m, compared with the median of the ground-truth pit measurements, which is 0.11 m. From best to worst, the ME of the model results ranges from 0.0032 to -0.066 m. This is 0.48-9.9% of the range of the

ground-truth debris thickness measurements, 0.0066-0.67 m, indicating that average model performance, or overall accuracy, is good. The ME values show that the energy-balance approaches and the EXT1 approach consistently underestimate median debris thickness while the SCA1, EXT2 and EXT3 approaches consistently overestimate median debris thickness, albeit by relatively small amounts. From best to worst, the MAE of the model results ranges from 0.040-0.095 m. This is 6-14% of the range of the ground-truth measurements, indicating that performance with respect to individual ground-truth measurements, or overall precision, can be poor.

Table 4.6 – Performance statistics, coefficient values and rankings for all model runs. h_{med} is median glacier-wide debris thickness.

Exp't (run)	Model	h_{med} (m)	ME (m)	MAE (m)	c_1	c_2	$T_{s_{min}}$ (°C)	$T_{s_{P95}}$ (°C)	k_d (W m^{-1} K)	Exp't rank	Overall rank
1(1)	SCA1	0.167	0.054	0.095	-	-	6.15	30.55	-	9	27
1(2)	SEB1	0.041	-0.053	0.053	-	-	-	-	-	7	17
1(3)	SEB2	0.045	-0.047	0.052	0.10	-	-	-	-	3	11
1(4)	SEB3	0.052	-0.039	0.050	1.27	-	-	-	-	1	9
1(5)	SEB4	0.046	-0.042	0.066	-	-	-	-	-	5	21
1(6)	DEB1	0.041	-0.048	0.066	-	-	-	-	-	8	23
1(7)	EXT1	0.055	-0.013	0.073	0.44	134.92	-	-	-	4	15
1(8)	EXT2	0.132	0.031	0.053	207.92	-9.28	-	-	0.74	1	7
1(9)	EXT3	0.129	0.032	0.069	791.93	-24.80	-	-	-	5	21
2(10)	SCA1	0.167	0.054	0.095	-	-	6.15	30.55	-	9	27
2(11)	SEB1	0.060	-0.028	0.048	-	-	-	-	-	3	2
2(12)	SEB2	0.066	-0.021	0.053	0.10	-	-	-	-	3	4
2(13)	SEB3	0.076	-0.011	0.057	1.27	-	-	-	-	1	5
2(14)	SEB4	0.062	-0.019	0.062	-	-	-	-	-	5	10
2(15)	DEB1	0.062	-0.005	0.067	-	-	-	-	-	3	11
2(16)	EXT1	0.055	-0.013	0.073	0.44	134.92	-	-	-	7	15
2(17)	EXT2	0.132	0.031	0.053	207.92	-9.28	-	-	0.74	6	7
2(18)	EXT3	0.129	0.032	0.069	791.93	-24.80	-	-	-	8	21
3(19)	SCA1	0.154	0.062	0.083	-	-	4.85	31.35	-	8	29
3(20)	SEB1	0.035	-0.066	0.066	-	-	-	-	-	8	26
3(21)	SEB2	0.038	-0.061	0.061	0.11	-	-	-	-	6	23
3(22)	SEB3	0.044	-0.053	0.053	1.27	-	-	-	-	1	13
3(23)	SEB4	0.039	-0.053	0.054	-	-	-	-	-	3	19
3(24)	DEB1	0.034	-0.064	0.064	-	-	-	-	-	7	25
3(25)	EXT1	0.075	-0.003	0.076	0.28	85.90	-	-	-	4	13
3(26)	EXT2	0.114	0.013	0.055	241.94	-10.61	-	-	0.78	1	6
3(27)	EXT3	0.126	0.032	0.065	631.82	-18.25	-	-	-	4	18
4(28)	DEB1	0.073	-0.030	0.042	-	-	-	-	-	1	2
5(29)	DEB1	0.110	0.003	0.040	-	-	-	-	-	1	1

Distributed debris thickness fields generated as part of Experiment 1, which used the 26-Aug-2016 daytime images and on-glacier meteorological data, are shown in Figure 4.16. Figure 4.16 demonstrates that all the approaches produce spatially variable debris thicknesses over the surface of Suldenferner Glacier that are comparable to the ground-truth pit measurements (Figure 4.16, bottom

left). That is, they indicate thin debris upglacier and towards the centreline and thick debris downglacier and towards the margins. They reproduce thick debris on the northern margin, above which there are south-facing rock slopes from which the sediment flux to the glacier surface is high, and thin debris downglacier of the Payerferner ice fall from which the ice flux is high. They also tend to reproduce thicker debris around the confluence of the Payerferner ice fall and Suldenferner Glacier proper, where there is a relict medial moraine.

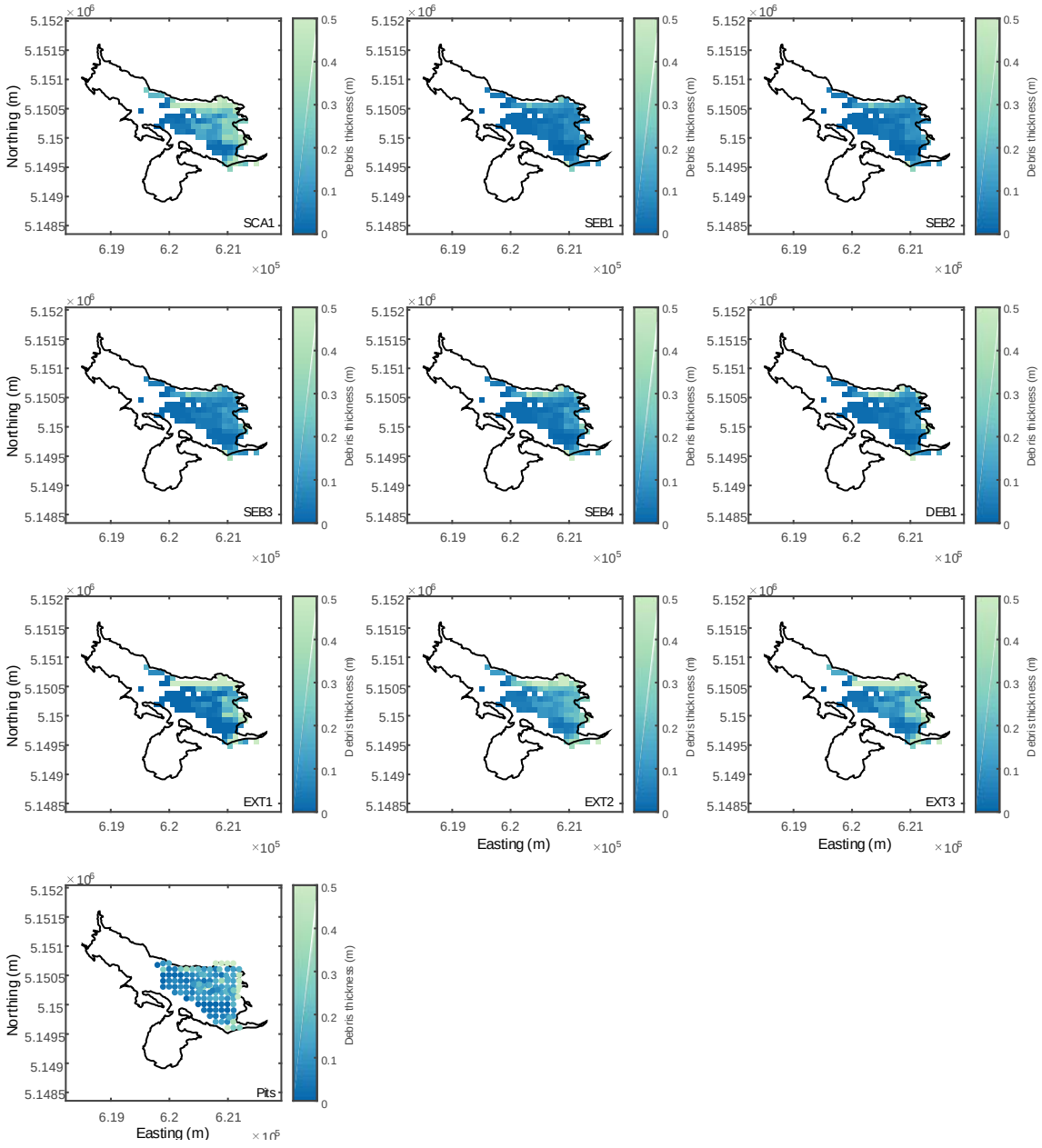

Figure 4.16 – Modelled debris thickness as given by the different approaches using Experiment 1 data. Ground-truth pit measurements of debris thickness are shown bottom left. Coordinate system is WGS84 UTM 32N.

In Figure 4.17, modelled debris thicknesses generated using Experiment 1 data are plotted against measured debris thicknesses. It shows that, although spatial patterns of debris thickness were reproduced, there are sometimes large differences between modelled and measured debris thicknesses for individual ground-truth pit measurements. This reinforces what is shown by the performance statistics: that while overall accuracy can be good, errors on individual measurements can be large and precision can be poor. Again, it can be seen that some approaches tend to underestimate while others tend to overestimate debris thickness. It is clear from these plots that, as should be expected, the errors on individual pit measurements increase with debris thickness.

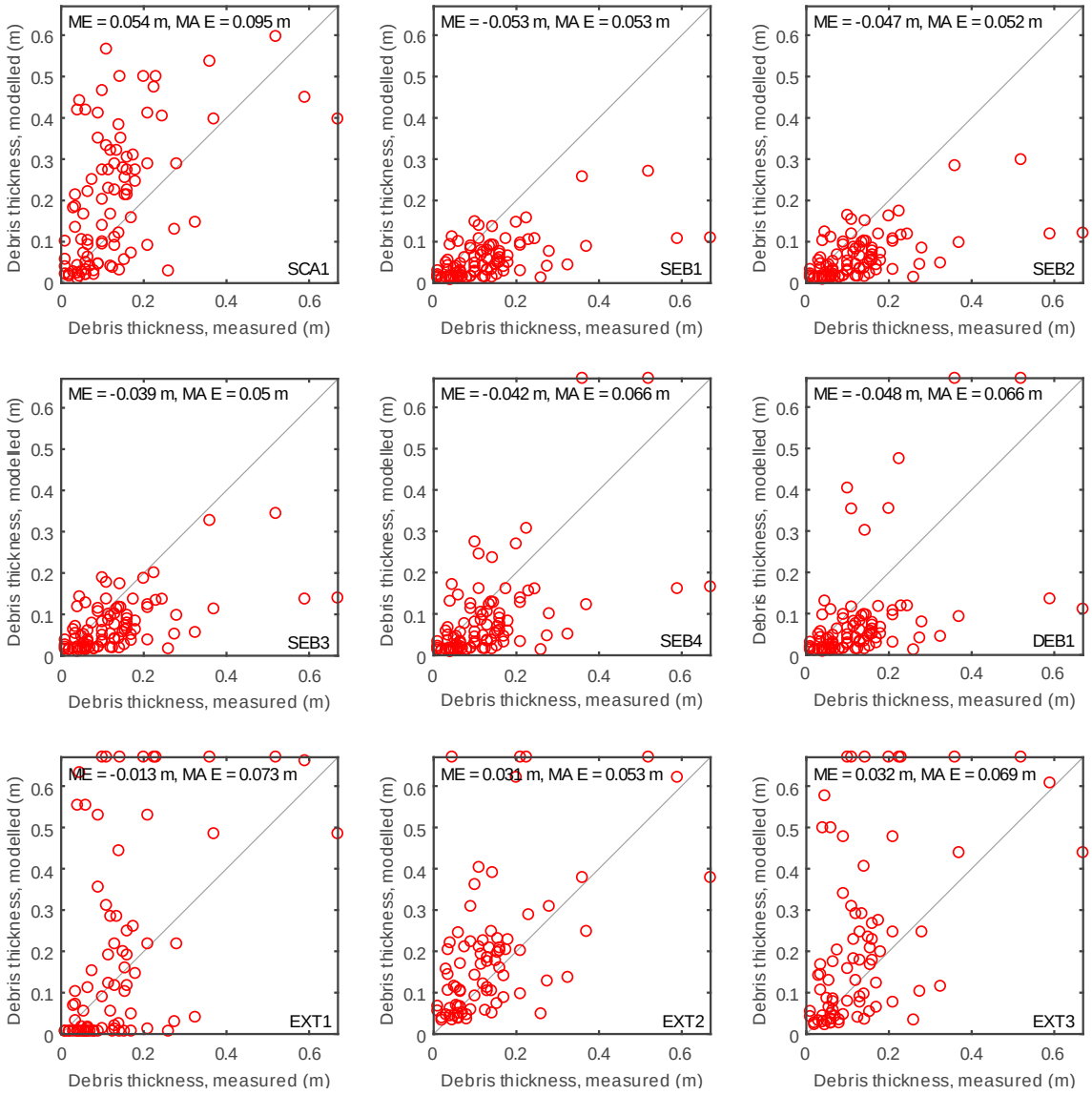

Figure 4.17 – Plots of modelled against measured debris thickness as given by the different approaches using Experiment 1 data.

All the models reproduced the general shape of the debris thickness frequency distribution (Figure 4.18). That is, they reproduced the skew towards thinner debris that is apparent in the pit measurements.

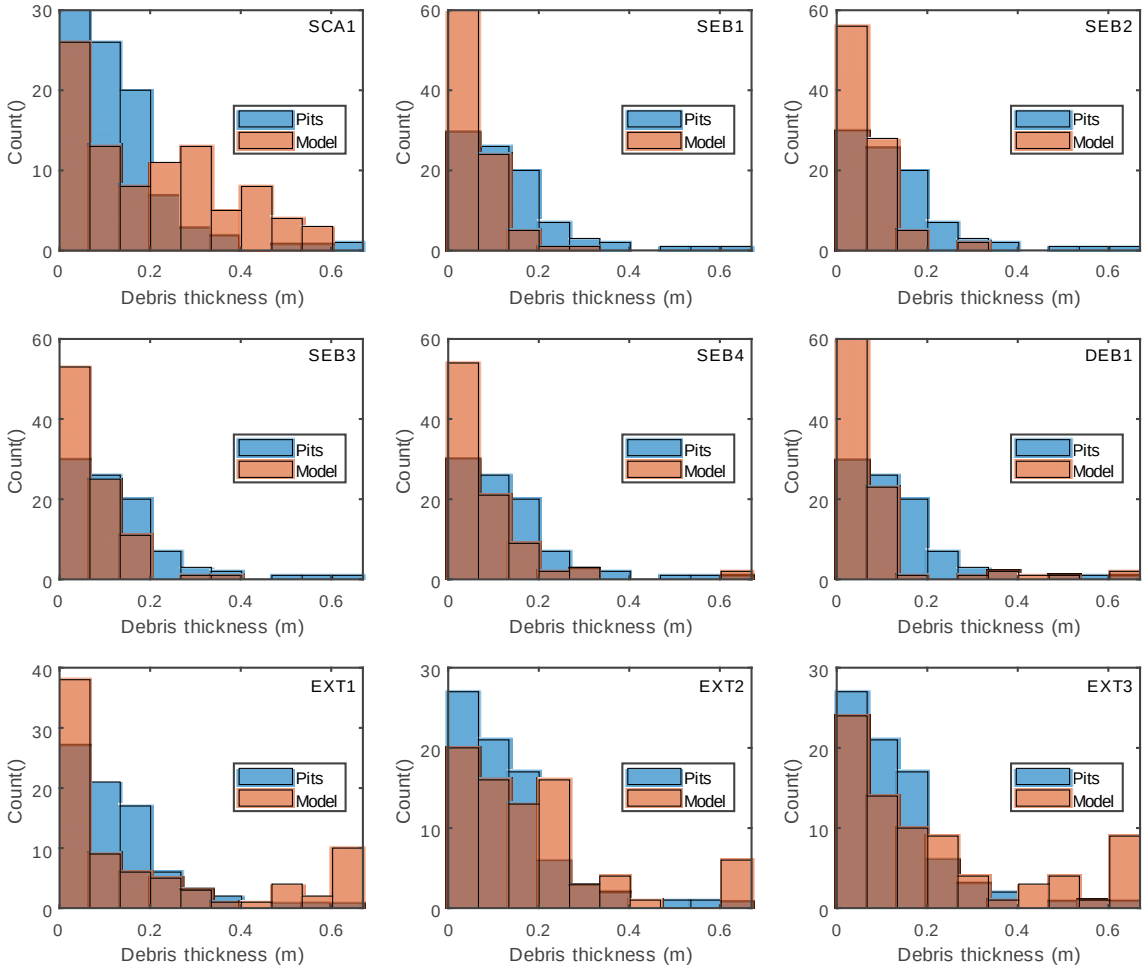

Figure 4.18 – Frequency distributions of debris thickness as given by the different approaches using Experiment 1 data.

Further, Figure 4.19 shows that most of the approaches reproduced a surface temperature-debris thickness curve that is similar in shape to the curve described by the pit measurements, whereby surface temperature increases rapidly with debris thickness at first, then asymptotes towards a maximum value. The exceptions to this are the SCA1 and EXT1 approaches, whose curves asymptote much more slowly and much more quickly, respectively, with respect to debris thickness, than the pit measurements. An interesting feature of these plots is that the data produced using the energy-balance approach tend to plot along the 'thin edge' of the pit measurements data envelope (see Figure 4.19

SEB1). Conversely, the extrapolation approaches and the scaling approach plot through the middle of this envelope.

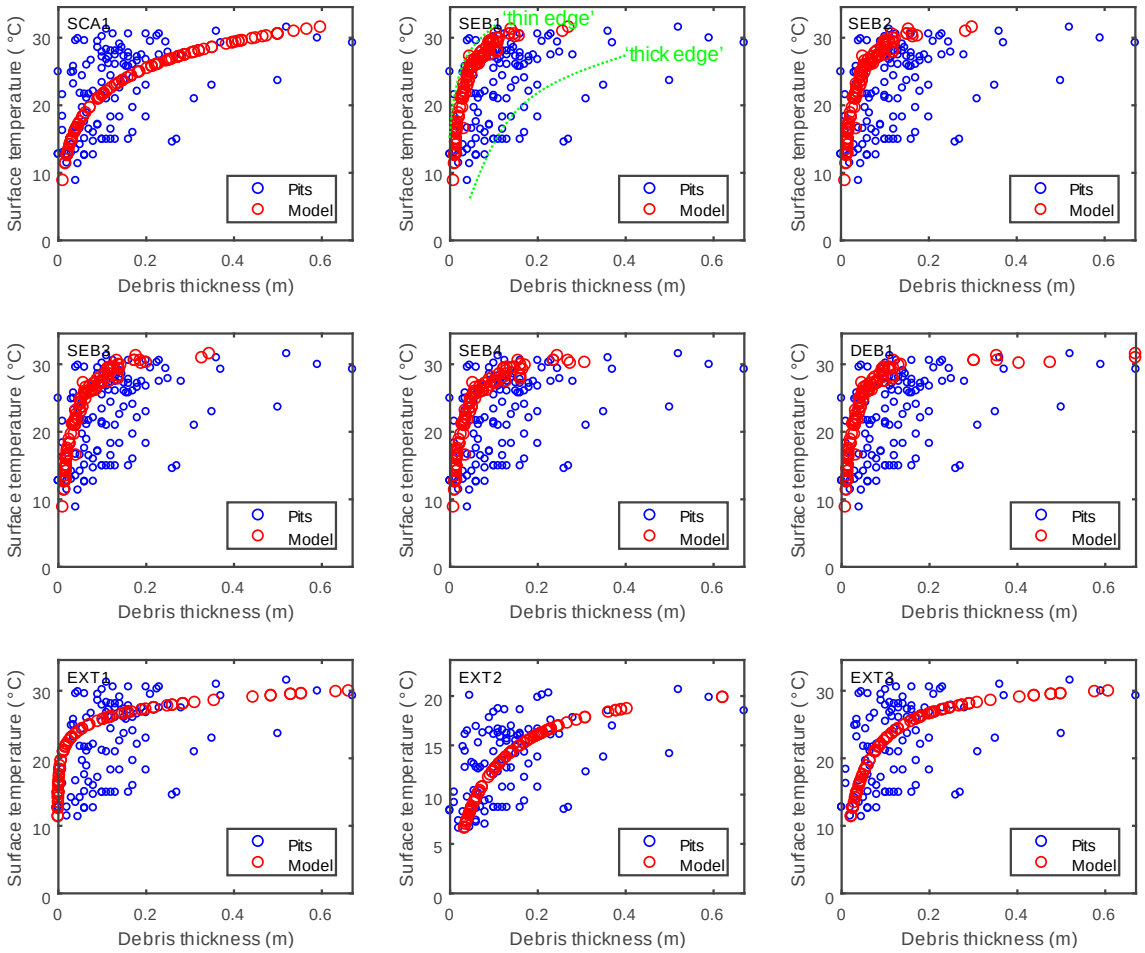

Figure 4.19 – Plots of surface temperature against debris thickness for each of the debris thickness quantification approaches using Experiment 1 data.

4.5.2 Comparison of different approaches

Of the nine different debris thickness quantification approaches, the EXT2 approach performed best overall, ranking first. The SEB3 approach ranked second, and the DEB1 approach ranked third (Table 4.7). The SEB3 approach and the EXT2 approaches performed joint best in Experiment 1, which used the 26-Aug-2016 daytime images with the on-glacier meteorological data; the SEB3 approach performed best in Experiment 2, which used the 26-Aug-2016 daytime images with the off-glacier meteorological data; and the EXT2 approach performed best in Experiment 3, which used the 02-Aug-2013 daytime images with the off-glacier meteorological data.

Table 4.7 – Mean overall rankings of different debris thickness quantification approaches.

Model	Mean overall rank
DEB1	3
EXT1	5
EXT2	1
EXT3	8
SCA1	9
SEB1	6
SEB2	4
SEB3	2
SEB4	7

The best two model runs overall were those for which the DEB1 approach was used with the 02-Jul-2015 night-time images, runs 28 and 29. Run 29, which used the off-glacier meteorological data, was the best, while Run 28, which used the onglacier meteorological data, was the second best. The results of Run 28 are shown in Figure 4.20. As the DEB1 approach was the only approach used in experiments 4 and 5, it ranked highest in both of these experiments.

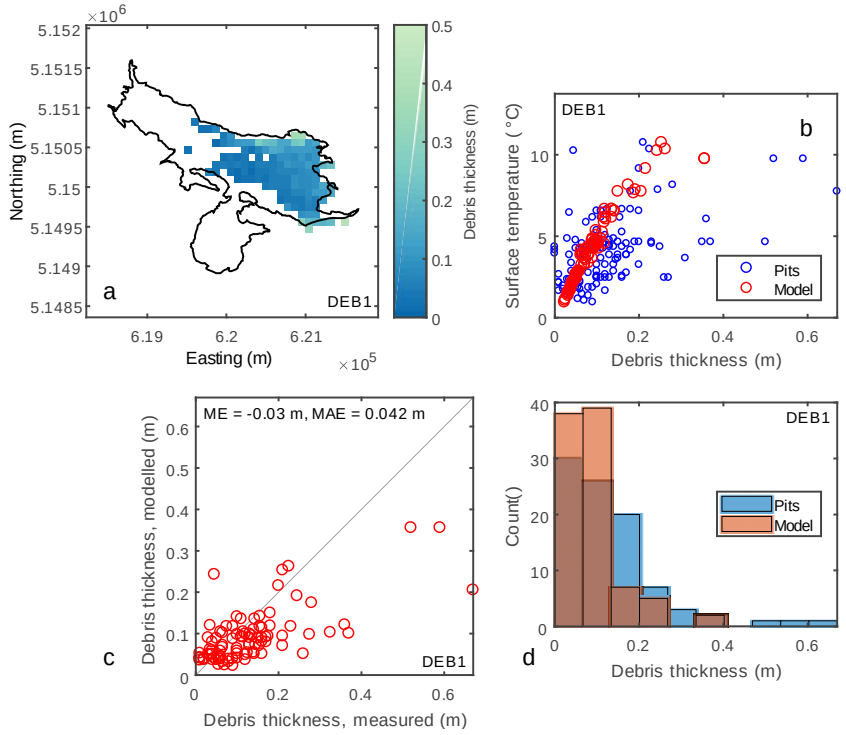

Figure 4.20 – Results of Run 28. (a) Distributed debris thickness output. (b) Modelled surface temperature against debris thickness. (c) Modelled against measured debris thickness. (d) Modelled and measured debris thickness histograms. Coordinate system is WGS84 UTM. UTM zone is 32N.

4.5.3 Sensitivity and transferability

Figure 4.21 shows the sensitivities of the nine debris thickness quantification approaches to perturbations in their input variables. One of the first things to be noticed is that all the energy-balance approaches have very similar sensitivities. They are sensitive to surface temperature, debris thermal conductivity, debris surface roughness length, incoming shortwave and longwave radiation, air temperature and, to a lesser extent, debris albedo. The scaling approach is insensitive to surface temperature but very sensitive to changes in the values that are used for h_{min} and h_{max}. The extrapolation approaches, which use only surface temperature as an input variable, are insensitive to changes in surface temperature. However, it is likely that they are sensitive to the location of the debris thickness measurements that were used in the process of fitting their free parameters, which is something that was not tested. Further, sensitivity to surface temperature was tested by perturbing all the pixels of each surface temperature image by the same amount, whereas in reality surface temperature errors are likely to vary between pixels, and inter-pixel surface temperature errors are likely to affect the scaling and extrapolation approaches disproportionately because the debris thickness estimates made using these approaches are derived from fitting to the measured surface temperature of individual pixels.

Comparing the mean of the overall ranks of the energy-balance runs for which on-glacier meteorological data was used with the mean of the overall ranks for which off-glacier meteorological data were used (Table 4.6) indicates that the energy-balance models perform similarly either way, but marginally better using off-glacier meteorological data (mean on-glacier rank is 14, mean off-glacier rank is 13).

It is difficult to assess the transferability of the methods because there are so few image sets. However, taking the mean of the overall ranks of the different experiments suggests performance varies considerably depending on the input data (i.e. satellite image, site of weather station) that are used. For example, the mean rank of Experiment 1 is 17, of Experiment 2 is 11 and of Experiment 3 is 19. The mean of the overall ranks for experiments 4 and 5 are 2 and 1, respectively.

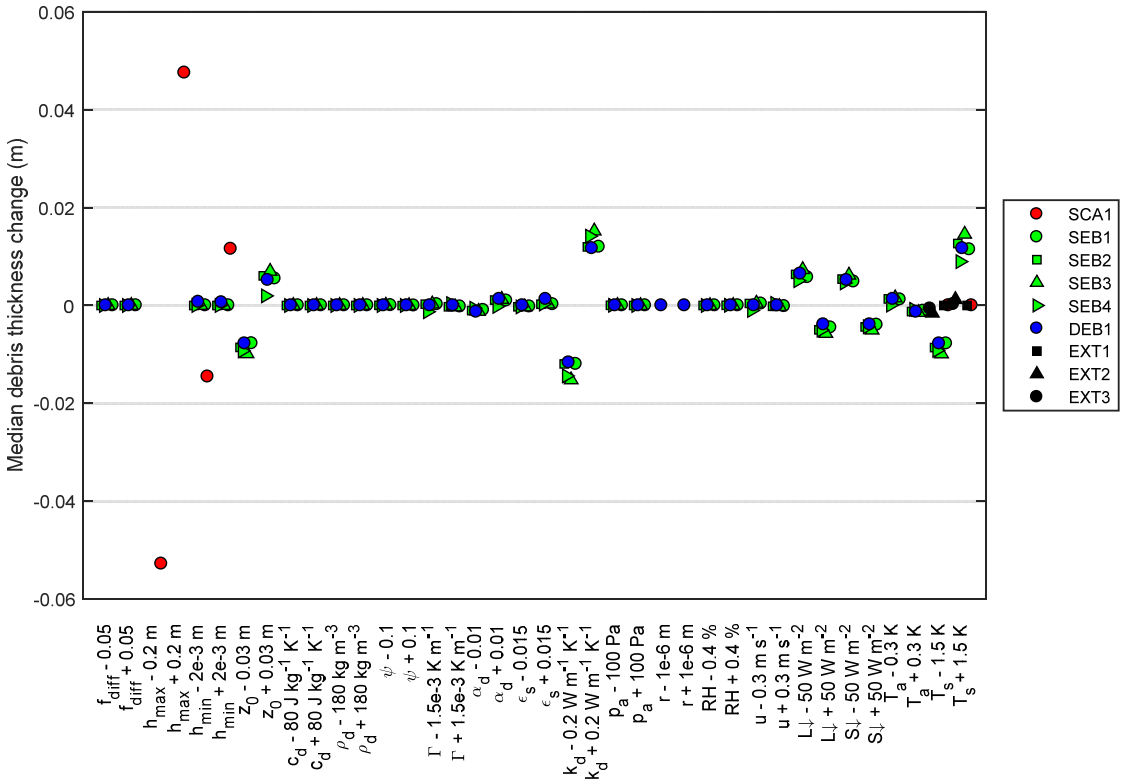

Figure 4.21 – Sensitivities of the different debris thickness quantification approaches to input variable perturbations.

4.5.4 Melt modelling

Cumulative melt for the debris-covered area of Suldenferner Glacier in the 2017 melt season had similar values and patterns when modelled using as input (1) inverse distance weighted (IDW) ground-truth debris thickness values, and (2) DEB1 approach-derived debris thickness values (Figure 4.22a, b). In both cases, most melt was modelled to occur where the debris is thin, near the Payerferner-Suldenferner confluence, and least melt was modelled to occur near the terminus and near the northern margin, where the debris is thick. However, it is apparent that cumulative melt calculated using the DEB1 debris thickness values is relatively homogenous, while cumulative melt calculated using the IDW ground-truth values is relatively heterogeneous. Melt modelling using the DEB1 debris thicknesses gives a moderately lower cumulative melt volume than melt modelling using the IDW ground-truth debris thicknesses (Figure 4.22c). However, melt volume rates are well matched (NSE = 0.93; Figure 4.22d). Total melt volume due to sub-debris melting for the whole debris-covered area during the 2017 melt season was estimated to be ~1.4 x 10^6 m^3 (1.3 x 10^6 m^3 using the DEB1 remote

sensing estimates of debris thickness, 1.5 x 10^6 m^3 using the IDW field measurements), while average melt volume rate was estimated to be as great as ~2000 m^3 hr^{-1} (1800 m^3 hr^{-1} using the remote sensing estimates of debris thickness, 2100 m^3 hr^{-1} using the field measurements).

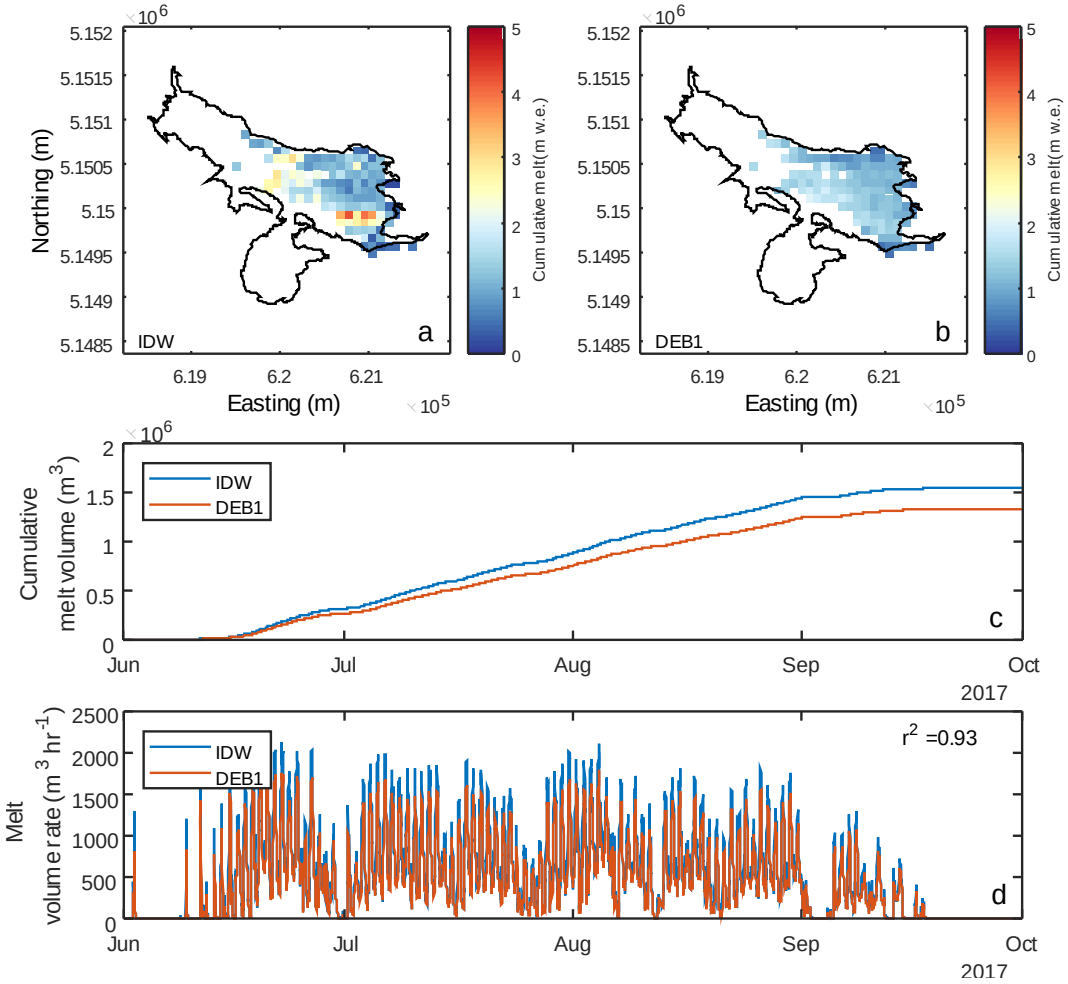

Figure 4.22 – Results of melt modelling for 2017 melt season. (a) Cumulative melt as modelled using inverse distance weighted measured debris thicknesses. (b) Cumulative melt as modelled using Run 29 modelled debris thickness. (c) Modelled evolution of cumulative melt through the melt season. (d) Modelled melt volume rate through the melt season. The coordinate system of (a) and (b) is WGS84 UTM, zone 32N.

4.6 Discussion

4.6.1 Comparison to ground-truth data

Data presented in Section 4.5.1 show that thermal remote sensing methods of quantifying supraglacial debris thickness are able to reproduce debris thickness measurements made in the field, and that surface temperature is a suitable remote sensing quantity with which to inverse-model supraglacial debris thickness. However, they also show that the precision of thermal remote sensing-derived debris thickness estimates can be poor and that most of the approaches tend to under or overestimate debris thickness to some extent. It is particularly striking that the precision of the remote sensing estimates of debris thickness decreases with debris thickness. This is because surface temperature sensitivity to debris thickness decreases as debris thickness increases. Therefore, as debris thickness increases, relatively small errors in input data can result in large errors in estimated debris thickness. The implication of this is that while thermal remote sensing approaches can be used effectively to quantify the thickness of thinner debris, which is more important in terms of melt modelling, they are less effective in quantifying the thickness of thick debris (cf. Schauwecker et al., 2015).

It seems likely that the energy-balance approaches underestimate debris thickness largely due to intra-pixel debris thickness variability (cf. Rounce and McKinney, 2014). If debris thickness is variable within individual pixels of a surface temperature image, thinner debris cover will be over-represented because surface temperature saturates towards greater values of debris thickness. This is why modelled debris thicknesses sit on the ‘thin edge’ of the pit measurements data envelope in Figure 4.19. Another reason the energy-balance approaches underestimate debris thickness could be that using a relatively low-resolution elevation model causes incoming shortwave radiation to be overestimated (cf. Rounce and McKinney, 2014). For example, low-resolution elevation models typically have smoother surfaces than high-resolution elevation models, so fewer pixels will be in the shade at any one time (cf. Arnold and Rees, 2009). Overestimating the shortwave radiative heat flux will cause the conductive heat flux to be artificially large, and modelled debris thickness will compensate by decreasing. The scaling and extrapolation approaches should not be affected so much by debris thickness variability or by elevation model resolution, but variously over or underestimate debris thickness depending how well their equations describe the relationship between surface temperature and debris thickness. For example, the EXT1 approach underestimates the thickness of thin debris, overestimates the thickness of thick debris, and underestimates median debris thickness (Figure 4.17). This suggests the surface temperature-debris thickness relationship is not well represented by an exponential fit. The same is

true for the SCA1 approach. The rational form of Equation (4.21) seems to satisfactorily describe the relationship between quasi-daily mean surface temperature and debris thickness, while the rational form of Equation (4.22), poorly describes the relationship between daytime surface temperature and debris thickness.

In terms of the energy-balance approaches, the problem of intra-pixel debris thickness variability is difficult to address. This is because accounting for intra-pixel debris thickness variability requires intra-pixel debris thickness to be known *a priori*, in which case the problem is circular. If higher resolution surface temperature imagery were available, the effect could be minimised. However, thermal-band satellite imagery is typically provided at lower spatial resolution than optical satellite imagery, and the highest spatial resolution thermal imagery currently available is that of Landsat 7 at 60 m. Using night-time imagery seems to go some way towards addressing the problem of intra-pixel debris thickness variability, and this is discussed further below (Section 4.6.2). The problem of elevation model resolution is more readily resolvable on the basis that high-resolution elevation models are increasingly freely available (e.g. Shean, 2017). The ALOS AW3D30 elevation model used in this study was resampled to 90 m in order that it was same resolution as the surface temperature images. However, with a few modifications and an increase in computational cost, the energy-balance approaches could be used with higher resolution elevation data as input.

4.6.2 Comparison of different approaches

The model ranking results indicate that the EXT2, then the SEB3, then the DEB1 approaches are the best approaches with which to quantify debris thickness by thermal remote sensing (Table 4.7). However, it is recommended that the EXT2 approach should be used if there are sufficient well-distributed field measurements of debris thickness to extrapolate from, while the DEB1 approach should be used if there are no field measurements of debris thickness to extrapolate from.

In the first instance, the EXT2 approach should be used because not only does it perform the best of all the models that were tested, but it is very simple and easy to implement. It performs well because, as long as there are enough *in-situ* debris thickness data, and as long as those data cover enough different types of the glacier surface, the fitting process accounts implicitly for the confounding factors that affect the energy-balance approaches, such as intra-pixel debris thickness variability and shading.

In the second instance, the DEB1 approach should be used over the SEB3 approach because, although the latter ranked higher than the former, it did so for the wrong reasons. With respect to the static energy-balance approaches, the intention of attaching a coefficient to the conductive heat flux, as in

Equation (4.10), is to improve the representation of the conductive heat flux (e.g. Rounce and McKinney, 2014). However, the value of such a coefficient is necessarily arbitrary because the nonlinearity of the temperature gradient within the debris must change with debris thickness and with, for example, location on the glacier and shading history (cf. Schauwecker et al., 2015). This is apparent from the debris temperature profiles shown in Figure 4.5 and the change of heat storage factor with time in Figure 4.4. Approximating the conductive heat flux in this way will cause the thickness of debris thicker than some threshold value to be underestimated and the thickness of debris thinner than some threshold value to be overestimated. Therefore, the conductive heat flux is better represented physically using the dynamic energy-balance approach. In fact, attaching a coefficient to the conductive heat flux in Equation (4.10) causes the SEB3 approach to rank higher than the DEB1 approach because it shifts the surface temperature-debris thickness curve to the right and in doing so reduces the confounding effects of intra-pixel debris thickness variability and DEM resolution. Although this could be viewed as an advantage, the value of the coefficient is arbitrary unless debris thickness is known in advance, in which case, as is discussed above, the problem becomes circular.

The two best model runs in terms of performance statistics were those in which the DEB1 approach was used with night-time surface temperature and emissivity images, indicating that there is some unexplored potential in the use of night-time thermal imagery for quantifying supraglacial debris thickness (experiments 4 and 5, Table 4.6). It is possible that the DEB1 approach works particularly well with night-time imagery because the surface temperature range of the debris is narrower at night, and because a narrower surface temperature range would act to minimise the effect of intra-pixel debris thickness variability on the debris thickness estimates. Additionally, the way in which incoming shortwave radiation is distributed becomes less important because there is no incoming shortwave radiation at the time of the night-time satellite images. The use of night-time thermal imagery is something that should be investigated further, although there are potential problems around georectification and cloud cover identification, which are both more problematic when using night-time imagery.

4.6.3 Sensitivity and transferability

The results of the sensitivity tests give an indication of which variables need to be well-constrained order for a particular approach to perform well, or which variables need most to be included in an uncertainty analysis if uncertainties are to be calculated. For example, in the case of the SCA1 approach, which is very sensitive to changes in the values that are used for h_{min} and h_{max}, h_{min} and h_{max} would need to be well-known in order for the approach to perform as expected. This highlights a

fundamental problem with the SCA1 approach, in that there is no way of knowing the values of these variables. In the case of the energy-balance approaches, the sensitivity tests show that, in order to accurately reproduce debris thickness, debris thermal conductivity and surface roughness length need to be well-constrained, as do surface temperature, incoming shortwave and longwave radiation and, to a lesser extent, air temperature, wind speed and debris albedo. These findings are similar to those of Rounce and McKinney (2014) and Foster et al. (2012). Surface roughness length and thermal conductivity are likely to be particularly problematic for glaciers on which they have not been measured, as both can vary widely, even on individual glaciers (Miles et al., 2017; Rowan et al., 2017). Incoming shortwave radiation and air temperature are less problematic because they are more predictable. However, wind speed, for example is very difficult to predict in mountain environments and is an important modifier of the turbulent heat fluxes. The extrapolation approaches are generally insensitive because they are fitted using *in-situ* debris thickness data. In this case, the sensitivity tests highlight one of the major benefits of the extrapolation approaches.

The fact that the approaches perform about the same or marginally better when forced using off-glacier meteorological data than when forced using on-glacier meteorological data indicates that on-glacier meteorological data is not a pre-requisite for estimating debris thickness from thermal satellite imagery. Although the off-glacier weather station is relatively close to Suldenferner Glacier, this finding lends confidence to the idea that the energy-balance approaches may be more widely applicable. Conversely, on the basis that model performance varies considerably depending on the input data that is used, input data quality is clearly an important aspect of the transferability of the various approaches.

With regards to the extrapolation approaches, the primary barriers to wider application are that field measurements of debris thickness are needed in order to carry out the fitting procedure, and that the relationship between debris thickness and surface temperature is likely to be distorted by elevation. The extrapolation approaches might perform better on Suldenferner Glacier, which is relatively small and whose debris cover occurs within a relatively narrow elevation range, than on other, larger glaciers. These barriers preclude the use of extrapolation approaches in more remote areas, where field measurements of debris thickness are difficult to make, and limit how useful they might be in mountain ranges such as the Himalaya, where glaciers can be considerably bigger. With regards to the energy-balance approaches, the barriers to wider application are the availability of good quality, high-resolution meteorological data and knowledge of the debris properties to which the energy-balance approaches are most sensitive, such as surface roughness length, thermal conductivity and albedo. As demonstrated by Kraaijenbrink et al. (2017), the scaling approach can be used over large areas and

where it is difficult to do fieldwork. However, this may be done at the expense of the quality of the output. In particular, where debris cover extends to high elevations, the value of $T_{s_{min}}$ could be close to 0°C, which could cause the scaling approach to significantly underestimate debris thickness.

The results of the sensitivity tests also show how perturbing the different input variables increases or decreases modelled debris thickness. For example, increasing debris albedo when using the energy-balance approaches causes the shortwave heat flux to decrease, which causes the conductive heat flux to compensate by decreasing also, which causes modelled debris thickness to increase. As a consequence, if albedo is overestimated, debris thickness will be overestimated as well (as can be seen in Figure 4.21). Conversely, if incoming longwave or incoming shortwave radiation are overestimated, the radiative heat fluxes will be too high, which will cause the conductive heat flux to compensate in the other direction, and debris thickness will be underestimated. An interesting case is that if the value used for the thermal conductivity of the debris is overestimated, debris thickness compensates by increasing and will be overestimated. Debris water content was not considered in the sensitivity analysis. However, increasing water content should decrease the conductive heat flux (Collier et al., 2014)[26] and cause debris thickness to be underestimated. It is crucial, then, that these input variables are known as accurately as possible, or, if this is not possible, that they are accounted for when making uncertainty estimates.

4.6.4 Melt modelling

The melt modelling data show that remote sensing-derived debris thickness estimates can be used as input to a distributed melt model with similar results to when field measurements of debris thickness are used. Using the remote sensing estimates instead of the field measurements leads to a slightly smaller estimate of total melt volume. However, the relatively high NSE value shown in Figure 4.22 indicates that it should be preferable, at least, to use remote sensing estimates of debris thickness to model melt than e.g. to assume that the glacier is debris-free or that it is covered in a debris layer of invariable thickness. Another implication, given the modelled melt patterns shown in Figure 4.22, where melt rates are highest upglacier towards the equilibrium line, is that the surface slope of the debris-covered tongue of Suldenferner Glacier is highly likely shallowing as a result of the current

[26] By reducing the thermal diffusivity of the debris cover via changes in its density, specific heat capacity and thermal conductivity. Collier et al. (2014) found that modelling the surface temperature of a 0.23 m debris layer both with and without representing changes in debris water content resulted in mean surface temperature differences of 0.2-0.6 °C.

debris thickness distribution, which is likely to result in reduced ice flow and stagnation into the future (e.g. Benn et al., 2012).

4.7 Summary

Nine different thermal remote sensing approaches to quantifying supraglacial debris thickness were tested against ground-truth measurements of debris thickness on Suldenferner Glacier, Italy. One was a scaling-type approach, four were static energy-balance approaches, one was a dynamic energy-balance approach, and the final three were extrapolation approaches. Median error (ME) and median absolute error (MAE) were used as measures of agreement between modelled and measured debris thickness, and as a basis for ranking the different approaches. Debris thickness was estimated using all nine approaches in combination with three sets of surface temperature and emissivity images, one set of which were night-time images, using both on- and off-glacier meteorological data. The key findings are as follows:

- Thermal remote sensing can be used to quantify supraglacial debris thickness on debris-covered glaciers. All of the approaches reproduce the spatial pattern of debris thickness shown by the ground-truth measurements. Additionally, all of the approaches reproduce the shape of the frequency distribution of the ground-truth debris thickness measurements, and all but one of the scaling approaches (SCA1) and one of the extrapolation approaches (EXT1) reproduce the relationship between surface temperature and debris thickness shown by the ground-truth measurements.
- The approaches are relatively good at quantifying debris thickness at the glacier scale. Median error is generally low, indicating good overall accuracy. However, all consistently over or underestimate debris thickness, even if only by small amounts. In particular, the energy-balance approaches tend to underestimate debris thickness, which is probably due to intra-pixel debris thickness variability and low elevation-model resolution. The approaches are not so good at quantifying debris thickness at individual locations on the glacier: median absolute error is generally high, indicating poor precision. Also, as should be expected, the precision and accuracy of debris thickness estimates decreases with increasing surface temperature as the conductive heat flux from the debris surface becomes negligible.
- On the basis of the performance of the different approaches, it is recommended that if there are well-distributed debris thickness measurements available to extrapolate from, the EXT2 extrapolation approach, which extrapolates debris thickness using pseudo-daily mean surface

temperatures, should be used to quantify supraglacial debris thickness. This approach had the best performance statistics overall, requires only surface temperature and debris thickness measurements as input data, is simple to implement, and is insensitive to surface temperature perturbations.

- If there are no debris thickness data available to extrapolate from, it is recommended that the DEB1 dynamic energy-balance approach, which minimises the mismatch between modelled and measured surface temperature by varying debris thickness in a dynamic energy-balance model, should be used to quantify debris thickness. The performance statistics of the SEB3 static energy-balance approach were slightly better than those of the DEB1 approach. However, the SEB3 approach employs a coefficient with the conductive heat flux, the value of which is arbitrary without knowing debris thickness *a priori*. The DEB1 approach is computationally expensive but physically realistic in the way it describes transient heat conduction through the debris.
- All the energy-balance approaches are sensitive to perturbations in debris thermal conductivity and surface roughness length, so these variables should be known or included in an uncertainty assessment. Additionally, the energy-balance approaches were found to perform slightly better when they were forced using off-glacier (but nearby) meteorological data than when they were forced using on-glacier meteorological data, indicating on-glacier meteorological data is not a pre-requisite for quantifying debris thickness by these approaches.
- A particularly interesting finding is that using the DEB1 approach with the night-time images provided the best results overall. This is likely because the effects of intra-pixel debris thickness variability and elevation model resolution are less of a problem when using night-time imagery. The implication of this is that night-time imagery should be used to quantify debris thickness where possible, and the use of night-time imagery for quantifying debris thickness should be investigated further in future studies.
- Finally, using remote sensing-derived debris thicknesses as input to a forward model of sub-debris melting was found to produce similar results as using inverse distance weighted *in-situ*-measured debris thicknesses as input to the same model. Therefore, debris thickness estimates made by thermal remote sensing approaches such as those that are recommended in this study, combined with a suitable glacier or melt model, should lead to improved prediction of sub-debris melting on debris-covered glaciers

.

5 Regional-scale thermal remote sensing

5.1 Context

Glacier modelling studies have demonstrated that the extent and thickness of supraglacial debris layers are important controls on total melt in glacierised watersheds and mountain ranges (e.g. Collier et al., 2015). This is because the surface energy and mass fluxes of debris-covered ice are strongly altered from those of debris-free ice depending on debris thickness. Across such large scales it is very difficult, if not impossible, to measure debris thickness by fieldwork alone, due to issues of time, cost and accessibility. Therefore, a remote sensing approach must be taken. However, while numerous remote sensing approaches have been developed to quantify debris thickness at the glacier scale(see Section 2.1), applying these approaches at larger scales is difficult and has been attempted only rarely (e.g. Kraaijenbrink et al., 2017; Groos et al., 2017). One of the primary reasons for this is data availability, or a lack thereof, and another is uncertainty about the validity of such approaches.

In terms of data availability, the wider use of remote sensing methods of quantifying debris thickness is limited by the availability of appropriate satellite imagery, whether it be thermal imagery, stereo optical imagery for elevation models, or SAR imagery. However, there are a number of additional considerations. For example, the use of energy-balance remote sensing methods (both thermal- and elevation-change type) is further limited by a lack of high-quality meteorological data and by incomplete knowledge of debris properties such as albedo, thermal conductivity and surface roughness length (e.g. Foster et al., 2012; Rounce and McKinney, 2014; Schauwecker et al., 2015; Rounce et al., 2018). The use of SAR remote sensing methods (e.g. Huang et al., 2017) is limited by a lack of knowledge of geophysical debris properties, such as dielectric permittivity, by the cost of the appropriate SAR imagery, and by the shallow viewing angle of SAR systems. Elevation-change type remote sensing methods require ice thickness and surface velocity data. A full account of these limitations is given in Section 6.1.2. In terms of uncertainty around the validity of remote sensing approaches to quantifying debris thickness, very few studies have been rigorously validated against

ground-truth data and there have been no intercomparison studies.[27] Chapter 4 showed that thermal remote sensing methods can be used to quantify supraglacial debris thickness, but that the best possible input data should be used, and uncertainties should be taken into account because precision can be poor.

As long as the problems of data availability and model validity remain unaddressed, accurately predicting sub-debris melting, and therefore the run-off from and mass balance of debris-covered glaciers, will remain impossible at the regional scale.

5.1.1 Aims and objectives

This chapter uses the DEB1 dynamic energy-balance approach, which is a thermal remote sensing approach that was developed in Chapter 4, to quantify supraglacial debris thickness on the glaciers of three well-studied watersheds in High Mountain Asia: the Langtang and Everest region watersheds, Nepal, and the Baltoro watershed, Pakistan. The DEB1 approach was used based on the findings of Chapter 4 and on the basis that there were insufficient suitable ground-truth data from which to extrapolate debris thickness using an extrapolation-type thermal remote sensing approach. After suitable satellite imagery had been found from which debris surface temperature could be derived, the problem of data availability was addressed by using a high-resolution reanalysis product as input meteorological data and including key meteorological variables and debris properties in an uncertainty analysis. The problems of validation and uncertainty were addressed by comparing the remote sensing estimates of debris thickness to some of the ground-truth debris thickness data presented in Chapter 3 combined with ground-truth data from two additional sources.

The aims of this chapter are to develop a framework for quantifying supraglacial debris thickness at the regional scale, and then to answer the following questions:

- Can a dynamic energy-balance model be used to quantify debris thickness from thermal satellite imagery and reanalysis meteorological data at the regional scale?
- If so, how do remotely sensed estimates of debris thickness compare to ground-truth measurements of debris thickness?
- What are the uncertainties associated with remotely sensed estimates of debris thickness? Do these uncertainties explain the difference between remote sensing estimates and ground-truth measurements and, if not, why not?

[27] Although this is changing now that a new IACS Working group has been set up on the topic of debris-covered glaciers: http://www.cryosphericsciences.org/wg_debrisCovGlaciers.html

- How does debris thickness vary between and within watersheds, and how will modelled debris thickness affect the glaciology of the different study sites into the future?

5.2 Study sites

5.2.1 Everest region watershed

The Everest region watershed (Figure 5.1), in the Himalaya of eastern Nepal, contains some of the highest mountains in the world: Everest, Cho Oyu, Makalu, Lhotse and Nuptse. Its glacierised area is 350 km^2 and its debris-covered area is 150 km^2. Its percentage debris-covered area is 42%, and it comprises 130 glaciers larger than 0.4 km^2. Its climate is dominated by the Indian monsoon, which occurs during the northern-hemisphere summer. Therefore, its glaciers are summer-accumulation type, i.e. most of their annual mass loss and mass gain occurs at the same time, during the northern-hemisphere summer (e.g. Wagnon et al., 2013). Glacial runoff flows into the river Dudh Koshi, which, in turn, flows into one of Nepal's major rivers, the river Koshi, and ultimately the Ganges. Total watershed area is 2600 km^2, and the local population is around 3500, supplemented by tens of thousands of tourists each year (Byers, 2005).

There is a well-documented trend towards glacier retreat and mass loss over the previous few decades. Bolch et al. (2008) and Thakuri et al. (2014) have each shown independently that glacier area is decreasing and debris-covered area is increasing, while Bolch et al. (2008), Nuimura et al. (2011), Thompson et al. (2016) and King et al. (2017) have all documented downwasting and negative geodetic mass balances. King et al. (2017) found that mass loss is spatially variable but particularly high around lacustrine terminating glaciers, while Quincey et al. (2009) observed minimal ice flow and widespread stagnation on glacier tongues. A major cause of mass loss is melting at widespread supraglacial ponds and ice cliffs (Benn et al., 2012; Thompson et al., 2016; Watson et al., 2016).

A number of studies have predicted that negative mass balance and mass loss in the Everest region will continue into the future and towards the end of the century (Shea et al., 2015; Soncini et al., 2016; King et al., 2017). Further, annual river discharge is predicted to decrease (Soncini et al., 2016).

5.2.2 Langtang watershed

The Langtang watershed (Figure 5.1), in the Himalaya of Central Nepal, has a glacierised area of 120 km^2, a debris-covered area of 44 km^2, and a percentage debris-covered area of 35%. It comprises 46

glaciers larger than 0.4 km^2. Similar to the Everest region watershed, its climate is dominated by the Indian monsoon, and its glaciers are temperate, summer-accumulation type. Runoff flows into the river Langtang Khola, which ultimately flows into the Ganges. Total watershed area is 520 km^2, and the local population is around 4500.

The annual mass balance of Langtang region glaciers was negative over the final quarter of the 20th century and the beginning of the 21st century and, as in the Everest region, highly spatially variable (Nuimura et al., 2017; Pellicciotti et al., 2015). Again, as in the Everest region, mass loss is associated with stagnation and retreat, and with surface features such as ice cliffs and ponds (Sakai et al., 2000; Sakai et al., 2002; Pellicciotti et al., 2015; Miles et al., 2016; Miles et al., 2017; Miles et al. 2018). In particular, mass loss on Lirung Glacier is thought to be accelerating due to a positive feedback between surface lowering and reduced ice flux (Nuimura et al., 2017).

The glacierised area and ice volume of the Langtang watershed are both predicted to decline steadily towards the end of the century, due to increases in air temperature. River discharge is expected to increase until around 2050 and then to decrease (Immerzeel et al., 2012; Immerzeel et al., 2013).

5.2.3 Baltoro watershed

The Baltoro watershed (Figure 5.1), in the Karakoram of northern Pakistan, is dominated by Baltoro Glacier, which is one of the longest glaciers in the world outside the Polar Regions. At its eastern end is K2, the second highest mountain in the world. The glacierised area of the Baltoro watershed is 860 km^2, its debris-covered area is 180 km^2 and its percentage debris-covered area is 20%. It comprises 33 glaciers larger than 0.4 km^2. Unlike the climates of the Langtang and Everest region watersheds, the climate of the Baltoro watershed is dominated by the mid-latitude westerlies,[28] which cause precipitation maxima during the northern-hemisphere winter, making Baltoro Glacier winter-accumulation type. Runoff from the Baltoro watershed flows into the river Shigar, which ultimately flows into the Indus. Total watershed area is around 1400 km^2, and local population is almost zero.

Observations have typically suggested that glaciers in the Karakoram are advancing and thickening (Hewitt, 2005; Kääb et al., 2015). Gardelle et al. (2013) found a stable to slightly positive geodetic mass balance for glaciers of the eastern Karakoram over the first decade of the 21st century, while Mayer et al. (2006) and Quincey et al. (2009) demonstrated that, unlike the larger glaciers of the Everest and Langtang regions, the majority of Baltoro Glacier is dynamically active. Advance and

[28] The Indian monsoon weakens towards the west, so the Karakoram does not get its summer snow like the Everest and Langtang regions.

positive or stable mass balance in the region has been attributed to recent increases in precipitation and slight decreases in air temperature (Hewitt, 2005; Quincey et al., 2009). Despite the fact that it is dynamically very active, there are lots of ponds and ice cliffs on the tongue of Baltoro Glacier, presumably due to its low surface slope, the number of which is increasing (Gibson et al., 2017). Conversely, debris-covered area is decreasing (Gibson et al., 2017).

Glacier area and ice volume are predicted to decrease into the future, while river discharge is expected to increase until around 2050 before dropping off towards the end of the century (Immerzeel et al., 2013).

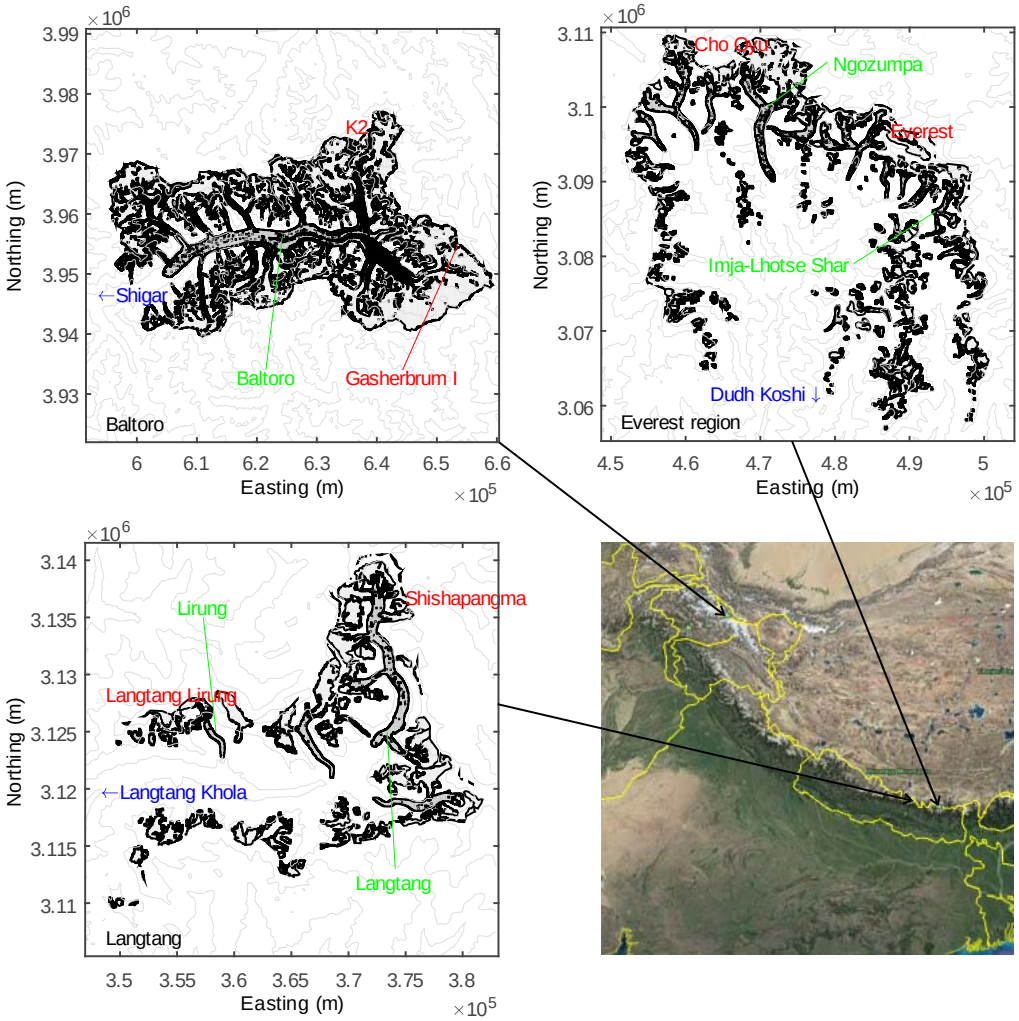

Figure 5.1 – The Baltoro, Everest region and Langtang watershed study sites. Debris-free ice is light grey and-covered ice is dark grey. Glacier outlines are from the Randolph Glacier Inventory v.6 (RGI Consortium, 2017). The bottom left image is from Google Earth. Elevation data are from the SRTM (Jarvis et al. 2008). Coordinate systems are WGS84 UTM, zones 43N, 45N and 45N for Baltoro, Everest and Langtang, respectively.

5.3 Data

5.3.1 Ground-truth debris thickness data

Ground-penetrating radar-derived field measurements of debris thickness, made on Lirung Glacier, Nepal, and Ngozumpa Glacier, Nepal, as described in Chapter 3, were used with additional pit measurements of debris thickness for Baltoro Glacier, Pakistan, and Imja-Lhotse Shar Glacier, Nepal, reported by Groos et al. (2017) and provided by David Rounce, respectively (see Figure 5.2), to test and validate remote sensing estimates of debris thickness. The range of debris thickness values from these four sources is 0.02-7.3 m.

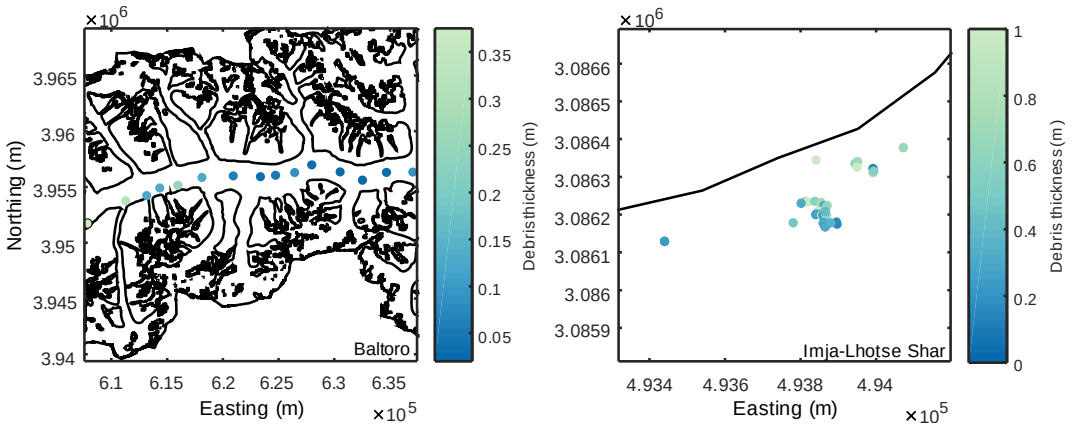

Figure 5.2 – Additional ground-truth debris thickness data, used for validation. Coordinate systems are WGS84 UTM. UTM zones are 43N for Baltoro and 45N for Imja-Lhotse Shar. Glacier outlines are from the Randolph Glacier Inventory v.5 (RGI Consortium, 2017)

5.3.2 Satellite imagery and elevation models

The DEB1 approach requires as input data a remotely sensed surface temperature image, an emissivity image and an elevation model.

Surface temperature images were generated using ‘raw’ scenes from the Landsat 8 Collection 1 Tier 1 scene collection. Landsat 8 Collection 1 Tier 1 ‘raw’ scenes are comprised of digital numbers that represent scaled radiance values. They are radiometrically calibrated and orthorectified, and their thermal bands (B10 and B11) are collected at 100-m resolution, then resampled to 30-m resolution. The best scene for each watershed was selected and downloaded using Google Earth Engine, by making a collection of scenes for each study site from all the scenes within the melt season and within the time period for which meteorological data were available. The scenes were ordered by cloud

cover, then inspected manually using bands B4, B3 and B2, in an optical composite. In cases in which there were multiple suitable scenes, the scene closest to the time of the ground-truth measurements was chosen. The melt season was defined as 15 May to 15 October, after Rounce and McKinney (2014). Ideally, given the findings of Chapter 4, night-time thermal imagery would have been used. However, there were too few night-time images to cover the study areas, so the Landsat 8 daytime imagery was the best available. In fact, the number of satellite images that met both the melt-season and the cloud-cover criteria was surprisingly few, given the frequency of Landsat 8 satellite passes. This is because, particularly in the Himalaya and less so in the Karakoram, cloud cover often obscures satellite images during the melt season.

Emissivity images were generated using the ASTER Global Emissivity Dataset (GED) v.3, which is described by Hulley et al. (2015), and which is provided globally at 100-m resolution.

For surface topography and elevation, the Shuttle Radar Topography Mission (SRTM) elevation dataset v.4 (CGIAR-CSI) was used (Jarvis et al., 2008). SRTM was chosen over ASTER GDEM v2 because intercomparison studies have found SRTM products to be more accurate (Frey et al., 2012; Gómez-Gutiérrez et al., 2011).

In order to reduce the effect of cloud and snow cover on the debris thickness estimates being made, cloud and snow cover images were generated using the quality assessment band (BQA) provided with the Landsat 8 scenes and used as masks.

Table 5.1 provides the details of the satellite data products that were used in this chapter.

Table 5.1 – Overview of the satellite data products that were used in this chapter.

Product	Variable	Time and date (UTC)	Study site
Landsat 8 Collection 1 Tier 1	Surface temperature	22-May-2014 04:41:40 04-Oct-2014 04:48:08 14-Jul-2013 05:31:12	Everest region Langtang Baltoro
SRTM v.4 (CGIAR-CSI)	Elevation	February 2000	All
ASTER GED v.3	Surface emissivity	2000-2008	All

5.3.3 Meteorological data

In High Mountain Asia, there are few high-altitude weather stations (Shea et al., 2015), while reanalysis datasets such as NCEP/NCAR and ERA-Interim are provided at low spatial and temporal

resolution (6-hour time intervals and > 0.75° grid size) and are therefore not suitable for direct use in glaciological analyses without downscaling (e.g. Rye et al., 2010; Collier et al., 2015; Mölg et al., 2014).

On this basis, the energy-balance component of the DEB1 approach was forced using meteorological data from the High Asia Refined (HAR) analysis dataset (Maussion et al., 2014).[29] Specifically, the meteorology fields that were used were surface incoming shortwave radiation, surface incoming longwave radiation, 2-m air temperature, 10-m wind speed, 2-m specific humidity, surface precipitation, surface snow depth and elevation. The HAR dataset is a high-resolution reanalysis dataset that is provided at 10-km spatial and hourly temporal resolution from October 2000 to October 2014, in NetCDF 4 format. It was generated from global analysis data (specifically, a Global Forecasting System dataset), by high-resolution atmospheric modelling, or physical downscaling, using the Weather Research and Forecasting (WRF) model. Because the HAR analysis was carried out at high spatial resolution, it includes glacierised elevations and surface types explicitly. This means that the HAR dataset, unlike other reanalysis datasets, can be used directly to force glacier mass- and energy-balance models (Mölg and Kaser, 2011). For example, Mölg et al. (2014) used HAR meteorology to model the mass balance of Zhandang Glacier, Tibet.

Figure 5.3 shows key meteorological variables over the Baltoro watershed at the time of the 14-Jul-2013 satellite pass. Low air temperatures and high values of incoming shortwave radiation can clearly be seen over the main northwest-southeast trend of the Karakoram.[30]

[29] Publicly available at https://www.klima.tu-berlin.de/index.php?show=forschung_asien_tibet_har&lan=en
[30] Incoming longwave radiation decreases with altitude because it is emitted by atmospheric gases and is strongly linked to air temperature. Both air temperature and humidity, or water vapour content, decrease with altitude, so incoming longwave radiation does as well.

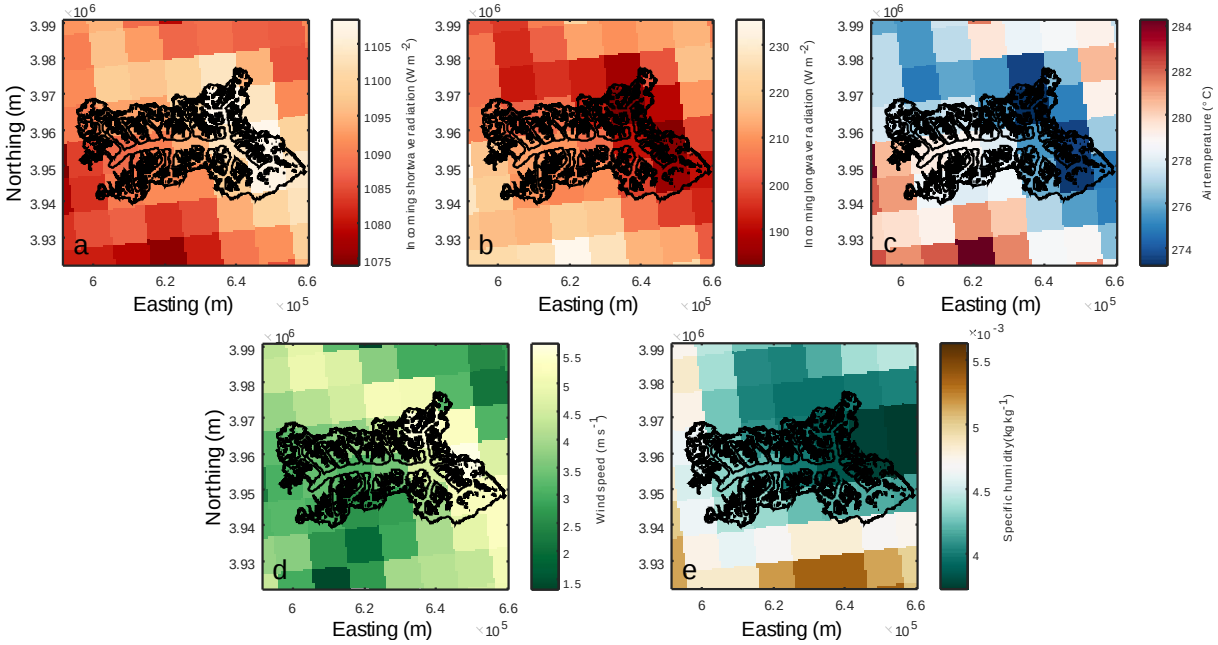

Figure 5.3 – HAR meteorology of the Baltoro watershed at time of the thermal image from which supraglacial debris thickness was quantified. (a), (b), (c), (d) and (e) are incoming shortwave radiation, incoming longwave radiation, air temperature, wind speed and specific humidity, respectively. Coordinate system is WGS84 UTM. UTM zone is 43N.

5.3.4 Geospatial data

RGI v.6 glacier outlines were used to define the spatial extent of the glaciers in each of the three watersheds (Pfeffer et al., 2014).

5.4 Methods

5.4.1 Quantifying debris thickness

Debris thickness was quantified using the DEB1 approach, as described in Sections 4.4.1.3.1, 4.4.2, 4.4.3. That is, for each debris-covered pixel of each watershed, the mismatch between modelled and measured surface temperature at the time of each surface-temperature satellite image, was minimised by iteratively varying debris thickness. However, a number of adaptations were made to the approach, to the ways in which some of the heat fluxes were calculated, and to the ways in which meteorological data were distributed, in order to minimise computing time, in order that the approach could be used

with HAR dataset meteorological data as input, and in order that the uncertainties around key input variables could be considered. These adaptations are as follows:

(1) The HAR dataset provides specific humidity rather than relative humidity at 2 m above the surface. Therefore, specific humidity at the debris surface was calculated by modifying Equation (4.35) such that:

$$q_s = q_a \frac{T_s}{T_a} \tag{5.1}$$

where q_a and q_s are atmospheric and debris surface specific humidity and T_a and T_s are air and debris surface temperature. This assumes, as does Equation (4.35), that water vapour in the atmospheric surface layer is well-mixed (cf. Collier et al., 2014).

(2) The HAR dataset was found, by visual inspection of optical satellite images, to indicate that there was snow on the ground when there was actually no snow on the ground. Thus a snow depth cut-off of 0.02 m was defined, i.e. HAR surface snow depths with values < 0.02 m were set to 0 m. This was done because the DEB1 approach sets modelled debris surface temperature to 0°C if there is snow on the ground, which causes debris thickness to be overestimated if there is, in reality, no ground snow.

(3) Because there was uncertainty around several of the key input variables to the DEB1 approach, Monte Carlo simulations were used to estimate the uncertainty of modelled debris thicknesses (see Section 5.4.8), and best estimates of debris thickness, for each pixel of each watershed, were considered to be the median of the debris thickness estimates made by those Monte Carlo simulations. 500 simulations were run in total, creating a probability density function of debris thickness for each pixel.

(4) The DEB1 approach requires minimum and maximum debris thickness values to be set in order that modelled debris thickness goes neither to zero nor to infinity if measured surface temperature is very low or very high, respectively. These values are used as the initial lower and upper limits of the root-finding method that is used to solve for debris thickness. Minimum debris thickness h_{min} was assumed to be the grain size of the debris, as in Section 4.4.4.3, and was set to 0.01 m after Kraaijenbrink et al. (2017). However, choosing a value for maximum debris thickness is more difficult because there is not an obvious physical limit on how thick a debris layer can become, and because choosing a very high limit significantly increases computing time, because thicker debris requires both more iterations of the root-finding method and a longer spin-up. In Chapter 4, a value of 0.67 m was used, because this was the maximum debris thickness measured on the glacier. In this chapter, it was

decided that an optimal value for maximum debris thickness would be the maximum depth to which the daily temperature wave can penetrate within the debris, because surface temperature sensitivity to debris thickness, and also melt sensitivity to debris thickness, is likely to be minimal beyond this point. On the assumption that debris surface temperature oscillates harmonically on a daily basis, the maximum depth to which the daily temperature wave can penetrate within the debris, and therefore h_{max}, is given by Carslaw and Jaeger (1959), and was calculated as:

$$h_{max} = \xi / \sqrt{\omega / 2\kappa_d} \tag{5.2}$$

where κ_d is the effective thermal diffusivity; ξ is $3\pi/4$, the first temperature minimum at depth for the temperature wave that was initiated during the coldest part of the night before; ω is $2\pi/T$, the angular frequency of the temperature oscillations at the surface, and T is the number of seconds in a day. Because thermal conductivity was included in the Monte Carlo simulations, thermal diffusivity and therefore h_{max}, were allowed to vary from one simulation to the next, and a new value of h_{max} was calculated for each simulation, depending on the thermal conductivity value that was being used in that simulation ($\kappa_d = k_d / C_d$, where k_d is the thermal conductivity and C_d is volumetric heat capacity of the debris). Values of h_{max} ranged from 0.23-0.45 m. Figure 5.4 shows how dimensionless temperature should vary with dimensionless depth in the debris according to Carslaw and Jaeger (1959). The DEB1 approach also requires a tolerance value to be set for the root-finding method. This was set to 0.005 m.

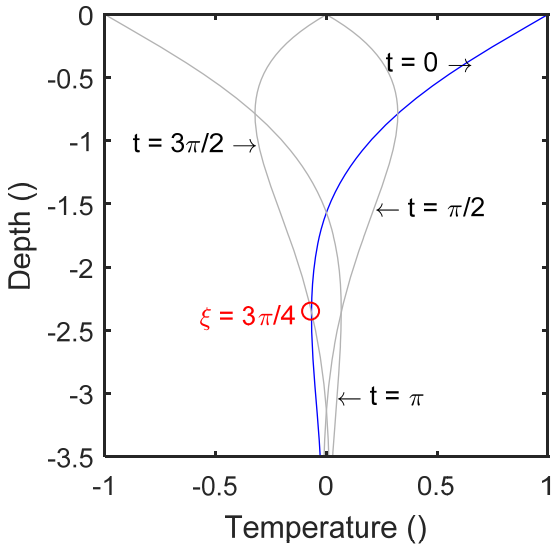

Figure 5.4 – Dimensionless depth against dimensionless temperature of a theoretical debris layer (after Carslaw and Jaeger, 1959), given harmonically oscillating surface temperature. t is the time of temperature wave initiation, where $t = 0$ (blue line) is the coldest part of the night before. The maximum depth to which the daily temperature wave can penetrate is $3\pi/4$, shown by the red marker.

(5) In Chapter 4, a spin-up time of 14 days was used. However, in this chapter, spin-up time was reduced to seven days, in order to reduce computing time. Because lower values of h_{max} were used in this chapter, and because thinner debris requires shorter spin-up times (see Figure 4.7), a spin-up time of seven days was considered to be sufficient.

(6) Air temperature was distributed according to the elevation, z, of each surface temperature pixel from the elevation of the HAR elevation field pixel that was closest to it by a constant environmental lapse rate of 0.0065 K m^{-1}:

$$T_a = T_{a_{HAR}} - \Gamma(z - z_{HAR}) \tag{5.3}$$

Where the subscript HAR indicates that the value of the variable is that which is associated with the closest pixel of the HAR dataset. The closest pixel of the HAR dataset to each surface temperature pixel was found by calculating the distances between the centre of each surface temperature pixel and the centres of all the HAR dataset pixels, then finding the minimum of those distances.

(7) Incoming shortwave radiation was calculated as described in Section 4.4.3, but with a few modifications. The HAR dataset provides surface incoming shortwave radiation normal to the

horizontal, so the same rules apply as if distributing shortwave radiation from a weather station, except that pixels in the HAR dataset are never shaded, so they were treated as if they were always in the sun. Therefore, there were only two conditions for distributing shortwave radiation: (1) if the surface temperature pixel was in the shade, $S\downarrow = S\downarrow_{HAR} f_{diff}$. (2) If the surface temperature pixel was in the sun, $S\downarrow = S\downarrow_{HAR} I/I_{HAR}$, where I and I_{HAR} were calculated as according to Equation (4.40). In the case of calculating I_{HAR}, p_a was calculated using the HAR elevation model. Clouds are accounted for in both the incoming shortwave and incoming longwave radiation products of the HAR dataset.

(8) The wind speed, incoming longwave radiation, specific humidity, precipitation and snow depth of each surface temperature pixel, and of each time step, were assumed to be the same as those of the closest pixel of the HAR dataset.

In addition to these adaptations, prior to debris thickness quantification, a pixel unmixing procedure was carried out in order to reduce the effects of supraglacial ponds and ice cliffs on modelled debris thickness (Section 5.4.6). The debris thickness quantification procedure was then applied only to unmixed surface temperature pixels that were at least partly debris covered. Unless otherwise stated, all the values that were used for constants and variables are the same as those given in Table 4.4. To run all the Monte Carlo simulations, and therefore to quantify debris thickness, took one to three weeks of computing time per watershed on a desktop computer.

5.4.2 Calculating surface temperature

Surface temperature images were generated using the first of the two Landsat 8 thermal bands (B10) and a single-channel atmospheric correction technique. Ideally both thermal bands would have been used according to a split-window atmospheric correction, but Landsat 8 has been affected by far out-of-field stray light in its thermal bands since it was launched, causing brightness temperature offsets, which affect the second thermal band particularly badly. As of April 2017, a stray-light correction was made on all Collection 1 data[31] (Gerace and Montanaro, 2017). However, at present it is recommended that only the first thermal band should be used for quantitative studies.

First, top-of-atmosphere spectral radiance was calculated from 'raw' scene digital numbers, according to the Landsat 8 Data Users Handbook:

$$L_{sen} = M_l Q_{cal} + A_l \tag{5.4}$$

[31] https://landsat.usgs.gov/april-25-2017-tirs-stray-light-correction-implemented-collection-1-processing

where L_{sen} is top-of-atmosphere spectral radiance, M_l is the B10 multiplicative scaling factor provided in the metadata, Q_{cal} are the digital numbers that represent scaled radiance values, and A_l is the B10 radiance additive scaling factor provided in the metadata. Second, top-of-atmosphere brightness temperature was calculated from top-of-atmosphere spectral radiance as:

$$T_{sen} = \frac{c_2}{\ln(c_1/L_{sen} + 1)} \tag{5.5}$$

where T_{sen} is top-of-atmosphere brightness temperature, and c_1 and c_2 are thermal conversion constants, again from the image metadata. Third, surface temperature was calculated using the single-channel atmospheric correction algorithm described by Jiménez-Muñoz et al. (2014):

$$T_s = \gamma\left[\frac{1}{\varepsilon_s}(\tau_1 L_{sen} + \tau_2) + \tau_3\right] + \delta \tag{5.6}$$

Here, ε_s is surface emissivity, for which the ASTER GDEM product was used, while γ and δ are parameters given by:

$$\gamma \approx \frac{T_{sen}^2}{b_\gamma L_{sen}}; \quad \delta \approx T_{sen} - \frac{T_{sen}^2}{b_\gamma} \tag{5.7}$$

where τ_1, τ_2 and τ_3 are atmospheric functions:

$$\tau_1 = \frac{1}{\psi}; \quad \tau_2 = -L\downarrow - \frac{L\uparrow}{\psi}; \quad \tau_3 = L\downarrow \tag{5.8}$$

where b_γ is a constant of value 1324, ψ is atmospheric transmissivity, and $L\downarrow$ and $L\uparrow$ are incoming and outgoing longwave radiation. Values of ψ, $L\downarrow$ and $L\uparrow$ were obtained for the centre point of each watershed using the NASA atmospheric correction parameter calculator,[32] which calculates atmospheric correction parameters from spectral response curves generated using the software MODTRAN (Barsi et al. 2003; Barsi et al. 2005).

Figure 5.5 shows surface temperature as calculated for the Langtang watershed at 04:48:08 UTC on 04-Oct-2014.

[32] https://atmcorr.gsfc.nasa.gov/

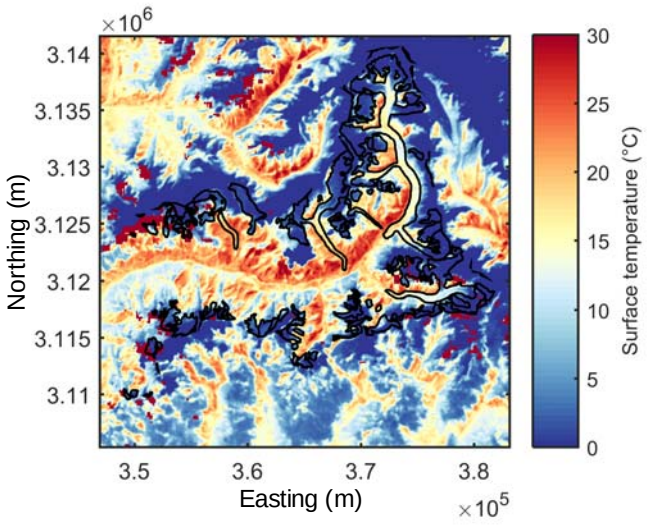

Figure 5.5 – Surface temperature of the Langtang watershed at 04:48:08 UTC on 04-Oct-2014, from which supraglacial debris thickness was quantified. Coordinate system is WGS84 UTM. UTM zone is 45N.

5.4.3 Calculating surface emissivity

The spectral range of the first Landsat 8 thermal band (B10), i.e. the band that was used to generate the surface temperature images, is 10.60-11.19 μm. Therefore, surface emissivity was calculated as the mean emissivity of the two most spectrally similar bands of the ASTER GED (B13 and B14), which together have a spectral range of 10.25-11.65 μm.

5.4.4 Delineating watersheds

The watersheds of the three study sites were delineated using the SRTM elevation model with the Watershed tool in ArcMap. Before using the Watershed tool, sinks in the elevation data were filled, then flow direction and flow accumulation images were created using the Fill Sinks, Flow Direction and Flow Accumulation tools. Pour points were picked manually at appropriate locations downstream of each of the glacierised areas.

5.4.5 Delineating debris cover and ponds

Debris-covered ice and supraglacial ponds were discriminated from debris-free ice within the RGI glacier outlines using a Google Earth Engine script (Kraaijenbrink et al., 2017).[33] This script uses Normalised Difference Vegetation Index (NDVI), Normalised Difference Snow Index (NDSI), surface temperature, surface slope and connected-pixel area thresholds to make a classification image. Debris cover is identified primarily using an NDSI threshold, and ponds are identified primarily using an NDVI threshold. Originally this script delineated debris cover using a thermal composite created from the entire Landsat archive. However, it was modified to delineate debris cover and ponds using only the Landsat 8 scene that was being used for the debris thickness calculations. Therefore, for each watershed, the extent of the debris cover and the location of supraglacial ponds was contemporaneous with the satellite image from which debris thickness was quantified. Delineated debris-covered areas and total glacierised areas are given in Section 5.2.

Table 5.2 – Overview of the thresholds used to classify debris cover and ponds from debris-free ice, from Kraaijenbrink et al. (2017).

Surface type	NDSI	NDVI	Slope (°)	Surface temperature (°C)	Connected area (m^2)
Debris	< 0.25				
Ice, ice cliffs	>=0.25				
Ponds	< 0.25	< -0.1	<= 20	> 5	
Small ponds	>= 0.25		<= 20	> 5	< 1500

5.4.6 Pseudo pixel unmixing

There are lots of supraglacial ponds, ice cliffs and patches of debris-free ice in the three study areas (Watson et al., 2016; Gibson et al., 2017; Miles et al., 2018). These are potentially problematic for the DEB1 approach because they are cold compared to the debris, which should cause debris thickness to be underestimated. In order to minimise the effect of ponds and patches of debris-free ice on the debris thickness estimates, a pseudo pixel unmixing procedure was carried out. Each surface temperature image was resampled to 120-m resolution, starting from its northwest corner, by taking the mean of each of its constituent 4x4 pixel blocks. The classification images (Section 5.4.5) were then used to

[33] This script is provided in the Supplementary Information of Kraaijenbrink et al (2017).

make pond/ice fraction images at the same resolution as the resampled surface temperature images, and unmixed surface temperature images were created as such:

$$T_{s_{deb}} = \frac{T_{s_{pix}} f_{pix} - T_{s_{ip}} f_{ip}}{f_{deb}} \tag{5.9}$$

where f_{pix} is pixel fraction (1), f_{ip} is ponds and ice cliffs fraction, f_{deb} is debris fraction $(1 - f_{ip})$, $T_{s_{pix}}$ is mixed resampled surface temperature, $T_{s_{deb}}$ is unmixed debris surface temperature and $T_{s_{ip}}$ is the surface temperature of ponds and ice cliffs, which was assumed 0°C. Assuming the surface temperature of ponds is 0°C is an underestimate if ponds are not frozen at their surfaces. However, measurements made in the Langtang watershed suggest the amount by which it is an underestimate is small[34] (Miles et al., 2016).

Because of the resolution of the Landsat imagery, not all ponds and ice cliffs were successfully delineated using the classification procedure described in Section 5.4.5. Therefore, a blanket surface temperature correction was made to account for missed ponds and ice cliffs:

$$T_{s_{deb_{corr}}} = \frac{T_{s_{deb}} A_{deb} - T_{s_{miss}} A_{miss}}{A_{deb_{corr}}} \tag{5.10}$$

Here $T_{s_{deb_{corr}}}$ is corrected unmixed surface temperature, $T_{s_{miss}}$ is the temperature of missed ponds and ice cliffs (also assumed to be 0°C), $A_{deb_{corr}}$ is debris area excluding missed ponds and ice cliffs, A_{miss} is missed ponds and ice cliffs area and A_{deb} is debris-covered area including missed ponds. For each of the three watersheds, log-linear relationships ($n_{ip} = c_1 {S_{ip}}^{c_2}$) were fitted to the number of ponds and ice cliffs against pond and ice cliff size, where n_{ip} is number of ponds and ice cliffs, S_{ip} is pond and ice cliff size and c_1 and c_2 are parameters that describe the log-linear fit, and missed pond and ice cliff area was calculated after Miles et al. (2017):

$$A_{miss} = \frac{\pi c_1}{4(c_2 + 1)} \left(S_{pix}\right)^{c_2 + 3} \tag{5.11}$$

where S_{pix} is the pixel size of surface temperature images prior to resampling (i.e. 30 m). Figure 5.6 shows how pond and ice cliff occurrence varies with pond and ice cliff size for the three watersheds, and suggests that the Everest region watershed has both the most and the biggest ponds and ice cliffs, followed by the Baltoro watershed, and then by the Langtang watershed. After accounting for missed

[34]Average pond temperature of Lirung ponds is 1-1.5°C.

ponds and ice cliffs, total pond and ice cliff areas for the Everest, Baltoro and Langtang watersheds were estimated to be 3.2, 3.7 and 0.61 km^2, respectively.

Ideally, pixel unmixing would have been carried out using surface temperatures calculated at the native resolution of Landsat 8 B10. However, as discussed above, Landsat 8 Collection 1 Tier 1 thermal bands are provided having been resampled to 30-m resolution, hence why this is a pseudo pixel unmixing.[35] Further, it should be noted that not all ice cliffs are accounted for by this pixel unmixing procedure because, unless they are large, they are not picked up by the classification algorithm.

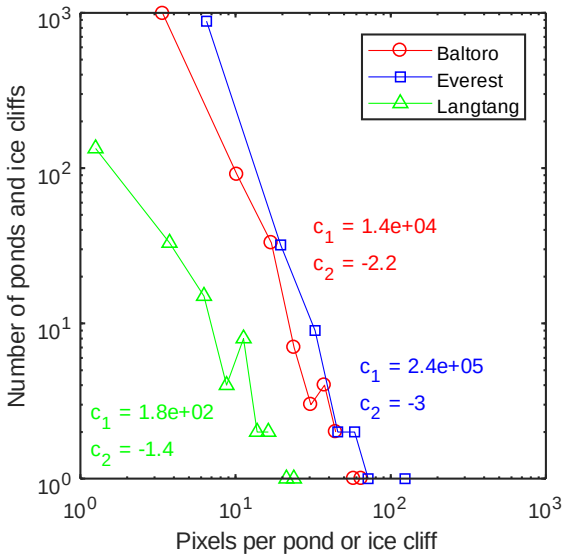

Figure 5.6 – Supraglacial pond and ice cliff data from which missed pond and ice cliff area was estimated for the three watersheds.

5.4.7 Masking clouds and snow

Landsat 8 Collection 1 data products include a quality assessment band (BQA), the bit values of which indicate scene pixels of cloud and snow. The quality assessment band is generated using the CFMask algorithm (Foga et al., 2017), which is an implementation of the MATLAB FMask algorithm (Zhu et al., 2015). Here, the quality assessment band was used to generate cloud and snow masks at the original resolution of the surface temperature images (30 m). Unmixed surface temperature pixels that contained one or more cloud pixels were excluded from the debris thickness calculations because cloud temperature is unknown. However, snow pixels were included in the pixel unmixing (in the

[35]NASA will provide Landsat 8 imagery at native resolution on request. However, this imagery is provided without having been radiometrically or geometrically corrected.

ponds and ice cliffs fraction), assuming they had a temperature of 0°C. Figure 5.7 shows an example of the cloud and snow masks that were generated. In this way, cloud and snow cover are accounted for in the debris thickness quantification procedure as best as possible.

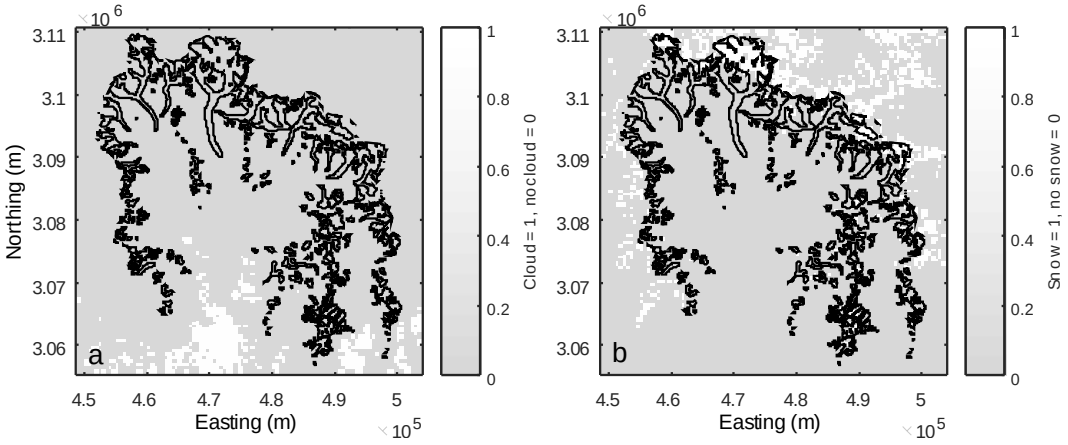

Figure 5.7 – (a) Cloud and (b) snow masks for the Everest region watershed, with glacier outlines in black. Coordinate system is WGS84 UTM. UTM zone is 45N.

5.4.8 Estimating uncertainty

Monte Carlo simulations were used to determine the uncertainty of the debris thickness estimates being made. For each surface temperature pixel of each watershed, the debris thickness model was run 500 times, each time using different input values for the variables around which the model was found to be most sensitive (see Section 4.5.3), i.e. incoming shortwave radiation, incoming longwave radiation, air temperature, wind speed, debris albedo, debris thermal conductivity, and debris surface roughness length. In this way, a probability density function of 500 debris thickness estimates was produced for each surface temperature pixel. Variable values or uncertainties were drawn from uniform distributions using the MATLAB function rand. The uncertainty on the surface temperature data was assumed to be +/- 1°C given low atmospheric water vapour content considering the scenes that were chosen are nearly cloud free (Jiménez-Muñoz et al., 2014), while uncertainties on incoming shortwave radiation, incoming longwave radiation, air temperature and wind speed were estimated to be +/- 50 W m^{-2}, +/- 50 W m^{-2}, +/- 0.3°C and +/- 0.3 m s^{-1}, respectively. These are roughly measurement errors. If applying an uncertainty made negative a variable that has to be positive, the value of that variable was set equal to zero (following Machguth et al., 2008). Debris albedo was assumed to range from 0.1 to 0.4, debris thermal conductivity was assumed to range from 0.5 to 2 W m^{-1} K^{-1}, and debris surface roughness length was assumed to range from 0.005 to 0.06 m (see Table 5.3).

Table 5.3 – Debris property ranges used in the Monte Carlo simulations, as estimated from the literature. (1) Albedo values > 0.4 assumed to be snow.

Study	Surface roughness length (m)	Thermal conductivity (W m^{-1} K^{-1})	Albedo ()	Glacier/region
Miles et al. (2017)	Appx. 0.03-0.05		Appx. 0.1-0.6	Lirung, Nepal
Inoue and Yoshida (1980)	0.0035-0.06			Khumbu, Nepal
Quincey et al. (2017)	0.0184-0.0243		0.21	Khumbu, Nepal
Takeuchi et al. (2000)	0.0063			Khumbu, Nepal
Rounce et al. (2015)	0.006-0.043	0.47-1.62		Imja-Lhotse Shar, Nepal
Kayastha et al. (2000)			Appx. 0.2-0.6	Lirung, Nepal
Conway and Rasmussen (2000)		0.85-1.28		Khumbu, Nepal
Nicholson and Benn (2012)		0.95-1.29	Appx. 0.1-0.3	Ngozumpa, Nepal
Rowan et al. (2017)		0.98-1.98		Everest region, Nepal
Range used in Monte Carlo simulations	0.005-0.06	0.5-2	0.1-0.4[1]	

5.4.9 Comparison to ground-truth data

Modelled debris thickness values were compared to measured, ground-truth debris thickness values by calculating median error (ME) and median absolute error (MAE), as in Section 4.4.6. Modelled debris thicknesses were found by nearest-neighbour interpolation using the locations of the measured debris thicknesses and, where there were multiple ground-truth measurements within an individual pixel of the model output, the mean of those ground-truth measurements was taken. Because surface temperature sensitivity to debris thickness decreases rapidly with increasing debris thickness, measured debris thicknesses were limited to 0.5 m in this comparison, after Huang et al (2017). Additionally, to assess how well the model was able to classify thick from thin debris, an ROC analysis was carried out following Herreid and Pellicciotti (2018) and Fawcett (2006). Modelled and measured debris thicknesses were classified as being either thick or thin around a value of 0.23 m, which is the minimum value of h_{max} that was used in the Monte Carlo simulations. The accuracy, precision and true-positive rate (TPR) of this classification were then calculated as:

$$\text{accuracy} = \frac{TP + TN}{TP + FP + FN + TN} \tag{5.12}$$

$$\text{precision} = \frac{TP}{TP + FP} \tag{5.13}$$

$$\text{TPR} = \frac{TP}{TP + FN} \tag{5.14}$$

where TP is true positive, i.e. measured thick debris that is also modelled as being thick, TN is true negative, i.e. measured thin debris that is also modelled as being thin, FP is false positive, i.e. measured thin debris that is modelled as being thick, and FN is false negative, i.e. measured thick debris that is modelled as being thin. TPR indicates the probability (where a value of one is 100% probable) of thick debris being correctly classified as thick debris.

5.4.10 Estimating melt-rates effects

First-order estimates were made of the percentage areas of the three study sites in which the melt rate of debris-covered ice is enhanced over the melt rate of debris-free ice. This was done using 'critical thickness' data reported by Reznichenko et al. (2010), critical thickness being the debris thickness at which sub-debris melt rate equals debris-free melt rate. Reznichenko et al. (2010) propose that critical thickness decreases as elevation and latitude increase due to associated reductions in diurnal temperature amplitudes and debris-free melt rates. Critical thickness also decreases as elevation increases due to increased shortwave radiation receipts and reduced atmospheric humidity. Therefore, a linear polynomial surface was fitted to data from the HMA region to derive an empirical relationship between elevation, latitude and critical thickness. This relationship was then used to determine whether the debris cover in the three study areas was thicker or thinner than the critical thickness, i.e. melt-reducing or melt-enhancing compared to debris-free ice. The fitted surface and the empirical relationship that was determined are shown in Figure 5.8. Unfortunately, there were only four points to fit this surface to. However, the relationship that was determined meets expectations of decreasing critical thickness with elevation and latitude, and the r^2 value is high, at 0.89.

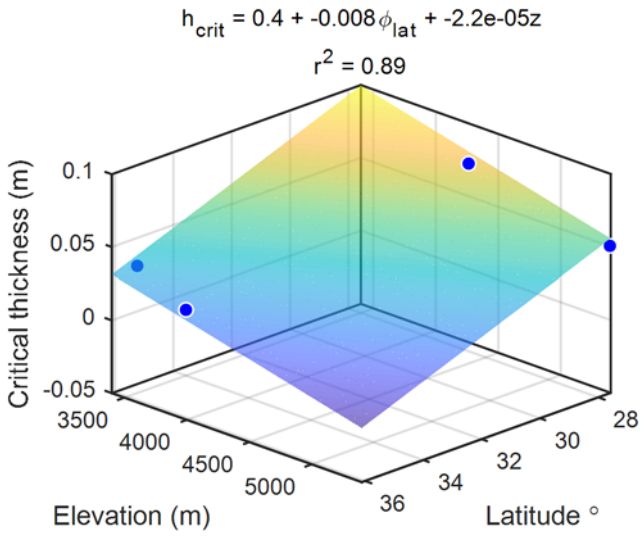

Figure 5.8 – Variation of critical thickness with elevation and latitude using data from Reznichenko et al. (2010)

5.4.11 Data preparation

DEMs and emissivity images were resampled to the same resolution as the unmixed surface temperature images by the nearest neighbour method. Satellite image time and date were extracted from the metadata of the surface temperature images, and the elevation model and emissivity images were resampled to same resolution as the surface temperature images using a nearest neighbour approach. Otherwise, data preparation was the same as in Section 4.4.9.

5.5 Results

5.5.1 Modelled debris thickness

Figure 5.9, Figure 5.10 and Figure 5.11 show best estimates of debris thickness for the Baltoro, Everest and Langtang watersheds, respectively, as determined by the DEB1 approach. Because of the maximum debris thickness limit that was imposed (Section 5.4.1), debris thickness estimates saturate at around 0.36 m. These estimates, i.e. those that consistently reach the maximum debris thickness limit, are best viewed as effective debris thicknesses, in that their associated variations in sub-debris melt rate due to debris thickness will be minimal. In all the watersheds, thinner debris occurs at higher elevations, upglacier and on tributary glaciers, and thicker debris occurs at lower elevations, downglacier and on debris-covered tongues. Visually, glaciers that flow south or east seem more likely to support thicker debris covers than those that flow north or west.

In the Baltoro watershed (Figure 5.9), there are clearly defined bands of thicker debris within thinner debris that run parallel to the centreline of Baltoro Glacier, and the debris cover near the northern margin of the debris-covered tongue is noticeably thicker than the debris cover near the southern margin. Debris cover on the tributaries to Baltoro Glacier support very thin debris cover, and there is a clear transition from thin to thick debris at the confluences of those tributaries with Baltoro Glacier proper.

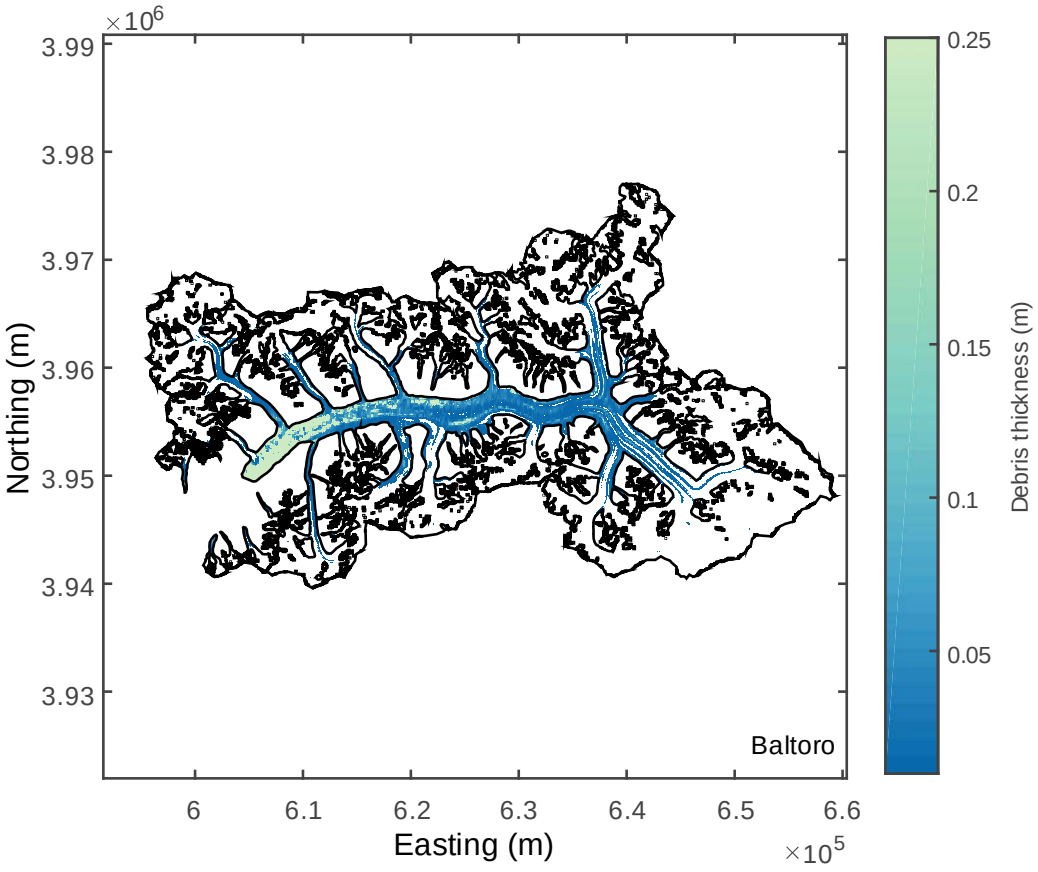

Figure 5.9 – Best-estimate (see Section 5.4.1) distributed supraglacial debris thickness of glaciers in the Baltoro watershed up to 0.25 m. Coordinate system is WGS84 UTM, zone 43N.

In the Everest region watershed (Figure 5.10), visual inspection suggests that the larger glaciers tend to be covered in thicker debris, while the smaller glaciers tend to be more dominated by thinner debris. On Khumbu Glacier, similar to Baltoro Glacier, the debris near the northwest margin is thick, while the debris nearer to the southeast margin is thin, and on Ngozumpa Glacier, there are clearly defined, isolated patches of thinner debris within thicker debris.

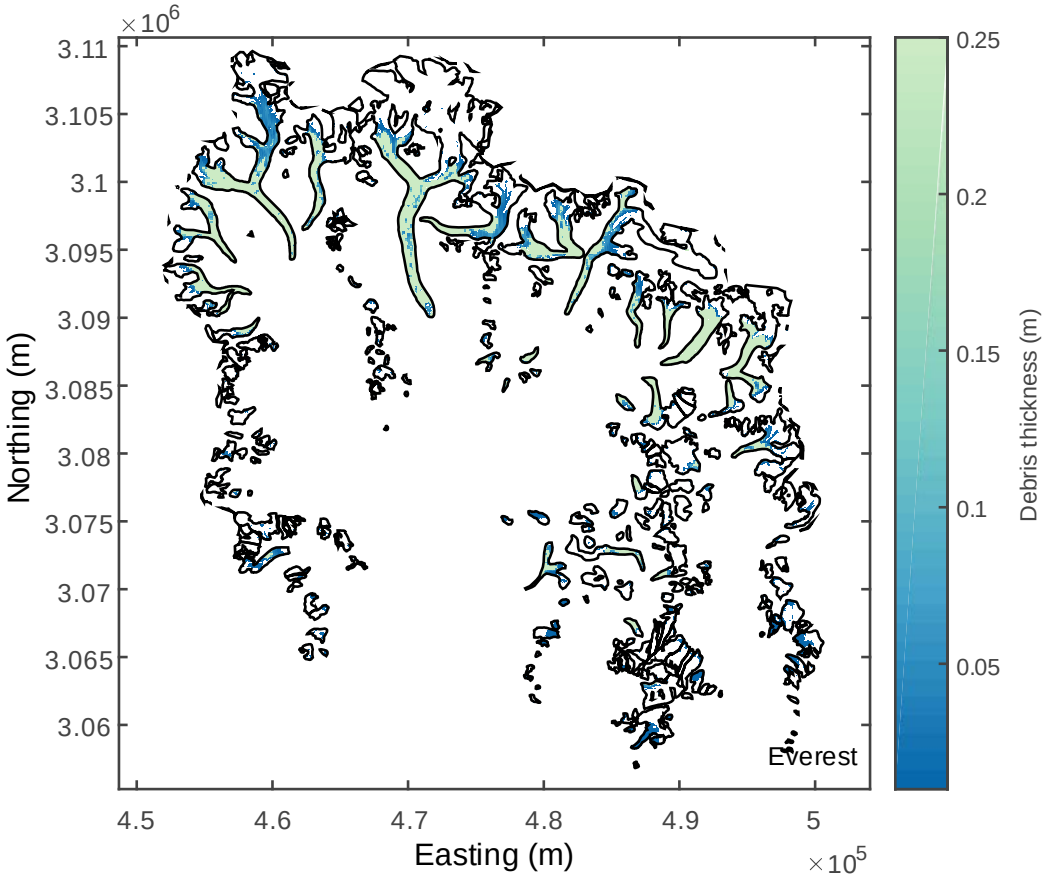

Figure 5.10 – Best-estimate (see Section 5.4.1) distributed supraglacial debris thickness of glaciers in the Everest region watershed up to 0.25 m. Coordinate system is WGS84 UTM, zone 45N.

In the Langtang watershed (Figure 5.11), the west-facing Langshisha Glacier shows a much more gradual transition from thinner to thicker debris downglacier than do other glaciers within the three study sites. Langtang Glacier, like Ngozumpa Glacier in the Everest region, has lots of isolated patches of thin debris on its lower tongue and, again, the smaller glaciers seem generally to support thinner debris while the larger glaciers support thicker debris.

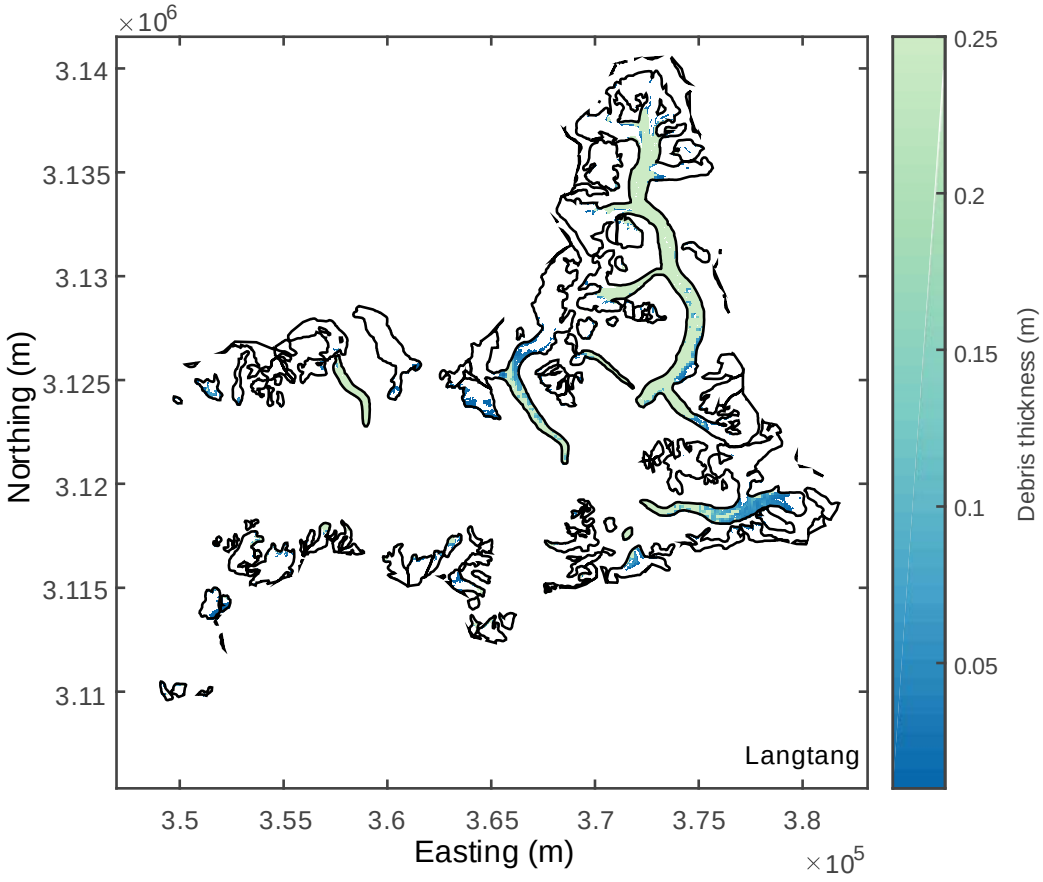

Figure 5.11 – Best-estimate (see Section 5.4.1) distributed supraglacial debris thickness of glaciers in the Langtang watershed up to 0.25 m. Coordinate system is WGS84 UTM, zone 45N.

In terms of debris thickness variability between sites, the debris cover on Baltoro Glacier is considerably thinner than on glaciers in the Everest region and Langtang watersheds. Mean best estimates are 0.065, 0.19 and 0.22 m, respectively.

In terms of debris thickness uncertainties, the minimum modelled uncertainty range – the uncertainty range being the difference between the minimum and maximum debris thickness estimates of a pixel – across the three study sites is 0.0025 m (from 0.013-0.015 m), while the maximum modelled uncertainty range is 0.44 m (from 0.013- 0.45 m). The smallest uncertainty ranges are associated with the thinnest debris and the largest uncertainty ranges are associated with the thickest debris. The mean uncertainty range for the Baltoro region is 0.097 m, for the Everest region is 0.27 m and for the Langtang region is 0.32 m.

Plotting debris thickness hypsometries confirms that debris thickness varies strongly with elevation, whereby debris is thicker at lower elevations and thinner at higher elevations (Figure 5.12).

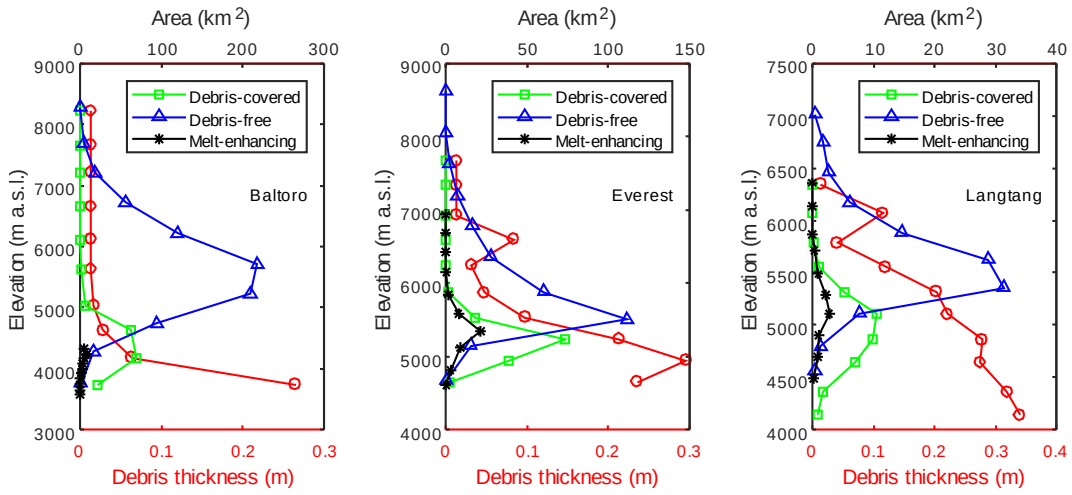

Figure 5.12 – Showing the debris thickness, debris-covered ice area, and debris-free ice area hypsometries of the three watersheds. Also showing the vertical distributions of estimated 'melt-enhancing' debris-covered area.

5.5.2 Comparison to ground-truth data

Comparing the modelled, remotely sensed debris thickness estimates to the ground-truth debris thickness data gives a relatively low ME of 0.022 m and a low MAE of 0.03 m (Figure 5.13a). Further, ROC analysis gives high accuracy (0.91), precision (0.96) and TPR (0.9) statistics when it comes to classifying debris cover as thick or thin (Figure 5.13b). These results generally indicate that that debris thickness is successfully modelled by the DEB1 approach. However, it is also clear from Figure 5.13a that the uncertainties associated with remote sensing estimates can be large, and, in some cases, that they are unable to explain the ground-truth measurements. Specifically, where debris thickness has been measured as being relatively thick (i.e. a few tens of centimetres), the DEB1 approach often estimates debris to be thin, or near the minimum debris thickness limit of 0.01 m.

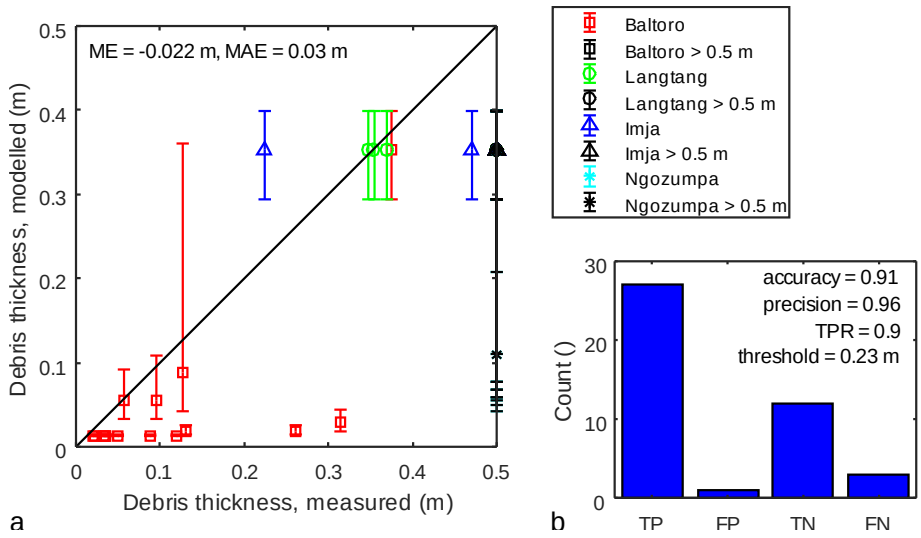

Figure 5.13 – (a) Modelled versus measured debris thickness for the three watersheds. (b) Results of ROC analysis of debris thickness classification.

5.5.3 Estimated melt-rate effects

Table 5.4 shows estimated effects of debris cover on melt rates in the three study areas. It indicates that the debris cover acts mostly to insulate the ice below it, but that over relatively large areas melt rates may also be increased by the presence of debris cover. Specifically, between 12 and 29% of debris cover may act to enhance melt rates, with the Everest region most affected. The mean critical thickness estimated for the Baltoro watershed is considerably thinner than the mean critical thickness estimated for the Langtang and Everest region watersheds. Plotting hypsometries of melt-enhancing debris-covered area (Figure 5.12) shows that, on Baltoro Glacier, most of the melt-enhancing debris occurs at low elevations near the terminus. However, in the Langtang and Everest region watersheds, melt-enhancing debris is more prevalent at higher elevations.

Table 5.4 – Estimated critical thicknesses and areal percentages of melt-enhancing and melt-reducing debris for the three watersheds.

Study site	Mean critical thickness (m)	Melt-enhancing (%)	Melt-reducing (%)
Baltoro	0.013	17	83
Everest region	0.057	29	71
Langtang	0.060	12	88

5.6 Discussion

5.6.1 Modelled debris thickness

Data presented in Section 5.5.1 show that a dynamic energy-balance model can be used in an inverse approach to quantify debris thickness at the regional scale from thermal satellite imagery combined with high-resolution meteorological reanalysis data. Modelled spatial patterns of debris thickness on glaciers in the three study areas are as expected, with thinner debris in upper ablation zones and thicker debris in lower ablation zones and on debris-covered tongues. However, the method presented cannot provide information about debris that is thicker than a few tens of centimetres, other than to indicate that it is thick, as was found in Chapter 4. This is an intrinsic limitation that occurs because surface-temperature sensitivity to debris thickness decreases as debris thickness increases. In this chapter, debris thickness was quantified over three watersheds with a combined glacierised area of 1300 km^2, but there is no reason the same approach could not be used to quantify debris thickness across the whole of the High Mountain Asia (which has a total glacierised area of 98000 km^2). The barriers to wider application that are discussed in Section 4.6.3 (i.e. availability of meteorological and debris properties data), have been overcome in this chapter, so the primary remaining limitation is that of computing time.

The high debris thickness variability between watersheds that is evident in the model outputs is likely a reflection of climatic variability. The Baltoro watershed, which is shown to support relatively thin debris cover, is located at higher latitude than the Everest and Langtang watersheds, so may have considerably lower debris-supply rates associated with lower mean annual temperature (Hales and Roering, 2007). The observation that larger glaciers have thicker debris covers may reflect the fact that thicker debris cover is a better insulator than thinner debris, allowing glaciers that support thicker debris to extend to lower elevations. The occurrence of thinner debris cover on north- and west-flowing glaciers and towards southeastern glacier margins is likely due to low debris-supply rates from north- and west-facing debris supply slopes, and high debris-supply rates from south- and east-facing debris supply slopes (cf. Nagai et al., 2013). Patches of apparently thin debris on Ngozumpa and Baltoro glaciers, may occur due to high intra-pixel debris thickness variability in these areas, or due to ponds or ice cliffs that were missed by the pixel unmixing procedure, both of which would act to reduce surface temperature and artificially lower estimated debris thickness.

Model outputs show similar patterns of debris thickness to previous work. For example, on Baltoro Glacier, previous work also indicates thicker debris downglacier and at medial moraines, and thinner

debris upglacier, on tributaries, and at confluences between tributaries and Baltoro proper (Mihalcea et al., 2008; Groos et al., 2018; Gibson et al., 2017). On the glaciers of the Everest region, Rounce and McKinney (2014) also estimate thick debris on the northwest margin of Khumbu Glacier, and thinner debris to the southeast. However, in terms of estimated debris thickness values, this study finds thinner debris in the Baltoro watershed, particularly at higher elevations, than Mihalcea et al. (2008) and Gibson et al. (2017), likely because Mihalcea et al. (2008) and Gibson et al. (2017) used an exponential scaling approach, which represents the relationship between debris thickness and surface temperature poorly (see Figure 4.19 EXT1). Further, while Rounce and McKinney (2014) predict relatively thin debris on the tongues of Imja-Lhotse Shar, Khumbu and Ngozumpa glaciers, estimates made here typically reach the maximum prescribed thickness value. This difference may occur because the Rounce and McKinney (2014) energy-balance approach does not include transient heat conduction through the debris, so is unable to predict thicker debris (see Figure 4.19 SEB3). In all cases, previous studies have higher maximum debris thickness values than this study because this study imposes a maximum debris thickness condition in its methodology.

As discussed in Section 4.6.3, the model is particularly sensitive to variations in surface temperature, surface roughness length, thermal conductivity, and to a lesser extent incoming shortwave and longwave radiation. In particular, variations in surface roughness length and thermal conductivity are expected to account for a large portion of the debris thickness uncertainty estimates made for the Langtang, Everest region and Baltoro watersheds, largely because both properties exhibit wide potential ranges in these areas (Table 5.3; Miles et al., 2016; Rowan et al., 2017).

5.6.2 Comparison to ground-truth data

Model performance statistics determined by comparing the remote sensing estimates of debris thickness to the ground-truth measurements show that the approach taken was reasonably successful, particularly in terms of classifying debris cover as being either thick or thin. However, it is also clear that there is a tendency for debris thickness to be underestimated and that modelled uncertainties are not always able to explain the field measurements, so the results presented should be treated with caution. The most likely reasons for this are high intra-pixel debris thickness variability and low elevation model resolution, both of which are discussed in detail in Section 4.6.1. In addition, it seems that a considerable number of ponds and ice cliffs were not successfully delineated by the classification procedure (Figure 5.14). While missed ponds were accounted for as best as possible (see Section 5.4.6), it is inevitable that debris thickness will be underestimated where ponds and ice cliffs were not correctly identified.

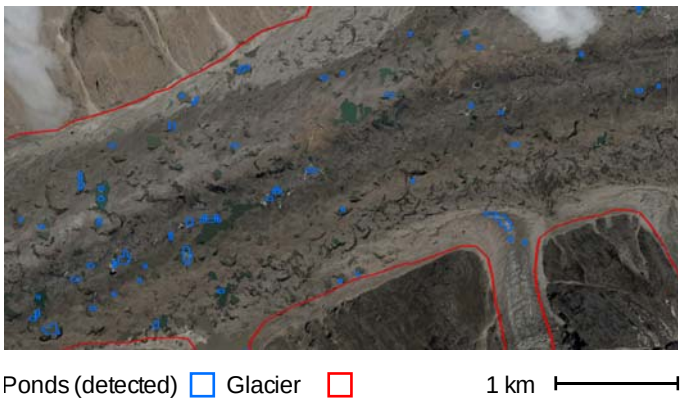

Figure 5.14 – 26-Jun-2014 WorldView image (accessed via Google Earth) of a portion of Baltoro Glacier, overlain with glacier outline and automatically delineated ponds.

Therefore, it is possible that using higher resolution elevation models and classifying the debris cover at higher resolution might help to better match remote sensing estimates to ground-truth measurements. Alternatively, night-time or higher resolution thermal imagery may lead to similar improvements (see sections 4.6.1 and 4.6.2), and improvements might be made by accounting for the spatial variability of the physical properties of the debris. For example, albedo is a key control on the surface energy balance, is likely to vary with variations in the local geology, and can be estimated using satellite imagery (Liang, 2001). Debris surface roughness and thermal conductivity also vary in space, although quantifying these properties remotely is more challenging. In addition, the energy-balance model that was inverted for debris thickness in this chapter is relatively simple, so there are a number of ways in which that could be improved as explained below.

In terms of the radiative fluxes, incoming shortwave radiation might be better represented if clear-sky direct radiation were to be calculated using individual transmittance factors instead of a bulk transmittance factor[36] (e.g. Strasser et al., 2004; Pellicciotti et al., 2011), and if surface slope were to be considered when calculating diffuse radiation (Munro and Young, 1982; Arnold et al., 1996). Additionally, clouds could be considered more explicitly and more accurately (Pellicciotti et al., 2011). Both diffuse shortwave and incoming longwave radiation might be better represented if a sky-view factor approach was used in order to account for the amount of 'visible' sky from which diffuse shortwave radiation could be coming, and for the longwave radiation that is emitted by the moraines and rock slopes around the glacier (Corripio, 2003; Arnold et al., 2006; Aubry-Wake et al., 2015).

In terms of the turbulent heat fluxes, it seems logical that the atmospheric surface layer of a debris-covered glacier should be considered potentially unstable, and that a stability correction should be

[36] Five individual transmittances are typically considered, including transmittance due to Rayleigh scattering, transmittance due to aerosols, and transmittance by trace gasses, by ozone and by water vapour.

included in the calculation of the turbulent heat fluxes, as it is here. This is because debris surface temperature can be much higher than air temperature during the day and, by that very fact, promote buoyancy effects. However, Steiner et al. (2018) found that using a Richardson-type stability correction, as is used here, when calculating the turbulent heat fluxes at debris-covered glacier surfaces, can cause the sensible heat flux to be overestimated, particularly on clear-sky days if wind speed is low, and recommend using no stability correction or a Monin-Obukhov-type correction instead. This is something that could be investigated further. The latent heat flux might be better represented by measuring debris surface relative humidity, or by modelling it by including debris water content in the surface energy balance (e.g. Collier et al., 2014). Additionally, it may be important to consider air-flow through porous debris, as a process that should cause more evaporation from thinner than thicker debris layers (Evatt et al., 2015).

The conductive heat flux might be better represented by considering water and ice in the debris cover and by allowing the physical properties of the debris such as density, specific heat capacity and thermal conductivity to vary accordingly with depth (e.g. Collier et al., 2014). Not accounting for water, as is done here, should result in the conductive heat flux being underestimated.[37] Additionally, if heat conduction to the ice below the debris were considered (e.g. Pellicciotti et al., 2009), it would be possible to use snow-free surface temperature images from outside the melt season to estimate debris thickness because there would be no requirement for ice below the debris to be melting.

Something that is altogether more difficult to deal with is that the energy-balance approach taken here do not consider atmosphere-glacier interactions or feedbacks. Collier et al. (2015) showed that the existence of a debris layer strongly alters the heat exchanges that occur between a glacier and the atmosphere. However, in this study, the atmosphere is effectively assumed to be two-dimensional, so these exchanges are not considered. For example, because air temperature is distributed around the glacier using a lapse rate, the air above the debris cannot be heated by the debris, and any heat transferred from the debris to the atmosphere is assumed to dissipate immediately. To include glacier-atmosphere interactions explicitly, the atmosphere above the glacier would have be considered three-dimensional (e.g. using WRF).

Additionally, it is possible that debris thickness estimates could be improved by calibrating model parameters using *in-situ* debris thickness measurements. In this case, some statistical performance measure or measures could be used to minimise the mismatch between modelled and measured debris thickness values by varying model inputs over their expected uncertainty ranges.

[37] Adding water and/or ice reduces the conductive heat flux (Collier et al. 2014).

Finally, it has to be taken into consideration that the field measurements of debris thickness that were used as ground-truth are not necessarily representative of their surface-temperature pixels, particularly because debris thickness is known to be highly variable over short spatial scales (Chapter 3). For example, the Baltoro Glacier and Imja-Lhotse Shar Glacier field measurements represent only single points on the glacier surface, so it is possible that remote sensing estimates of debris thickness would better match ground-truth measurements if more ground-truth measurements had been made in each pixel.

5.6.3 Estimated melt-rate effects

Data presented in Section 5.5.3 suggest that the majority of the debris cover in all three watersheds acts to insulate the ice below it. The implication of this is that the debris should generally act as a kind of buffer against climatic change, as is hypothesised by Scherler et al. (2011). However, the altitudinal distribution of melt-enhancing versus melt-reducing debris cover may have important implications for ice dynamics. For example, enhanced melt rates due to debris cover over relatively large areas at higher elevations in the Langtang and Everest region watersheds (Figure 5.12) should act to reduce ice flow, which should lead to stagnation, surface-slope reduction and gradual thinning and decay, through the formation of ponds, ice cliffs and hummocky surface topography, which should promote processes of gravitational reworking (e.g. Benn et al., 2012; also see Section 3.6.4). Conversely, enhanced melt rates due to debris cover over relatively large areas at lower elevations in the Baltoro watershed are consistent with a more typical surface mass balance gradient and active ice flow. The modelled altitudinal occurrence of melt-enhancing versus melt-reducing debris cover is consistent with observed surface velocities in the three regions (Mayer et al., 2006; Quincey et al., 2009; Quincey et al., 2009; Miles et al., 2017).

5.7 Summary

The supraglacial debris thickness of the glaciers of three watersheds in High Mountain Asia was quantified from thermal satellite imagery and high-resolution meteorological reanalysis data using a dynamic energy-balance model in an inverse approach. Debris-covered ice was classified from debris-free ice and supraglacial ponds, and clouds and snow cover were masked out prior to the analysis. Debris thickness uncertainties were estimated from uncertainties in key meteorological and debris properties inputs using Monte Carlo simulations. Remote sensing estimates of debris thickness were compared with field measurements of debris thickness from four glaciers (two in the Everest region

watershed, one in the Langtang watershed and one in the Baltoro watershed), which were used as ground truth, and the effects of modelled debris thickness on ice-melt rates were estimated. The key findings are as follows:

- The approach that was tested can be used to estimate supraglacial debris thickness at regional scales and could be applied over the whole of High Mountain Asia with relatively few adjustments in order to improve current estimates of future surface mass balance. Debris thickness estimates are limited to a few tens of centimetres because surface temperature is increasingly insensitive to debris thickness as debris thickness increases. However, ice-melt rate is also increasingly insensitive to debris thickness as debris thickness increases, so the impact of this issue should be minimal.
- Although there were relatively few data points at which the approach could be validated, comparing remotely sensed estimates of debris thickness with field measurements of debris thickness indicates that the approach performs relatively well, particularly in terms of classifying thicker from thinner debris cover. However, it tends to underestimate debris thickness, confirming the findings of Chapter 4, and modelled uncertainties are large and are not always able to explain the difference between remote sensing estimates and field measurements. These issues are due primarily to problems of intra-pixel debris thickness variability, spatial resolution and ponds and ice cliffs being missed during the classification procedure. Therefore, improvements could be made by using night-time thermal imagery or higher resolution thermal and elevation model datasets. Additional improvements may be made by making the energy-balance model itself more physically realistic.
- Modelled debris thickness estimates observe expected spatial patterns in the sense that thinner debris cover occurs at higher elevations and thicker debris cover occurs at lower elevations, and that debris thickness tends to increase with distance downglacier. Modelled debris thickness appears to be greater on south- and east-facing glaciers, likely due to higher debris-supply rates from south- and east-facing debris supply slopes, and the debris cover in the Baltoro watershed is considerably thinner than the debris cover on glaciers in the Everest region and Langtang watersheds, possibly due to differences in debris-supply rate as a function of differences in climate.
- Modelled debris thickness estimates suggest debris cover mostly insulates glacier surfaces in the three study areas, indicating that debris cover should act primarily as a buffer against climatic change. However, in the Everest and Langtang region watersheds, melt rates may be enhanced due to the presence of debris cover at higher elevations and reduced due to the presence of debris cover at lower elevations, in which case there are considerable implications for future ice

dynamics and surface mass balance via differential melting, which will cause surface slope reduction, reduced ice flow and, ultimately, stagnation.

6 Synthesis and conclusions

The aims of this thesis were to (1) make local-scale *in-situ* field measurements of supraglacial debris thickness on a number of glaciers using GPR and by manual excavation, (2) test and develop thermal remote sensing approaches to quantifying supraglacial debris thickness at the glacier scale, and (3) use one of the thermal remote sensing approaches to quantify debris thickness at the regional scale on glaciers in HMA. This work was motivated by the need for improved ability to understand and predict glacier change under conditions of variable debris thickness on glaciers in temperate mountain ranges. It was focussed on HMA because debris-covered glaciers are widespread in HMA, and because there is a particular need for improved predictions of glacier change in HMA given the large downstream population that is dependent on glacial runoff as part of its water supply. However, most of its findings are globally applicable. Here, in Section 6.1, the findings of this thesis are reviewed in the context of previous work on debris thickness quantification, and, in Section 6.3, discussions are had about their glaciological implications. The extent to which the aims of this thesis were achieved are discussed in Section 6.2, and some possible future research directions are outlined in Section 6.4.

6.1 Synthesis of results

6.1.1 Local-scale debris thickness quantification

In Chapter 3, debris thickness was quantified by both GPR and by manual excavation on three debris-covered glaciers in the European Alps and the Himalaya. Here, in light of the findings of this thesis, the strengths and weaknesses of these two methods are put in context of the other method of quantifying debris thickness *in situ*, described in Section 2.5.2: surveying debris exposures above ice cliffs. Ultimately, it seems appropriate that if the debris cover on a glacier is mostly thin (i.e. less than 10-20 centimetres), debris thickness should be measured *in situ* by manual excavation. However, where thicker debris is also present, then a combination of methods might be more appropriate, e.g. manual excavation and GPR or manual excavation and ice-cliff survey. One of the key difficulties in

this respect is that it can be difficult to know in advance even roughly how thick a glacier's debris cover might be.

6.1.1.1 Manual excavation

Measuring debris thickness by manual excavation of pits, proved to be very effective on Suldenferner Glacier, where the debris cover is mostly quite thin (see Chapter 3). Some of the key strengths of measuring supraglacial debris thickness by manual excavation are that: (1) it is easy and time efficient to dig shallow pits through thin debris (e.g. Reid et al., 2012 dug > 1000 pits on Haut Glacier d'Arolla, where the debris is very thin), (2) there is very little uncertainty around measurements made by digging pits when the debris is thin, (3) it is relatively easy to make well-distributed measurements across the surface of a glacier following, for example, a random or stratified sampling pattern, and (4) there is no need for specialist equipment or expertise. Some of the key weaknesses are that: (1) it is prohibitively physically difficult and time-consuming to dig deep pits through thick debris, (2) there is considerable uncertainty around measurements when the debris is thick because the opening of the pit has to be wide, and (3) it may lead to a sampling bias towards thinner debris, which is easier to dig through.

A few simple calculations can give an idea of how difficult and how time consuming it might be to dig pits of various depths in order to measure debris thickness. Assuming the debris naturally forms a cone shape as a pit is dug, where the radius of that cone is defined by the debris' angle of repose, the volume of material to be excavated is a function of debris thickness and the angle of repose of the debris, as such:

$$V_p = \frac{1}{3}\pi\left(\frac{h}{\tan\alpha}\right)^2 h \tag{6.1}$$

where V_p is debris volume, h is debris thickness and α is the angle of repose of the debris. Assuming debris is excavated at a constant rate, excavated debris volume is proportional to the time taken to dig: $V_p = c_1 t$, where c_1 is excavation rate and t is time taken to dig. Therefore, if it takes, for example, 15 s to dig a 0.1 m deep pit, and the angle of repose of the debris is 36° (Shroder et al., 2000), excavation rate is 0.48 m^3 hr^{-1}, and it will take 0.52 hr to dig a 0.5 m deep pit, or 4.2 hr to dig a 1 m deep pit. If debris density is 1.8 x 10^3 kg m^{-3}, as given in Chapter 4, the mass of debris to be excavated from 0.1, 0.5 and 1 m deep pits is 3.7, 460 and 3700 kg, respectively. This is shown graphically in Figure 6.1.

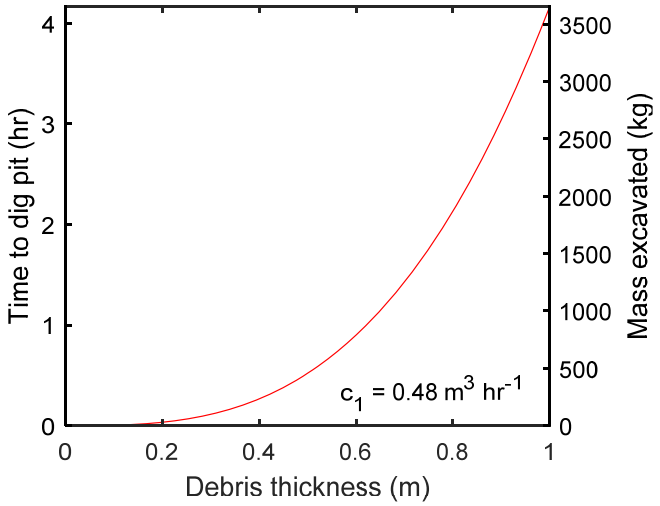

Figure 6.1 – Time taken and mass of excavated debris versus debris thickness, given a constant excavation rate of 0.48 m^3 hr^{-1}.

6.1.1.2 Surveying exposures above ice cliffs

In the literature, debris thickness has been measured by surveying debris exposures above ice cliffs in two ways: (1) using photogrammetry (Nicholson and Mertes, 2017), and (2) using a theodolite (Nicholson and Benn, 2012). The key strengths of these methods are that: (1) relatively little time and effort is required to take photographs or use a theodolite in the field, and (2) it is similarly easy to measure the thickness of thick and thin debris. The key weaknesses are that: (1) measurements made at ice cliffs may not be representative of debris thickness over a wider area because ice cliffs occur in atypical glacier surface settings, (2) the angle of the ice surface under the debris is unknown, so there is uncertainty around the measurements that are made as a result (Nicholson and Mertes, 2017), (3) measurements can only be made where there are ice cliffs, and (4) some specialist equipment or computer software is necessary (e.g. a theodolite or a DGPS). Additionally, in the case of photogrammetry, there might be significant processing time and, because processing is not usually done in the field, there is a chance that insufficient data will be collected to create a consistent, dense point cloud (Westoby et al., 2012).

6.1.1.3 Ground-penetrating radar

In Chapter 3, GPR was found to be a useful tool with which to measure supraglacial debris thickness on Lirung and Ngozumpa glaciers, Nepal. Some of the key strengths of using GPR are that: (1) GPR

data are relatively quick and easy to collect in field, (2) measurements can be made accurately and precisely over a wide range of debris thicknesses (see Section 3.7), (3) it is possible to make measurements where the debris is thick, at least up to around 5 m, and where no other methods can, and (4) the uncertainties on measurements are relatively easy to calculate (see Section 3.4.2.7). Some of the key weaknesses are that: (1) it is difficult to follow, for example, a random sampling strategy using GPR: surveying is generally limited to transects, (2) due to transmitter blanking it is difficult to measure the thickness of debris that is thinner than around 0.1 m, (3) specialist equipment is required (GPR systems can be financially expensive), (4) processing time can be considerable, and (5) there is some subjectivity around manually picking the ice surface in debris-cover radargrams. In terms of weaknesses (4) and (5), processing time could be significantly reduced if processing was done regularly and programmatically, and subjectivity could be reduced by developing an autopicking routine (e.g. Schannwell et al., 2014).

6.1.2 Glacier- and regional-scale debris thickness quantification

The problem of remotely sensing debris thickness is a particularly difficult one. In Chapter 4, a variety of thermal remote sensing approaches to quantifying supraglacial debris thickness were tested and developed on a glacier in the European Alps. In Chapter 5, one of these thermal remote sensing approaches was applied in High Mountain Asia. However, elevation change and SAR remote sensing methods have also been investigated in the literature. The basic principles of these methods are described in Section 2.5. Here, the strengths and weaknesses of thermal remote sensing approaches are summarised in the context of elevation change and SAR methods. In doing this, assumptions, transferability, data availability and sensitivities are discussed. As is the case for the *in-situ* methods, these three types of remote sensing method have different strengths and weaknesses. It therefore seems appropriate that the development of all of them should continue. In some cases, the methods complement each other and could be used in combination. In particular, the thermal- and elevation change-type methods could be used together with the same energy-balance model, whereby the mismatch would be minimised between modelled and measured surface temperature and also between modelled and measured surface mass balance. For example, Fürst et al. (2017) estimate ice thickness by defining a cost function that penalises the mismatch between modelled and measured surface velocity and also between modelled and measured surface mass balance.

6.1.2.1 Thermal remote sensing

In chapters 4 and 5, thermal remote sensing was used to good effect to quantify the supraglacial debris thickness of Suldenferner Glacier, Italy, and of the glaciers in three watersheds in HMA. The findings of this thesis, combined with the findings of Mihalcea et al. (2008), Mihalcea et al. (2008), Foster et al. (2012), Rounce and McKinney (2014), Schauwecker et al. (2015), suggest that the key strengths of using thermal remote sensing are that: (1) good accuracy can be achieved in comparison to field measurements and that estimated debris thicknesses can be used successfully to model sub-debris melting (see Chapter 4), (2) estimated debris thicknesses are fully distributed, (3) thermal remote sensing is computationally inexpensive compared to e.g. elevation change remote sensing, (4) thermal satellite imagery is collected relatively frequently and is freely available, (5) there is minimal processing required in order to derive surface temperatures from thermal imagery. The key weaknesses are that: (1) the spatial resolution of thermal satellite imagery is low compared to the spatial variability of the debris cover, which results in debris thickness being underestimated due to intra-pixel debris thickness variability, (2) there can be relatively few high-quality thermal images that occur within the melt season from which to quantify debris thickness, particularly in areas such as HMA, where there is often heavy cloud cover, particularly during the monsoon, (3) there are issues of meteorological data availability, (4) debris properties such as thermal conductivity and surface roughness are often poorly constrained, and (5) performance is poor for thicker debris because surface temperature sensitivity to debris thickness decreases as debris thickness increases. Additionally, if Landsat thermal imagery is being used, because Landsat thermal bands are not provided at native resolution, a full pixel unmixing for ponds and ice cliffs, cannot be achieved.

6.1.2.2 Elevation change remote sensing

Only one study to date has estimated supraglacial debris thickness by elevation change remote sensing (Rounce et al., 2018). However, it finds that the method has good potential. The key strengths of elevation change remote sensing are that: (1) it is seemingly better than thermal- and SAR-type methods at estimating the thickness of thick debris cover because melt sensitivity to debris thickness is greater than surface temperature and SAR backscatter sensitivity to debris thickness for thicker debris, (2) the elevation model data required as input are increasingly available at high spatial resolution, (3) debris thickness estimates have been found to be reproducible and to compare well to ground truth. The key weaknesses are that: (1) in order to calculate flux divergences and therefore ‘measured’ surface mass balance, both ice thickness and depth-integrated ice flow have to be estimated, which

adds considerable uncertainty; ice thickness estimation is a difficult problem in itself, particularly for debris-covered glaciers (Farinotti et al., 2017), while ice flow estimation requires surface velocities to be quantified and for ice flow due to sliding to be estimated, (2) debris thickness estimates are likely to be worse for thicker debris because melt sensitivity to debris thickness decreases with increasing debris thickness, (3) there are issues of meteorological data availability, (4) debris properties are generally unknown or poorly constrained, (5) accurately quantifying surface velocities, which is often done by feature tracking, is not trivial, particularly in areas where there are few surface features to track and/or where ice-flow is slow, and where surface feature displacements are small, (6) it is computationally expensive compared to thermal- and SAR-type methods, (7) it has not yet been used to estimate distributed thicknesses, due to problems associated with ice flow and the advection of surface features, and (8) calculating elevation changes is not trivial due to the need for various bias corrections (e.g. King et al., 2017).

6.1.2.3 Synthetic-aperture radar remote sensing

As in the case of elevation change remote sensing, only one study has used SAR remote sensing to quantify supraglacial debris thickness (Huang et al., 2017). Again, the results are promising. Some of the key strengths of using SAR imagery to quantify debris thickness are that: (1) SAR is able to penetrate cloud cover, which is a big advantage in areas that are commonly cloudy such as HMA, (2) SAR images can be provided at high spatial resolutions of < 10 m, minimising the effects of intra-pixel debris thickness variability and problems associated with supraglacial ponds and ice cliffs, (3) there is no need for meteorological data or e.g. ice thickness data; only SAR images and an elevation model, for geometric corrections, are required as remote sensing inputs, (4) the method is computationally inexpensive, and (5) good accuracy can be achieved in comparison to field measurements (Huang et al., 2017). The key weaknesses are that: (1) high-resolution SAR data is, or at least has been, financially expensive; ALOS PALSAR imagery is now free and unrestricted,[38] but ALOS-2 PALSAR-2 imagery is currently more than around £1500 per scene[39], (2) there is considerable uncertainty around the value of debris properties such as dielectric constant, which are required as input variables (Huang et al., 2017), (3) the shallow viewing angle of SAR systems means there are often considerable data gaps in mountain regions, (4) similar to thermal- and elevation change-type remote sensing methods, sensitivity to SAR backscatter decreases with increasing debris thickness such that at 1270 MHz (L-band SAR), maximum penetration depth is around 0.5 m.

[38] https://earthdata.nasa.gov/unrestricted-palsar-asf-daac
[39] https://www.asf.alaska.edu/sar-data/palsar/alos-acquisition-maps/

However, a new ESA satellite to be launched in 2021 will have P-band SAR, which, at 435 MHz, will have a penetration depth of around 1.5 m.[40]

6.2 Achievement of aims

Given the background and motivation provided in Section 1.1, the primary aims of this thesis are outlined in Section 1.2. The aims of individual chapters are outlined in sections 3.1.1, 4.1.1 and 5.1.1. All of these aims have been met. Here, a brief summary is made of how these aims were met, and of some of the contributions this thesis has made to the field of glaciology.

First, *in-situ* field measurements of debris thickness were made successfully on three glaciers (Chapter 3), addressing the lack of existing *in-situ* debris thickness data outlined in Section 1.1. In doing this, GPR was tested as a novel means of measuring debris thickness in the field and was found to be viable. A new workflow was developed for making GPR measurements and for calculating associated uncertainties. Further, field measurements were used successfully to investigate inter- and intra-glacier debris thickness variability and the relationships of debris thickness with various remote sensing quantities. The outcome of the aim to investigate processes of gravitational reworking and the relationship of debris thickness with topographic parameters was particularly interesting, and a mechanism was proposed by which relatively high-sub debris melt rates can occur on potentially large areas (up to 32% of debris-covered area) of the surfaces of debris-covered glaciers. The data and work of Chapter 3 have been used in a number of publications: Rounce et al. (2018), Nicholson and Mertes (2017), Nicholson et al. (2018) and McCarthy et al. (2017).

Second, nine different thermal remote sensing approaches to quantifying debris thickness, several of which were developed for this thesis, were successfully tested against each other and against a large dataset of field measurements at the glacier scale (Chapter 4). Such a comparison had not been carried out before, nor had such remote sensing estimates of debris thickness been compared with such a large dataset of field measurements. It was found that remote sensing can be used to reproduce field measurements of debris thickness and that sub-debris melting modelled using remote sensing estimates of debris thickness compares well to sub-debris melting modelled using field measurements. These findings increase confidence in the validity of thermal remote sensing methods of quantifying debris thickness and provide justification for future work. If field measurements are available to extrapolate from, it was found that debris thickness should be extrapolated using remote sensing-

[40] https://spacenews.com/airbus-uk-to-build-europes-biomass-satellite-featuring-first-use-of-p-band-radar/

derived pseudo daily mean surface temperatures and, if not, that it should be determined iteratively by minimising the mismatch between remotely sensed surface temperatures and surface temperatures determined using a dynamic energy-balance model (these two approaches are described in Sections 4.4.1.4.1 and 4.4.1.3.1, respectively). A finding that is particularly novel and interesting is that the best results overall were achieved using the dynamic energy-balance approach with night-time thermal imagery. Night-time thermal imagery had not before been used to quantify debris thickness, yet may be very useful for doing so because it minimises the effect of problems associated with spatial resolution and intra-pixel debris thickness variability. Limitations and sensitivities were successfully investigated and are discussed in detail in Section 4.6. In addition, measurements of various debris properties such as grain size, thermal conductivity, surface roughness, and albedo were made. These data will be useful for future energy and mass balance modelling studies of debris-covered glaciers.

Third, a dynamic energy-balance model, used in an inverse approach to quantify debris thickness, was successfully run at the regional scale using thermal satellite imagery and high-resolution meteorological reanalysis data (Chapter 5). Best estimates of debris thickness and associated uncertainty were made using Monte Carlo simulations, and debris thickness estimates were successfully tested against field measurements. While the number of field measurements that were used was limited, and while it is clear that there is room for improving model performance, the remote sensing estimates compared favourably to the ground-truth data. Modelled uncertainties were found not to capture the errors on ground-truth data, and there was a tendency for debris thickness to be underestimated and the reasons for this were discussed (Section 4.6.1). Debris thickness variability between and within watersheds was successfully investigated and found to be high, possibly controlled by the aspect of debris supply slopes and local climatic conditions. Finally, a particularly interesting finding is that debris cover may act to enhance melt rates over relatively large glacier surface areas (up to 29% of total debris-covered area in the Everest region).

6.3 Glaciological implications

Supraglacial debris thickness is a strong control on the sub-debris ice-melt rates of debris-covered glaciers, such that melt rate can vary by an order of magnitude depending on debris thickness (Section 2.3). This thesis has made recommendations on how best to quantify supraglacial debris thickness at local to regional scales, having investigated, tested, developed and improved a range of different methods of doing so, and having comprehensively reviewed existing literature on the subject. As such, it should lead to improved representation of supraglacial debris cover in glacier models at a range of

scales, which, in turn, should lead to improved understanding of past and present glacier change, and to improved prediction of future glacier change in temperate mountain ranges, both of which are essential to predicting future water supply in glacierised regions and glacier contributions to sea-level rise. Improved representation of supraglacial debris cover in glacier models is particularly important in terms of modelling glacier change in HMA, where debris-covered glaciers are common and where large numbers of people depend to some extent on glacial runoff as a part of their water supply (Pritchard, 2017). However, the findings of this thesis could also lead to improvements in current understanding of the processes that distribute debris on debris-covered glaciers (Nakawo et al., 1986; Anderson and Anderson, 2018); to improved understanding of the climatic conditions that cause debris-covered glaciers to form; and to improved ice thickness estimation, because ice thickness inversions often prescribe surface mass balance gradients, which should ideally be adjusted to account for debris cover (Farinotti et al., 2009; Huss and Farinotti, 2012; Maussion et al., 2018). The finding that gravitational reworking potentially causes the formation of hotspots of sub-debris melting on large areas of debris-covered glacier surfaces implies that gravitational reworking could be important at large scales as a promoter of mass loss and glacier change. Further, the finding that sub-debris melt rates may be increased by the presence of debris cover over relatively large areas of HMA glaciers at higher elevation has important implications for ice dynamics and for what the future of glacier change in HMA might look like. One particularly important implication is that ice flow might be reduced due to surface slope reduction, causing downwasting, decay and potentially a proliferation of glacial lakes (Benn et al., 2012).

6.4 Future work

The findings of this thesis pave the way for improved quantification of supraglacial debris thickness at local to regional scales. However, they also pose new questions and open the door to a number of future research directions.

In terms of quantifying debris thickness *in situ*:

- Despite the best efforts of this thesis, there are still relatively few glaciers worldwide on which field measurements of supraglacial debris thickness have been made. Therefore, future work should continue to measure supraglacial debris thickness *in situ*. Methodologically, this should be done using a combination of methods: manual excavation, surveying debris exposures above ice cliffs and, given the success of the work carried out in Chapter 3, by GPR. Preferably, field

measurements should be made on strategically-located 'benchmark' glaciers, or glaciers that are well-instrumented with weather stations and at which mass balance measurements can be made. This will enable further understanding of surface processes on debris-covered glaciers and further development of remote sensing approaches to quantifying debris thickness. It will also lead to improvements in the way the surface mass balance of debris-covered glaciers is modelled.

- The use of Unmanned Aerial Vehicles (UAVs) in Earth science is increasing and UAV-mounted GPR is beginning to be used successfully in some fields of research (e.g. Cerquera et al., 2017). Therefore, it may soon become possible to make GPR measurements of debris thickness in the field by UAV, at very high spatial resolution. Similarly, it should already be possible to assess debris thickness at ice cliffs using UAVs, following Nicholson and Mertes (2017) and e.g. Immerzeel et al. (2014). Alternatively, helicopter-borne GPR could be used to measure supraglacial debris thickness, as it has been for measuring on-glacier snow accumulation (Machguth et al., 2006). In these ways, potentially high-accuracy measurements could be made over relatively large areas and on parts of glaciers that would otherwise be difficult to access. Airborne methods could act as a good bridge between *in-situ* and remote sensing methods of quantifying debris thickness.
- The spatial variability of supraglacial debris thickness should continue to be investigated to try to establish the effects of debris thickness variability and processes of gravitational reworking on sub-debris melt rates. In particular, landscape evolution-type modelling experiments in combination with very high spatial resolution field measurements of debris thickness might work quite effectively towards this end, whereby field measurements could be used as the starting point for a coupled slope stability-surface mass balance model.

In terms of quantifying debris thickness by remote sensing:

- One of the major limitations to developing and testing new methods is that there is still a lack of field measurements available for calibration and validation. Therefore, a debris thickness database should be set up in which field measurements of debris thickness can be stored in one place and made freely accessible. The World Glacier Monitoring Service recently initiated the Glacier Thickness Database, which is a database of *in-situ* ice thickness measurements (Gärtner-Roer et al., 2014), and which might serve as a good model for a debris thickness equivalent.
- Remote sensing methods of quantifying debris thickness should continue to be developed and tested. To aid this process, efforts should be made to make debris thickness quantification model code publicly available. Further, there should be more of an effort in the future to calculate debris thickness uncertainties (as e.g. Kraaijenbrink et al., 2017; Rounce et al., 2018; Chapter 5 of this

thesis). Model intercomparison experiments, such as the one carried out in Chapter 4 and the one recently announced by the new IACS Working Group on debris-covered glaciers,[41] offer the potential to better understand the strengths and weaknesses of different methods, so it may soon become appropriate to combine methods into ensembles, or to employ different methods, depending on strengths and weaknesses, in different glaciological settings.

- As remote sensing data becomes increasingly widely and freely available, and as powerful remote sensing tools like Google Earth Engine develop traction, it should become possible not only to map supraglacial debris thickness on a global scale using the sorts of methods that are tested in this thesis, but also to update remotely sensed debris thickness estimates semi-periodically, as new satellite data are collected. For example, to support agricultural studies, global surface temperature inversion-derived evapotranspiration products are now available through EEFlux, an evapotranspiration tool on Google Earth Engine, which leverages the Landsat archive back to 1984 and global-scale meteorological reanalysis data.[42]
- The approaches presented in this thesis are a good basis on which to build, but there are a number of areas in which improvements could be made. Specifically, in terms of the DEB1 approach used in Chapters 4 and 5, a number of potential improvements are outlined in Section 5.6.2. Future work should focus on making these improvements. Both the EXT1 and the DEB1 approaches developed in this thesis should be validated further on different glaciers and in different glacierised regions, in order to test their wider transferability. Night-time thermal imagery should certainly be investigated more thoroughly, as it seems that there are potentially several benefits associated with using night-time that have been overlooked until now, and the possibility of extrapolating existing debris thickness measurements using DEB1 approach could also be explored.
- Better estimates of debris thickness could be made by remote sensing methods if satellite sensors were designed more appropriately to the problem of quantifying debris thickness. In particular, higher spatial resolution thermal satellite imagery would minimise the problem of intra-pixel debris thickness variability and make it easier to identify ponds and ice cliffs for pixel unmixing purposes. Further, if high spatial resolution thermal imagery were to be collected at higher temporal resolution, there would be more cloud-free thermal images from which to quantify debris thickness. In terms of SAR-type remote sensing methods, the advent of P-band SAR, with a penetration depth of around 1.5 m, will also present opportunities for future work.

[41] http://www.cryosphericsciences.org/wg_debrisCovGlaciers.html
[42] https://eeflux-level1.appspot.com/

- Finally, a clear step forward would be that debris thickness estimates made by remote sensing approaches, such as the one that is outlined in Chapter 5, should be increasingly used in glacier models at a range of scales. Good progress is being made in this direction. For example, thermal remote sensing estimates of debris thickness have been used in glacier models to predict the future of glacier change in HMA, and to hindcast glacier change in the Karakoram (Kraaijenbrink et al., 2017; Groos et al., 2017). However, the debris thickness estimates that were used in these studies were possibly not optimal. Ultimately, debris cover and debris thickness should begin to be integrated into global-scale glacier models, such as those of Marzeion et al. (2012), Radić et al. (2014), Huss and Hock (2015) and Maussion et al. (2018).

References

Anderson, L. S., and R. S. Anderson. 2018. Debris Thickness Patterns on Debris-Covered Glaciers. *Geomorphology*, 311.

Anderson, L. S., and R. S. Anderson. 2016. Modeling Debris-Covered Glaciers: Response to Steady Debris Deposition. *The Cryosphere*, 10, 3.

Annan, A. P. 2009. Electromagnetic Principles of Ground Penetrating Radar. *Ground Penetrating Radar Theory and Applications*, edited by H. M. Jol, 1st ed., Elsevier.

Arnold, N., and G. Rees. 2009. Effects of Digital Elevation Model Spatial Resolution on Distributed Calculations of Solar Radiation Loading on a High Arctic Glacier. *Journal of Glaciology*, 55, 194.

Arnold, N. S., et al. 1996. A Distributed Surface Energy-Balance Model for a Small Valley Glacier. I. Developtnent and Testing for Haut Glacier d'Arolla, Valais, Switzerland. *Journal of Glaciology*, 42, 240.

Arnold, N. S., et al. 2006. Topographic Controls on the Surface Energy Balance of a High Arctic Valley Glacier. *Journal of Geophysical Research: Earth Surface*, 111, 2.

Aubry-Wake, C., et al. 2015. Measuring Glacier Surface Temperatures with Ground-Based Thermal Infrared Imaging. *Geophysical Research Letters*, 42.

Azam, M. F., et al. 2018. Review of the Status and Mass Changes of Himalayan-Karakoram Glaciers. *Journal of Glaciology*, 64, 243.

Banerjee, A. 2017. Brief Communication: Thinning of debris-covered and debris-free glaciers in a warming climate. *The Cryosphere*, 11, 1.

Barrette, P. D., and G. W. Timco. 2008. Laboratory Study on the Sliding Resistance of Level Ice and

Rubble on Sand. *Cold Regions Science and Technology*, 54, 2.

Bastiaanssen, W. G. M., et al. 1998. A Remote Sensing Surface Energy Balance Algorithm for Land (SEBAL). 1. Formulation. *Journal of Hydrology*, 212–213.

Bastiaanssen, W. G. M., et al. 1998. A Remote Sensing Surface Energy Balance Algorithm for Land (SEBAL) 2. Validation. *Journal of Hydrology*, 212–213.

Beauducel, F. 2015. *LL2UTM and UTM2LL*. MATLAB File Exchange.

Benn, D. I., et al. 2003. Glaciated Valley Landsystems. *Glacial Landsystems*, Arnold, London.

Benn, D. I., et al. 2012. Response of Debris-Covered Glaciers in the Mount Everest Region to Recent Warming, and Implications for Outburst Flood Hazards. *Earth-Science Reviews*, 114, 1–2.

Benn, D. I., et al. 2017. Structure and Evolution of the Drainage System of a Himalayan Debris-Covered Glacier, and Its Relationship with Patterns of Mass Loss. *The Cryosphere*, 11, 5.

Benn, D. I., and D. J. A. Evans. 2014. *Glaciers and Glaciations*. 2nd ed., Routledge.

Benn, D. I., and F. Lehmkuhl. 2000. Mass Balance and Equilibrium-Line Altitudes of Glaciers in High-Mountain Environments. *Quaternary International*, 65–66, April.

Bennett, M., and N. Glasser. 2011. *Glacial Geology: Ice Sheets and Landforms*. John Wiley & Sons.

Bolch, T., et al. 2008. Planimetric and Volumetric Glacier Changes in the Khumbu Himal, Nepal, since 1962 Using Corona, Landsat TM and ASTER Data. *Journal of Glaciology*, 54, 187.

Bolch, T., et al. 2012. The State and Fate of Himalayan Glaciers. *Science*, 336, 6079.

Booth, A. D., et al. 2013. A Comparison of Seismic and Radar Methods to Establish the Thickness and Density of Glacier Snow Cover. *Annals of Glaciology*, 54, 64.

Booth, A. D., et al. 2010. Semblance Response to a Ground-Penetrating Radar Wavelet and Resulting Errors in Velocity Analysis. *Near Surface Geophysics*, 8, 3.

Bradford, J. H., et al. 2005. Measuring Thaw Depth beneath Peat-Lined Arctic Streams Using Ground-Penetrating Radar. *Hydrological Processes*, 19, 14.

Braithwaite, R. J., and O. B. Olesen. 1989. Calculation of Glacier Ablation from Air Temperature, West Greenland. *Glacier Fluctuations and Climatic Change*, Springer, Dordrecht.

Brandt, O., et al. 2007. Detection of Buried Ice and Sediment Layers in Permafrost Using Multi-Frequency Ground Penetrating Radar: A Case Examination on Svalbard. *Remote Sensing of Environment*, 111, 2.

Bristow, C. S., and H. M. (eds) Jol. 2003. *Ground Penetrating Radar in Sediments*. Geological Society of London.

Brock, B., et al. 2010. Meteorology and Surface Energy Fluxes in the 2005–2007 Ablation Seasons at the Miage Debris-covered Glacier, Mont Blanc Massif, Italian Alps. *Journal of Geophysical Research: Atmospheres*, 115, D9.

Brock, B. W., and N. S. Arnold. 2000. A Spreadsheet-Based (Microsoft Excel) Point Surface Energy Balance Model for Glacier and Snowmelt Studies. *Earth Surface Processes and Landforms*, 25, October.

Brun, F., et al. 2017. A Spatially Resolved Estimate of High Mountain Asia Glacier Mass Balances from 2000 to 2016. *Nature Geoscience*, 10, September.

Brutsaert, W. 2013. *Evaporation into the Atmosphere: Theory, History and Applications*. Springer Science & Business Media.

Buri, P., and F. Pellicciotti. 2018. Aspect Controls the Survival of Ice Cliffs on Debris-Covered Glaciers. *Proceedings of the National Academy of Sciences*, 115, 17.

Buri, P., et al. 2015. A grid-based model of backwasting of supraglacial ice cliffs on debris-covered glaciers. *Annals of Glaciology*, 57, 71.

Byers, A. 2005. Contemporary Human Impacts on Alpine Ecosystems in the Sagarmatha (Mt. Everest) National Park, Khumbu, Nepal. *Annals of the Association of American Geographers*, 95, 1.

Carenzo, M., et al. 2016. An Enhanced Temperature Index Model for Debris-Covered Glaciers Accounting for Thickness Effect. *Advances in Water Resources*, 94.

Carlson, T. N., et al. 1995. A New Look at the Simplified Method for Remote Sensing of Daily Evapotranspiration. *Remote Sensing of Environment*, 54, 2.

Carslaw, H. S., and J. C. Jaeger. 1959. *Conduction of Heat in Solids*. Oxford Science Publications.

Cassidy, N. 2009. Ground Penetrating Radar Data Processing, Modelling and Analysis. *Ground Penetrating Radar Theory and Applications*, edited by Harry M Jol, 1st ed., Elsevier.

Cerquera, M. R. P., et al. 2017. UAV for Landmine Detection Using SDR-Based GPR Technology. *Robots Operating in Hazardous Environments*, InTech.

Chudley, T. R., and I. C. Willis. 2018. Glacier Surges in the North-West West Kunlun Shan Inferred from 1972 to 2017 Landsat Imagery. *Journal of Glaciology*.

Collier, E., et al. 2015. Impact of Debris Cover on Glacier Ablation and Atmosphere-Glacier Feedbacks in the Karakoram. *The Cryosphere*, 9, 4.

Collier, E., et al. 2014. Representing Moisture Fluxes and Phase Changes in Glacier Debris Cover Using a Reservoir Approach. *The Cryosphere*, 8, 4.

Conway, H., and L. A. Rasmussen. 2000. Summer Temperature Profiles within Supraglacial Debris on Khumbu Glacier, Nepal. *Debris-Covered Glaciers*, IAHS Publication 264.

Cook, J. C. 1975. Radar Transparencies of Mine and Tunnel Rocks. *Geophysics*, 40, 5.

Corripio, J. G. 2003. Vectorial Algebra Algorithms for Calculating Terrain Parameters from Dems and Solar Radiation Modelling in Mountainous Terrain. *International Journal of Geographical Information Science*, 17, 1.

Courault, D., et al. 2005. Review on Estimation of Evapotranspiration from Remote Sensing Data: From Empirical to Numerical Modeling Approaches. *Irrigation and Drainage Systems*, 19, 3–4.

Crawford, T. M., and C. E. Duchon. 1999. An Improved Parameterization for Estimating Effective Atmospheric Emissivity for Use in Calculating Daytime Downwelling Longwave Radiation. *Journal of Applied Meteorology*, 38, 4.

Dahlke, H. E., et al. 2012. Contrasting Trends in Floods for Two Sub-Arctic Catchments in Northern Sweden - Does Glacier Presence Matter? *Hydrology and Earth System Sciences*, 16, 7.

Dallimore, D. R., and J. L. Davis. 1992. Ground Penetrating Radar Investigations of Massive Ground Ice. *Geological Survey of Canada*, 90–4.

Davis, J. L., and A. P. Annan. 1989. Ground-Penetrating Radar for High-Resolution Mapping of Soil and Rock Stratigraphy. *Geophysical Prospecting*, 37, May 1988.

Degenhardt, J. J., et al. 2003. GPR Survey of a Lobate Rock Glacier in Yankee Boy Basin, Colorado, USA. *Geological Society, London, Special Publications*, 211, 1.

Dehecq, A., et al. 2016. Analysis of Optical Imagery Reveals Regionally Coherent Slowdown in High Mountain Asia in Response to Glacier Thinning. *American Geophysical Union, Fall Meeting 2016, Abstract #C11E-07*.

Dehecq, A., et al. 2015. Deriving Large-Scale Glacier Velocities from a Complete Satellite Archive: Application to the Pamir-Karakoram-Himalaya. *Remote Sensing of Environment*, 162.

Dilley, A. C., and D. M. O'Brien. 1998. Estimating Downward Clear Sky Long-Wave Irradiance at the Surface from Screen Temperature and Precipitable Water. *Quarterly Journal of the Royal Meteorological Society*, 124.

Diolaiuti, G., et al. 2003. Belvedere Glacier, Monte Rosa, Italian Alps: Tongue Thickness and Volume Variations in the Second Half of the 20th Century. *Arctic, Antarctic, and Alpine Research*, 35, 2.

Douglas, J. S., et al. 2016. Incorporating Distributed Debris Thickness in a Glacio-Hydrological Model: Khumbu Himalaya, Nepal. *The Cryosphere Discussions*.

Egli, P., et al. 2016. An Improved Method to Compute Supra Glacial Debris Thickness Using Thermal Satellite Images Together with an Energy Balance Model in the Nepal Himalayas. *EGU General Assembly Conference Abstracts*, 18.

Evatt, G. W., et al. 2015. Glacial Melt under a Porous Debris Layer. *Journal of Glaciology*, 61, 229.

Farinotti, D., et al. 2009. A Method to Estimate Ice Volume and Ice Thickness Distribution of Alpine Glaciers. *Journal of Glaciology*, 55, 191.

Farinotti, D., et al. 2017. How Accurate Are Estimates of Glacier Ice Thickness? Results from ITMIX, the Ice Thickness Models Intercomparison EXperiment. *The Cryosphere*, 11, 2.

Fatichi, S. 2009. *IDW*. MATLAB File Exchange.

Fawcett, T. 2006. An Introduction to ROC Analysis. *Pattern Recognition Letters*, 35, 6.

Fetter, C. 2018. *Applied Hydrogeology*. Waveland Press.

Finsterwalder, S., et al. 1887. Die Zunge Des Sulden-Ferners Im September 1886. *Zeitschrift Des Deutschen Und Oesterreichischen Alpenvereins*, 18.

Foga, S., et al. 2017. Cloud Detection Algorithm Comparison and Validation for Operational Landsat Data Products. *Remote Sensing of Environment*, 194.

Foster, L. A., et al. 2012. A Physically Based Method for Estimating Supraglacial Debris Thickness from Thermal Band Remote-Sensing Data. *Journal of Glaciology*, 58, 210.

Frey, H., et al. 2012. Compilation of a Glacier Inventory for the Western Himalayas from Satellite Data: Methods, Challenges, and Results. *Remote Sensing of Environment*, 124.

Fujita, K. 2008. Effect of Precipitation Seasonality on Climatic Sensitivity of Glacier Mass Balance. *Earth and Planetary Science Letters*, 276, 1–2.

Fujita, K., and A. Sakai. 2014. Modelling Runoff from a Himalayan Debris-Covered Glacier. *Hydrology and Earth System Sciences*, 18, 7.

Fyffe, C. L., et al. 2014. A Distributed Energy-Balance Melt Model of an Alpine Debris-Covered Glacier. *Journal of Glaciology*, 60, 221.

Gades, A., et al. 2000. Radio Echo-Sounding through Supraglacial Debris on Lirung and Khumbu Glaciers, Nepal Himalayas. *Debris-Covered Glaciers*, 264, 264, IAHS Publication 264.

Gardelle, J., et al. 2013. Region-Wide Glacier Mass Balances over the Pamir-Karakoram-Himalaya during 1999-2011. *The Cryosphere*, 7, 4.

Gardner, A. S., et al. 2013. A Reconciled Estimate of Glacier Contributions to Sea Level Rise: 2003 to 2009. *Science*, 340, 6134.

Gärtner-Roer, I., et al. 2014. A Database of Worldwide Glacier Thickness Observations. *Global and Planetary Change*, 122.

Gerace, A., and M. Montanaro. 2017. Derivation and Validation of the Stray Light Correction Algorithm for the Thermal Infrared Sensor Onboard Landsat 8. *Remote Sensing of Environment*, 191.

Gibson, M. J., et al. 2017. Changes in Glacier Surface Cover on Baltoro Glacier, Karakoram, North Pakistan, 2001–2012. *Journal of Maps*, 13, 2.

Gibson, M. J., et al. 2017. Temporal Variations in Supraglacial Debris Distribution on Baltoro Glacier, Karakoram between 2001 and 2012. *Geomorphology*, 295, November.

Gillespie, A., et al. 1998. A Temperature and Emissivity Separation Algorithm for Advanced Spaceborne Thermal Emission and Reflection Radiometer (ASTER) Images. *IEEE Transactions on Geoscience and Remote Sensing*, 36, 4.

Gómez-Gutiérrez, Á., et al. 2011. Testing the Quality of Open-Access DEMs and Their Derived Attributes in Spain : SRTM , GDEM and PNOA DEM. *Geomorphometry*, December 2015.

Goodsell, B., et al. 2005. The Structural Glaciology of a Temperate Valley Glacier : Haut Glacier d ' Arolla , Valais , Switzerland. *Arctic, Antarctic, and Alpine Research*, 37, 2.

Groos, A. R., et al. 2017. A First Attempt To Model Region-Wide Glacier Surface Mass Balances in the Karakoram: Findings and Future Challenges. *Geografia Fisica e Dinamica Quaternaria*, 40, December.

Gusmeroli, A., et al. 2015. Active Layer Stratigraphy and Organic Layer Thickness at a Thermokarst Site in Arctic Alaska Identified Using Ground Penetrating Radar. *Arctic, Antarctic, and Alpine Research*, 47, 2.

Hagg, W., et al. 2008. Sub-Debris Melt Rates on Southern Inylchek Glacier, Central Tian Shan. *Geografiska Annaler, Series A: Physical Geography*, 90 A, 1.

Hales, T. C., and J. J. Roering. 2007. Climatic Controls on Frost Cracking and Implications for the Evolution of Bedrock Landscapes. *Journal of Geophysical Research: Earth Surface*, 112, 2.

Hambrey, M. J., et al. 2008. Sedimentological, Geomorphological and Dynamic Context of Debris-Mantled Glaciers, Mount Everest (Sagarmatha) Region, Nepal. *Quaternary Science Reviews*, 28, 11–12.

Han, H., et al. 2006. A Simple Model to Estimate Ice Ablation under a Thick Debris Layer. *Journal of Glaciology*, 52, 179.

Hartmann, D. L. 2013. *Global Physical Climatology*. Newnes.

Hay, J. E., and B. B. Fitzharris. 1988. A Comparison of the Energy-Balance and Bulk-Aerodynamic Approaches for Estimating Glacier Melt. *Journal of Glaciology*, 34, 117.

Heid, T., and A. Kääb. 2012. Repeat Optical Satellite Images Reveal Widespread and Long Term Decrease in Land-Terminating Glacier Speeds. *The Cryosphere*, 6, 2.

Heimsath, A. M., et al. 2012. Soil Production Limits and the Transition to Bedrock-Dominated Landscapes. *Nature Geoscience*, 5, 3.

Herreid, S., and F. Pellicciotti. 2018. Automated Detection of Ice Cliffs within Supraglacial Debris Cover. *The Cryosphere*, 12, 5.

Hewitt, K. 2011. Glacier Change, Concentration, and Elevation Effects in the Karakoram Himalaya, Upper Indus Basin. *Mountain Research and Development*, 31, 3.

Hewitt, K. 2005. The Karakoram Anomaly? Glacier Expansion and the "Elevation Effect", Karakoram Himalaya. *Mountain Research and Development*, 25, 4.

Hock, R. 1999. A Distributed Temperature-Index Ice- and Snowrnelt Model Including Potential Direct Solar Radiation. *Journal of Glaciology*, 45, 149.

Hock, R. 2003. Temperature Index Melt Modelling in Mountain Areas. *Journal of Hydrology*, 282, 1–4.

Hock, R., and C. Noetzli. 1997. Area Melt and Discharge Modelling of Storglaciaren, Sweden. *Annals of Glaciology*, 24.

Hooke, R. 2005. *Principles of Glacier Mechanics*. Cambridge University Press.

Huang, L., et al. 2018. Analysis of Thickness Changes and the Associated Driving Factors on a Debris-Covered Glacier in the Tienshan Mountain. *Remote Sensing of Environment*, 206.

Huang, L., et al. 2017. Estimation of Supraglacial Debris Thickness Using a Novel Target Decomposition on L-Band Polarimetric SAR Images in the Tianshan Mountains. *Journal of Geophysical Research: Earth Surface*, 122, 4.

Hulley, G. C., et al. 2015. The ASTER Global Emissivity Dataset (ASTER GED): Mapping Earth's Emissivity at 100 Meter Spatial Scale. *Geophysical Research Letters*, 42, 19.

Huss, M., et al. 2007. Retreat Scenarios of Unteraargletscher, Switzerland, Using a Combined Ice-Flow Mass-Balance Model. *Arctic Antarctic and Alpine Research*, 39, 3.

Huss, M., and D. Farinotti. 2012. Distributed Ice Thickness and Volume of All Glaciers around the Globe. *Journal of Geophysical Research: Earth Surface*, 117, 4.

Huss, M., and R. Hock. 2015. A New Model for Global Glacier Change and Sea-Level Rise. *Frontiers in Earth Science*, 3, September.

Immerzeel, W. W., et al. 2010. Climate Change Will Affect the Asian Water Towers. *Science*, 328, 5984.

Immerzeel, W. W., et al. 2014. High-Resolution Monitoring of Himalayan Glacier Dynamics Using

Unmanned Aerial Vehicles. *Remote Sensing of Environment*, 150, June.

Immerzeel, W. W., et al. 2012. Hydrological Response to Climate Change in a Glaciated Catchment in the Himalayas. *Climatic Change*, 110, 3–4.

Immerzeel, W. W., et al. 2013. Rising River Flows throughout the Twenty-First Century in Two Himalayan Glacierized Watersheds. *Nature Geoscience*, 6, 9.

Inoue, J., and M. Yoshida. 1980. Ablation and Heat Exchange over the Khumbu Glacier. *Journal of the Japanese Society of Snow and Ice*, 41, Special.

IPCC. *Global Warming of 1.5°C. Summary for Policymakers*. October 2018.

Jacobsen, D., et al. 2012. Biodiversity under Threat in Glacier-Fed River Systems. *Nature Climate Change*, 2, 5.

Jakob Fürst, J., et al. 2017. Application of a Two-Step Approach for Mapping Ice Thickness to Various Glacier Types on Svalbard. *The Cryosphere*, 11, 5.

Jarvis, A., et al. 2008. *Hole-Filled SRTM for the Globe Version 4*.

Jiménez-Muñoz, J. C., et al. 2014. Land Surface Temperature Retrieval Methods from Landsat-8 Thermal Infrared Sensor Data. *Geoscience and Remote Sensing Letters, IEEE*, 11, 10.

Jol, H. M., and C. S. Bristow. 2003. Ground Penetrating Radar in Sediments: Advice on Data Collection, Basic Processing and Interpretation, a Good Practice Guide. *Ground Penetrating Radar in Sediments*, 211, 1.

Juen, M., et al. 2014. Impact of Varying Debris Cover Thickness on Ablation: A Case Study for Koxkar Glacier in the Tien Shan. *The Cryosphere*, 8, 2.

Juszak, I., and F. Pellicciotti. 2013. A Comparison of Parameterizations of Incoming Longwave Radiation over Melting Glaciers: Model Robustness and Seasonal Variability. *Journal of Geophysical Research Atmospheres*, 118, 8.

Kääb, A., et al. 2015. Brief Communication: Contending Estimates of 2003-2008 Glacier Mass Balance over the Pamir-Karakoram-Himalaya. *Cryosphere*, 9, 2.

Kääb, A., et al. 2012. Contrasting Patterns of Early Twenty-First-Century Glacier Mass Change in the Himalayas. *Nature*, 488, 7412.

Kaser, G., et al. 2010. Contribution Potential of Glaciers to Water Availability in Different Climate Regimes. *Proceedings of the National Academy of Sciences of the United States of America*, 107, 47.

Kayastha, R. B., et al. 2000. Practical Prediction of Ice Melting beneath Various Thickness of Debris Cover on Khumbu Glacier, Nepal, Using a Positive Degree-Day Factor. *Debris-Covered Glaciers*, IAHS Publication 264.

Kearney, K. 2016. *Inpolygons*. MATLAB File Exchange.

Kellerer-Pirklbauer, A. 2008. The Supraglacial Debris System at the Pasterze Glacier, Austria: Spatial Distribution, Characteristics and Transport of Debris. *Zeitschrift Für Geomorphologie*, 52, 1.

King, O., et al. 2018. Contrasting Geometric and Dynamic Evolution of Lake and Land-Terminating Glaciers in the Central Himalaya. *Global and Planetary Change*, 167, November 2017.

King, O., et al. 2017. Spatial Variability in Mass Loss of Glaciers in the Everest Region, Central Himalayas, between 2000 and 2015. *The Cryosphere*, 11, 1.

Kirkbride, M. P., and P. Deline. 2013. The Formation of Supraglacial Debris Covers by Primary Dispersal from Transverse Englacial Debris Bands. *Earth Surface Processes and Landforms*, 38, 15.

Knoll, C., and H. Kerschner. 2009. An Airborne Laser Scanner Data Based Glacier Inventory for South Tyrol , Italy. *Annals of Glaciology*, 50, 53.

Koblick, D. 2013. *SolarAzEl*. MATLAB File Exchange.

Konrad, S. K., and N. F. Humphrey. 2000. Steady-State Flow Model of Debris-Covered Glaciers (Rock Glaciers). *Debris-Covered Glaciers*, IAHS Publication 264.

Konzelmann, T., and A. Ohmura. 1995. Radiative Fluxes and Their Impact on the Energy Balance of the Greenland Ice Sheet. *Journal of Glaciology*, 41, 139.

Kraaijenbrink, P., et al. 2016. Seasonal Surface Velocities of a Himalayan Glacier Derived by Automated Correlation of Unmanned Aerial Vehicle Imagery. *Annals of Glaciology*, 57, 71.

Kraaijenbrink, P. D. A., et al. 2017. Impact of a Global Temperature Rise of 1.5 Degrees Celsius on Asia's Glaciers. *Nature*, 549.

Kuhn, M., et al. 1997. Eastern Alpine Glacier Activity and Climatic Records since 1860. *Annals of Glaciology*, 24.

Lambrecht, A., et al. 2011. A Comparison of Glacier Melt on Debris-Covered Glaciers in the Northern and Southern Caucasus. *The Cryosphere*, 5, 3.

Lapazaran, J. J., et al. 2016. On the Errors Involved in Ice-Thickness Estimates II: Errors in Digital Elevation Models of Ice Thickness. *Journal of Glaciology*, 62, 236.

Lawson, D. 1979. *Semdimentological Analysis of the Western Terminus Region of the Matanuska Glacier, Alaska*.

Leclercq, P. W., and J. Oerlemans. 2012. Global and Hemispheric Temperature Reconstruction from Glacier Length Fluctuations. *Climate Dynamics*, 38, 5–6.

Lejeune, Y., et al. 2013. A Physically Based Model of the Year-Round Surface Energy and Mass Balance of Debris-Covered Glaciers. *Journal of Glaciology*, 59, 214.

Liang, S. 2001. Narrowband to Broadband Conversions of Land Surface Albedo I Algorithms. *Remote Sensing of Environment*, 76, 2.

Lønne, I., and T. Lauritsen. 1996. The Architecture of a Modern Push-Moraine at Svalbard as Inferred from Ground-Penetrating Radar Measurements. *Arctic and Alpine Research*, 28, 4.

Machguth, H., et al. 2008. Exploring Uncertainty in Glacier Mass Balance Modelling with Monte Carlo Simulation. *The Cryosphere*, 2, 2.

Machguth, H., et al. 2006. Strong Spatial Variability of Snow Accumulation Observed with Helicopter-Borne GPR on Two Adjacent Alpine Glaciers. *Geophysical Research Letters*, 33, 13.

Marzeion, B., et al. 2012. Past and Future Sea-Level Change from the Surface Mass Balance of Glaciers. *The Cryosphere*, 6, 6.

Mattson, L. E., et al. 1993. Ablation on Debris Covered Glaciers: An Example From the Rakhiot Glacier, Punjab, Himalaya. *Snow and Glacier Hydrology*, edited by J. G. Young, IAHS Publication 218.

Maussion, F., et al. 2014. Precipitation Seasonality and Variability over the Tibetan Plateau as Resolved by the High Asia Reanalysis. *Journal of Climate*, 27, 5.

Maussion, F., et al. 2018. The Open Global Glacier Model (OGGM) v1.0. *Geoscientific Model Development Discussions*.

Mayer, C., et al. 2006. Glaciological Characteristics of the Ablation Zone of Baltoro Glacier, Karakoram, Pakistan. *Annals of Glaciology*, 43.

McCarthy, M., et al. 2017. Ground-Penetrating Radar Measurements of Debris Thickness on Lirung Glacier, Nepal. *Journal of Glaciology*, 63, 239.

Mertes, J. R., et al. 2016. A Conceptual Model of Supra-Glacial Lake Formation on Debris-Covered Glaciers Based on GPR Facies Analysis. *Earth Surface Processes and Landforms*, 42.

Mihalcea, C., et al. 2006. Ice Ablation and Meteorological Conditions on the Debris-Covered Area of Baltoro Glacier, Karakoram, Pakistan. *Annals of Glaciology*, 43.

Mihalcea, C., et al. 2008. Spatial Distribution of Debris Thickness and Melting from Remote-Sensing and Meteorological Data, at Debris-Covered Baltoro Glacier, Karakoram, Pakistan. *Annals of Glaciology*, 48, 1.

Mihalcea, C., et al. 2008. Using ASTER Satellite and Ground-Based Surface Temperature Measurements to Derive Supraglacial Debris Cover and Thickness Patterns on Miage Glacier (Mont Blanc Massif, Italy). *Cold Regions Science and Technology*, 52, 3.

Miles, E. S., et al. 2017. Highly Variable Aerodynamic Roughness Length (Z0) for a Hummocky Debris-Covered Glacier. *Journal of Geophysical Research: Atmospheres*, 122, 16.

Miles, E. S., et al. 2017. Pond Dynamics and Supraglacial-Englacial Connectivity on Debris-Covered Lirung Glacier, Nepal. *Frontiers in Earth Science*, 5, September.

Miles, E. S., et al. 2016. Refined Energy-Balance Modelling of a Supraglacial Pond, Langtang Khola, Nepal. *Annals of Glaciology*, 57, 71.

Miles, E. S., et al. 2017. Spatial, Seasonal and Interannual Variability of Supraglacial Ponds in the Langtang Valley of Nepal, 1999-2013. *Journal of Glaciology*, 63, 237.

Miles, E. S., et al. 2018. Surface Pond Energy Absorption Across Four Himalayan Glaciers Accounts for 1/8 of Total Catchment Ice Loss. *Geophysical Research Letters*, 45, 19.

Milner, A. M., et al. 2017. Glacier Shrinkage Driving Global Changes in Downstream Systems. *Proceedings of the National Academy of Sciences*, 114, 37.

Mölg, T., et al. 2014. Mid-Latitude Westerlies as a Driver of Glacier Variability in Monsoonal High Asia. *Nature Climate Change*, 4, 1.

Mölg, T., and D. R. Hardy. 2004. Ablation and Associated Energy Balance of a Horizontal Glacier Surface on Kilimanjaro. *Journal of Geophysical Research D: Atmospheres*, 109, 16.

Mölg, T., and G. Kaser. 2011. A New Approach to Resolving Climate-Cryosphere Relations: Downscaling Climate Dynamics to Glacier-Scale Mass and Energy Balance without Statistical Scale Linking. *Journal of Geophysical Research Atmospheres*, 116, 16.

Moore, P. L. 2018. Stability of Supraglacial Debris. *Earth Surface Processes and Landforms*, 43, 1.

Moorman, B. J., et al. 2003. Imaging Periglacial Conditions with Ground-Penetrating Radar. *Permafrost and Periglacial Processes*, 14, 4.

Moorman, B. J., and F. A. Michel. 2000. The Burial of Ice in the Proglacial Environment on Bylot Island, Arctic Canada. *Permafrost and Periglacial Processes*, 11, 3.

Munro, D. S., and G. J. Young. 1982. An Operational Net Shortwave Radiation Model for Glacier Basins. *Water Resources Research*, 18, 2.

Murray, F. W. 1967. On the Computation of Saturation Vapor Pressure. *Journal of Applied Meteorology*, 6, 1.

Nagai, H., et al. 2013. Southwest-Facing Slopes Control the Formation of Debris-Covered Glaciers in the Bhutan Himalaya. *The Cryosphere*, 7, 4.

Nakawo, M., et al. 2000. *Debris-Covered Glaciers*. IAHS Publication 264.

Nakawo, M., et al. 1986. Processes Which Distribute Supraglacial Debris on the Khumbu Glacier, Nepal Himalaya. *Annals of Glaciology*, 8.

Nakawo, M. 1979. Supraglacial Debris of G2 Glacier in Hidden Valley, Mukut Himal, Nepal. *Journal of Glaciology*, 22, 87.

Nakawo, M., and B. Rana. 1999. Estimate of Ablation Rate of Glacier Ice under a Supraglacial Debris Layer. *Geografiska Annaler, Series A: Physical Geography*, 81, 4.

Nakawo, M., and G. J. Young. 1982. Estimate of Glacier Ablation under a Debris Layer from Surface Temperature and Meteorological Variables. *Journal of Glaciology*, 28, 98.

Neal, A. 2004. Ground-Penetrating Radar and Its Use in Sedimentology: Principles, Problems and Progress. *Earth-Science Reviews*, 66, 3–4.

Nicholson, L., et al. 2018. Supraglacial Debris Thickness Variability: Impact on Ablation and Relation to Terrain Properties. *The Cryosphere*, 12.

Nicholson, L., and D. I. Benn. 2006. Calculating Ice Melt beneath a Debris Layer Using Meteorological Data. *Journal of Glaciology*, 52, 178.

Nicholson, L., and D. I. Benn. 2012. Properties of Natural Supraglacial Debris in Relation to Modelling Sub-Debris Ice Ablation. *Earth Surface Processes and Landforms*, 38, 5.

Nicholson, L., and J. Mertes. 2017. Thickness Estimation of Supraglacial Debris above Ice Cliff Exposures Using a High-Resolution Digital Surface Model Derived from Terrestrial Photography. *Journal of Glaciology*, 63, 242.

Nobes, D., et al. 1994. Ground-Penetrating Radar Profiles of Rubble-Covered Temperate Glaciers: Results from the Tasman and Mueller Glaciers of the Southern Alps of New Zealand. *SEG Technical Program Expanded Abstracts 1994*, Society of Exploration Geophysicists.

Nuimura, T., et al. 2017. Downwasting of the Debris-Covered Area of Lirung Glacier in Langtang Valley, Nepal Himalaya, from 1974 to 2010. *Quaternary International*, 455.

Nuimura, T., et al. 2012. Elevation Changes of Glaciers Revealed by Multitemporal Digital Elevation Models Calibrated by GPS Survey in the Khumbu Region, Nepal Himalaya, 1992-2008. *Journal of Glaciology*, 58, 210.

Nuimura, T., et al. 2011. Temporal Changes in Elevation of the Debris-Covered Ablation Area of Khumbu Glacier in the Nepal Himalaya since 1978. *Arctic, Antarctic, and Alpine Research*, 43, 2.

Oerlemans, J. 1992. Climate Sensitivity of Glaciers in Southern Norway: Application of an Energy-Balance Model to Nigardsbreen, Hellstugubreen and Alfotbreen. *Journal of Glaciology*, 38, 129.

Oerlemans, J. 2005. Extracting a Climate Signal from 169 Glacier Records. *Science*, 308, 5722.

Oerlemans, J. 2001. *Glaciers and Climate Change: A Meteorologist's View*. CRC Press.

Oestrem, G. 1959. Ice Melting under a Thin Layer of Moraine, and the Existence of Ice Cores in Moraine Ridges. *Geografiska Annaler*, 41, 4.

Oke, T. R. 2002. *Boundary Layer Climates*. Routledge.

Owen, L. A., et al. 2003. Contemporary Sediment Production and Transfer in High-Altitude Glaciers. *Sedimentary Geology*, 155, 1–2.

Peixoto, J. P., and A. H. Oort. 1996. The Climatology of Relative Humidity in the Atmosphere. *Journal of Climate*, 9, 12.

Pellicciotti, F., et al. 2005. An Enhanced Temperature-Index Glacier Melt Model Including the Shortwave Radiation Balance: Development and Testing for Haut Glacier d'Arolla, Switzerland. *Journal of Glaciology*, 51, 175.

Pellicciotti, F., et al. 2015. Mass-Balance Changes of the Debris-Covered Glaciers in the Langtang Himal, Nepal, from 1974 to 1999. *Journal of Glaciology*, 61, 226.

Pellicciotti, F., et al. 2009. On the Role of Subsurface Heat Conduction in Glacier Energy-Balance Modelling. *Annals of Glaciology*, 50, 50.

Pellicciotti, F., et al. 2009. On the Role of Subsurface Heat Conduction in Glacier Energy-Balance Modelling. *Annals of Glaciology*, 50, 50.

Pellicciotti, F., et al. 2011. Transmission of Solar Radiation through Clouds on Melting Glaciers: A Comparison of Parameterizations and Their Impact on Melt Modelling. *Journal of Glaciology*, 57, 202.

Pellikka, P., and W. G. Rees. 2009. *Remote Sensing of Glaciers: Techniques for Topographic, Spatial, and Thematic Mapping of Glaciers*. CRC Press.

Petropoulos, G., et al. 2009. A Review of Ts/VI Remote Sensing Based Methods for the Retrieval of Land Surface Energy Fluxes and Soil Surface Moisture. *Progress in Physical Geography*, 33, 2.

Pfeffer, W. T., et al. 2014. The Randolph Glacier Inventory: A Globally Complete Inventory of Glaciers. *Journal of Glaciology*, 60, 221.

Plewes, L. A., and B. Hubbard. 2001. A Review of the Use of Radio-Echo Sounding in Glaciology. *Progress in Physical Geography*, 25, 2.

Potter, E. R., et al. 2018. Dynamical Drivers of the Local Wind Regime in a Himalayan Valley. *Journal of Geophysical Research: Atmospheres*, 123.

Prata, A. J. 1996. A New Long-Wave Formula for Estimating Downward Clear-Sky Radiation at the Surface. *Quarterly Journal of the Royal Meteorological Society*, 122, 533.

Pratap, B., et al. 2015. Influence of Debris Cover and Altitude on Glacier Surface Melting: A Case Study on Dokriani Glacier, Central Himalaya, India. *Annals of Glaciology*, 56, 70.

Pritchard, H. D. 2017. Asia's Glaciers Are a Regionally Important Buffer against Drought. *Nature*, 545, 7653.

Purdie, H. 2013. Glacier Retreat and Tourism: Insights from New Zealand. *Mountain Research and Development*, 33, 4.

Quincey, D. J., et al. 2017. Evaluating Morphological Estimates of the Aerodynamic Roughness of Debris Covered Glacier Ice. *Earth Surface Processes and Landforms*, 42, 15.

Quincey, D. J., et al. 2017. The Changing Water Cycle: The Need for an Integrated Assessment of the Resilience to Changes in Water Supply in High-Mountain Asia. *Wiley Interdisciplinary Reviews: Water*, 5, February.

Quincey, D. J., et al. 2009. Ice Velocity and Climate Variations for Baltoro Glacier, Pakistan. *Journal of Glaciology*, 55, 194.

Quincey, D. J., et al. 2011. Karakoram Glacier Surge Dynamics. *Geophysical Research Letters*, 38, 18.

Quincey, D. J., et al. 2005. Optical Remote Sensing Techniques in High-Mountain Environments: Application to Glacial Hazards. *Progress in Physical Geography*, 29, 4.

Quincey, D. J., et al. 2009. Quantification of Everest Region Glacier Velocities between 1992 and 2002, Using Satellite Radar Interferometry and Feature Tracking. *Journal of Glaciology*, 55, 192.

Rabbani, A., and S. Ayatollahi. 2015. Comparing Three Image Processing Algorithms To Estimate the Grain-Size Distribution of Porous Rocks From Binary 2D Images and Sensitivity Analysis of the Grain Overlapping Degree. *Special Topics & Reviews in Porous Media: An International Journal*, 6, 1.

Radić, V., et al. 2014. Regional and Global Projections of Twenty-First Century Glacier Mass Changes in Response to Climate Scenarios from Global Climate Models. *Climate Dynamics*, 42, 1–2.

Radić, V., and R. Hock. 2006. Modeling Future Glacier Mass Balance and Volume Changes Using ERA-40 Reanalysis and Climate Models: A Sensitivity Study at Storglaciaren, Sweden. *Journal of Geophysical Research: Earth Surface*, 111, 3.

Ragettli, S., et al. 2015. Unraveling the Hydrology of a Himalayan Catchment through Integration of High Resolution in Situ Data and Remote Sensing with an Advanced Simulation Model. *Advances in Water Resources*, 78.

Rana, B., et al. 1998. Glacier Ablation Under Debris Cover: Field Observations on Lirung Glacier, Nepal Himalayas. *Proceedings of the International Conference on Ecohydrology of High Mountain Areas*.

Reddy, S. M., et al. 1993. Structural Evolution of the High Himalayan Gneiss Sequence, Langtang Valley, Nepal. *Geological Society, London, Special Publications*, 74, 1.

Reid, T. D., et al. 2012. Including Debris Cover Effects in a Distributed Model of Glacier Ablation. *Journal of Geophysical Research Atmospheres*, 117, 17.

Reid, T. D., and B. W. Brock. 2010. An Energy-Balance Model for Debris-Covered Glaciers Including Heat Conduction through the Debris Layer. *Journal of Glaciology*, 56, 199.

Reynolds, J. 2011. *An Introduction to Applied and Environmental Geophysics*. 2nd ed., John Wiley & Sons.

Reznichenko, N., et al. 2010. Effects of Debris on Ice-Surface Melting Rates: An Experimental Study. *Journal of Glaciology*, 56, 197.

RGI Consortium. 2017. *Randolph Glacier Inventory – A Dataset of Global Glacier Outlines: Version 6.0: Technical Report*. Global Land Ice Measurements from Space, Colorado, USA.

Richardson, J. M., and M. S. Brook. 2010. Ablation of Debris-Covered Ice: Some Effects of the 25 September 2007 Mt Ruapehu Eruption. *Journal of the Royal Society of New Zealand*, 40, 2.

Richardson, S., and J. Reynolds. 2000. An Overview of Glacial Hazards. *Quaternary International*, 6566.

Rounce, D. R., et al. 2015. Debris-Covered Glacier Energy Balance Model for Imja-Lhotse Shar Glacier in the Everest Region of Nepal. *The Cryosphere*, 9.

Rounce, D. R., et al. 2018. Quantifying Debris Thickness of Debris-Covered Glaciers in the Everest

Region of Nepal Through Inversion of a Subdebris Melt Model. *Journal of Geophysical Research: Earth Surface*, 123.

Rounce, D. R., and D. C. McKinney. 2014. Debris Thickness of Glaciers in the Everest Area (Nepal Himalaya) Derived from Satellite Imagery Using a Nonlinear Energy Balance Model. *The Cryosphere*, 8, 1.

Rowan, A. V., et al. 2015. Modelling the Feedbacks between Mass Balance, Ice Flow and Debris Transport to Predict the Response to Climate Change of Debris-Covered Glaciers in the Himalaya. *Earth and Planetary Science Letters*, 430.

Rowan, A. V., et al. 2017. Multiannual Observations and Modelling of Seasonal Thermal Profiles through Supraglacial Debris in the Central Himalaya. *The Cryosphere Discussions*.

Rye, C. J., et al. 2010. Modeling the Surface Mass Balance of a High Arctic Glacier Using the ERA-40 Reanalysis. *Journal of Geophysical Research: Earth Surface*, 115, F2.

Sakai, A., et al. 2002. Characteristics Balance of Ice Cliffs on Debris-Covered Distribution Energy Glaciers , Nepal Himalaya. *Arctic, Antarctic, and Alpine Research*, 34, 1.

Sakai, A., et al. 2000. Role of Supraglacial Ponds in the Ablation Process of a Debris-Covered Glacier in the Nepal Himalayas. *Debris-Covered Glaciers*, IAHS Publication 264.

Santillan, J. R., and M. Makinano-Santillan. 2016. Vertical Accuracy Assessment of 30-M Resolution ALOS, ASTER, and SRTM Global DEMS over Northeastern Mindanao, Philippines. *International Archives of the Photogrammetry, Remote Sensing and Spatial Information Sciences - ISPRS Archives*, 41, June.

Sass, O. 2006. Determination of the Internal Structure of Alpine Talus Deposits Using Different Geophysical Methods (Lechtaler Alps, Austria). *Geomorphology*, 80, 1.

Sass, O., and K. Wollny. 2001. Investigations Regarding Alpine Talus Slopes Using Ground-Penetrating Radar (GPR) in the Bavarian Alps, Germany. *Earth Surface Processes and Landforms*, 26, 10.

Schannwell, C., et al. 2014. An Automatic Approach to Delineate the Cold-Temperate Transition Surface with Ground-Penetrating Radar on Polythermal Glaciers. *Annals of Glaciology*, 55, 67.

Schauwecker, S., et al. 2015. Remotely Sensed Debris Thickness Mapping of Bara Shigri Glacier,

Indian Himalaya. *Journal of Glaciology*, 61, 228.

Scherler, D., et al. 2011. Hillslope-Glacier Coupling: The Interplay of Topography and Glacial Dynamics in High Asia. *Journal of Geophysical Research: Earth Surface*, 116, 2.

Scherler, D., et al. 2008. Remote Sensing of Environment Glacier-Surface Velocities in Alpine Terrain from Optical Satellite Imagery — Accuracy Improvement and Quality Assessment. *Remote Sensing of Environment*, 112, 10.

Scherler, D., et al. 2011. Spatially Variable Response of Himalayan Glaciers to Climate Change Affected by Debris Cover. *Nature Geoscience*, 4, 3.

Sensors and Software. 1999. *Technical Manual 24. PulseEKKO 1000 RUN. User's Guide v1.2*.

Sharp, R. P. 1949. Studies of Superglacial Debris on Valley Glaciers. *American Journal of Science*, 247, 5.

Shaw, T. E., et al. 2016. Air Temperature Distribution and Energy-Balance Modelling of a Debris-Covered Glacier. *Journal of Glaciology*, 62, 231.

Shea, J. M., P. Wagnon, et al. 2015. A Comparative High-Altitude Meteorological Analysis from Three Catchments in the Nepalese Himalaya. *International Journal of Water Resources Development*, 31, 2.

Shea, J. M., W. W. Immerzeel, et al. 2015. Modelling Glacier Change in the Everest Region, Nepal Himalaya. *The Cryosphere*, 9, 3.

Shean, D. 2017. *High Mountain Asia 8-Meter DEM Mosaics Derived from Optical Imagery, Version 1*. Boulder, Colorado USA. NASA National Snow and Ice Data Center Distributed Active Archive Center.

Shroder, J. F., et al. 2000. Debris-Covered Glaciers and Rock Glaciers in the Nanga Parbat Himalaya, Pakistan. *Geografiska Annaler, Series A: Physical Geography*, 82, 1.

Sinisalo, A., et al. 2003. Snow-Accumulation Studies in Antarctica with Ground-Penetrating Radar Using 50, 100 and 800 MHz Antenna Frequencies. *Annals of Glaciology*, 37.

Soncini, A., et al. 2016. Future Hydrological Regimes and Glacier Cover in the Everest Region: The Case Study of the Upper Dudh Koshi Basin. *Science of the Total Environment*, 565, June, Elsevier B.V.

Spencer, J. W. 1971. Fourier Series Representation of the Position of the Sun. *Search*, 2, 5.

Steiner, J. F., et al. 2015. Modelling Ice-Cliff Backwasting on a Debris-Covered Glacier in the Nepalese Himalaya. *Journal of Glaciology*, 61, 229.

Steiner, J. F., et al. 2018. The Importance of Turbulent Fluxes in the Surface Energy Balance of a Debris-Covered Glacier in the Himalayas. *Frontiers in Earth Science*, 6, October.

Steiner, J. F., and F. Pellicciotti. 2016. Variability of Air Temperature over a Debris-Covered Glacier in the Nepalese Himalaya. *Annals of Glaciology*, 57, 71.

Strasser, U., et al. 2004. Spatial and Temporal Variability of Meteorological Variables at Haut Glacier d'Arolla (Switzerland) during the Ablation Season 2001: Measurements and Simulations. *Journal of Geophysical Research: Atmospheres*, 109, D3.

Suzuki, R., et al. 2007. Spatial Distribution of Thermal Properties on Debris-Covered Glaciers in the Himalayas Derived from ASTER Data. *Bulletin of Glaciological Research*, 24.

Takeuchi, Y., et al. 2000. Characteristics of Ablation and Heat Balance in Debris-Free and Debris-Covered Areas on Khumbu Glacier, Nepal Himalayas, in the Pre-Monsoon Season. *IAHS Publication*, 264, 2.

Thakuri, S., et al. 2014. Tracing Glacier Changes since the 1960s on the South Slope of Mt. Everest (Central Southern Himalaya) Using Optical Satellite Imagery. *The Cryosphere*, 8, 4.

Thompson, S., et al. 2016. Stagnation and Mass Loss on a Himalayan Debris-Covered Glacier: Processes, Patterns and Rates. *Journal of Glaciology*, 62, 233.

Thompson, S. S., et al. 2012. A Rapidly Growing Moraine-Dammed Glacial Lake on Ngozumpa Glacier, Nepal. *Geomorphology*, 145–146.

Unsworth, M. H., and J. L. Monteith. 1975. Long-Wave Radiation at the Ground. *Quarterly Journal of the Royal Meteorological Society*, 101, 430.

Varnes, D. J. 1978. Slope Movements Types and Processes. *Landslides Analysis and Control*, edited by R.L. Schuster and R.J. Krizek, National Academy Press.

Vincent, C., et al. 2016. Reduced melt on debris-covered glaciers: investigations from Changri Nup Glacier, Nepal. *The Cryosphere*, 10.

Wagnon, P., et al. 2007. Four Years of Mass Balance on Chhota Shigri Glacier, Himachal Pradesh, India, a New Benchmark Glacier in the Western Himalaya. *Journal of Glaciology*, 53, 183.

Wagnon, P., et al. 2013. Seasonal and Annual Mass Balances of Mera and Pokalde Glaciers (Nepal Himalaya) since 2007. *The Cryosphere*, 7, 6.

Wang, L., et al. 2011. Spatial Distribution of the Debris Layer on Glaciers of the Tuomuer Peak, Western Tian Shan. *Journal of Earth Science*, 22, 4.

Watson, C. S., et al. 2016. The Dynamics of Supraglacial Water Storage in the Everest Region, Central Himalaya. *Global and Planetary Change*, 142, .

Wei, Y., et al. 2010. Influence of Supraglacial Debris on Summer Ablation and Mass Balance in the 24k Glacier, Southeast Tibetan Plateau. *Geografiska Annaler, Series A: Physical Geography*, 92, 3.

Westoby, M. J., et al. 2012. "Structure-from-Motion" Photogrammetry: A Low-Cost, Effective Tool for Geoscience Applications. *Geomorphology*, 179.

Wilson, N. J., et al. 2014. Mapping and Interpretation of Bed-Reflection Power from a Surge-Type Polythermal Glacier, Yukon, Canada. *Annals of Glaciology*, 55, 67.

Wirbel, A., et al. 2018. Modelling Debris Transport within Glaciers by Advection in a Full-Stokes Ice Flow Model. *The Cryosphere*, 12, 1.

Woodward, J., and M. Burke. 2007. Applications of GPR to Glacial and Frozen Materials. *Journal of Environmental & Engineering Geophysics*, 12, 1.

World Economic Forum. 2015. *Global Risks 2015: 10th Edition*.

Wu, Z., and S. Y. Liu. 2012. Imaging the Debris Internal Structure and Estimating the Effect of Debris Layer on Ablation of Glacier Ice. *Journal of the Geological Society of India*, 80, 6.

Xu, B., et al. 2009. Black Soot and the Survival of Tibetan Glaciers. *Proceedings of the National Academy of Sciences*, 106, 52.

Yilmaz, Ö. 2001. *Seismic Data Analysis*. Vol. 1, Society of Exploration Geophysicists.

Zhang, G., et al. 2015. An Inventory of Glacial Lakes in the Third Pole Region and Their Changes in Response to Global Warming. *Global and Planetary Change*, 131.

Zhang, Y., et al. 2011. Distribution of Debris Thickness and Its Effect on Ice Melt at Hailuogou Glacier, Southeastern Tibetan Plateau, Using in Situ Surveys and ASTER Imagery. *Journal of Glaciology*, 57, 206.

Zhu, Z., et al. 2015. Improvement and Expansion of the Fmask Algorithm: Cloud, Cloud Shadow, and Snow Detection for Landsats 4-7, 8, and Sentinel 2 Images. *Remote Sensing of Environment*, 159.